Microfluidic-based In-Situ Functionalization for Detection of Proteins in Heterogeneous Immunoassays

by

Sasan Asiaei

A thesis
presented to the University of Waterloo
in fulfillment of the
thesis requirement for the degree of
Doctor of Philosophy
in
Mechanical Engineering

Waterloo, Ontario, Canada, 2012

Author's Declaration

I hereby declare that I am the sole author of this thesis. This is a true copy of the thesis, including any required final revisions, as accepted by my examiners.

I understand that my thesis may be made electronically available to the public.

Abstract

One the most daunting technical challenges in the realization of biosensors is functionalizing transducing surfaces for the detection of biomolecules. Functionalization is defined as the formation of a bio-compatible interface on the transducing surfaces of bio-chemical sensors for immobilizing and subsequent sensing of biomolecules. The kinetics of functionalization reactions is a particularly important issue, since conventional functionalization protocols are associated with lengthy process times, from hours to days. The objective of this thesis is the improvement of the functionalization protocols and their kinetics for biosensing applications. This objective is realized via modeling and experimental verification of novel functionalization techniques in microfluidic environments. The improved functionalization protocols using microfluidic environments enable in-situ functionalization, which reduces the processing times and the amount of reagents consumed, compared to conventional methods.

The functionalization is performed using self-assembled monolayers (SAMs) of thiols. The thiols are organic compounds with a sulphur group that assists in the chemisorption of the thiol to the surface of metals like gold. The two reactions in the functionalization process examined in this thesis are the SAM formation and the SAM/probe molecule conjugation. SAM/probe molecule conjugation is the chemical treatment of the SAM followed by the binding of the probe molecule to the SAM. In general, the probe molecule is selective in binding with a given biomolecule, called the target molecule. Within this thesis, the probe molecule is an antibody and the target molecule is an antigen. The kinetics of the reaction between the probe (antibody) and the target biomolecule (antigen) is also studied. The reaction between an antigen and its antibody is called the immunoreaction. The biosensing technique that utilizes the immunoreaction is immunoassay.

A numerical model is constructed using the finite element method (FEM), and is used to study the kinetics of the functionalization reactions. The aim of the kinetic studies is to achieve both minimal process times and reagents consumption. The impact of several important parameters on the kinetics of the reactions is investigated, and the trends observed are explained using kinetic descriptive dimensionless numbers, such as the Damköhler number and the Peclet number. Careful numerical modeling of the reactions contributes to a number of findings. A considerably faster than conventional SAM formation protocol is predicted. This fast-SAM protocol is capable of reducing the process times from the conventional 24-hours to 15 minutes. The numerical simulations also predict that conventional conjugation protocols result in the overexposure of the SAM and the probe

molecule to the conjugation reagents. This overexposure consequently lowers conjugation efficiencies. The immunoreaction kinetics of a 70 kilo-Dalton heat shock protein (HSP70) with its antibody in a hypothetical microchannel is also investigated through the FEM simulations. Optimal reaction conditions are determined, including the flow velocity and the surface concentration of the immobilized probes (antibodies).

Based on the numerical results and a series of experimental studies, the fast-SAM protocol application is successfully confirmed. Moreover, the optimum reagent concentration for a given one-hour conjugation process time is determined. This functionalization protocol is successfully applied to immobilize the HSP70 antibody on gold surfaces. The use of the fast-SAM protocol and the predicted optimum conjugation conditions result in binding of the HSP70 antibody on gold, with the same or superior immobilization quality, compared to the conventional protocols. Upon implementation of a $70\ \mu m.s^{-1}$ flow velocity, the reaction is observed to complete in around 30-35 minutes, which is close to the numerically predicted 30 minutes and 16 seconds. This immunoreaction time is considerably less than conventional 4-12 hour processes.

The modified in-situ functionalization techniques achieved here are promising for substantially reducing the preparation times and improving the performance of biosensors, in general, and immunoassays, in particular.

Acknowledgements

First and foremost, I would like to express my sincere gratitude to my supervisor, Professor Patricia Nieva for giving me the opportunity to work on this thesis. Thank you for all of the support you have given me.

I would like to thank my colleagues Brendan Smith, Chelsea Marr, and specially, Ryan Denomme for their precious help during the experimental phase of my research. In particular, their help on implementing the modified functionalization protocols in the QCM and LSPR setups is acknowledged. I have been so fortunate to attend and research among the members of the Sensors and Integrated Microsystems laboratory (SIMSLAB). Thanks to all SIMSLAB members for creating a very friendly and intellectually stimulating environment. Specially, thanks to the previous lab managers of the SIMSLab, Gabriel Krausz, and Jeff McIsaac.

I owe a debt of gratitude to Professor Matt Vijayan, from the Biology Department, for providing valuable consultation, guidance, and assistance in the biological aspects of my project. Also, from Professor Vijayan's lab, I would like to thank Maryam Kamkar and Nita Modi for all of their help throughout my project. Moreover, I would like to acknowledge the warm support and thoughtful discussions I received from professor Spafford and his lab members, specially, Adriano Senatore and Adrienne Boone.

I also wish to thank the members of my dissertation committee, professors Metin Renksizbulut and Serhiy Yarusevych for having accepted to spend their valuable times on reading my thesis and to provide me with their insightful comments and suggestions. I would like to thank professor Ravi Selvaganapathy for participating in my defence exam as the external faculty member.

I extend my deepest gratitude to my parents Shahlawash and Ahamd, and also to my sister Saghar for their wholehearted support and confidence in me. To my parents, I owe all I have ever accomplished, and I would always be indebted to them. I truly believe that I was so fortunate and prosperous to get acquainted and fall in love with my beloved Narges, and finally marry her in the first year of my PhD. I would always appreciate her heartfelt, wise, and continual support and encouragement during the demanding period of my PhD.

Dedication

To the promised existent the “Mahdi“,
To my parents, Shahlawash Sadeghi and Ahmad Asiaei,
and To my beloved spouse, Narges Kermani.

Table of Contents

List of Figures

List of Tables

List of Abbreviations

11-MUA	11-mecaptoundecanoic acid
1-OT	1-octanethiol
Ab	Antibody
Ag	Antigen
BDF	Backward differentiation formula
CCT	Covalent coupling technique
CD	Compact disc
DI	De-ionized
EBL	Electron beam lithography
EDC	1-ethyl-3-(3-dimethylaminopropyl)
FT-IR	Fourier Transform Infrared
HIA	Heterogeneous immunoassays
HOBt	N-hydroxybenzotriazole
IA	Immunoassay
Ig	Immunoglobulin
IgG	Immuno gamma globulin
IPA	Isopropyl alcohol
kDa	kilo-Daltons
LOD	Limit of detection
LSPR	Localized surface plasmon resonance
MUMPS	Multi-frontal massively parallel sparse direct solver
NHS	N-Hydroxysuccinimide
PBS	phosphate buffered saline
PDMS	Poly dimethylsiloxane
PET	Poly ethylene terephthalate
PMMA	Poly methylmethacrylate
RI	Refractive Index
SAM	Self-assembled monolayer
SERS	Surface enhanced Raman scattering
SMI	Spatially Modulated Illumination microscopes
SPR	Surface plasmon resonance

μCP	Micro-contact printing

List of Symbols

u_{avg}	The average flow velocity in the microchannel $[m/s]$
h	The height of the microchannel $[m]$
h_{min}	The minimum height that contains total amount of reactants needed for the completion of reaction $[m]$
ρ	The density $[kg/m^3]$
μ	The dynamic viscosity $[Pa.s]$
Re	The Reynolds number
L_e	The entrance length $[m]$
∇	The gradient vector operator
p	The pressure $[Pa]$
$\underset{u}{\rightarrow}$	The velocity vector $[m/s]$
c	The instantaneous concentration of the reagents in the bulk fluid $[moles/m^3]$ or $[M]$
D	The diffusion coefficient of the reagents $[m^2/s]$
D_s	The surface diffusion coefficient of the reagents $[m^2/s]$
R_s	The reaction rate term $[moles/m^2.s]$
c_0	The input concentration of the reagents $[M]$
c_s	Surface concentration of bound (reacted) analytes $[moles/m^2]$
$\underset{n}{\rightarrow}$	The unit normal vector to the surface
θ_0	Total surface concentration of binding (reaction) sites $[moles/m^2]$
θ'	The instantaneous surface concentration of available binding (reaction) sites $[moles/m^2]$
k_a	The association constant $[1/(Ms)]$
k_d	The dissociation constant $[1/s]$
k_t	The rearrangement rate constant in the thiol self-assembly $[1/s]$
Pe	The Peclet number
Da	The Damköhler number
δ_c	The thickness of the depletion zone
ϵ	The binding (adsorption) capacity (Dimensionless)
β	The reaction or convection capacity (Dimensionless)
c_s^*	The dimensionless surface concentration of bound (reacted) analytes: $c_s^* = c_s/\theta_0$
T_{comp}	The reaction completion time $[s]$

t^*	The dimensionless time: $t^* = t/T_{comp}$
x^*	The dimensionless length: $x^* = x/l$
u^*	The dimensionless velocity: $u^* = u/u_{avg}$
x_{trv}	The distance that the analyte can convectively travel [m]
f	The natural resonance frequency [Hz]
Δm	The mass change in unit area [kg]

List of Notations

$A \sim B$	A is approximately equal to B
$A \overset{f}{\Rightarrow} B$	When condition (or reaction) f is present, A results in B
$A \ll B$	A is much smaller than B
A_B	A in the medium or reaction B
$A_{,f,B}$	A of the reagent or molecule f in the medium B
$A \overset{f}{\rightarrow} B$	f changes from the amount A to the amount B
$A < f < B$	f is between the amounts A and B
$A \equiv B$	A is identical to B
A': B"	A minutes and B seconds

Chapter 1
Introduction

1.1 Motivation

One the most challenging steps in the realization of biosensors is the functionalization of transducing surfaces for the detection of biomolecules [1]. Functionalization is defined as the formation of a bio-compatible interface on the transducing surfaces of bio-chemical sensors, for immobilizing and subsequent sensing of biomolecules [1, 2]. The conventional functionalization techniques are associated with lengthy process times and high levels of consumption of the sample analyte. These two shortcomings can be addressed by implementation and modification of the conventional functionalization techniques in microfluidic environments [3, 4]. The functionalization techniques used in microfluidic systems are often based on the physical entrapment of a "probe molecule" behind a membrane. The probe molecule is selective in binding with a given biomolecule, called the target molecule. The physical entrapment technique results in low levels of sensitivity, since various biomolecules are caught behind the membrane, leading to the binding of the unwanted molecules, known as non-specific binding [5, 6]. The physical entrapment technique might also result in the denaturation of proteins [1]. Accordingly, it is necessary to modify the conventional functionalization techniques that are used in microfluidic systems [7]. The resulting functionalization techniques should efficiently prevent non-specific binding and produce biologically compatible interfaces (bio-interfaces) [7, 8].

One method suitable for the functionalization involves self-assembled monolayers (SAMs) of thiols that can easily form a packed, robust, and thin organic monolayer [9, 10]. Thiols are organic compounds that contain a sulfhydryl group (–SH) on one end of their chain of carbon-containing atoms. The thiols have a high affinity for being chemisorbed to the surface of metals, such as gold, from their sulfhydryl group [9]. Once bound to the probe molecules, in a process called conjugation, the SAM forms a highly specific detection surface and mimics the natural environment for molecular recognition on the transducer interface. The SAM is conventionally formed by the incubation of the transducer surfaces in the thiolic solution for 24 hours [11, 12]. Microfluidics has the potential to enhance the slow kinetics of the self-assembly by the magnification of the thiol replenishment rate to the transducer surface [3, 4].

The kinetic aspects of the conventional SAM formation protocols have been carefully studied [9, 13]. Nevertheless, only a few studies have focused on the kinetics of the thiolic self-assembly on the transducer surfaces of microfluidic-based biosensors [14-18]. Moreover, the kinetics of the relevant functionalization reactions have not been thoroughly examined. Major reactions involved include SAM formation on the transducer surfaces, chemical treatment of SAMs for binding probe molecules, and binding of the target molecule by the probe [1]. Other than the self-assembly reaction, the SAM/probe molecule conjugation, and the probe/target molecule binding reactions are also prone to lengthy processes, between 1-3 hours and 4-12 hours, respectively [12, 19-21]. Microfluidics has the potential to enhance the kinetics of the above-mentioned reactions [3, 4]. This improvement occurs because while the conventional methods rely only on diffusion as the reagents transport mode, microfluidics adds convection to better replenish the reagents to the reaction surfaces. At the time of writing this thesis, no comprehensive report has been found on the microfluidic-based formation and treatment of the SAMs for immobilization of the probe molecules, called here in-situ functionalization, and the associated kinetics.

This thesis deals with the improvement of the kinetics of conventional functionalization reactions, which have lengthy processes. The kinetics of the reactions involved are studied, aiming for minimal process times and reagent consumption. This investigation is done through the numerical modeling of reactions occurring in microfluidic environments. The reactions considered include the SAM formation, the SAM/antibody (probe) conjugation, and the antibody/antigen binding. Numerical examination of the kinetics of self-assembly and conjugation reactions in microchannels are performed in this thesis, for the first time. Modeling is followed by experiments for verification and characterization purposes. The success of the in-situ functionalization protocols is assessed by attaching proteins and their probe molecules to the bio-interface, and characterizing the resulting loading densities. The self-assembly process time is successfully decreased from 24-hours (conventional protocols) to 15 minutes. Within this thesis, the probe molecule is an antibody and the target molecule is an antigen. The reaction between an antigen and its antibody is called the immunoreaction, and the biosensing technique that utilizes the immunoreaction is termed immunoassay [20, 22]. The in-situ functionalization technique described above is a novel, promising candidate for implementation in biosensors, in general, and immunoassays, in particular.

1.2 Immunoassay

The immunoassay technique, its underlying concept, application and classification are introduced in this section.

1.2.1 Immunoreaction

The immune system in an organism is defined as the biological structures and processes that protect the organism against disease. Upon the exposure of the organism to external invading substances, such as bacteria and viruses, special protein called antibodies (Abs) are secreted into the blood to neutralize the invading substance [23, 24]. This external substance that stimulates the Ab secretion is called an antigen (Ag). An Ab specifically binds to the corresponding Ag and neutralizes it upon binding or initiates further immunological reactions, such as cell killing and inflammation. The specific binding of an Ab and its corresponding Ag is termed an immunoreaction [20-22]. The specificity of the Ab-Ag binding reaction is due to the complementary structure of these two proteins [20, 21, 23].

Abs belong to immunoglobulin (Ig) proteins with a Y-shaped structure, schematically shown in Figure 1.1. An Ab has a base "constant region" part that is the same for all Igs in the same class, but the tip can be different and is termed the "variable region". Abs and Ags have complimentary binding structures, respectively named the paratope and epitope, which result in the specificity of the Ab-Ag interaction. A paratope is located on the tip of the "Y" shape of an Ab, i.e., the variable region, and has a structure analogous to a lock that is unique for each type of Ab. The paratope is specific for a particular epitope on an Ag, analogous to a key [23, 24]. This paratope lock enables the Ab to uniquely recognize a specific Ag (key), from other biomolecules.

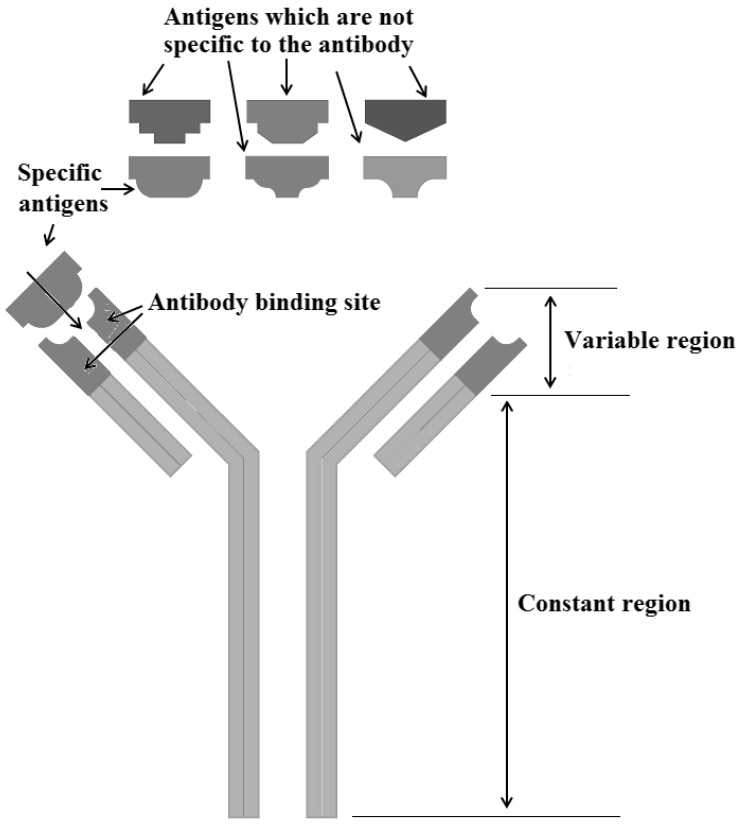

Figure 1.1: Schematic structure of an antibody molecule, the antibody uniquely recognizes a specific antigen, from other biomolecules. Produced from [23, 24].

1.2.2 Immunoassays: Concept, Application and Classification

The specificity of Ab/Ag immunoreaction can be used to measure the presence or concentration of a substance, called an analyte, in solutions. This biochemical technique is called an immunoassay (IA) [22, 23].

The immunoassay technique was firstly used in the late 1950s for analyzing hormones [25, 26]. Soon after, the application was extended to detection and quantification of a wide spectrum of analytes from therapeutic drugs, enzymes, vitamins to tumor markers, infectious agents, environment and agriculture [20, 27].

Based on where the immunoreaction takes place, an immunoassay can be classified as homogeneous or heterogeneous. In a homogeneous IA, the immunoreaction happens in a homogeneous liquid. Because of this homogeneity of the reaction medium, homogeneous IA is faster

than the heterogeneous counterpart, since the reaction surface area is the maximum possible, but sensing is difficult to develop. This difficulty occurs because the detection mechanism used should accumulate randomly distributed weak signals from a rather large volume of the reaction medium. Thus, the sensitivity is low; otherwise the sensor becomes bulky and analyte consumption will be relatively high for each test, sometimes making the IA impossible. Homogenous IAs are mainly used to monitor the relatively high concentration of drugs in blood [21].

In heterogeneous IAs, there is a liquid-solid interface on which the Ab binds to the Ag. The solid interface efficiently separates bound and free reagents. Moreover, the Abs can be densely immobilized on the interface, even from dilute solutions, enabling a higher level of sensitivity for the Ag. The interface can be conveniently placed in the platform, introducing flexibility to suit different sensing mechanisms. Accordingly, heterogeneous IAs are more sensitive and adaptable techniques than homogeneous IAs [22, 27, 28]. In this thesis, the focus is on heterogeneous immunoassays.

1.2.3 Heterogeneous Immunoassay (HIA): Components and Stages

Heterogeneous immunoassays (HIA) have basically three components: the capture system, the analyte, and the detection system. Either an Ab or Ag is immobilized on the solid interface to probe the target molecule (analyte), forming a capture system, and the other one will be detected by being bound (analyte). The third component of an HIA is the detection system that translates the binding of the probe molecule and the analyte to a physical measurable signal.

Conducting an HIA involves five stages, which are the immobilization of Abs to a solid surface (functionalization), immunoreaction, blocking of non-specific binding, washing the unbound molecules away from the reaction medium, and detection [20, 21, 28]. This thesis mainly practices the first stage, and its relevant techniques are briefly introduced below.

1.3 Functionalization in Heterogeneous Immunoassays

The following topics are presented in this section: the functionalization techniques used in HIAs, the microfluidic-based functionalization in HIAs, the operational aspects of the microfluidic HIAs, the kinetic aspect of the functionalization reactions in microfluidic HIAs, and possible kinetic improvements.

1.3.1 Functionalization Techniques

A variety of probe molecule immobilization/surface functionalization techniques are available for implementation in HIAs, depending on the sensing mechanisms and the nature of the biological components [1]. The probe molecule may be adsorbed directly by the transducer surface [1], physically entrapped behind a membrane or a polymer gel [1], covalently coupled to the sensing surface or attached onto an immobilized polymer or monolayer on the transducing surface [1, 29]. Direct adsorption of the ligand onto the transducing surface has been used in test setups as a temporary means of performance assessment and as a simple, inexpensive, and single-use method [1]. However, this technique is relatively unstable and denatures the protein of interest over time [1]. Entrapment of the probe molecule near the transducer surface is useful for macromolecules, such as cells and organelles [1, 5]. However, the associated low rates of diffusion of macromolecules give a slow response time, and the proteins are prone to denaturation [1, 5]. Covalent coupling has a number of advantages over the aforementioned techniques in terms of stable coupling capabilities, close contact distances of analytes with the transducer surface, and rapid response times [1, 29]. Despite relatively high costs associated with the derivation and the limited binding sites leading to relatively shorter lifetimes, the higher reliability and the higher corresponding signal quality have led to a widespread implementation of the covalent coupling methods in biosensing applications, including HIAs [1, 19].

1.3.2 Covalent Coupling Functionalization Techniques

The functionalization in HIAs is most commonly realized through the covalent coupling of polymers [29] or through the formation of the thiolic SAMs on metal surfaces [1]. Polymer-based functionalization has been widely used in surface plasmon resonance (SPR) detection techniques, and has been the primary method implemented in commercial biosensors of the past decade [30, 30-32]. The polymer is uniformly spread over the entire transducing surface of the biosensor. Therefore, upon

the binding of the analyte to the transducing surface, a uniformly distributed signal is generated. Despite numerous successful demonstrations, polymeric functionalization cannot be employed in all detection systems, especially in optical nanoparticle-based sensing techniques such as localized surface plasmon resonance (LSPR) and surface enhanced Raman scattering (SERS) [33]. In these nanoparticle-based techniques, the detection signal should purely result from the binding of analytes to the metal nanoparticles [33]. Thus, the rest of the substrate should be kept free from any binding. Otherwise, there will be signal interference from the binding of biomolecules to the nanoparticles and the rest of the substrate. Alternatively, using SAMs allows the probe molecules to be localized to the metal nanoparticles, due to the preferential assembly of the SAM molecules on metals and minimal or no assembly on the surrounding substrate. Accordingly, the detection signal is solely generated from binding to the nanoparticles. Thus, SAM-based covalent coupling is preferred for the functionalization of nanoparticle-based detection systems. One of the reasons behind the adoption of SAM-based functionalization in this research is its broader application area compared to polymers.

Since the first demonstration of SAMs in 1946 [34], functionalization with SAMs has been implemented in all the detection systems that can be used in HIAs from optical [14], to electrochemical [17], and mechanical techniques [15]. SAMs have the potential to minimize the spontaneous adsorption of proteins and other molecules to the surface of noble metals such as gold, helping to lower the non-specific adsorption [9]. SAMs can also mimic the natural environment for molecular recognition on the transducer interface [10]. Due to the nano-scale thickness of SAMs, the immobilized target biomolecules are kept in close contact with the transducer surface, increasing the sensitivity, thereby enabling a faster response to the binding event [35]. Apart from the general implications of SAMs, the wide acceptance of SAMs in the biosensing market is also attributed to their straightforward chemical process of self-assembly on metal surfaces [9, 10, 17].

Thiols self-assembly protocols have been extensively explored, and different aspects of the topic have been thoroughly studied, including the SAM formation chemical process, packing density calculations, and surface topography and characterization [9, 13]. SAMs are often formed by the chemisorption of thiols on metal surfaces, such as those of gold and silver, through the formation of strong covalent metal-thiol surface bonds, from the sulfur group of the thiol [9, 13, 35]. The chemisorption is accomplished through immersion of the metal surface in a thiolic solution, conventionally for 24 hours [11, 12]. SAMs are very prone to be oxidized when exposed to air; therefore, the handling of SAMs remains problematic [36]. In order to avoid oxidation of the SAM

throughout the functionalization processes, the surfaces loaded with the SAM should be kept away from air. Under these requirements, microfluidics is a good candidate for the functionalization environment. Moreover, microfluidic can potentially improve the slow kinetics of conventional SAM formation protocols. To the best of our knowledge, microfluidic-based self-assembly of thiols has not been comprehensively examined in the literature. In this regard, the research outlined in the following sections will contribute to achieving a faster than conventional SAM-based in-situ functionalization process to be used in bio-chemical sensors, including HIAs.

1.3.2.1 Self-Assembled Monolayers

Bio-chemical sensing, in general, and immunoassay conduction, in particular, requires localization or attachment of the molecular receptors (probes) near to or on the transducing surfaces of the biosensors (functionalization) [1]. In order to minimize the spontaneous adsorption of proteins and other molecules to the transducing surfaces, and also to mimic the natural environment for analyte recognition, SAMs of thiols have been formed on the metal transducing surface of several bio-chemical sensors [9, 37]. Upon SAM formation, a highly packed monolayer of nanometer thickness is formed on the metallic surface, minimizing the spontaneous adsorption to metallic surfaces [9, 10]. These promising attributes of the SAMs for bio-sensing applications are attributed to their chemical structure [9, 10].

A succinct technical definition of SAMs is organized layers of amphiphilic molecules of which one end of the molecule, the "head group", shows a high affinity for being chemisorbed to a substrate (which is gold in this case), while the terminal functional group of the "tail" end is tailored for capturing a foreign species of choice [9, 13], presented schematically in Figure 1.2.

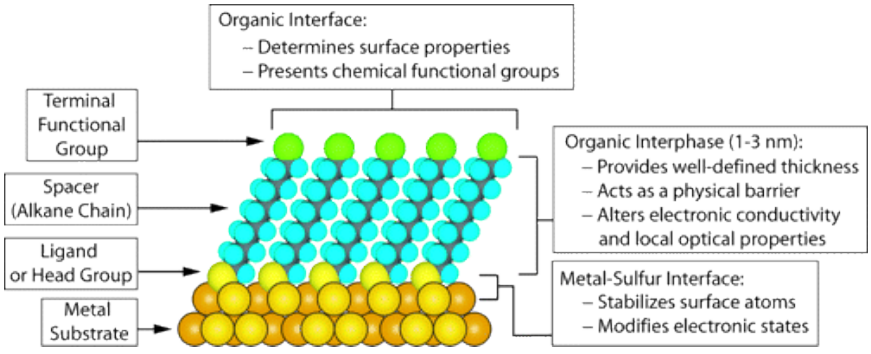

Figure 1.2: Schematic diagram of a thiolic SAM on gold, its functional groups and structure, reprinted with permission from [9].

SAMs can be formed with a variety of functional head and end groups to suit the immobilization of the biomolecule of interest [9]. Here, thiolic SAMs with carboxylic end groups are used. These thiols are chemisorbed to the surface of gold by their head groups, and form a packed, uniform monolayer over the surface. At the same time, their carboxylic end groups are exposed to the analyte-carrying medium, such as buffer fluids, enabling conjugation with Abs [9, 10].

Thiols employed in this research are 11-mecaptoundecanoic acid (11-MUA) with carboxylic end groups, and 1-octanethiol (1-OT), which serves as a spacer and support for 11-MUA [1, 11, 38]. These two thiols have been chosen mainly for their kinetic properties. Film mass and coverage thickness measurements showed that shorter chain monolayers of thiols with 8 and 12 carbons in their molecular chains, C_8 and C_{12}, have considerably faster kinetics than longer chain molecules. These short-chain thiols attain more than 80% of their final coverage in the first few minutes or hours of the self-assembly, depending on the thiol concentration in solution [39]. In comparison, longer-chain thiols (C_{16} and C_{18}), receive only 40%–50% of their final coverage in the same period [39]. For this research,11-MUA and 1-OT are adopted since they are in the C_8-C_{12} range of chain length. The packing density of the two thiols is 4.4×10^{14} molecules/cm^2 [11]. Accordingly, there are around 60000 thiols in $1.4 \times 10^{-10}\ cm^2$ [38]. Throughout this chapter, a $1\ mM$ mixture of (3: 1) 1-OT: 11-MUA in ethanol is used. This mixture produces a surface fraction of 10:1 of the corresponding thiols [38]. This fraction is crucial for prohibiting steric hindrance that occurs when the terminal functional groups of adjacent SAM molecules are blocking each other's binding to the Abs [11]. Calculations show that for the above SAM, there are around 6000 carboxyl ended thiols per $1.4 \times 10^{-10}\ cm^2$ of the transducing surface that could be conjugated with Abs of interest [38].

The next step in functionalization after formation of a thiolic SAM is to mediate attachment of the Abs to the SAM. This mediation is necessary since SAMs and Abs do not have chemically active groups in common, and therefore, they can hardly be attached to each other in their natural state. The following section covers the process of Ab/SAM conjugation mediation, called crosslinking [19].

1.3.2.2 Antibody/SAM Conjugation

Crosslinking is the chemical process of forming intermolecular linkages between molecules of interest [1, 19]. Crosslinking of biological molecules, often called bio-conjugation, normally has a low yield and is not necessarily limited to a single reagent. The simplest form of the bio-conjugation is the so-called zero-length crosslinking, in which the reagent (crosslinker) mediates the conjugation

of two molecules by forming a bond with no additional atoms [19]. In other words, one atom of the first molecule has a covalent bond to an atom of the second molecule without any intermediate molecule. This direct covalent bonding is especially important when the presence of intervening linkers is detrimental to the intended functionality of the conjugating biomolecules [19].

The zero-length crosslinking reagents described in this research are mainly used to initialize an amide bond between an amine and a carboxylic acid [1, 19]. Here, the focus is on conjugation of Abs with an abundance of amine groups and the carboxylic groups present on the surface of the self-assembled thiolic monolayer. For this aim, the most popular type of zero-length crosslinker, carbodiimide, is used. The concept presented here can be easily modified for immobilization of other proteins with a variety of functional groups [1, 19].

The functionalization in this research is accomplished by conjugating an Ab from its amine group to the exposed carboxylic group of a thiolic SAM. The Ab can specifically bind the Ag (analyte) of interest. Ab molecules, in general, have three amine functional groups available for conjugation with carboxylic acids [1, 19]: lysine ε-amine, the N-terminus and the α-amine group. In addition, the carboxylate groups present at C-terminus can be conjugated, but are not considered here [19]. The carbodiimide used in this research is EDC, also called EDAC or EDCI, acronyms for 1-ethyl-3-(3-dimethylaminopropyl) carbodiimide. When EDC reacts with a carboxylic group, a highly reactive intermediate chemical called o-acylisourea is formed [19]. The carboxylic group could be the end group of a thiolic SAM on gold, represented here by R in Figure 1.3 below.

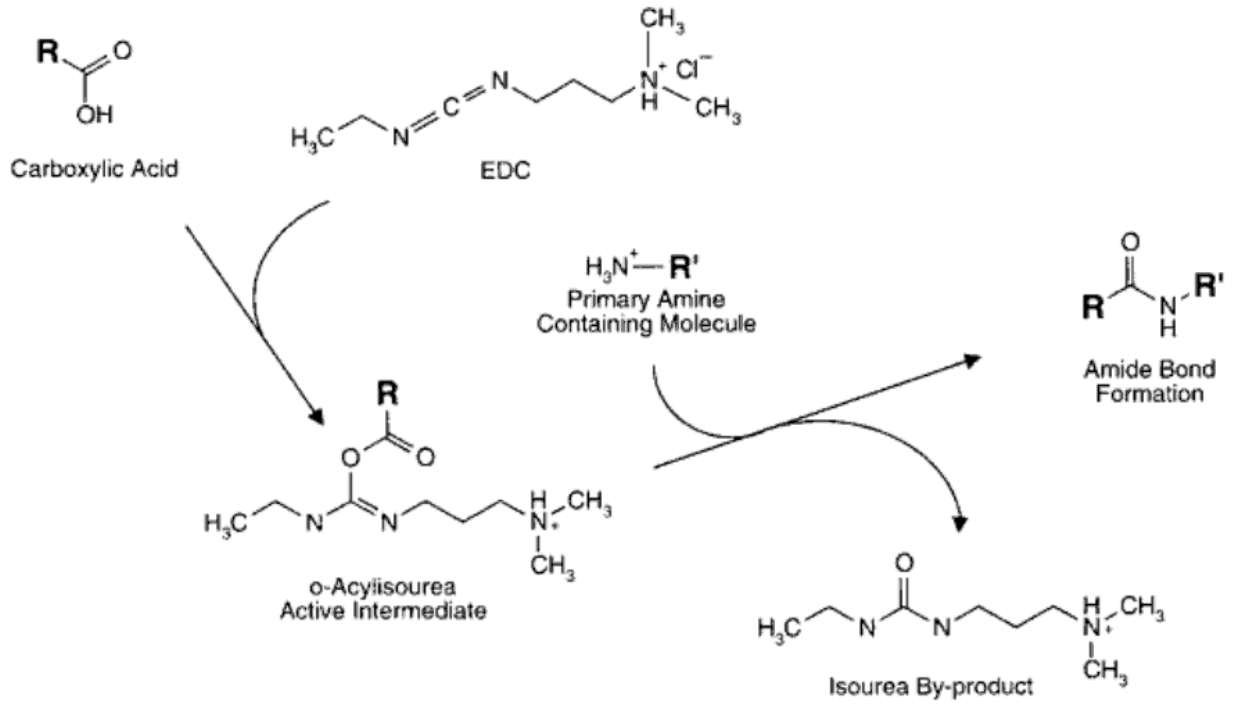

Figure 1.3: Amide bond formation between carboxylic group of SAMs (*R*) and amine group of antibodies (R′). The by-product of the reaction is an isourea. Reprinted with permission from [19].

This active ester (o-acylisourea) reacts with a nucleophile, such as an amine group of an Ab (R'), to form an amide bond [1, 19]. Because of this nucleophilic activity, there is a controversy in the choice of appropriate pH of the reaction. While carboxylates are activated most efficiently at pH 3.5-4.5, amide bond formation has its highest rate at pH 4-6. Furthermore, the EDC carbodiimide is more stable in solution at or above pH 6.5. Finally, EDC hydrolysis, as the major competing reaction, occurs at the highest level in an acidic pH. Therefore, it has been concluded that EDC-mediated amide bond formation has its best yield in a range of pH between 4.5 and 7.5. Also, when EDC conjugation is performed for a molecule that has both carboxylates and amines, such as Abs here, the molecules under conjugation may be attached to each other instead of reacting with the carboxyl-containing molecule (SAM), in a process called clustering. In such circumstances, implementing carbodiimides in slightly alkaline pH conditions limits the unfavorable cluster formation [19]. Based on the above facts, the pH is kept at 7.4 in all the experiments outlined in this chapter.

1.3.3 Microfluidics-based Functionalization by Self-Assembled Monolayers

Microfluidics is defined as liquid or gas manipulation in microchannels with cross-sectional dimensions in the order of 10-100 μm [28]. The technology emerged in the 1970s during development of a miniaturized gas chromatograph in Stanford University [40]. In the 1990s, microfluidics blossomed due to the availability of the fabrication and simulation techniques required, and moreover, growing interest in biology and biotechnology [41, 42]. There are a number of advantages that resulted in the "vast interest and fast rising" of microfluidics over conventional analytical instruments, including reduced analysis time, consumption of reagents, and cost of power and material, as well as increased portability and flexibility of design [28]. Valuable reviews have been written on the capabilities of microfluidics in biosensing applications [43-51]. In all these microfluidic biosensors, the formation of reliable capture systems (functionalization) has always been a critical performance requirement [7, 8].

One of the early microfluidic demonstrations for in-situ functionalization was a planar micromosaic HIA [52]. Strands of Ags were placed along micrometer-wide intersecting lines to capture fluorescently labeled Abs from a series of analytes. The performance of the device as a dense HIA, with nanoliter consumption of reagents was promising [52]. However, the technology suffered from a laborious labeling process and a lack of reliable immobilization. A second non-covalent method for in-situ functionalization involved the entrapment of DNA hydrogel "plugs" in microfluidic channels [5]. In this approach, labeling and the problems associated with the physical entrapment techniques employed were two major obstacles to overcome [5, 6]. The labeling process used alters the natural form of the analyte and limits its functionality, thus prohibiting a vast spectrum of the bio-chemical reactions from being studied [14]. The labeling problems were mainly addressed through the development of label-free optical and electro-chemical detection mechanisms [8, 33, 53]. On the other hand, the problems associated with the entrapment technique have been alleviated using covalent coupling techniques (CCTs) on the microchannel walls [54].

The introduction of CCTs in microfluidics has had many implications for the functionalization of HIAs with optical and electro-chemical detection systems, including: the elimination of non-specific adsorption, increased binding affinity, and enhanced specificity [9, 10]. Regarding the detection systems, except for the optical refractive index (RI)-based techniques, miniaturization often results in a shorter optical path length and, subsequently, reduced sensitivity [8]. The optical path length refers to the distance that light travels inside a sample analyte [7, 8]. In RI-based techniques, the RI change

due to the molecular interactions is measured and correlated to the sample concentration of analytes or surface density of the immobilized target biomolecules, instead of the total sample mass. Therefore, miniaturization does not affect the sensitivity in RI-based techniques [14]. In labeled techniques in which the sensitivity heavily depends on the optical path length, CCTs have contributed little to a solution for most of the aforementioned problem of miniaturization [14]. Therefore, researchers have explored the utilization of CCTs with label-free approaches [8, 14]. Another performance requirement for the CCTs used in the functionalization of microfluidic systems is imposing minimal decay levels on the detection signal. Additionally, the non-specific binding should be minimized through the CCT used for the functionalization [55].

The SAMs utilization in the functionalization of microfluidic HIAs can fulfill all the above-mentioned requirements of an effective functionalization process. The nanometer thickness of the SAM imposes minimum resistance to the transfer of the detection signal [9, 10]. Non-specific binding often results from the spontaneous adsorption of proteins to the surface of metals such as gold and silver. Upon formation, SAMs cover the whole metallic transuding surface, eliminating the exposure of the metallic surface to proteins, and thus, non-specific binding [9, 10]. Moreover, SAMs form a packed, dense, and chemically stable bio-interface. Therefore, the environmental properties of the capture system, such as pH and temperature, can be reliably controlled in SAM-based interfaces [9, 10]. SAM interfaces are usually produced external to the sensor platform, called ex-situ, and then assembled into the sensor, often generating disposable microfluidics as an independent unit to be added to the sensor [56]. The addition of a new unit to the sensor platform may cause some technical problems, including handling problems. In contrast, in-situ functionalization of SAMs for label-free detection systems not only can eliminate the necessity of an additive disposable microfluidic unit but also addresses the technical shortcomings outlined in Section 1.1. Thus, in-situ functionalization with SAMs, as a nearly unexplored technique, shows potential for fulfilling the technical requirements of an effective capture system in HIAs [7].

1.3.4 Operational Aspects of Microfluidic HIAs

The specific operational aspects of a microfluidic HIA are reviewed below, including the solid phase, surface modification (functionalization) and Ab/Ag immobilization, delivery of sample/reagent solutions, and detection. This research deals mainly with the functionalization aspect; however, others are briefly discussed as well.

1.3.4.1 Solid phase

There are three major types of solid phases in microfluidic HIAs: the walls of a microchannel, beads, and gold-coated surfaces.

The most common materials used for fabricating microchannels are silicon, glass and polymer materials such as poly ethylene terephthalate (PET), polycarbonate, polystyrene (only as a flat substrate for a hybrid chip), poly methylmethacrylate (PMMA), and the most popular one, poly dimethylsiloxane (PDMS) [57-60].

Beads with normal diameters of one or two orders lower than the size of the microchannels holding them have been employed as the solid phase for immunoreaction. Employment of beads significantly increases the surface area on which the Ab can be immobilized. Beads are often fabricated from polymers or silica [45, 61-63].

Implementation of gold film substrates in the capture or detection systems of HIAs is relatively recent [28]. Gold films are used in the form of planar gold and nanoparticles on which the immunoreaction takes place [1, 64]. Use of gold films in HIAs have been demonstrated in a number of detection system technologies [14, 17, 29, 65-67], among the most successful are electrochemical [68, 69] and SPR HIAs [70, 71], which use planar gold substrates, and LSPR HIAs [53], in which gold in the form of nanoparticles is employed in the detection system.

1.3.4.2 Functionalization

The most reliable functionalization method is through covalent bonding of polymers or SAMs on the gold surfaces. This bonding can be done passively or actively. In passive approaches, after SAM or polymer implantation, various reagents may be used to activate the SAM or polymer to covalently bind the probe molecule [19], including carbodiimides, succinimidyl esters, glutaraldehyde and silanes [19]. After immobilization of the probe molecule, the capture system is ready to bind the target analyte. There are also techniques for active functionalization, which locally deliver proteins to a solid surface. Ink-jet printing or microarraying with fine metal tips or by electrospray are among the examples [72]. Micro-contact printing (μCP) is another successful active patterning technique. In this technique, a PDMS “stamp” bearing geometric patterns transfers “ink” from SAMs, to a gold surface [60]. This thesis focuses on the passive functionalization of gold surfaces with SAMs.

1.3.4.3 Delivery of sample or reagent solutions

The solution transport platform is the driving component of a microfluidic analytical device. Several typical flow systems are employed in HIAs, including pressure-driven flow, capillary flow, centrifugal force-driven flow and electrokinetically-driven flow. A number of valuable books and reviews are available covering the different techniques of fluid transport in microfluidic systems [73-77]. The definition and application of each technique are included in the following.

1) Pressure-driven flow

The most extensively used method of sample delivery in microfluidic IAs is pressure driven flow, since in this technique the fluid pumping is independent of the fluid composition and the properties of the channel surface. Moreover, the pressure difference required across the microchannels is exerted mostly by a syringe pump, which allows for a precisely controlled flow rate. Pressure-driven flow in microfluidic IAs is basically an incompressible flow in a conduit with constant cross-section, known as Poiseuille flow. In pressure driven flow, the electroviscous effect might become important in the presence of the electromagnetic field of electrodes in a microfluidic chip, resulting in flow retardation of less than 10% [78]. In this research, no significant electromagnetic field is present, and the samples are delivered using the pressure-driven flow, employing a syringe micropump.

2) Capillary flows

The surface tension of liquids naturally induces capillary flow [75]. Capillary flow does not require any energy supply, making the assay cheap and portable. However, channel geometry, sample surface wetting properties, and viscosity control the flow direction and velocity, limiting the assay time [75]. Because of the above facts, this flow platform has rarely been demonstrated successfully. The "micromosaic" design introduced in Section 1.3.2.1 is one of the few successful demonstrations of this flow delivery technique [52].

3) Centrifugal force-driven flow

Centrifugal microfluidic biodisks, also called bio-affinity CDs, work based on analytes' radial movement in the microchannels of an IA with the shape of a commercial compact disc (CD). The centrifugal forces are induced due to the rotation of the CD [79]. The fluid flow velocity, and thus, incubation time can be controlled by the angular velocity of the CD, according to the surface

hydrophobicity level of the sample under study. The rotational symmetry of the CD allows for parallelization of the assays in one disk [80].

4) Electrokinetically-driven flow

Electrokinetics results from the surface charge densities accumulated on solid surfaces due to contact with an aqueous solution. These surface charges, in turn, influence the liquids' ion distribution near the solid-liquid interface. Accordingly, the surfaces attract the counter ions from the bulk liquid. Near the solid, the bulk liquid obtains higher concentrations of ions with the same sign as the solid charge, called co-ions. Upon movement of the bulk liquid by an external force such as pressure difference, the ions around the interface are displaced, inducing an ion imbalance. This latter charge state brings in a net flow of ions and surrounding fluid particles in the counter direction of the main flow, called electrokinetic flow [74]. The electrokinetic transport phenomena have been extensively implemented in microfluidic IAs by applying electric fields, called electroosmosis [78]. There is another important electrokinetic phenomenon in microfluidic IAs called electrophoresis, i.e., induced movement of proteins inside the sample due to their surface charge density under applied electromagnetic fields. The main advantage of electrokinetic pumping is fluid pumping without moving parts. Moreover, there is a possibility to tune the flow rate by tuning the magnitude of the applied electric field [74]. Throughout the experiments in this thesis, no significant applied electric or magnetic fields are present, therefore, electrokinetic effects are safely ignored.

1.3.4.4 Detection

Different detection systems have been employed in HIAs, in two categories: labeled and label-free methods. The labeled approach is mainly used for detection in conventional IAs, although there are a few demonstrations of labeled approaches in microfluidic HIAs as well [81]. Because in labeled techniques sensitivity is dependent on the cross-sectional path length, sensitivity is reduced due to miniaturization (Section 1.3.2.1) [81]. Fluorescence is still widely used in HIAs due to the ease of label integration [28]; however, fluorescence requires the use of bulky microscopes, and therefore, limits the portability of the platform [8].

With the increasing need for portable platforms, interest in label-free approaches has increased. After fluorescence technique, the second most common technique used in the detection system of HIAs is electrochemical detection, which brings in high levels of sensitivity. In electrochemical detection, the sensitivity is increased due to miniaturization. Optical techniques also have the

potential of miniaturization without lowered sensitivity levels [14]. Some of the optical label-free platforms used in microfluidic HIAs include SPR [70, 71], LSPR, and refractometric techniques [8, 53].

1.3.5 Kinetic Improvements

In-situ functionalization can potentially enhance the slow preparation and reaction kinetics of conventional HIAs. HIA assay times are mainly limited by the passive diffusion rate of the analytes into the capture system to react with the immobilized probe. This penetration distance falls in the order of millimeters in microtitre wells [28]. The diffusion time (t) can be approximated by the Enistein-Smoluchowski equation [82-84]:

$$t = \frac{d^2}{2D} \tag{1.1}$$

where D is the diffusion coefficient, d is the diffusion distance, and t is the diffusion time. For a typical immunoglobulin (Ig) molecule, such as an Ab, $D = 4 \times 10^{-7}\ cm^2.s^{-1}$ [85]. Assuming the diffusion distance to be $1\ mm$, the diffusion time, in other words the incubation time, is approximately 3 hours and 30 minutes. This calculation shows that conventional HIAs have long incubations, which is sometimes unacceptable for practical bio-medical applications. In addition, the long assay time of conventional HIAs is a big obstacle to overcome in the realization of a portable device. Microfluidics can not only help the replenishment of analytes to the reaction site, but also, the size scale used in microfluidic devices helps to dramatically reduce the diffusion distance of the analytes from the source to the reaction site on the capture system. For instance, in the above example, let us assume that the distance is reduced from $1\ mm$ ($1000\ \mu m$) to $500\ \mu m$, which is an easily achievable miniaturization in microfluidic applications [28, 74, 77]. The diffusion time will be theoretically reduced 4 times to around one hour, which saves a considerable amount of time. The long assay times of conventional HIAs necessitate a comprehensive study of the kinetics of reactions involved in HIA preparation stages, from the functionalization processes to the analytes binding reaction, looking for possible kinetics enhancements. In this thesis, it is demonstrated that the preparation times of an HIA can be considerably reduced. This kinetics enhancement is realized through the modification of the conventional functionalization protocols used, or the implementation of a microfluidic-based flow-through mass transport, compared to conventional static incubation processes, or a combination of these two.

1.4 Objective of This Thesis and Contributions

The objective of this thesis is to improve the kinetics of functionalization reactions in HIAs, via modeling and implementation of SAM-based in-situ functionalization techniques. This objective is realized through careful numerical examination of the chemical reactions encountered in the HIAs by the finite element method. The following reactions are examined: self-assembly of thiols on gold surfaces, conjugation of Abs with the SAM, and also the Ab/Ag immunoreaction. Main modeling predictions are experimentally verified for a 70 kilo-Dalton heat shock protein (HSP70) and other model analytes, such as a biotin-streptavidin pair and a typical IgG Ab. The functionalization protocol findings are general enough to be used for improving the kinetics of functionalization reactions in biosensors, in general, and the HIAs, in particular, with different detection systems and for a variety of target analytes.

The contributions of the above mentioned objective can be itemized as follows:

- Development of a numerical model for studying the self-assembly kinetics of thiols on gold surfaces in microchannels. The model is capable of examining the effect of fluidic and geometrical parameters on the self-assembly kinetics such as concentration of thiols, flow velocity, microchannel height, and packing density of SAM on the reaction surface.
    - Estimation and enhancement of the kinetics of thiols self-assembly on gold. The process time for self-assembly of thiols on gold is decreased from 24 hours, in conventional protocols, to 15 minutes.
- Development of a numerical model for studying the kinetics of Ab/SAM conjugation. The model is capable of examining the effect of fluidic and geometrical parameters mentioned above for the self-assembly of thiols.
    - Estimation of the required process time for the completion of the conjugation reaction at different flow velocities and concentrations. Implementation of such process time results in the highest level of reaction yield and antibody (probe) surface loading density.

1.5 Model Analytes

The conduction of HIAs, in general, and the modification of in-situ functionalization protocols, in particular, requires optimizing the different reactions involved in HIAs for a specific type of protein. This requirement arises because proteins have different chemical structures, and hence, their corresponding optimum functionalization protocols might be slightly different [1]. Microfluidic HIAs can probe a variety of proteins with practical significance in clinical diagnostics [22, 47, 86], environmental science [49, 87, 88], food science [89] and bio-security [90]. In this thesis, a 70 kilo-Dalton heat shock protein (HSP70) is focused on, i.e., a molecular chaperone that serves in cell protection from stress [91]. HSP70 has found considerable importance in environmental [92, 93], agricultural [94], and human health monitoring applications, such as cardiovascular health monitoring [95], immunity [96], and cancer vaccine adjutants [97]. Moreover, a biotin-streptavidin pair is employed for verification of the functionalization protocols. The other analyte which is used in this chapter is a fluorescently tagged protein: tetramethyl-rhodamine conjugated goat immuno gamma globulin, for characterization purposes. This protein does not have any special biosensing significance. HSP70 and biotin-streptavidin will be briefly introduced in the following section.

1.5.1 70 kDa Heat Shock Proteins

Heat Shock Proteins (HSPs) are a family of ubiquitous proteins found in almost all living organisms and act in the protein folding mechanisms for cell protection, under externally applied stress [91]. HSPs perform in proteins stabilization [98, 99], refolding of denatured proteins [98, 100, 101], and degradation of denatured proteins [102]. The heat shock proteins are named based on their size in kilo-Daltons (kDa). HSP70, as a member of this large family, is constantly present inside of cell, but its intracellular or inside cell concentration level is increased in response to external stress stimuli, called up-regulation. Depending on the organism, these stress stimuli may include elevated environmental temperatures [103], dehydration [104], food deprivation [105], osmotic stress [106], oxygen starvation [107], and the presence of heavy metals [108] and other forms of pollution [109].

HSP70 has been much focused on in health care, showing practical significance as an important factor in extracellular (outside the cell) immune activation, by marking the surface of tumors or virally infected cells [110-115], and serving as a danger signal for cellular stress or death [116, 117]. The protein is up-regulated in malignant tumours of breast, bone, and gastric (stomach) cancers, as well as renal cell tumours (kidney cancer) and leukemia (blood cancer) [118-120]. HSP70 over-

expression in blood plasma has also been reported as a reliable tumour marker for early stage prostate cancer [121]. Additionally, the protein's elevated levels in the hearts of patients has served as an indicator for cardiac health [122], a well-known risk factor for heart attack (myocardial infarction) [123], and weakened enlarged hearts (dilated cardiomyopathy) [124], which is linked to congestive heart failure. HSP70 has also served as a sensitive biomarker for arsenic poisoning [125]. The above facts highlight the necessity of developing and/or optimizing a reliable functionalization protocol for efficient HSP70 immobilization and sensing.

1.5.2 Biotin-Streptavidin

Biotin is a water-soluble B-complex vitamin also named Vitamin H or B7. Streptavidin is a 60 kDa protein, with an extraordinarily high affinity for binding biotin. The dissociation constant (K_d) of the biotin-streptavidin pair is on the order of $\sim 10^{-14}\ mol.L^{-1}$ [126], and therefore, the binding of biotin to streptavidin is one of the strongest non-covalent bonds known. Due to the high level of streptavidin-biotin pair resistance to organic solvents, denaturants and extremes of temperature and pH, they are extensively employed in molecular biology and bio-nanotechnology [126]. Here, these promising properties are used for preliminary experiments and functionalization assessments purposes.

1.6 Overview of This Thesis

This thesis covers the following materials:

Chapter 1: The background, motivation, and objectives of this research are presented and the literature on microfluidic-based functionalization techniques in heterogeneous immunoassays is reviewed.

Chapter 2: The construction of the numerical models is presented. The models are used to study, predict and modify the kinetics of the main reactions encountered in the microfluidic-based functionalization and the conduction of the heterogeneous immunoassays, aiming at optimizing the kinetics of the reactions.

Chapter 3: The experimental verification of the main model predictions on the functionalization reactions involved in the microfluidic heterogeneous immunoassays are described. Moreover, the performance of the modified functionalization protocols is compared to that of conventional counterparts.

Chapter 4: The main contributions and conclusions of the thesis are summarized and possible extensions of the current research work are proposed.

Chapter 2
Modeling the Kinetics of Reactions Involved in Microfluidic-based Functionalization Processes

2.1 Introduction

Chapter 1 was devoted to a review of the theoretical background on the conventional thiolic SAM-based functionalization processes. Modeling the reactions and investigation of the experimental protocols are necessary since the microfluidic HIA environments differ from the conventional HIAs in their analyte diffusion distance, surface-to-volume ratio, and also the solution operation method, i.e., operation under flow conditions rather than static incubations (pipetting) [28]. Constructing the models required is the subject of the current chapter, and the final experimentations performed to verify the main findings of the numerical model are detailed in the next chapter.

A comprehensive numerical study on the kinetics of the reactions involved in the in-situ functionalization processes is necessary, before the functionalization experiments are conducted. This necessity is due to the considerable number of independent parameters that are present in each stage of the functionalization processes. As a result, a purely experimental approach seems to be a very cumbersome task to complete [127]. Constituent kinetic parameters include flow rate, reagents concentration, and geometrical parameters such as microchannel height. Additionally, there are at least three major reactions in the SAM-based HIAs that require modeling, namely SAM formation, Ab/SAM conjugation, and Ag/Ab immunoreaction. The considerable number of reactions involved further increases the number of required experiments to reach the optimal condition for assaying the model analyte of interest. To achieve the optimal performance of a microfluidic HIA for the detection of proteins, it is essential to understand the role of the constituent parameters in each reaction and how they interact in the overall kinetics [28]. In this regard, a numerical study can target either a low limit of analyte detection (LOD), or minimal detection times, or reduced reagent consumption, or minimized assay preparation times (enhanced kinetics). The latter is the main focus of this chapter.

There have been a number of studies on experimental and numerical analysis of the kinetics of mass transport/reaction events in microfluidic immunoassays, and their findings can be used here [127-137]. There are also a few analytical solutions available [138]. There have been far fewer research works on reaction kinetics of an IA from the perspective of reaction condition optimization.

An early numerical study used a simple two-compartment model describing the transport and binding of the sample analytes via convection and diffusion in a Biacore sensing platform [130, 131]. A spatially homogeneous, constant concentration of analytes was supplied throughout the reaction chamber, and a transport coefficient (k_m) was used to describe the diffusion of analytes between the bulk solution (outer compartment) and the sensor surface (inner compartment). While the model gave a reasonable estimate of the reaction rate constants, it failed under highly transport-limited conditions due to the presence of spatial heterogeneity and the depletion of the bulk fluid from analytes [132, 133]. Transport-limitation refers to the reaction conditions in which the analytes' rate of transport to the reaction surface is the limiting progress-rate factor for the reaction [28, 136]. A computational reaction/diffusion model was developed by Vijayendran to analyze transport-limited reactions. However, it did not include the convection effect; thus, it was not able to describe the flow rate dependency of the binding kinetics [133]. Zimmermann modeled the reaction kinetics and included the convection effects in the capillary-driven flow microchannels, using a finite difference method [134]. Hu et al. investigated the Ab/Ag reaction kinetics in a microfluidic HIA using a two-dimensional numerical model [127]. In this work, the mass transport (convection and diffusion) of the Ags was coupled to the binding reaction between the Ags and immobilized Abs, and the model was employed for optimization of a reaction patch design in a microfluidic chip. Later on, capturing biomolecules in different geometric designs was numerically modeled by Jome et al. [135], using the same modeling approach as the latter work mentioned before. In the model, biomolecules inside the bulk fluid were treated like a continuum medium, and the flow pattern and geometry of the designs were compared in terms of target capturing efficiency. Despite the comprehensive numerical investigations conducted, it seems that the fundamental interrelations between the constitutive kinetic parameters, such as concentration, flow velocity, microchannel height, and probe loading density, are not much studied.

This chapter deals with the simulation of the kinetics of main reactions encountered in the conduction of HIAs, using FEM. The following reactions are numerically studied: SAM formation, Ab/SAM conjugation, and Ag/Ab immunoreaction. The numerical model simultaneously solves the convection and diffusion equations coupled with the surface reaction formulations [127].

The model is used to find optimal reaction conditions, aiming at minimal assay preparation times, while keeping the analyte consumption reasonable. For this purpose, the effects of following parameters on the reaction kinetics are studied: flow rate, reagents concentration, microchannel

height, and the surface density of reaction sites. The trends seen in the numerical simulations are explained according to the dimensionless numbers such as the Damköhler number and the Peclet number [28, 139].

2.2 Mathematical Models and Numerical Methods

It is assumed in the mathematical model that the reagents (analytes) flow in a rectangular microchannel, with the configuration shown in Figure 2.1. The width of the microchannel is considerably larger than its height (h), so that the concentration variation across the width can be neglected and the flow can reasonably be considered two-dimensional. Because of the low Reynolds numbers ($\mathrm{Re}_{2\mathrm{h}} \leq 1$) encountered in microfluidic applications [77], a fully developed laminar flow inside the microchannel is expected here. A considerable electrical force is not present, and the gravity can be neglected because of the relatively small height of the microchannel. It is also assumed that the temperature variations during the reactions are not significant. Therefore, the change in the physical properties due to temperature variation is minimal and reasonably neglected. The reaction surface throughout the simulations starts typically at $\mathrm{X} = 80\ \mu m$ away from the channel inlet. The entrance length (L_e) is defined as the distance from the inlet end of the microchannel after which the flow is fully developed. The maximum entrance length is calculated as follows, from the maximum Reynolds number ($\mathrm{Re}_{2\mathrm{h},max} = 2\rho u_{avg,max} h_{max} \mu^{-1}$) and for laminar flows [139, 140]:

$$\frac{L_{e,max}}{2h_{max}} \sim 0.06\mathrm{Re}_{2\mathrm{h},max} \xrightarrow{\mathrm{Re}_{2\mathrm{h},max}<1} L_{e,max} \sim 1.6\ \mu m$$

where

$\rho = 1000\ kg/m^3$	density of the PBS (fluid used)
$u_{avg,max} = 1500\ \mu m.s^{-1}$	maximum flow velocity considered
$h_{max} = 100\ \mu m$	maximum height of the microchannel considered
$\mu = 8.9 \times 10^{-4}\ Pa.s$	dynamic viscosity of the PBS
$L_{e,max}$	maximum entrance length

Therefore, the reactions always take place in the fully developed region ($L_e \ll \mathrm{X}$).

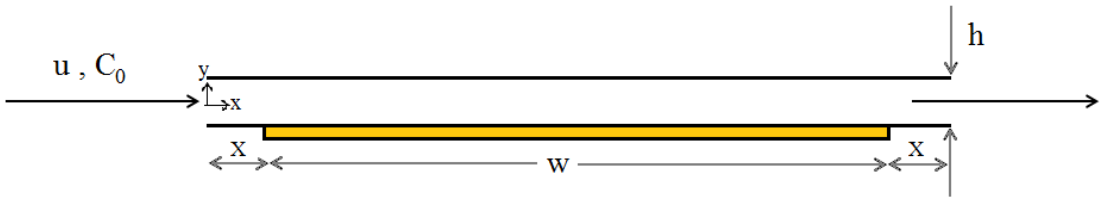

Figure 2.1: Schematic of the fluid flow pattern inside the microchannel (not to scale). Analytes enter the channel from the left inlet and exit from the right outlet. Reactions take place within a width w (= 1500 µm). X is the distance of the reaction surface from the inlet, and h is the microchannel height.

2.2.1 Bulk Reagents Transport

Determination of the velocity field is the first step toward finding the reaction progress rate. The reagents are released into the microchannel from the left inlet, with a concentration of c_0 (Figure 2.1). In this configuration, the velocity field can be described by the two dimensional Navier-Stokes and the continuity equations as

$$\rho(\vec{u}.\nabla)\vec{u} = -\nabla p + \mu\nabla^2\vec{u} \tag{2.1}$$

$$\nabla.\vec{u} = 0 \tag{2.2}$$

where ρ denotes the density ($\rho_{ethanol} = 0.789,\ \rho_{water} = 1\ g.cm^{-1}$), $\vec{u}$ is the velocity vector, p is the pressure, and μ is the dynamic viscosity of the carrier fluid ($\mu_{ethanol} = 1.74 \times 10^{-3}$, $\mu_{water} = 8.9 \times 10^{-4}$ Pa. s). Eq. (2.2) can be put into dimensionless form using the following dimensionless parameters [141]:

$$x^* = \frac{x}{2h}, y^* = \frac{y}{2h}, \vec{u}^* = \frac{\vec{u}}{u_{avg}}, p^* = \frac{2ph}{\mu u_{avg}}, \nabla^* = 2h\nabla \tag{2.3}$$

Here, u_{avg} is the average flow velocity inside the microchannel, and x^* and y^* are the dimensionless coordinates. Substitution of the corresponding variables from Eq. (2.3) to Eq. (2.1) yields:

$$\mathrm{Re}_{2h}[(\vec{u}^*.\nabla^*)\vec{u}^*] = -\nabla^* p^* + \nabla^{*2}\vec{u}^* \tag{2.4}$$

Because of the low Reynolds numbers encountered here ($\mathrm{Re}_{2h} \ll 1$), the left-hand term in Eq. (2.4) is negligible. Therefore, the Navier-Stokes equations, given in Eq. (2.1), reasonably simplify to the

Stokes equations ($0 = -\nabla p + \mu \nabla^2 \vec{u}$). The inlet receives a net constant velocity of the fluid, represented here by a constant cross-sectional average velocity: u_{avg}. The outlet experiences the atmospheric pressure, and all walls are in no-slip condition [139, 140]. The fluid is assumed to be driven by applying an appropriate pressure difference across the two ends of the microchannel.

Upon determination of the velocity field, one can find the instantaneous concentration of the reagents across the bulk fluid. Reagents are transported to the reaction surface by diffusion and convection. Reagents binding to the reaction surface deplete the bulk fluid from the reagents. The resulting concentration gradient in the bulk fluid is described by the governing transient equation of convection-diffusion as follows:

$$\frac{\partial c}{\partial t} + \vec{u}.\nabla c = \nabla.(D\nabla c) \tag{2.5}$$

where c is the concentration of reagents, and D is the diffusion coefficient ($D_{,thiols,ethanol} = 5.7 \times 10^{-10}$, $D_{,Ab,PBS} = 10^{-11}\, m^2.s^{-1}$) [127, 142]. The latter equation (convection-diffusion) is assumed decoupled from the Navier-Stokes equations (Eq. 2.1). This assumption is valid for dilute solutions with no effect of the solute on the flow pattern, which applies here [135]. The next step is finding the instantaneous concentration of reacted reagents on the reaction surface.

2.2.2 Surface Reaction Kinetics

The last step for the determination of the reaction progress rate is finding the instantaneous concentration of the reacted reagents. The time evolution of the reacted reagents' surface concentration on the reaction surface (c_s) is related to the reaction rate term (R_s), taking into account the surface diffusion of the reagents, described by Eq. (2.6):

$$\frac{\partial \mathrm{c_s}}{\partial \mathrm{t}} + \nabla.(-\mathrm{D_s}\nabla \mathrm{c_s}) = \mathrm{R_s} \tag{2.6}$$

where D_s is the surface diffusion coefficient of the reagents ($D_{s,thiols,ethanol} = 2 \times 10^{-9}$, $D_{s,Ab,PBS} = 1 \times 10^{-9}\, m^2.s^{-1}$) [39, 127].

The velocity and bulk concentration fields were previously determined from Eq. (2.1), (2.2) and Eq. (2.5), respectively. The bulk concentration field manifests itself in the mass flux terms, consisting of the diffusive ($-D\nabla c$) and the convective flux terms ($c\vec{u}$), and in the reaction rate term (R_s). At the

reaction surface, the surface concentration of reacted reagents (c_s) is coupled with the bulk concentration of reagents (c) by the boundary condition of Eq. (2.5):

$$\vec{n}.(-D\nabla c + c\vec{u}) = -R_s \tag{2.7}$$

where $\vec{n}$ is the unit normal vector to the surface. There is an "insulating" condition governing the material balance of the reagent molecules at the surfaces with no reaction [135], which means the sum of the convective and diffusive terms, $-D\nabla c$ and $c\vec{u}$, should be zero at these surfaces:

$$\vec{n}.(-D\nabla c + c\vec{u}) = 0 \tag{2.8}$$

The other boundary conditions of Eq. (2.5) are:

- The inlet is held at constant concentration: $c = c_0$ (2.9)
- At the outlet, the mass flux is specified as follows: $\vec{n}.(-D\nabla c) = 0$ (2.10)

Eq. (2.10) assumes that the x component of the concentration gradient ($\partial c/\partial x$) is zero at the outlet. In other words, the latter boundary condition implies that the outlet is placed far enough from the reaction surface such that the depletion of analytes on the reaction surface does not affect the concentration of analytes in the outlet. In the following section, reaction rate formulations corresponding to each reaction considered in this thesis are presented.

2.2.3 Reaction Rate Formulations

The mathematical formulation constructed above is applicable for all the reactions considered in this thesis, i.e., SAM formation, Ab/SAM conjugation, and the Ab/Ag immunoreaction. However, the reaction rates follow slightly different functions for each case. In the following, the reaction rate functions are formulated.

2.2.3.1 SAM's Kinetics Rate

Langmuir kinetics model has been employed in the majority of research on SAM's kinetics, and includes a rate of reaction proportional to the surface density of the available reaction sites. Langmuir kinetic models often assume a diffusion-limited reaction for thiols self-assembly, which means the reaction rate is limited by the rate of thiol diffusion toward the reaction surface [13]. Nonlinear optical experiments [143], as well as SPR [144], QCM [145] and AFM [146], have found consistent descriptions of SAM growth kinetics using the Langmuir model. However, use of a diffusion-limited

Langmuir model is suitable only for very low concentrations of thiol adsorbates such as $1\ \mu M$ [39]. Moreover, a Langmuir model does not include the mutual repositioning of thiol species within the monolayer, called rearrangement. Thiol self-assembly has two stages: first, an initial fast stage, in which in the first few minutes of the self-assembly, more than 80% of the monolayer is formed, followed by a second, relatively slow rearrangement stage [13].

At each moment, the coverage (θ) is defined as the ratio between the surface density of the chemisorbed (reacted) thiol molecules (c_s) to their maximum possible surface density (θ_0): $\theta = c_s.\theta_0^{-1}$. The coverage rate is proportional to the reaction rate. Damos et al. [147] showed that the coverage rates at the initial and rearrangement stages of the self-assembly can be respectively described by:

$$\frac{d\theta_1}{dt} = k_a c - (k_a c + k_d + k_t)\theta_1 - k_a c\theta_2 \tag{2.11}$$

$$\frac{d\theta_2}{dt} = k_t\theta_1 \tag{2.12}$$

where the coverage in the first stage of the chemisorption is θ_1, and θ_2 is the coverage of a rearranged assembled monolayer. k_a, k_d, and k_t denote the association, dissociation, and rearrangement rate constants, respectively [147]. In this definition, the total SAM coverage is composed of the coverage from the initial fast stage of the self-assembly added to the coverage from the slower rearrangement stage. Thus, the total SAM coverage rate is also a function of these two rates. As mentioned before, the reaction rate is proportional to the total coverage rate:

$$R_s = \theta_0 \times \frac{d\theta}{dt} = \theta_0 \times \left(\frac{d\theta_1}{dt} + \frac{d\theta_2}{dt}\right) \tag{2.13}$$

in which θ_0 is the total number of the thiol chemisorption sites available in the unit area. Substituting Eq. (2.11)-(2.13) into Eq. (2.6) yields the following governing equation for the thiols' rate of surface concentration change on the reaction surface:

$$\frac{\partial \mathrm{c_s}}{\partial \mathrm{t}} = \nabla.(\mathrm{D_s}\nabla \mathrm{c_s}) + k_a c(\theta_0 - c_s) - k_d\theta_0\theta_1 \tag{2.14}$$

The FEM package (COMSOL Multiphysics 4.2), solves Eq. (2.1)-(2.5) and Eq. (2.14), via Eq. (2.7) for $\mathrm{c_s}$, taking into account the boundary conditions listed in Section 2.2.2. The self-assembly completion level at each moment can be evaluated by computing the c_s/θ_0 ratio that approaches unity upon reaction completion.

Deriving an approximate analytical solution for Eq. (2.14) is also possible [134]. In Eq. (2.14), D_s and c_s in the first right-hand term are much smaller than the c multiplied term (second right-hand term). Therefore, one can reasonably ignore the first right hand term (diffusion). In Eq. (2.11)-(2.12), k_t is around two orders of magnitude less than k_a: $k_a = 11.5 \times 10^{-3} m^3.(mol.s)^{-1}$, and $k_t = 4.5 \times 10^{-4} s^{-1}$ [147]. Thus, θ can be reasonably approximated with θ_1. The last right-hand term in Eq. (2.14) becomes $-k_d c_s$ because $\theta.\theta_0 = c_s$. Accordingly, one can derive the following approximate analytical solution for the surface concentration of chemisorbed thiol molecules [134]:

$$c_s = \frac{k_a \theta_0 c}{k_a c + k_d}\left(1 - e^{-(k_a c + k_d)t}\right) \tag{2.15}$$

2.2.3.2 SAM/Antibody Conjugation Kinetics Rate

Section 1.3.2.2 introduced the procedure of amide bond formation between the amine group of Abs and the carboxyl group of SAMs in the presence of EDC. To enhance the reaction yield, additives such as N-Hydroxysuccinimide (NHS)[1] are widely used [19, 148]. The chemical structures of EDC and NHS are schematically shown in Figure 2.2.

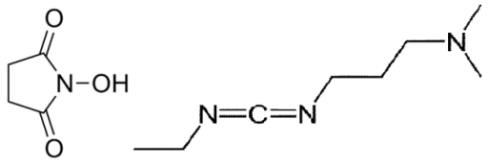

Figure 2.2: Left: EDC, right: NHS

The typical reaction for coupling the carboxylic acid groups of SAMs with the amine residue of Abs in the presence of EDC/NHS is depicted below in Figure 2.3 [19]. NHS promotes the generation of active esters, such as NHS ester in the figure (k_2 reaction path). An NHS ester is capable of efficient acylation of amines, including Abs (k_3 reaction path). As a result, the amide bond formation reaction, which typically does not progress efficiently, can be enhanced using NHS as a catalyst [19].

1- The sulfonated NHS, sulfo-NHS, has also been implemented widely in amide bond formation reactions with an identical reaction path [19].

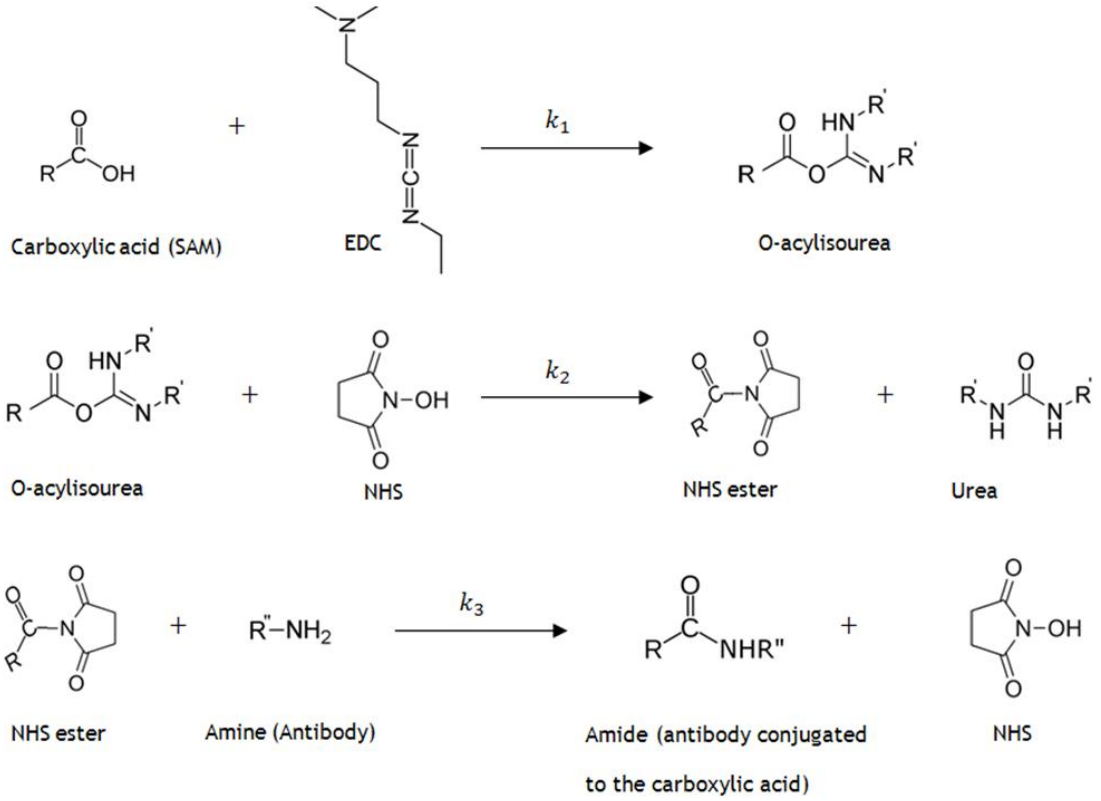

Figure 2.3: NHS catalyzed conjugation of antibodies to carboxylic-acid ended SAMs through EDC mediation. EDC reacts with the carboxylic acid and forms o-acylisourea, a highly reactive chemical that reacts with NHS and forms an NHS ester. The latter chemical compound quickly reacts with an amine (antibody) to form an amide. Urea is the product of these reactions.

There are a number of studies on the EDC/NHS mediated conjugation reactions depicted in Figure 2.3, and a few of them examine its kinetics [19, 149-151]. Figure 2.3 represents an extended form of the zero-length conjugation reaction introduced in Section 1.3.2.2 (Figure 1.3), incorporating NHS as a yield increasing catalyst. The general stoichiometry of the reaction involves a carboxylic acid (SAM here), an amine (Ab here), and EDC to produce the final amide (Ab conjugated SAM here) and urea. Unfortunately, the recommended concentration ratio of the crosslinking reagents inside the buffer, i.e., the ratio of EDC and NHS with respect to adsorbates and each other, does not follow a unified pattern from one study to another [151]. The kinetics of the reactions outlined in Figure 2.3 is investigated for EDC and various carboxylic acids in aqueous solutions, however, in the absence of NHS as a catalyst [150]. A relatively recent experimental study verified a catalytic role for a yield-increasing reagent, called N-hydroxybenzotriazole (HOBt), which acts the same as NHS

[149]. Chan et al. experimentally demonstrated that the amide formation rate, i.e., the k_3 reaction path in Figure 2.3, is dependent on the concentration of the carboxylic acid and EDC in the buffer solution, and independent of the amine and catalyst reagent concentration [149]. It was shown that the amide bond formation kinetics is controlled by the reaction between the acid (11-MUA thiol here) and EDC to give the O-acylisourea, marked as the rate-determining step (k_1 reaction path in the figure) [149]. Compared to the k_1 reaction path, other reactions that result in formation of NHS-ester and the amide are determined to be considerably faster, i.e., the k_2 and k_3 reaction paths [149]. The resulting reaction rate follows Eq. (2.16) below, to be used in Eq. (2.6)-(2.7) for the Ab/SAM conjugation reaction model:

$$R_s = k_e[EDC][RCO_2H]_s \tag{2.16}$$

where k_e is the kinetics rate constant, and $[EDC]$ denotes the molar concentration of EDC. $[RCO_2H]_s$ is the instantaneous surface concentration of the carboxylic groups available for conjugation with Abs. $[RCO_2H]_s$ equals the initial surface concentration of the carboxylic acids (θ_0), minus the amount bound with Abs (c_s): $[RCO_2H]_s = \theta_0 - c_s$. For the case of Ab/SAM conjugation, the parameter c in Eq. (2.5) is the EDC concentration: $c = [EDC]$. Accordingly, after some mathematical simplifications, Eq. (2.6) will have the following form for the Ab/SAM conjugation reaction:

$$\frac{\partial \mathrm{c_s}}{\partial \mathrm{t}} = \nabla.(\mathrm{D_s}\nabla \mathrm{c_s}) + k_e c(\theta_0 - c_s) \tag{2.17}$$

Same as the SAM-formation kinetics, Eq. (2.1)-(2.5) and (2.17) are solved via Eq. (2.7) for $\mathrm{c_s}$, which is here the instantaneous surface concentration of the Abs bound. The reaction progress can be assessed at each moment by comparing the $\mathrm{c_s}/\theta_0$ ratio, which is shown in Section 2.4.2.1 to approach unity upon reaction completion.

2.2.3.3 Immunoreaction Kinetics Rate

The immunoreaction between the probing molecule (Ab) and the analyte (Ag) can be described by the following reaction rate function [28, 127]:

$$\mathrm{R_s} = k_a c\theta' - k_d c_s : c + \theta' \underset{\mathrm{k_d}}{\overset{\mathrm{k_a}}{\rightleftarrows}} c_s \tag{2.18}$$

where $\mathrm{R_s}$ is the reaction rate function, k_a and k_d are respectively the association (forward) and dissociation (backward) rate constants, c is the concentration of analytes, θ' is the surface concentration of available binding sites, and c_s is the surface concentration of adsorbed analytes (Ags). Eq. (2.18) states that unbound analytes in the bulk fluid are exchanged with the immobilized analytes on the reaction surface. The reaction rate depends on analytes concentration in the bulk, available binding sites on the reaction surface, and forward/backward rate constants.

The immunoreaction progress rate can be found by the substitution of $\mathrm{R_s}$ from Eq. (2.18) into Eq. (2.6). The surface concentration of ready-to-bind sites (θ') is equal to the difference between the initial surface concentration of binding sites (θ_0), and the surface concentration of adsorbed analytes (c_s): $\theta' = \theta_0 - c_s$. After some mathematical simplifications, one reaches the following equation that describes the immunoreaction progress rate:

$$\frac{\partial \mathrm{c_s}}{\partial \mathrm{t}} + \nabla.(-\mathrm{D_s}\nabla \mathrm{c_s}) = k_a c(\theta_0 - c_s) - k_d c_s \tag{2.19}$$

In Eq. (2.19), the analytes' bulk concentration (c) must be solved in combination with the mass transport equations, Eq. (2.1)-(2.5), for finding the instantaneous surface concentration of adsorbed Ags (c_s). Mass balance in the bulk, Eq. (2.5), is coupled with the surface reaction, Eq. (2.19), by imposing the boundary conditions of Eq. (2.5), discussed in Section 2.2.2. Eq. (2.19) can also be analytically solved [134], resulting in the same solution represented by Eq. (2.15), in Section 2.2.3.1.

2.2.4 Numerical Solver

The differential equations constructed in Section 2.2 for the numerical model were solved by a FEM software package, COMSOL Multiphysics 4.2 (Stockholm, Sweden). For kinetic analysis, triangular 2D elements were used for meshing. The independency of simulation results from the mesh size was accessed, and the mesh size was refined until the difference between the numerical results of the finer mesh and the coarser mesh became less than 1%. The solver used was "multi-frontal

massively parallel sparse direct solver" (MUMPS). The time dependent solver had a maximum absolute tolerance of 10^{-3}, and the method used was backward differentiation formula (BDF) [152]. The numerical model was verified for the three reactions formulated in Section 2.2.3, by comparing the simulation results with the analytical solution (Eq. 2.15) and or experimental results available in the literature [28, 127, 147, 149], detailed in Sections 2.4.1, 2.4.2, and 2.4.3.

The coupled equations of the 2D velocity field (Eq. 2.1 and 2.2), convection-diffusion mass transport (2D-Eq. 2.5), and 1D reaction-diffusion (Eq. 2.6) were simultaneously solved by COMSOL Multiphysics®. Calculation of the velocity field (Eq. 2.1 and 2.2) allows calculation of the concentration field in the bulk via Eq. (2.5). By determination of the concentration field, the surface concentration of the reagents (c_s) can be calculated via Eq. (2.6). The latter parameter is a measure of the progress of the reaction. The 1-D diffusion-reaction equation (Eq. 2.6) was coupled to the 2-D convection-diffusion equation (Eq 2.5) using the weak-form PDE interface of COMSOL. Implementation of partial differential equations in boundaries is more convenient using the weak-form of the original PDE (Eq. 2.6), particularly for building models with extra equations on boundaries, such as the reactions encountered here [153].

2.3 Kinetic Descriptive Dimensionless Numbers

Dimensionless numbers can express the relative importance of various phenomena present in fluidic processes. In this thesis, dimensionless numbers help to study the impact of each variable on the overall kinetics. The kinetics variables included here are flow velocity (u_{avg}), input concentration of reagents (c_0), microchannel height (h), and surface concentration of binding (reaction) sites (θ_0). There are a number of fundamental dimensionless numbers in the microfluidic applications, among which the Peclet number (Pe) and the Damköhler number (Da) are the two main kinetic descriptive ones. The Pe, and Da, along with two other less well-known numbers, are listed below [28, 135, 139]:

$$\mathrm{Pe} = \frac{u_{avg} h}{D} \tag{2.20}$$

$$\mathrm{Da} = \frac{k_a \theta_0}{\frac{D}{h} + u_{avg}} \tag{2.21}$$

$$\epsilon = \frac{c_0 h}{\theta_o} \tag{2.22}$$

$$\beta = \frac{k_a \theta_0 l}{u_{avg} h} \tag{2.23}$$

in which l stands for the length of the reaction surface. The Peclet number is a measure of convection to diffusion transportation strengths. The Damköhler number compares the relative rates of reaction and mass transport. ϵ is a measure of the amount of analytes available in the bulk fluid compared to the surface density of binding sites available on the reaction surface and is often called binding or adsorption capacity. β compares the reaction strength with the convection capacity [135]. In most of the studies on the reaction kinetics of biosensors, the conventional form of Da in which the mass transport results only from diffusion, is used [133, 135, 136]:

$$\mathrm{Da} = \frac{k_a \theta_0}{\frac{D}{h}} \tag{2.24}$$

In these studies, the Damköhler number compares the strength of reaction with diffusion. However, the combined role of convection and diffusion in mass transport cannot be directly evaluated against the reaction rate yet. Gao proposed using a modified Damköhler number which included the contribution of convection to the overall mass transport as well, which is adopted here in Eq. (2.21) [28]. This expression compares the strength of two simultaneous processes: the denominator $(D/h + u_{avg})$ is a measure of the delivery rate of adsorbates to the reaction surface by diffusion and convection, and the numerator $(k_a \theta_0)$ is a measure of the adsorbates' binding rate. Accordingly, the Damköhler number can be used to quickly estimate the nature of the reaction kinetics, in the following manner:

In the definition used in Eq. (2.21), if Da ~1, transport and reaction have equally important roles in the kinetics; otherwise, the overall progress rate is governed by the slower process (transport rate or reaction rate). If $\mathrm{Da} > 1$, the kinetics is more transport-limited, and improvements in the transport of the reagents via increasing the flow rate can effectively enhance the kinetics. On the other hand, if $\mathrm{Da} < 1$, the kinetics is more reaction-limited, and the flow rate increase does not impact the kinetics as much as the former case.

The dimensionless numbers listed here are used to explain the kinetic trends seen in simulations.

2.4 Results and Discussion

The numerical model was verified for the three kinetic models presented in Section 2.2, by comparing the simulation results with the analytical solution (Eq. 2.15) and experimental results available in the literature. The simulation findings were in good agreement with the literature data [28, 127, 147, 149]. Model verification, numerical findings, and explanation of the kinetic trends, using dimensionless numbers, are detailed in this section.

2.4.1 SAM-Formation Kinetics

The model developed for SAM-formation kinetics was verified by comparing the simulation results with the analytical solution and literature data. First, the final surface concentration of thiol species was analytically computed via Eq. (2.15) and then compared with the simulation outcomes. The analytical results were consistent with their simulation counterparts, with a less than 5% variation, summarized for a number of concentrations in Table 2.1 below.

Table 2.1: Comparison of analytical and simulation results for c_s at the self-assembly completion, the results differ by less than 5% for each concentration.

Analytical calculations ($mol.m^{-2}$)	Simulation results ($mol.m^{-2}$)	Concentration (mM)
7.2621×10^{-10}	7.2647×10^{-10}	10
7.2246×10^{-10}	7.2838×10^{-10}	5
6.9380×10^{-10}	7.2661×10^{-10}	1

Second, simulated self-assembly completion times agreed very well with the literature results for the 1 mM concentration of 11-MUA in ethanol, with less than 5% variation [147]. The self-assembly was considered completed when the surface concentration of thiol species (c_s) exceeded 99.6% of its maximum possible value ($\theta_0 = 7.3 \times 10^{-10}\ mol.m^{-2}$), for the first time. All the calculations were based on the properties of 11-MUA. This assumption is reasonable, since the chain lengths of the two thiols employed in this research are close to each other, i.e., a 10 carbon chain for 11-MUA and 8 for 1-OT. Thiols with the same or a close number of carbons in their chain are experimentally shown to have almost the same kinetic properties [39].

The model developed was used to study the effect of some important parameters affecting the SAM-formation kinetics, including the concentration of thiol molecules in the bulk, the flow velocity, the microchannel height, and the surface concentration of self-assembly sites on the reaction surface. Unless stated otherwise, the height of the microchannel under study was kept at $40\,\mu m$. A constant input thiol concentration of $10\,mM$ and inlet flow velocity of $150\ \mu m.s^{-1}$ were assumed. The rate constants used were $k_a = 11.5 \times 10^{-3} m^3.(mol.s)^{-1}$, $k_d = 6 \times 10^{-4} s^{-1}$, and $k_t = 4.5 \times 10^{-4} s^{-1}$ [147].

2.4.1.1 The Concentration and Flow Velocity Effects on the Self-assembly Kinetics

Figure 2.4 below is a plot of the self-assembly completion time predicted for constant thiol concentrations of $10\,\mu M$ to $10\,mM$ (10000 μM), in logarithmic scale. In this figure, the simulation results for the zero-flow mode are compared to the case of an inlet flow velocity of $150\ \mu m.s^{-1}$. The self-assembly completion time is shown to decrease nearly exponentially with the increasing concentration. This trend is in accordance with the exponential analytical representation of the reaction progress rate (Eq. 2.15). For instance, the model predicted that the self-assembly can be completed in 303 minutes for the $100\,\mu M$ concentration, while the corresponding time is 15 minutes for a $10\,mM$ input concentration of thiols. These findings are very promising for biosensing applications, since SAMs are conventionally formed from $1\,mM$ solutions after a 24-hour self-assembly time [11, 12]. Here, it is shown by simulation that a considerably faster self-assembly is feasible by adaptation of the thiol concentration in the bulk fluid. Physically, the augmentation of reagents concentration normally results in a faster process, since the number of reagents (in unit volume) that can approach a reaction spot is increased.

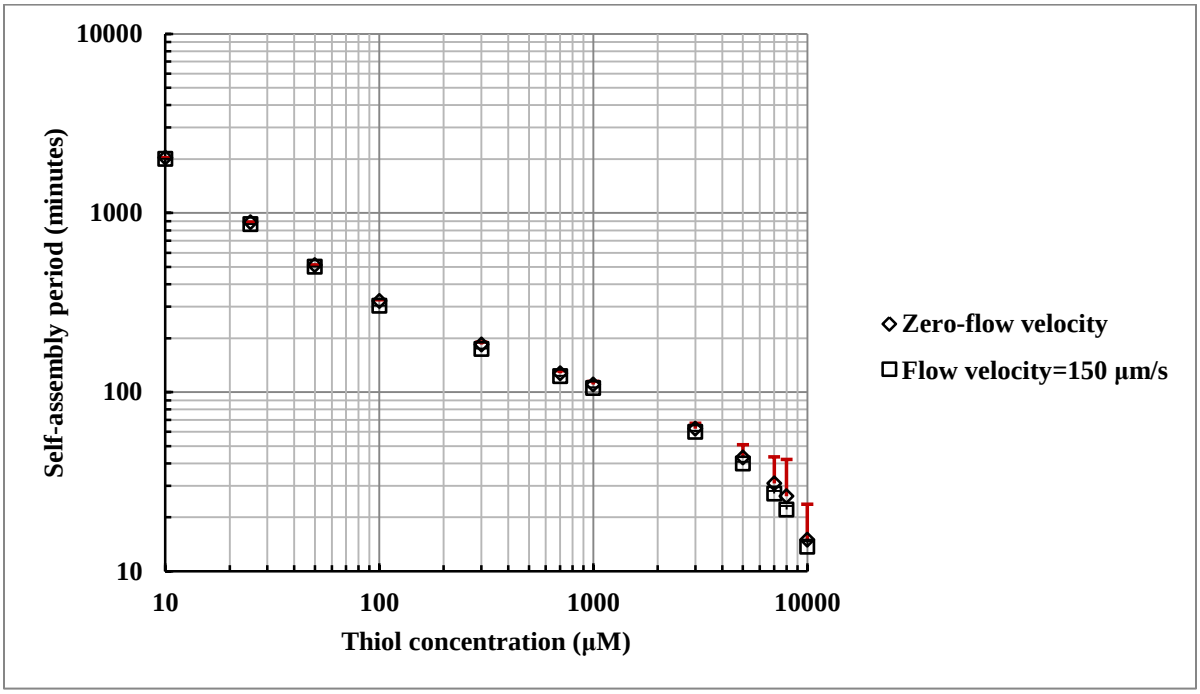

Figure 2.4: Simulated self-assembly periods predicted for different initial concentrations of thiols in ethanol and two flow velocities, plotted in log scale. Self-assembly time decreases substantially with increasing thiol concentration in the bulk fluid. The flow velocity does not play an important role. The bars show the decrease of self-assembly periods by percent; the reduction amount is always below 16%.

Figure 2.4 also demonstrates that increasing the flow velocity does not lead to a considerably faster overall self-assembly. The reaction completion time is at best improved by 16% for the $8\,mM$ concentration, and by less than 7% on average, across all the thiol concentrations (for $c_0 = 8\,mM$ and $u_{avg} = 150\,\mu m.s^{-1}$, $T_{comp} = 22':5''$). This observation is counter-intuitive, since using a higher flow rate usually results in a higher thiol transport rate to the reaction surface, and consequently, a faster reaction is normally expected. The weak flow rate dependency observed can be attributed to the reaction-limited nature of the kinetics [28, 135, 138]. A better understanding of the issue is possible by examining the transient process of the thiol self-assembly kinetics.

Figure 2.5 shows that upon velocity increase, faster transient processes are observed. In the figure, the predicted transient process of SAM formation for a constant input concentration of $10\,mM$, under various flow velocities is plotted for the first 4 minutes of the process. The curves show the time evolution of the dimensionless surface concentration of bound thiols ($c_s^* = c_s.\theta_0^{-1}$) on the reaction

surface. The time is non-dimensionalized by the process completion time of the zero-velocity case ($T_{comp} = 15$ minutes: $t^* = t.T_{comp}^{-1}$), and the velocity by a nominal velocity of $100\,\mu m.s^{-1}$: $u^* = u_{avg}/(100\,\mu m.s^{-1})$. The curves in all the flow velocities exhibited a sharp increase of adsorbates' surface concentration, in quite a short period of time. Then the curves approached a plateau of unity, which implies that completion of the self-assembly is close, as almost all the potentially available self-assembly sites are going to be occupied by the thiols. However, the self-assembly completion time was observed to be almost the same for all velocities (see Figure 2.4). Figure 2.5 demonstrates that increasing the flow rate beyond a flow velocity of around $u^* = 1.5$ ($u_{avg} = 150\,\mu m.s^{-1}$) does not contribute to further kinetic enhancements, even for transient processes. For velocities higher than $u^* = 1.5$, the c_s^* values differ by less than 1% between the curves at each moment. At this flow velocity, the weak potential of the reaction-limited kinetics for enhancement by the mass transport magnification is nearly completely employed.

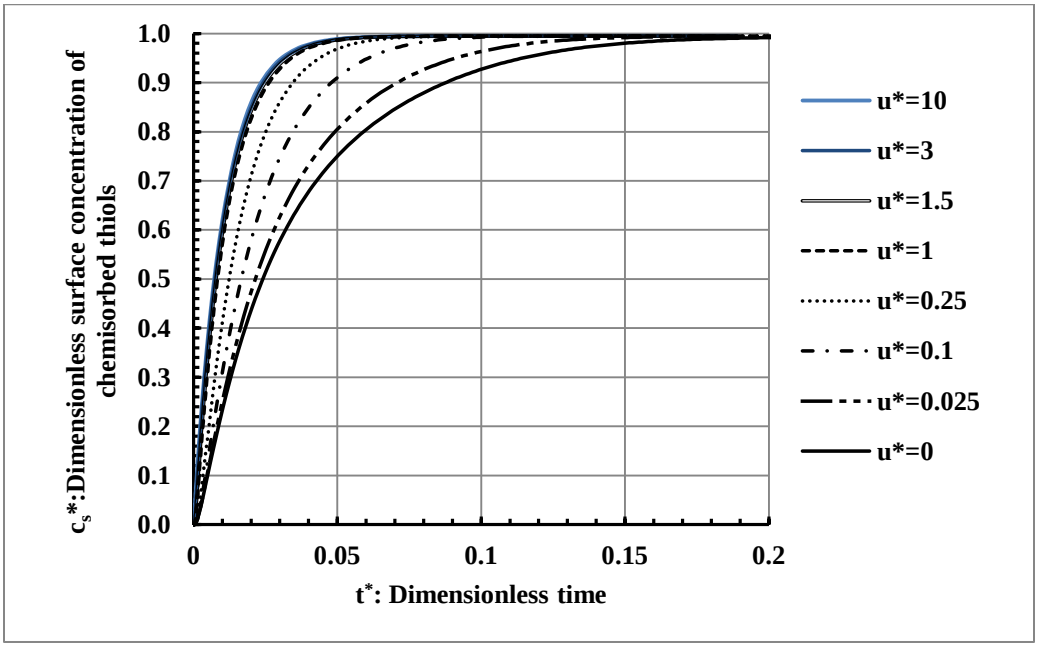

Figure 2.5: Simulated transient process of self-assembly kinetics, dimensionless surface concentration of chemisorbed thiols for a 10 mM concentration of thiols, plotted at different flow velocities in the first few minutes of the reaction. Velocity and time are non-dimensionalized by a nominal velocity of 100 $\mu m.s^{-1}$ ($u^* = u_{avg}/(100\,\mu m.s^{-1})$ and process time of the zero-flow velocity case: $T_{comp} = 15$ minutes ($t^* = t.T_{comp}^{-1}$). An increase in the flow velocity results in a faster transient process for lower flow rates.

Calculation of the Damköhler and Peclet numbers helps in explaining the weak flow rate dependency observed in the self-assembly kinetics. In the current self-assembly process, the Damköhler number is $\mathrm{Da} = 5.11 \times 10^{-8}$, assuming a flow velocity of $u^* = 1.5$ ($u_{avg} = 150\ \mu m.s^{-1}$), and for the zero-flow velocity case $\mathrm{Da} = 5.89 \times 10^{-7}$, calculated from Eq. (2.21):

If $u_{avg} = 150\ \mu m.s^{-1}$:

$$\mathrm{Da} = \frac{k_a \theta_0}{\frac{D}{h} + u_{avg}} = \frac{11.5\times10^{-3} m^3.(mol.s)^{-1} .\ 7.3\times10^{-10} mol.m^{-2}}{\frac{5.7\times10^{-10}\ m^2.s^{-1}}{40\times10^{-6}\ m} + 150\times10^{-6} m.s^{-1}} = \frac{8.4\times10^{-12}}{1.43\times10^{-5} + 1.50\times10^{-4}} = 5.11 \times 10^{-8}$$

As noted in Section 2.3, the Damköhler number is a measure of the reaction strength at the surface compared to the mass transport power. For this clearly low Damköhler number ($\mathrm{Da} = 5.89 \times 10^{-7}$), the reaction rate strength is much less than the mass transport capacity, and the kinetics is evidently reaction-limited. This fact also implies that further increase in the flow rate does not contribute to a noticeably better overall kinetics. The Peclet number, for the flow velocity of $150\ \mu m.s^{-1}$ ($u^* = 1.5$) is 10.53, which means convection has 10 times greater contribution than diffusion in the mass transport. Based on the transient process behavior observed in Figure 2.5, one can propose that around the flow velocity of $150\ \mu m.s^{-1}$ ($u^* = 1.5$), the mass transport is using almost the whole potential of convection, and no more transient enhancement is achievable by an increase in the flow velocity. In Section 2.5, the flow rate dependency of the self-assembly kinetics is compared to the same aspect of the other reactions considered in this research, i.e., Ab conjugation and immunoreaction.

The impact of the bulk concentration of the thiols on the SAM growth kinetics can be further examined by consideration of the change in the adsorption capacity (ϵ: Eq. 2.22), upon concentration variation. Figure 2.6 below illustrates the effect of the ϵ on the self-assembly kinetics. The evolution of surface concentration of adsorbed thiols (c_s) along the reaction surface was simulated for two representative high ($c_0^{*,high} = 10$) and low ($c_0^{*,low} = 0.01$) concentrations of thiols. The concentration is non-dimensionalized by a nominal concentration of $10\ mM$: $c_0^* = c_0/(10\ mM)$. The figure at the same time demonstrates the depletion effect. The depletion describes situations in which the concentration of analytes in the solution decreases along the flow direction, because of the analytes consumption on the reaction surface, also known as the moving front phenomenon [28, 134].

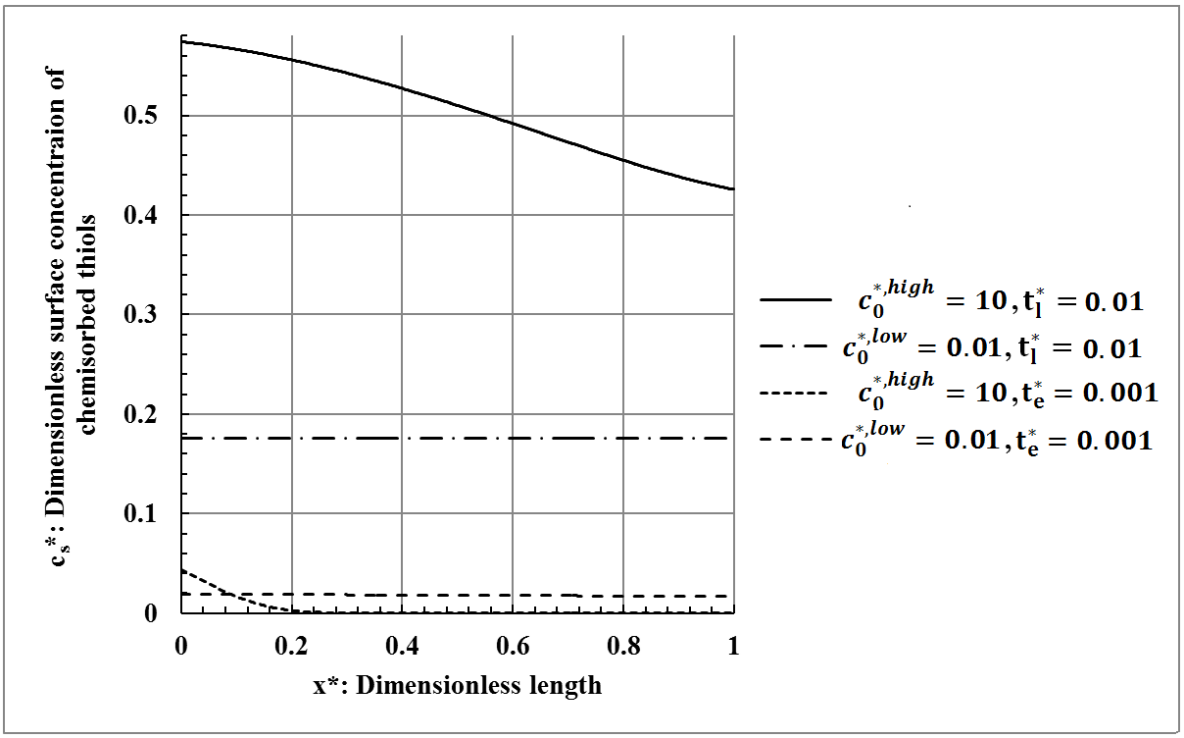

Figure 2.6: Simulated early variation of dimensionless surface concentration of chemisorbed thiols along the reaction surface for initial concentrations of $c_0^{*,low} = 0.01$ and $c_0^{*,high} = 10$ at two instants of self-assembly, $t_e^* = 0.001$ and $t_l^* = 0.01$. Concentration is non-dimensionalized by a reference thiol concentration of 1 mM: $c_0^* = c_0/(1\ mM)$, time has become dimensionless by the corresponding process time (T_{comp}) of each concentration: $t^* = t.T_{comp}^{-1}$, and length by the total length of the reaction surface: $x^* = x/l$. Samples with a higher concentration better deplete the bulk fluid from thiol adsorbates.

Figure 2.6 shows that $c_0^{*,high}$ has instantaneously faster adsorption relative to the $c_0^{*,low}$, due to the higher adsorption capacity (ϵ) associated with the $c_0^{*,high}$. In the figure, the dimensionless surface concentration of species ($c_s^* = c_s.\theta_0^{-1}$) on the reaction surface was depicted for two early self-assembly times of $t_e^* = 0.001$ and $t_l^* = 0.01$. Time is non-dimensionalized with T_{comp}, i.e., the self-assembly completion time corresponding to each concentration: $t^* = t.T_{comp}^{-1}$. The curves were plotted for the $c_0^{*,high}$ and $c_0^{*,low}$ concentrations, along the dimensionless reactive length: $x^* = x/l$. The velocity was set at $150\ \mu m.s^{-1}$. At the $t_l^* = 0.01$, the transient process is faster for the $c_0^{*,high}$. At this time, there should be enough thiol molecules present through the length of the microchannel.

This speculation is reasonable because thiol molecules have filled almost the whole length of the microchannel by convection, even if the diffusion transport is neglected. The process completion time (T_{comp}) can be looked up from Figure 2.4. The length that the thiols can convectively travel during the t_1^* interval, x_{trv}, can be calculated as the following ($x_{trv} = u_{avg}.t$):

$$x_{trv} = \begin{cases} 1350\ \mu m\text{: } if\ c_0 = 10\ mM, and\ \mathrm{T_{comp}} \sim 15\ minutes \\ > 2000\ \mu m\text{: } if\ c_0 = 10\ \mu M, and\ \mathrm{T_{comp}} \sim 2000\ minutes \end{cases}$$

On the other hand, in the t_e^*, the self-assembly in the $c_0^{*,high}$ case progresses faster at the inlet end and slows down along the length of the reaction surface toward the microchannel outlet, compared to the $c_0^{*,low}$ case. This observations was expected since the adsorption capacity (ϵ), is considerably higher in the $c_0^{*,high}$ case. According to Eq. (2.22):

$$\epsilon = \begin{cases} 5.48 \times 10^5\text{: } for\ c_0^{*,high} \\ 5.48 \times 10^2\text{: } for\ c_0^{*,low} \end{cases}$$

As mentioned in Section 2.3, ϵ compares the amount of analytes available in the bulk fluid with the total number of binding sites available on the reaction surface. In other words, ϵ measures the amount of analytes approaching each reaction spot. For the $c_0^{*,high}$, the reaction benefits from an instantaneously faster adsorption due to the higher amount of analytes available for each reaction site, implied in the corresponding higher adsorption capacity (ϵ). As a result of this higher adsorption rate, the reaction surface can deplete the bulk fluid from thiols at a relatively higher rate than the lower concentration cases. In the $\mathrm{t}_e^* = 0.001$ and $c_0^{*,high}$ case, the reaction was progressing faster at the beginning. However, the reaction was decelerated along the length of the reaction surface, since the amount of thiols entering the microchannel at the tiny interval ($\mathrm{t}_e^* = 0.001$) were probably not great enough. The faster progress of the reaction also justifies the depletion effect observed at the input end. For both times in the $c_0^{*,high}$ concentration, the depletion effect is illustrated by a noticeable variation of the surface concentration of adsorbed thiols along the reaction surface length. On the other hand, a hardly noticeable corresponding variation is present for the $c_0^{*,low}$ case. This observation confirms that increasing the ϵ results in enhanced transient kinetics in the self-assembly process (Figure 2.5).

2.4.1.2 The Micro-Channel Height Effect on the Self-assembly Kinetics

Deeper microchannels are intuitively expected to have better self-assembly kinetics than thinner ones, since there are more thiol adsorbates present in deeper microchannels. In Figure 2.7, the SAM reaction kinetics for three microchannel heights is simulated assuming an input thiol concentration of $10\ mM$, flow velocity of $150\ \mu m.s^{-1}$ and heights of 10, 40 and 80 μm. In the figure, time is non-dimensionalized by dividing it by a nominal 15-minute process ($T_{comp} = 15$ minutes), and the height by a nominal value of $40\ \mu m$ ($h^* = h/(40\ \mu m)$). The results show that the microchannel height variation brings about minor changes in the self-assembly kinetics.

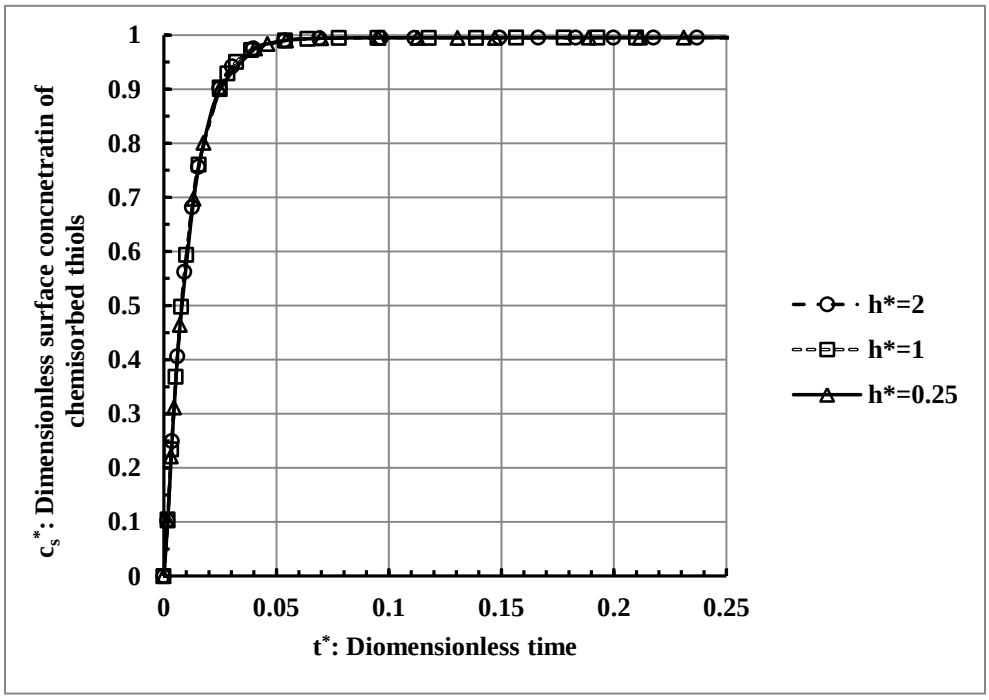

Figure 2.7: Simulated evolution of chemisorbed thiols' surface concentration (c_s^*) via time (dimensionless), for self-assembly from a concentration of $10\ mM$ and plotted for different microchannel heights. The height is non-dimensionalized by a reference height of $40\ \mu m$: $h^* = h/(40\ \mu m)$, and time is non-dimensionalized by a nominal process time (T_{comp}) of 15 minutes : $t^* = t.T_{comp}^{-1}$. The insignificant role of the microchannel height on the self-assembly kinetics is demonstrated, showing less than 1% of difference between the curves at each moment.

Figure 2.7 shows that the SAM-formation kinetics is nearly independent of the microchannel height. In other words, the c_s^* values differ by less than 1% between the curves at each moment. This independence can be explained by considering the kinetics' descriptive dimensionless numbers. According to Eq. (2.20), the Peclet number is a linear function of the microchannel height. Increasing the height, for instance from $0.25 \overset{h^*}{\rightarrow} 2$ ($10 \overset{h}{\rightarrow} 80\ \mu m$), i.e., for around one order of magnitude, increases the Peclet number from the initial value of 2.63 to 21.05. Thus, the weight of convection is further increased for around one order of magnitude with respect to the diffusion strength. The impact of convection was initially around three times greater than diffusion. Therefore, convection transport becomes the truly dominant mass transport mechanism. However, as shown in Section 2.4.1.1, thiol self-assembly has a reaction-limited nature: $\mathrm{Da} = 4.6 \times 10^{-8}$ for $h^* = 0.25$ ($h = 10\ \mu m$). Therefore, increasing the strength of convection may not necessarily result in a faster kinetics. During the microchannel height variation considered here, the Damköhler number does not undergo a noticeable change. Accordingly, the kinetics remains fully reaction-limited. Thus, a negligible alteration in the kinetic properties is expected. According to Eq. (2.21):

$$0.25 \overset{h^*}{\rightarrow} 2 \overset{self-assembly}{\Longrightarrow} 4.6 \times 10^{-8} \overset{\mathrm{Da}}{\rightarrow} 5.34 \times 10^{-8}$$

It is worth noting that further increase of the microchannel height from $80\ \mu m$ ($h^* = 2$) to $800\ \mu m$ ($h^* = 2$), or even higher to $5\ mm$ ($h^* = 125$), is not expected to result in a noticeably better kinetics. This expectation is reasonable because the kinetics remains highly reaction-limited ($\mathrm{Da} \sim 10^{-8}$), and the Peclet number augmentation occurs in a completely convection-dominated mass transport ($\mathrm{Pe} \sim 21$). The following calculation shows that increasing the channel height to $5\ mm$ ($h^* = 125$) results in minor changes in the Damköhler number. The latter parameter and the Peclet number are calculated according to Eq. (2.21) and Eq. (2.20), respectively:

$$\text{if } u_{avg} = 150\ \mu m.\, s^{-1} \text{and } h = 5\ mm \overset{self-assembly}{\Longrightarrow} \begin{cases} \mathrm{Da} = 5.59 \times 10^{-8} \\ \mathrm{Pe} = 1315 \end{cases}$$

The zero-flow case demonstrated the same trend as the flow-through mode, showing a weak impact from microchannel height variations on the kinetics. Due to the increase (decrease) of the microchannel height around the nominal height of $40\ \mu m$ ($h^* = 1$), the process time decreased (increased) by less than 1%. The same trend occurs because, during the height variations, the kinetics remains reaction-limited in nature ($\mathrm{Da} \ll 1$). To confirm that the kinetics remains reaction-limited

during the height variations, the Damköhler number for the zero-flow mode is calculated as follows, for the typical channel heights considered in the simulations and according to Eq. (2.21):

$$\mathrm{Da} = \begin{cases} 1.47 \times 10^{-7}: \text{if } h^* = 0.25\ (h = 10\ \mu m\ ) \\ 5.89 \times 10^{-7}: \text{if } h^* = 1\ (h = 40\ \mu m) \\ 7.36 \times 10^{-5}: \text{if } h^* = 125\ (h = 5\ mm) \end{cases}$$

From the hydrodynamic point of view, the observed weak dependency of the kinetics on the microchannel height is attributed to the considerably low rate of growth of the thiol depletion zone inside the microchannel. Due to this low growth rate, the thickness of the depletion zone (δ_c) is much less than the height of the microchannel ($\delta_c \ll h$), confirmed by the numerical simulations. Thus, for the heights considered here, the upper wall cannot noticeably affect the thickness of the depletion zone formed over the reaction surface. As a result, the overall kinetics remains nearly independent from the microchannel height variations considered here.

The observed independence of the reaction progress rate from the channel height can be explained physically based on the thin thickness (relative to the channel heights studied here) of the depletion zone (δ_c) over the reaction surface. The relative thickness of the depletion zone (δ_c) compared to the channel height can be approximated as follows. Total amount (in moles) of reagents needed for the completion of the reaction, C_{comp}, equals the total amount of thiols that can be chemisorbed to the reaction surface. The minimum height that contains C_{comp} is designated here by h_{min}. The latter parameter is a function of the thiol concentration in the bulk fluid (c_0) and surface concentration of reagents (θ_0) and can be formulated as follows:

$$\mathrm{C}_{comp} = \theta_0 ld = c_0 ldh_{min} \Rightarrow h_{min} = \frac{\theta_0}{c_0} \tag{2.25}$$

where d is the depth of the microchannel and l is the length of the reaction surface. If $\theta_0 = 7.3 \times 10^{-10}\ mol.m^{-2}$, then Eq. (2.25) yields:

$$\begin{cases} h_{min} = 7.3 \times 10^{-5} \mu m\ (< 1\ nm), \text{if: } c_0 = 10\ mM \\ h_{min} = 7.3 \times 10^{-2} \mu m, \text{if: } c_0 = 10\ \mu M \end{cases}$$

The above calculation shows that for microchannel heights exceeding a few micrometers, there is an abundance of thiols present in the reaction environment ($h_{min} \ll h$). In other words, total amount of

reagents needed for the completion of reaction is contained in the first few nanometers of bulk fluid above the reaction surface. Moreover, due to the reaction-limitation (Da$\sim 10^{-7} \ll 1$), the rate of reaction, and accordingly the depletion rate of reagents, is significantly lower than the mass transport rate. Therefore, the thickness of depletion zone is much less than the height of microchannel ($\delta_c \ll h$). Thus, the reagents can be effectively replenished on the reaction surface from the first few nanometers of the bulk fluid above the reaction surface and the distance of the upper wall from the reaction surface (h) does not noticeably impact this replenishment rate. Thus, variations in h do not affect the reaction progress rate.

2.4.1.3 The Effect of the Available Self-assembly Sites on the Kinetics

The number of available self-assembly sites, or the number of thiol molecules that can be chemisorbed to the unit surface area (θ_0), is a function of the type of thiol molecules chosen and also the molar fraction of each type of the thiols in the solution, in the case of multi-component monolayers [38]. The number of available self-assembly sites, also called the active site concentration, directly affects the concentration of Abs bound to the SAM in immunoassays, and potentially, the SAM formation, Ab conjugation, and immunoreaction completion times. These effects occur because magnification of the θ_0 leads to a higher number of self-assembly sites to be occupied by the adsorbates. This situation intuitively suggests an increased reaction time.

The transient time evolution of the surface concentration of the thiols for three dimensionless active site concentrations of $\theta_0^* = 1, 10, 100$ and 1000 ($\theta_0^* = \theta_0/(7.3 \times 10^{-10}\, mol.m^{-2})$ is plotted in Figure 2.8 below. Simulation results show that θ_0 plays an insignificant role in the kinetics. The dimensionless surface concentration of the thiols ($c_s^* = c_s.\theta_0^{-1}$) changes among the curves by less than 1% at each moment. Time is non-dimensionalized by the reaction completion time of the zero-velocity case: $t^* = t/\mathrm{T}_{comp}$ ($\mathrm{T}_{comp} = 15$ minutes).

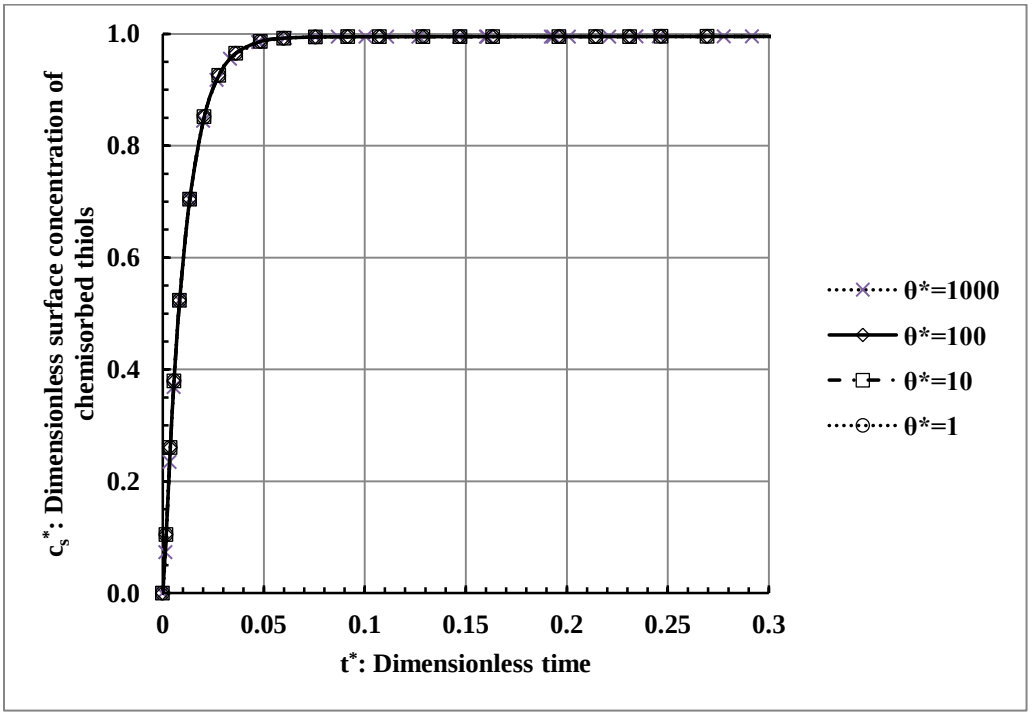

Figure 2.8: Simulated dimensionless surface concentration of chemisorbed thiols (c_s^*) via time (dimensionless), for an input 10 mM thiol concentration, plotted for different available chemisorption sites in unit area (θ_0 in $mol.m^{-2}$), exhibiting minimal effects on the kinetics. The difference between the curves is less than 1% at each moment. Time and θ_0 are respectively non-dimensionalized by a nominal process time of 15 minutes and a reference packing density of $7.3 \times 10^{-10}\ mol.m^{-2}$: $t^* = t/\mathrm{T}_{comp}$, $\theta_0^* = \theta_0/(7.3 \times 10^{-10}\ mol.m^{-2})$.

Figure 2.8 shows that the θ_0 has a minimal impact on the self-assembly kinetics, which is highly reaction-limited: $\mathrm{Da} = 5.11 \times 10^{-8}$, Section 2.4.1.1. A slower reaction is normally expected due to the increase of θ_0. This expectation is reasonable because an increase in the θ_0, e.g., for two orders of magnitude from the initial value of $\theta_0^* = 1$ ($\theta_0 = 7.3 \times 10^{-10}\ mol.m^{-2}$), linearly increases the number of reaction sites that should be occupied by thiols. Therefore, a slower kinetics is normally expected. However, a noticeable kinetic change is not observed here since the kinetic alteration is happening in a fully reaction-limited region: $5.11 \times 10^{-8} < \mathrm{Da} < 5.11 \times 10^{-6}$. The reaction progress rate in such situations is nearly insensitive to the change of the reaction rate potential (k_a: numerator of the Da) relative to the mass transport strength (denominator of Da). The insensitivity is due to the significantly low reaction progress rate relative to the mass transport,

manifested in a low Damköhler number. In such situation, change of θ_0 does not noticeably alter the kinetic properties, unless the Da is increased considerably close to the transport-limited region (Da$\sim$1), where reaction rate potential is comparable to the mass transport strength. On the other hand, the adsorption capacity is decreased from the $\epsilon = 5 \times 10^5$ at the same pace, for two orders of magnitude from the initial value, according to Eq. (2.22). A decrease in the adsorption capacity (ϵ) is also expected to cause a slower kinetics. This expectation is reasonable because with lower adsorption capacities, there are more binding sites available for occupation by the thiols, for the same amount of thiols present in the bulk fluid. However, the net change in the overall kinetics due to the θ_0 variation is not noticeable here, since the nature of the kinetics remains reaction-limited after the θ_0 alteration ($5.11 \times 10^{-8} < \text{Da} < 5.11 \times 10^{-6}$). In other words, since in the course of θ_0 variation, the relative strength of reaction does not undergo a significant change with respect to the mass transport strength, θ_0 increase cannot effectively decelerate the kinetics. In general, due to the θ_0 increase, the kinetics might become either much slower, moderately slower or remain nearly intact. This kinetics change mainly depends on the state of the kinetics before the change, i.e., being reaction- or transport-limited. Effects of the active site concentration (θ_0) on the other reactions considered in this research, i.e., conjugation and immunoreaction, are compared to the self-assembly kinetics in Section 2.5.2, by consideration of the dimensionless groups such as Da and ϵ.

Physically, θ_0 directly impacts the minimum number of reactants needed to complete the reaction: C_{comp} (Eq. 2.25). As discussed in Section 2.4.1.2, C_{comp} is directly related to the minimum height of the microchannel (h_{min}) which if filled with the reactants, has enough reactants for the completion of reaction. For a given concentration (c_0), microchannel height (h), and a nominal θ_0, the minimum required height of the microchannel for reaction completion can be determined from Eq. (2.25). Depending on the ratio of this minimum height (h_{min}) with respect to the actual height of the microchannel (h), change of θ_0 might have negligible impact on, or noticeably alter the reaction progress rate, as detailed in the following:

If $h_{min} \ll h$, such as the self-assembly kinetics, then there is an abundance of reactants available in the bulk fluid, and due to the reaction limitation (Da $\ll$ 1) the thickness of the depletion zone is much less than the height ($\delta_c \ll h$). Thus, change of θ_0 has negligible effects on the reaction progress rate (see Section 2.4.1.2).

If $h_{min} \sim h$, then change of θ_0 might noticeably impact the reaction progress rate, since the amount of reactants available in the bulk approaches the minimum required for completion of the reaction. The latter situation exists for the immunoreaction kinetics and will be examined in Section 2.4.3.3.

For $\theta_0 = 7.3 \times 10^{-10}\ mol.m^{-2}$, Eq. (2.25) yields:

$$\begin{cases} h_{min} = 7.3 \times 10^{-5} \mu m\ (< 1\ nm), \text{if: } c_0 = 10\ mM \\ h_{min} = 7.3 \times 10^{-2} \mu m, \text{if: } c_0 = 10\ \mu M \end{cases}$$

The above calculations show that for microchannel heights exceeding a few micrometers, e.g., $h = 40\ \mu m$, there is an abundance of thiols present in the reaction environment ($h_{min} \ll h$). Therefore, by increasing the θ_0, even for two orders of magnitude, h_{min} increases to few microns and is still considerably less than h. Thus, the reaction progress rate is not affected by the change of θ_0.

2.4.2 Antibody/SAM Conjugation Kinetics

The model was employed to find the conjugation completion times, and the outcomes were verified and agreed with the available experimental result [149], with less than 3% of difference for an EDC concentration of $0.7\ mM$. The conjugation kinetics was studied against the variation of the major kinetics parameters such as the EDC concentration, the flow velocity, and the microchannel height. NHS has a catalytic role; therefore, its effects were excluded from the simulations. As stated earlier, the Ab concentration does not impose a significant impact on the kinetics, since the reaction of EDC and the carboxylic group of thiols is the rate-determining step, discussed in Section 2.2.3.2. Impacts of the temperature variations were also ignored. Unless stated otherwise, the following assumptions were made: the height of the microchannel was set at $40\ \mu m$, simulations were conducted for an inlet flow velocity of $150\ \mu m.s^{-1}$, using a $5\ mM$ EDC buffer. The rate constant of Eq. (2.16) was $k_e = 4.6 \times 10^{-3}\ m^3.(mol.s)^{-1}$, corresponding to a pH of around 7.4 [149], i.e., the normal pH of the buffer fluids used in this research. In Section 1.3.2.1, the number of carboxyl-ended thiols in each $1.4 \times 10^{-10}\ cm^2$ of the substrate was found to be around 6000 sites that could be conjugated with the Ab of interest [38]. This number of available carboxylic groups corresponds to $7.3 \times 10^{-11}\ mol.m^{-2}$ of conjugation sites for Abs. A maximum of 60% of these carboxylic groups can be conjugated to the Abs, corresponding to a surface concentration of $\theta_0 = 4.38 \times 10^{-11}\ mol.m^{-2}$ [154]. The conjugation reaction was considered completed when, for the first time, the surface

concentration of conjugated Abs (c_s) passed 99% of the total surface concentration of the carboxylic groups on the reaction surface (θ_0), i.e., $c_s.\theta_0^{-1} > 0.99$.

2.4.2.1 The EDC Concentration and the Flow Rate Effects on the Conjugation Kinetics

The predicted Ab/SAM conjugation completion times are shown in Figure 2.9 below, for the input concentrations of EDC between 0.1-100 mM, simulated for two cases of zero-flow mode (traditional incubation or pipetting) and the flow-through conjugation. The parameters under consideration here are the concentration of EDC and the flow velocity.

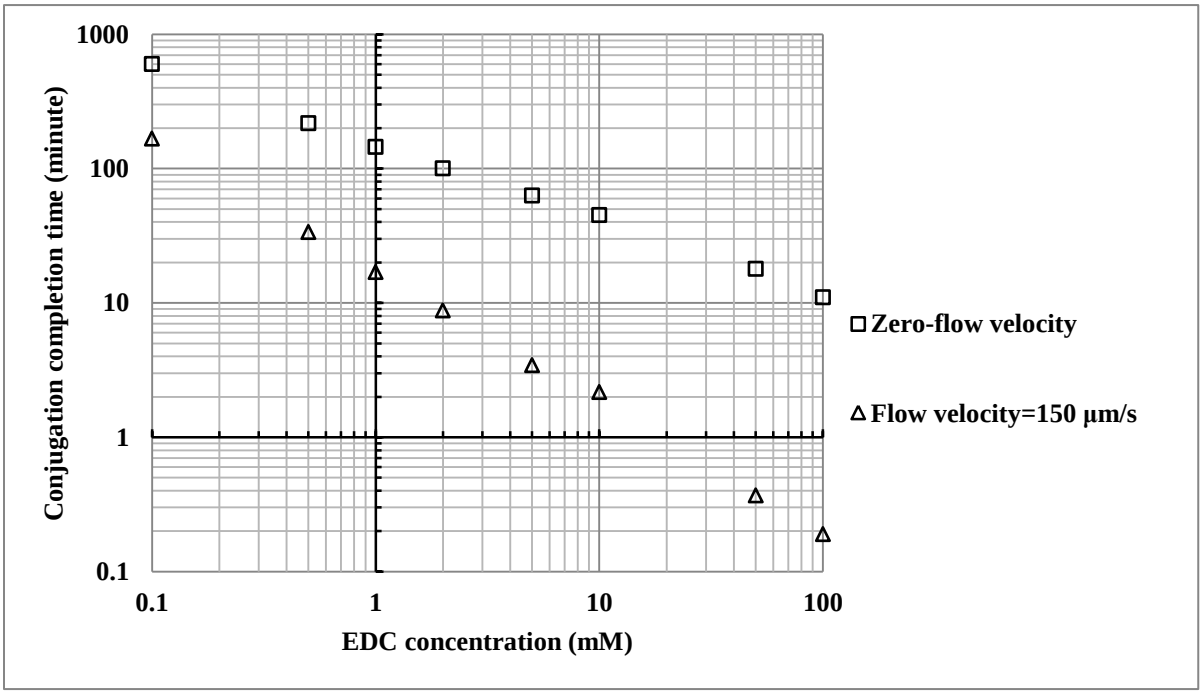

Figure 2.9: The calculated antibody/SAM conjugation completion times predicted for different EDC concentrations, plotted in the logarithmic scale for two flow velocities. Use of higher flow velocities decreases the process time by about one order of magnitude. Increase of the EDC concentration almost exponentially enhances the kinetics.

Figure 2.9 depicts the time period required to conjugate the Ab molecules from their amine group to the carboxylic head groups of the thiolic SAM, as a function of the initial concentration of the EDC molecules in the bulk fluid. Simulation results show a nearly exponential reduction of the process time via increasing the EDC concentration. The trend observed here is expected because, due to Eq.

(2.15) (with $k_d = 0$), the analytical solution of the reaction is an exponential function of concentration and time. For example, the process time is decreased from 605 minutes to 11 minutes upon increasing the EDC concentration from 0.1 to $100\,mM$, for the zero-flow mode. Similar observations are made for the flow-through mode as well. Physically, augmentation of the reagents concentration normally results in a faster process, since the number of reagents (in unit volume) that can approach a reaction spot is increased. Upon conjugation initiation from a $5\,mM$ EDC sample, the reaction is predicted to become complete in around one hour ($T_{comp} = 63$ minutes) for the zero-flow case. This process time is in agreement with the one-hour conjugation process that is recommended in conventional protocols. However, in conventional protocols, higher concentrations of EDC are suggested for such a process time, such as 50 or $100\,mM$. According to the figure, the times needed for Ab conjugation in these higher concentrations of EDC are considerably lower than the process times reported in the literature [12, 19]. Samples with EDC concentrations of $50\,mM$ and $100\,mM$ correspondingly require 18 and 11 minutes of incubation for the conjugation completion, while the recommended incubation times are between one to three hours [12, 19]. This issue has a particular importance, as an improper process time might result in an incomplete conjugation, leaving unreacted carboxylic groups or unwanted reaction by-products on the bio-interface [151].

The impact of process time on conjugation success can be investigated through analysis of the chemical composition of the reaction surface. Determination of the by-product composition on the reaction surface helps reveal the possible reactions paths. Sam et al., investigated the formation of the chemical by-products at varying EDC/NHS concentrations, using a constant 90-minute process time [151]. The role of different EDC/NHS concentrations on the reaction yield was studied by utilization of the infrared spectroscopy. They reported the presence of acid and anhydride by-products for the $2\,mM$ EDC/NHS samples undergoing a 90-minute reaction. Anhydride is the product of reaction between the o-acylisourea and an additional carboxylic acid (see Figure 2.3). These chemical by-products are indicative of unbound carboxylic groups on the reaction surface, suggesting an incomplete reaction. This finding is in agreement with the simulation results here, as the conjugation completion time for a $2\,mM$ EDC concentration was expected to be more than 90 minutes, i.e., predicted to be 100 minutes (Figure 2.9). At the 50-100 mM EDC concentrations, urea derivatives were present [151]. This observation also matches our model predictions, in the sense that a sample with 50-100 mM EDC concentration needs between 10-20 minutes for conjugation completion (Figure 2.9). Therefore, the presence of urea derivatives after a 90-minute process may suggest

overexposure to the crosslinking reagents. This speculation is reasonable because the presence of these by-products implies the reaction of urea, as a main conjugation product, with the other chemicals present in the reaction medium. This side reaction proceeds when enough time is available. It is worth noting that urea is carried away from the reaction environment if the reaction surface is rinsed after the conjugation completion [19]. At the $5\,mM$ EDC/NHS concentration, no by-products were observed and the reaction was completed [151]. However, the numerical model predicts that a conjugation process of around one hour (63 minutes) is enough for the completion of the conjugation process from a $5\,mM$ EDC/NHS sample. In this concentration, urea derivatives were not detected after 90 minutes, which is approximately 30 minutes above the model predictions. The absence of these by-products is attributed to the low concentration of EDC used, which is at least one order of magnitude less than the case of 50 or $100\,mM$ samples. As a result, almost all the crosslinking reagents were probably consumed in the conjugation process and not enough reagents were available for reaction with urea, despite a prolonged process. Based on these experimental observations, and also, according to the simulation results, it is concluded here that in the conventional protocols [12, 19], the Ab/SAM complexes have been overexposed to higher than needed EDC/NHS concentrations. Overexposure has resulted in lower conjugation efficiencies and increased by-products. This conclusion is partially verified in Chapter 3, by examining the Ab loading densities resulting from the conduction of the conjugation reaction.

Figure 2.9 also shows that using the flow-through mode has a significant potential for enhancing the conjugation kinetics. Upon increasing the flow velocity from zero to $150\,\mu m.s^{-1}$, the kinetics was enhanced by at least 5 times in lower concentrations of EDC, such as $0.1\,mM$, to at least one order of magnitude in the higher concentrations, such as $100\,mM$. Calculation of the Damköhler number and binding capacity is helpful in explaining the trend seen here. The Damköhler number in the conjugation kinetics is heavily dependent on the flow velocity. In other words, change of velocity can considerably alter the ratio of reaction progress rate with respect to the mass transport strength. For instance, in the case of zero velocity, the $\mathrm{Da} = 8.1 \times 10^{-7} (\sim 10^{-6})$, i.e., around three orders of magnitude more than the case of flow-assisted mode ($\mathrm{Da} = 1.34 \times 10^{-9}$), implying a considerable potential for kinetics enhancement via implementation of the flow-through mode. The Damköhler number calculation for the flow-assisted mode is repeated below, from Eq. (2.21), for a $150\,\mu m.s^{-1}$ flow velocity:

$$\mathrm{Da} = \frac{k_a \theta_0}{\frac{D}{h} + u_{avg}} = \frac{4.6 \times 10^{-3} m^3.(mol.s)^{-1}\ .\ 4.38 \times 10^{-11} mol.m^{-2}}{\frac{1 \times 10^{-11}\ m^2.s^{-1}}{40 \times 10^{-6}\ m} + 150 \times 10^{-6} m.s^{-1}} = \frac{2.02 \times 10^{-13}}{2.5 \times 10^{-7} + 1.5 \times 10^{-4}}$$
$$= 1.34 \times 10^{-9}$$

In both the zero-flow velocity and flow-through modes, the kinetics is reaction-limited. Nevertheless, use of flow-through mode has resulted in a significant decrease of conjugation completion time. This observation can be explained by careful consideration of the reaction-limitation and also the binding capacity of the reaction. Reaction-limitation refers to situations in which increase of flow velocity is not expected to cause a considerable kinetics enhancement. However, the latter condition does not correspond to a complete independency of the reaction-progress rate from the flow rate. In other words, there is always a possibility to increase the rate of reaction by augmentation of the mass transport rate (though not necessarily significant). On the other hand, the binding capacity ($\epsilon = c_0 h.\theta_0^{-1}$) is relatively high in the conjugation reaction. According to Eq. (2.22), for $h = 40\ \mu m$, and $\theta_0 = 4.38 \times 10^{-11} mol.m^{-2}$, the binding capacity range is calculated as follows:

$$0.1\ mM < c_0 < 100\ mM \xrightarrow{Conjugation} 9.13 \times 10^4 < \epsilon < 9.13 \times 10^7$$

Due to the high ϵ amounts calculated above, there is an abundance of the adsorbates present in the bulk fluid for each reaction site. In such situation, if the adsorbates are better driven to the reaction surface (for example by use of flow-through mode), the high level of ϵ allows for a considerable overall kinetic enhancement. The binding capacity for the self-assembly reaction is around four orders of magnitude less than that of the conjugation reaction. Therefore, the flow rate dependency of the self-assembly kinetics is much less than that of the conjugation. Effects of the flow velocity on the other reactions considered in this research, i.e., self-assembly and immunoreaction, are compared to the conjugation kinetics in Section 2.5.1.2.

Figure 2.9 also demonstrates that the conjugation kinetics gains a higher flow rate dependency via an increase in the EDC concentration. Upon utilization of the flow-through mode, the conjugation completion time is decreased by 33% in the lower EDC concentration of $0.1\ mM$, with respect to the original process time. The corresponding change is 98% for the higher concentration of $100\ mM$. Upon elevation of the EDC concentration, the binding capacity (ϵ) is linearly magnified. According to Eq. (2.22), a magnified ϵ implies fewer binding sites available for the analytes binding, assuming a fixed number of analytes is present in the bulk fluid. Therefore, the binding sites are expected to be

occupied faster, relative to the original case, resulting in an enhanced kinetics. Accordingly, one can expect a higher level of sensitivity toward flow velocity in the higher concentrations of EDC ($0.1 < c_0 < 100\ mM$).

Other than the long-term kinetics, flow velocity can affect the transient processes, illustrated in Figure 2.10 below.

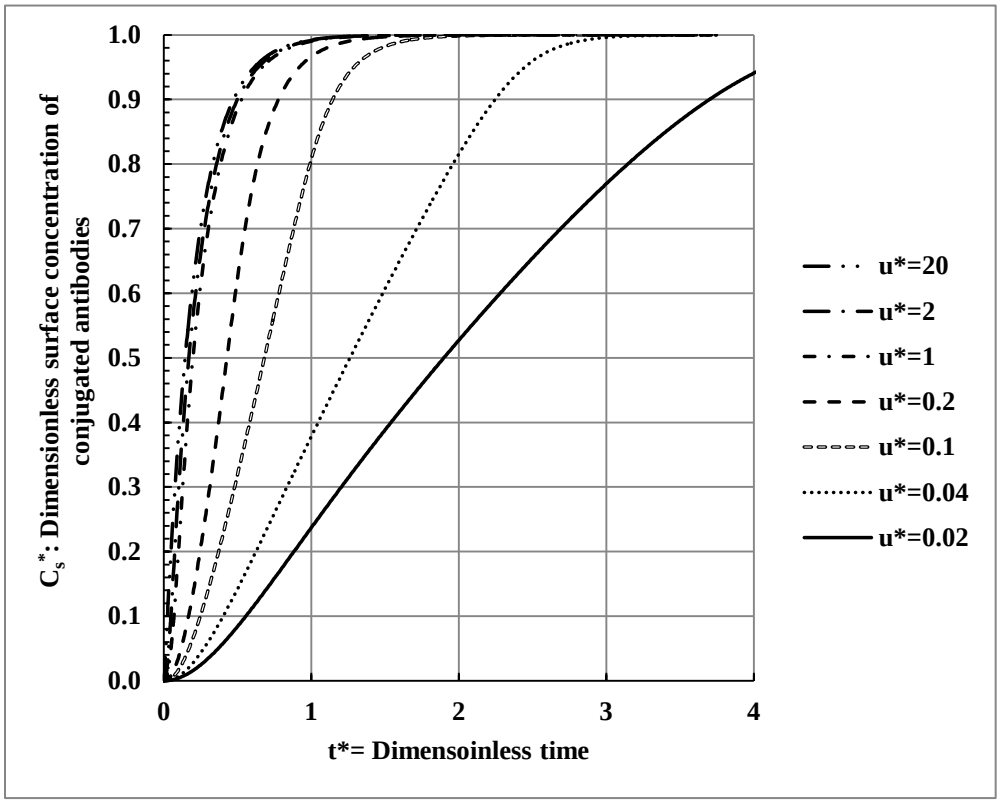

Figure 2.10: Simulated transient curves of the dimensionless surface concentration of conjugated antibodies (c_s^*) at some typical flow velocities and an EDC concentration of 5 mM. The velocity and time are non-dimensionalized by a nominal flow velocity of 75 $\mu m.s^{-1}$ ($u^* = u_{avg}/(75\ \mu m.s^{-1})$) and its corresponding process time (T_{comp}) of 3 minutes and 34 seconds ($t^* = t.T_{comp}^{-1}$). An increase in the flow velocity results in faster transient processes for the lower flow rates.

Figure 2.10 is a plot of the instantaneous dimensionless surface concentration of Abs ($c_s^* = c_s.\theta_0^{-1}$) over time, simulated for a variety of flow velocities. The velocity and time are non-dimensionalized by a typical flow velocity of $75\ \mu m.s^{-1}$ ($u^* = u_{avg}/(75\ \mu m.s^{-1})$) and its corresponding process

time (T_{comp}) of 3 minutes and 34 seconds ($t^* = t/T_{comp}$). No further significant improvement can be seen in the transient kinetics after the flow velocity is increased beyond $u^* = 1$ ($75\ \mu m.s^{-1}$), as the c_s^* values differ by less than 1% between the curves at each moment. This observation may be attributed to employment of the maximum possible transport capacity for the kinetic enhancement at that velocity, bearing in mind that the kinetics has a reaction-limited nature. Beyond this flow velocity, increasing the flow rate does not result in a noticeable transient kinetics improvement; however, the reagent consumption increases, leading to additional costs.

Figure 2.11 below summarizes the simulated Ab conjugation completion times for a number of flow velocities from zero to $1500\ \mu m.s^{-1}$, corresponding to $0 \leq u^* \leq 20$ in Figure 2.10. A unique attribute of this kinetics is the sensitivity toward mass transport augmentation. The completion time is reduced around six times from 63 to 12 minutes through a tiny increase in the velocity from zero to $1.5\ \mu m.s^{-1}$ ($u^* = 0.02$).

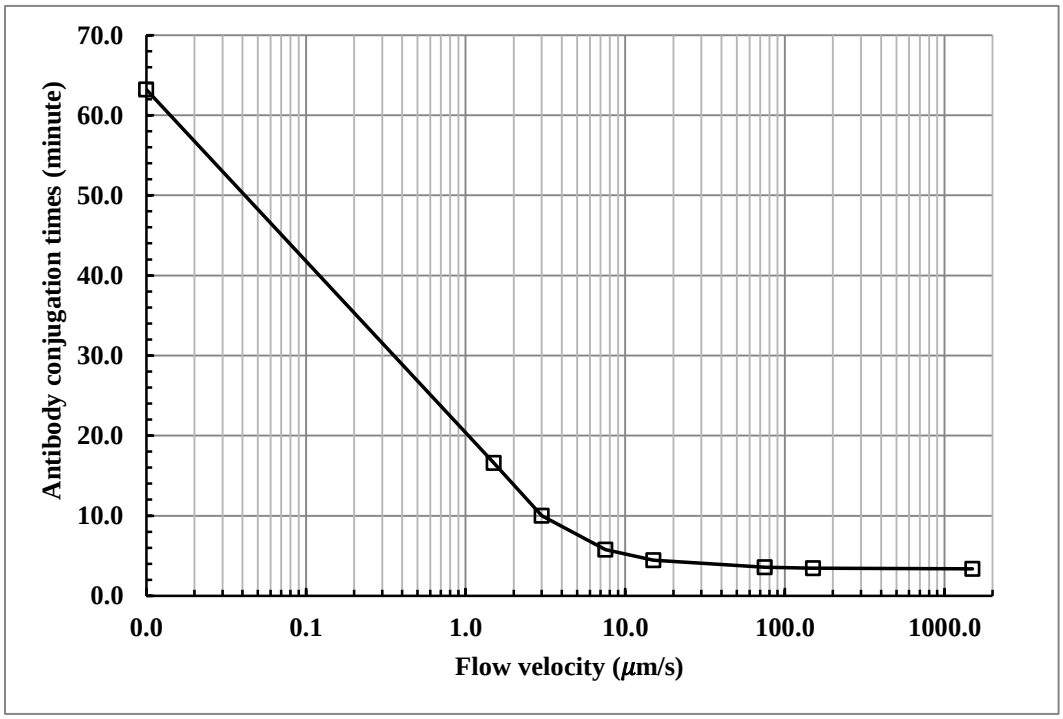

Figure 2.11: Model-predicted antibody conjugation completion times in minutes, with an input 5 mM EDC concentration, plotted for various inlet flow velocities (in log scale), showing a significant reduction in the process times, resulting from using the flow-through mode. Data points are connected by straight-line segments to aid visualization.

The kinetic enhancement is due to an existing potential for enhancing the reaction progress rate by increasing the replenishment rate of reactants on the reaction surface, discussed earlier in this section. The latter phenomenon corresponds to the presence of a high binding capacity ($\epsilon \sim 10^7$) and a considerable change in the ratio of reaction potential compared to the mass transport strength, i.e., the Damköhler number. The latter parameter (Da) reduces for around one order of magnitude upon an increase in the flow velocity from zero to $1.5\ \mu m.s^{-1}$ ($u^* = 0.02$). According to Eq. (2.21), the Damköhler number variation can be calculated as follows:

$$0 \xrightarrow{u_{avg}} 1.5\ \mu m.s^{-1} \xrightarrow{Conjugation} 8.1 \times 10^{-7} \xrightarrow{\text{Da}} 1.15 \times 10^{-7}$$

Figure 2.11 also shows that increasing the flow velocity does not necessarily lead to considerably reduced process times. For example, no significant reduction in the process time is achievable beyond a flow velocity of $15\ \mu m.s^{-1}$, corresponding to $u^* = 0.2$ in Figure 2.10. The process time decreases from $4'{:}26''$ by around 22% to $3'{:}27''$ even after increasing the flow velocity by one order of magnitude to $150\ \mu m.s^{-1}(u^* = 2)$. Comparing Figure 2.10 and Figure 2.11 reveals that the flow rate affects transient processes more than long-term runs. While the transient curves are "saturated" at a nominal flow velocity of around $75\ \mu m.s^{-1}(u^* = 1)$, the saturation in the conjugation completion times happens at a considerably lower velocity of around $15\ \mu m.s^{-1}$ ($u^* = 0.2$). These observations imply that the Ab-conjugation kinetics can be easily enhanced by the implementation of low-flow velocities of around $15\ \mu m.s^{-1}$ ($u^* = 0.2$), and there is no need for higher velocities. In this reaction, the use of higher than $15\ \mu m.s^{-1}$ velocities results in almost linearly increased reagent consumption, without a noticeable improvement in the kinetics. The total consumption of the reagents is proportional to the product of the flow velocity and the reaction completion time [127]. Increase of flow velocity beyond a certain value ($u^* \sim 0.2$) loses its role in enhancing the conjugation reaction rate. The latter condition emerges because the kinetic approaches a highly reaction-limited state, in which total potential of flow velocity for kinetic enhancement is almost completely used. The latter situation corresponds to a reaction condition in which the reaction rate gains such a low proportion compared to the mass transport strength that increasing the supply rate of reactants does not result in a noticeably faster process. In such states, the reaction rate is the limiting rate factor, not the replenishment rate.

2.4.2.2 The Micro-Channel Height Effect on the Conjugation Kinetics

Figure 2.12 presents the transient Ab conjugation process for a number of microchannel heights with respect to time (dimensionless). Time is non-dimensionalized by the corresponding process time ($\mathrm{T}_{comp} = 3'\colon 27''$): $t^* = t.\mathrm{T}_{comp}^{-1}$, and the height is non-dimensionalized by a reference height of 40 μm: $h^* = h/(40\ \mu m)$. It can be observed that increasing the microchannel height does not contribute to a clearly better kinetics, as the resulting kinetic curves differ by less than 1% at each moment. This finding is counter-intuitive, since deeper microchannels have intrinsically more reagents available for reaction, and as a result, they are expected to have a faster reaction.

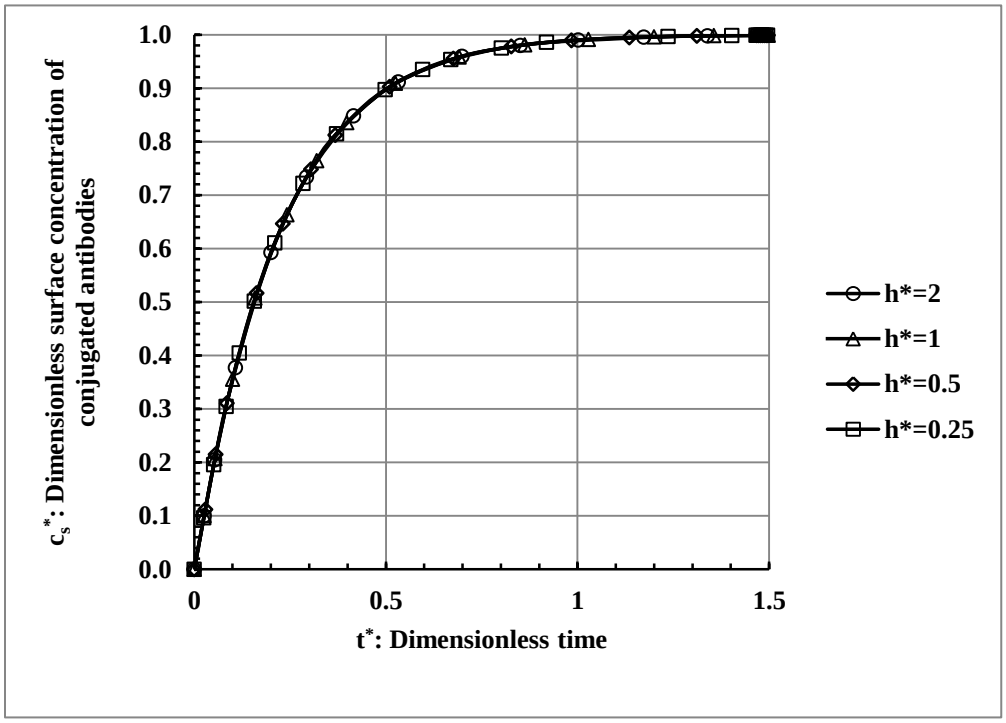

Figure 2.12: Simulated transient evolution of dimensionless surface concentration of conjugated antibodies (c_s^*), for a number of microchannel heights. The EDC input concentration is 5 mM, and flow velocity is 150 $\mu m.s^{-1}$. The height is non-dimensionalized by a reference height of 40 μm: $h^* = h/(40\ \mu m)$, and time is non-dimensionalized by the corresponding process time ($\mathrm{T}_{comp} = 3'\colon 27''$): $t^* = t.\mathrm{T}_{comp}^{-1}$. Increasing the microchannel height cannot effectively enhance the kinetics, and less than 1% of difference is observed between the resulting curves at each moment.

Calculation of the Damköhler number and the Peclet number helps to explain the kinetics' weak dependency on the microchannel height, using the same reasoning as for the case of the SAM kinetics, detailed in Section 2.4.1.2. Using a deeper microchannel magnifies the Peclet number; however, the Damköhler number remains almost unchanged, according to Eq. (2.21):

$$0.25 \overset{h^*}{\rightarrow} 2 \overset{Conjugation}{\Longrightarrow} \begin{cases} 1.33 \times 10^{-9} \overset{\mathrm{Da}}{\rightarrow} 1.34 \times 10^{-9} \\ 150 \overset{\mathrm{Pe}}{\rightarrow} 1200 \end{cases}$$

Augmentation of the Peclet number brings about a higher convection strength for the reaction compared to the diffusion rate. Thus, one can normally expect to observe an enhanced kinetics due to the higher convective replenishment rates. However, the reaction progress rate is not much altered from the original state, since the higher replenishment rate occurs in a highly reaction-limited condition (Da$\sim 10^{-9}$) where the reaction has already benefited from a high level of mass transport.

As with the self-assembly kinetics (Section 2.4.1.2), the zero-flow case demonstrated the same trend as the flow-through mode, showing a weak impact from microchannel height variations on the kinetics. Due to the increase (decrease) of the microchannel height around the nominal height of 40 μm ($h^* = 1$), the process time decreased (increased) by less than 1%. This observation is expected because the kinetics remains reaction-limited (Da $\ll 1$). To confirm the reaction-limited nature of the kinetics during the height variations, the Damköhler number for the zero-flow mode is calculated as follows, for a number of channel heights and according to Eq. (2.21):

$$\mathrm{Da} = \begin{cases} 2.01 \times 10^{-7}\text{: if } h^* = 0.25 \ (h = 10\ \mu m) \\ 1.61 \times 10^{-7}\text{: if } h^* = 2 \ (h = 80\ \mu m) \\ 1.01 \times 10^{-4}\text{: if } h^* = 125 \ (h = 5\ mm) \end{cases}$$

Regarding the hydrodynamic point of view, and the same as self-assembly kinetics (Section 2.4.1.2), the thickness of the depletion zone (δ_c) is much less than the height of the microchannel (h). Therefore, height variations considered does not noticeably affect the kinetics.

Physically, as mentioned for the self-assembly kinetics in Section 2.4.1.2, for microchannel heights exceeding a few micrometers, there is an abundance of reagents present in the reaction environment. Due to the reaction limitation (Da $\ll 1$) the thickness of the depletion zone is much less than the height ($\delta_c \ll h$). Therefore, change of microchannel height does not affect the reaction progress rate. h_{min} is a measure of the level of abundance of reagents in the reaction environment (Section 2.4.1.2)

and is calculated below for the conjugation kinetics, according to Eq. (2.25), and for $\theta_0 = 4.38 \times 10^{-11}\, mol.m^{-2}$:

$$\begin{cases} h_{min} = 4.38 \times 10^{-7} \mu m\ (< 1\ nm), \text{if: } c_0 = 100\ mM \\ h_{min} = 4.38 \times 10^{-4} \mu m\ (< 1\ nm), \text{if: } c_0 = 0.1\ mM \end{cases}$$

The above calculations show that for microchannel heights exceeding a few micrometers, there is always an abundance of reagents present in the reaction environment ($h_{min} \ll h$). Therefore, change of microchannel height does not affect the conjugation rate.

2.4.2.3 The Effect of the Available Conjugation Sites on the Kinetics

A higher number of conjugation sites in unit area (θ_0) intuitively results in longer process times for the immobilization of the Abs. This trend occurs because for a higher θ_0, there are more conjugation sites that should be occupied by the Abs, assuming other parameters remain the same. However, simulation results show that the θ_0 variation has minimal effects on the conjugation kinetics.

Figure 2.13 below presents the transient process of the conjugation reaction for a flow velocity of $150\ \mu m.s^{-1}$, in the first few minutes of the reaction. The dimensionless surface concentrations of bound Abs ($c_s^* = c_s.\theta_0^{-1}$) are plotted against time, for a number of θ_0 values. θ_0 is non-dimensionalized by a reference value of $4.38 \times 10^{-11}\ mol.m^{-2}$: ${\theta_0}^* = \theta_0/(4.38 \times 10^{-11}\ mol.m^{-2})$ and time is non-dimensionalized by the corresponding process time ($\mathrm{T}_{comp} = 3'\!:27''$): $t^* = t.\mathrm{T}_{comp}^{-1}$. As shown in the figure, the resulting kinetic curves do not noticeably differ from one another, and the difference in c_s^* values is less than 1% at each moment. The trend seen and also the reasoning behind the observations made are the same as the thiol self-assembly kinetics (Section 2.4.1.3). Further discussion on the trend observed here and comparison to other reactions considered in this thesis is presented in Section 2.5.2, using dimensionless groups.

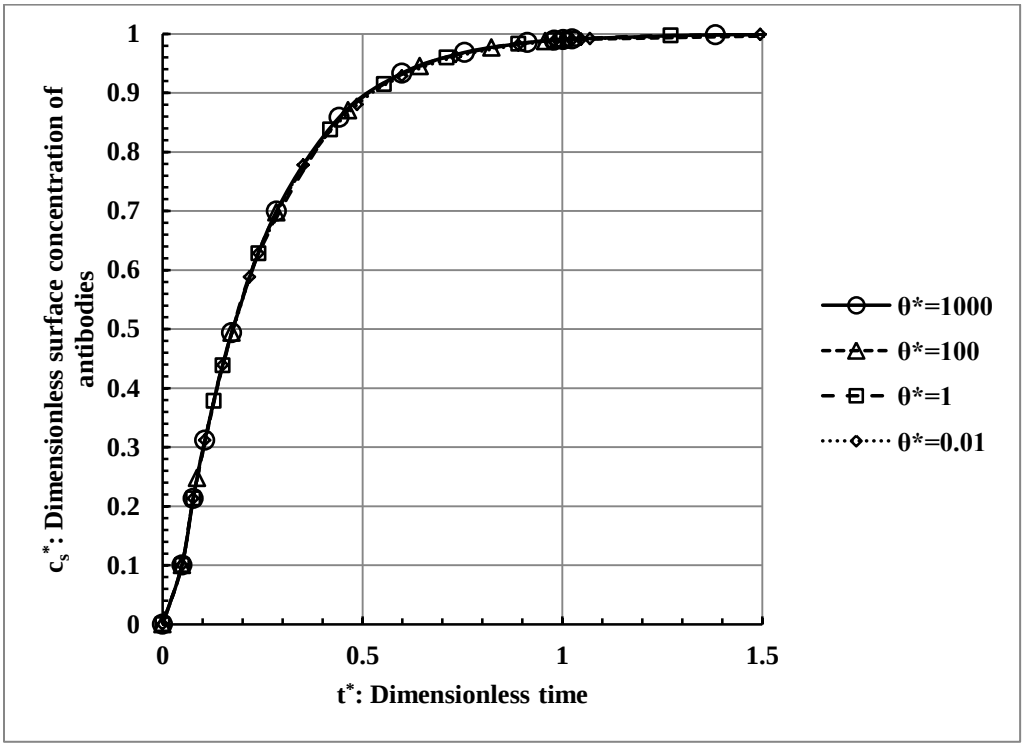

Figure 2.13: Surface concentration of conjugated antibodies via time, simulated for a number of initial surface concentrations of available conjugation sites (θ_0), demonstrating minimal effects on the kinetics with less than 1% of variation at each moment. θ_0 is non-dimensionalized by a reference value of $4.38 \times 10^{-11}\ mol.m^{-2}$: ${\theta_0}^* = \theta_0/(4.38 \times 10^{-11}\ mol.m^{-2})$, the EDC input concentration is $5\ mM$, flow velocity is $150\ \mu m.s^{-1}$, and time is non-dimensionalized by the corresponding process time ($T_{comp} = 3'\!:27''$): $t^* = t.T_{comp}^{-1}$.

Physically, θ_0 directly determines the abundance or shortage of reagents in the reaction environment, mentioned in Section 2.4.1.3. h_{min} is a measure of the level of abundance of reagents in the reaction environment (Section 2.4.1.2). The latter parameter is calculated below for the conjugation kinetics, according to Eq. (2.25), and for $\theta_0 = 4.38 \times 10^{-11}\ mol.m^{-2}$:

$$\begin{cases} h_{min} = 4.38 \times 10^{-7} \mu m\ (< 1\ nm), \text{if: } c_0 = 100\ mM \\ h_{min} = 4.38 \times 10^{-4} \mu m\ (< 1\ nm), \text{if: } c_0 = 0.1\ mM \end{cases}$$

The above calculations show that for microchannel heights exceeding a few micrometers, there is an abundance of reagents present in the reaction environment ($h_{min} \ll h$). As a result, even by

increasing the θ_0 for three orders of magnitude, h_{min} increases to around one micron and h is still considerably higher than h_{min} . Thus, the reaction progress rate is not affected by the change of θ_0.

The surface concentration of available conjugation sites can be modified by changing the type of functionalization method employed, such as use of polymers instead of thiols here [1, 19], or the implementation of other self-assembly techniques, such as by silanization of glass or PDMS instead of gold in this research [54].

2.4.3 HSP70 Immunoreaction Kinetics

The numerical model constructed in this research for the Ab/Ag binding kinetics was verified and agreed very well with other results, with less than 1% of variation in the reaction completion times [127, 136]. In this section, the proposed model is employed to examine the effects of some important parameters on the immunoreaction kinetics of HSP70, including the analyte concentration (c), the flow velocity (u_{avg}), the microchannel height (h), and the surface concentration of available binding sites (θ_0). Unless otherwise notified, the following parameters were used: $k_a = 1.82 \times 10^5\ M^{-1}.s^{-1}$ (association rate constant of HSP70), $k_d = 10^{-2}\ s^{-1}$ (dissociation rate constant) [31, 155], $\theta_0 = 4.68 \times 10^{-11}\ mol.m^{-2}$ (surface concentration of available binding sites). The latter assumes that 60% of the available carboxylic sites were conjugated with the Abs [154]. The k_a and k_d values are in the typical range of binding-rate constants for immunoassays: $10^5 \leq k_a \leq 10^7\ \ M^{-1}.s^{-1}$and $10^{-2} \leq k_d \leq 10^{-4}s^{-1}$ [130, 133, 156]. A flow velocity of $150\ \mu m.s^{-1}$ was typically assumed. The bulk concentration of HSP70 was kept at $c_0 = 65.7\ nM$, provided that most clinical diagnostic IAs can process analytes in a concentration range between 1-100 nM [28]. HSP70 with the concentration of $65.7\ nM$ is used later to assess the functionalization protocol performance, detailed in the next chapter. The diffusion constant of the Ag (HSP70) in the solution was assumed to be $D = 4 \times 10^{-11}m^2.s^{-1}$ [85], and the surface diffusion constant of the Ag was $D_s = 2 \times 10^{-13}m^2.s^{-1}$ [85]. The height of the microchannel was set at $40\ \mu m$. In the flow-through mode, the immunoreaction was deemed completed when the surface loading density of Ags reaches its maximum possible value ($c_{s,max}$), for the first time. $c_{s,max}$ depends on the input concentration of analytes, shown in the following section. In the zero-flow mode, the reaction was considered completed when at least 99% of $c_{s,max}$ is achieved, for the first time. The latter lower criterion of simulation termination was chosen to avoid excessively long simulation times.

2.4.3.1 The Flow Rate and HSP70 Concentration Kinetic Effects

The major difference between the conventional and the microfluidic-based IAs is that the operation is under the flow-through mode in the latter case, which further highlights the importance of studying the flow velocity effects on the kinetics. Moreover, concentration and velocity are probably the easiest parameters to vary for modification of the microfluidic IAs' performance.

Figure 2.14 below shows that using the microfluidic flow-through mode results in a significant time saving compared to the conventional incubation method. Figure 2.14 depicts the calculated HSP70' immunoreaction completion times simulated for the two flow velocities of $u_{avg} = 0$ (conventional incubation) and $u_{avg} = 150\,\mu m.s^{-1}$, plotted for a number of HSP70 input concentrations, in the range of 1-100 nM. Simulations predict that the zero-flow case necessitates around 350-800 minutes for finishing the immunoreaction process, i.e., a nearly exponential reduction in the incubation time (see Eq. (2.15)). Physically, the augmentation of the analytes concentration normally results in a faster process, since the number of reagents (in unit volume) that can approach a reaction spot is increased. The latter time span ($350 < \mathrm{T}_{comp} < 800$ minutes) is in agreement with the incubation times reported for conventional IAs in the literature [20, 21, 28]. The corresponding incubation times are expected to decrease to around 23-60 minutes, by employing a flow velocity of $150\,\mu m.s^{-1}$. Calculation of the Damköhler number is helpful for explaining the trend seen here. The same as the conjugation kinetics, the Damköhler number in the immunoreaction kinetics is heavily dependent on the flow velocity. In other words, change of velocity can considerably alter the ratio of the reaction progress rate with respect to the mass transport strength, manifested in a considerable change in the Damköhler number. The Damköhler number variations can be calculated by Eq. (2.21):

$$0 \xrightarrow{u_{avg}} 150\mu m.s^{-1} \xRightarrow{Immunoreaction} 7.88 \times 10^{-3} \xrightarrow{\mathrm{Da}} 5.22 \times 10^{-5}$$

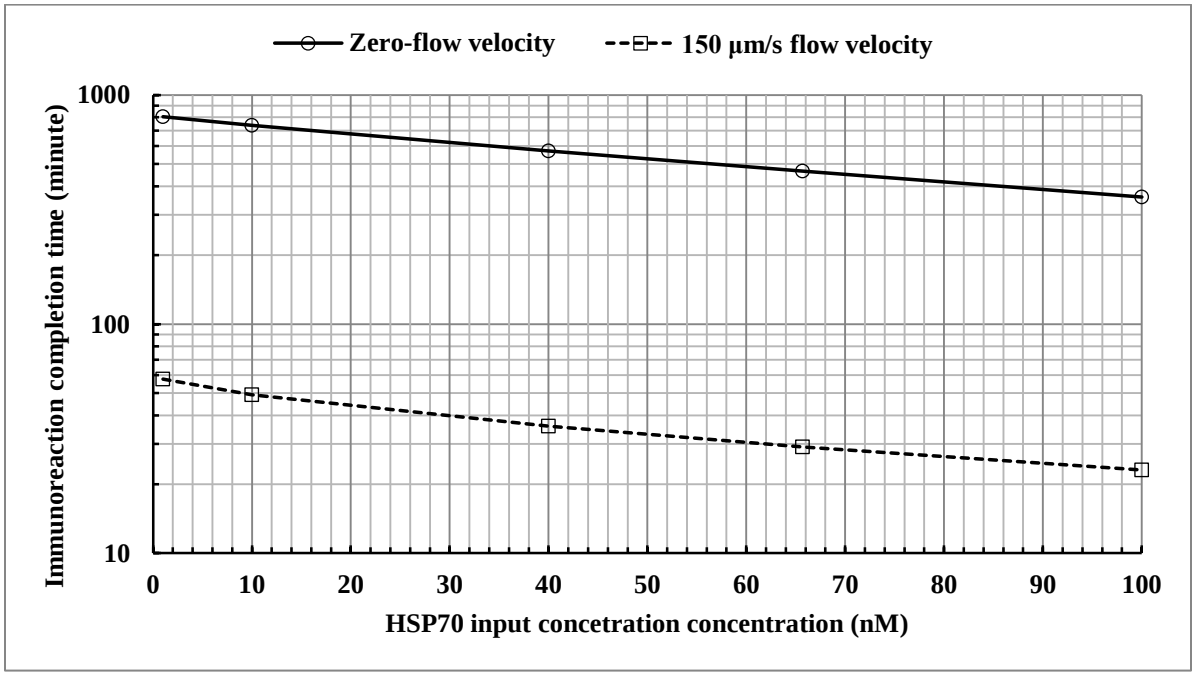

Figure 2.14: Simulated immunoreaction completion times in minutes (log scale), plotted for two flow velocities: zero and $150\ \mu m.s^{-1}$ for a number of input HSP70 concentrations (nM). Higher input protein concentrations result in nearly exponentially faster reactions. Upon utilization of the flow-through mode, the process times are decreased by at least one order of magnitude, at each concentration. Data points are connected by straight-line segments to aid visualization.

In both the zero-flow velocity and flow-through modes, the kinetics is reaction-limited (Da < 1). Nevertheless, the immunoreaction is at least 4 orders of magnitude more transport-limited than the conjugation and self-assembly kinetics. In fact, the immunoreaction is very close to the transport-limited region (Da$\sim 10^{-2}$) and this condition fairly justifies the considerable flow rate dependency observed in Figure 2.14.

In Figure 2.15 below, the flow rate dependency of the immunoreaction kinetics is examined by calculating its process completion time, for a number of flow velocities between 0 and $1500\ \mu m.s^{-1}$. The more intense the change in the process time was, the more data points were added. Use of the flow-through mode, even for a low flow velocity of $2.5\ \mu m.s^{-1}$, has substantially enhanced the kinetics, by around one order of magnitude. This kinetic improvement occurs because the reaction in the zero-flow case is very close to the transport-limited region (Da$\sim 10^{-2}$), and very sensitive toward

the flow velocity change. As mentioned in Section 2.3, transport-limitation refers to reaction conditions in which increase of the reagents replenishment rate on the reaction surface results in a considerable enhancement of the reaction progress rate. The closer the reaction is to the reaction-limitation, the more enhanced the reaction becomes.

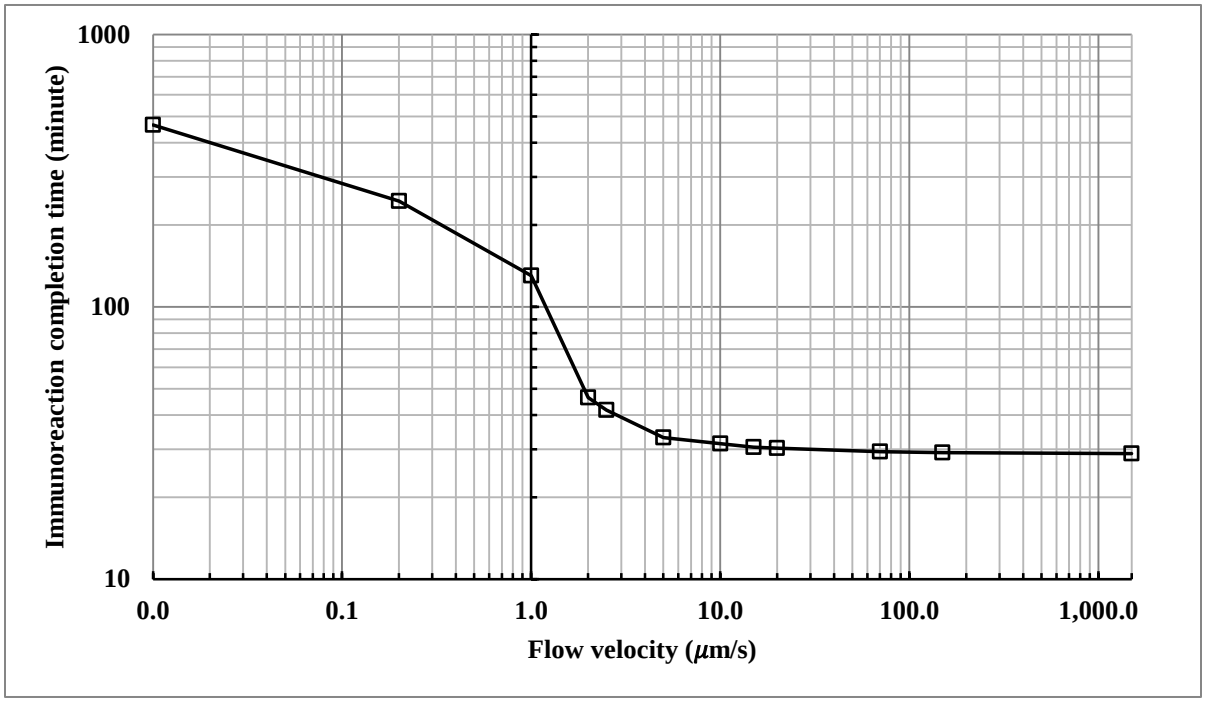

Figure 2.15: Predicted immunoreaction completion time for different flow velocities and a constant HSP70 input concentration of $65.7\ nM$. The Process time decreases substantially if the flow velocity is increased, and remains almost constant using flow velocities around or above $20\ \mu m.s^{-1}$. Data points are connected by straight-line segments to aid visualization.

Figure 2.15 also demonstrates that increasing the flow velocity beyond around $15\ \mu m.s^{-1}$ does not contribute to a significantly better kinetics. The process time, $T_{comp} = 30':30"$, decreases by less than 5% even after increasing the flow velocity by two orders of magnitude to $1500\ \mu m.s^{-1}$. Moreover, the sharpest decrease in the reaction completion time occurs in the range of 1-15 $\mu m.s^{-1}$. The process time is reduced by more than 76% upon employment of the $15\ \mu m.s^{-1}$ flow velocity, compared to that of $1\ \mu m.s^{-1}$ velocity ($T_{comp} = 130':10"$). Increasing the velocity beyond $15\ \mu m.s^{-1}$, even by two orders of magnitude to $1500\ \mu m.s^{-1}$, is observed to bring an insignificant improvement to the overall kinetics. This observation is expected because an almost fully reaction-

limited condition is reached at the velocity of $15\,\mu m.s^{-1}$. On the other hand, due to this velocity increase, the analyte consumption is almost linearly increased by two orders of magnitude- a drawback. The total consumption of the analytes is proportional to the product of the flow velocity and the reaction completion time [127]. Lower flow velocity ranges, such as 1-15 $\mu m.s^{-1}$ here, are sometimes used for assaying low-concentration samples. Beyond this range, increasing the velocity contributes to elevated analyte consumptions, but hardly improves the kinetics. In such situations, the sample volume is limited or increasing the concentration of analyte to enhance the kinetics is impossible or ineffective [28]. As a result, use of a low flow velocity helps to reduce the sample analyte consumption.

To further study the kinetic trends linked with different velocities, the transient process of the reaction is also simulated. In Figure 2.16 below, the velocity and time are non-dimensionalized by a typical flow velocity of $70\,\mu m.s^{-1}$ ($u^* = u_{avg}/(70\,\mu m.s^{-1})$) and its corresponding process time (T_{comp}) of 29 minutes and 22 seconds ($t^* = t.T_{comp}^{-1}$). The dimensionless surface concentrations of bound Ags ($c_s^* = c_s.\theta_0^{-1}$) are plotted for flow velocities ranging from zero (static incubation) to $u^* = 20$, for the $0 \leq t^* \leq 1$ period. The numerically predicted transient processes associated with the low velocity range of $0 \leq u^* \leq 0.21$ ($0 \leq u \leq 15\,\mu m.s^{-1}$) are compared with the kinetics of higher velocities, in the range of $0.29 \leq u^* \leq 20$ ($20 \leq u \leq 1400$).

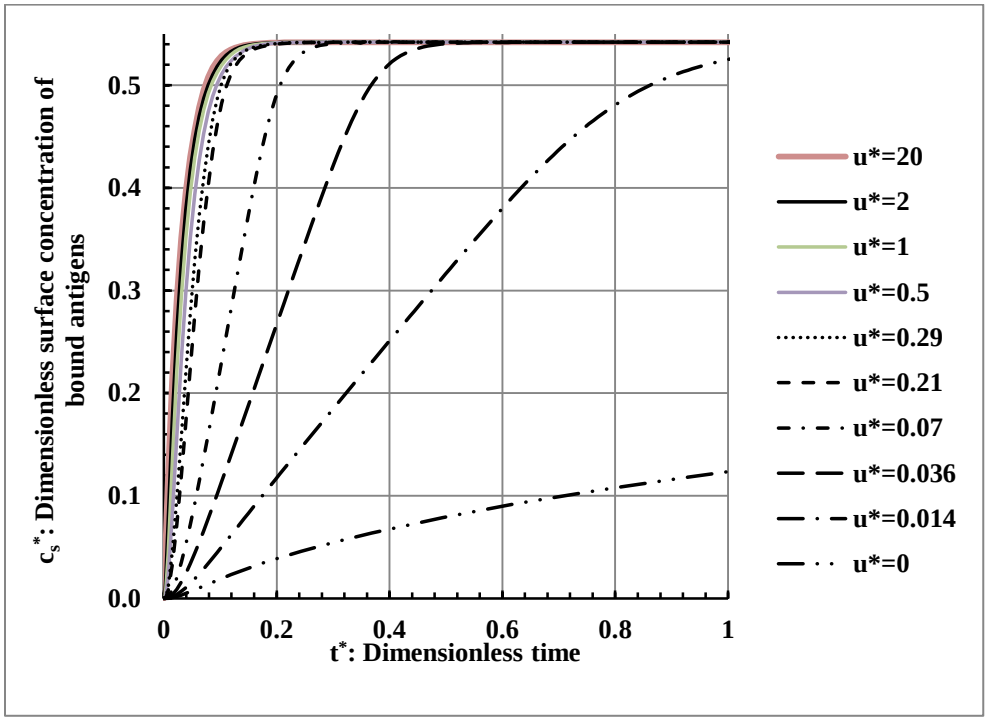

Figure 2.16: Predicted transient process of HSP70 binding: dimensionless surface concentration of bound antigens (c_s^*) calculated for a number of flow velocities (dimensionless) and constant inlet antigen concentration of $65.7\ nM$. The velocity and time are respectively non-dimensionalized by a typical flow velocity of $70\ \mu m.s^{-1}$ ($u^* = u_{avg}/(70\ \mu m.s^{-1})$) and its corresponding process time (T_{comp}) of 29 minutes and 22 seconds ($t^* = t.T_{comp}^{-1}$). Lower flow velocities demonstrate slower kinetics.

In Figure 2.16, the simulated transient kinetic curves under different flow velocities are plotted, to better illustrate the flow rate dependency of the reaction. Beyond $u^* = 0.014$ ($u = 1\ \mu m.s^{-1}$), there is a sharp increase in the dimensionless surface concentration of the bound Ags (c_s^*), and then the curves slowly approach a plateau of $c_s^* = 0.542$. This plateau value is comparable to the analytically calculated amount of 0.545 from Eq. (2.15).

Figure 2.16 shows that increasing the flow velocity results in faster transient processes and long-term kinetics. However, beyond a certain flow velocity of around $u^* = 1$ ($u = 70\ \mu m.s^{-1}$), no further significant enhancement is possible for the kinetics. Beyond this velocity the c_s^* values differ by less than 1% on average between the curves at each moment. At this flow velocity, the potential of the flow-through mode to magnify the reaction-limited kinetics is almost completely employed. In

addition, beyond the flow velocity of $u^* = 0.21$ ($u = 15\,\mu m.s^{-1}$), the kinetic curves do not substantially differ from one another. The c_s^* values are increased by less than 5.3% on average, across all the times. This observation is in close agreement with the results of Figure 2.15 that shows almost the same process times for the velocities beyond $15\,\mu m.s^{-1}$ ($u^* = 0.21$). For example the reaction completion time, $T_{comp} = 30':30"$, is improved by only 5.4% upon increasing the velocity by two orders of magnitude to $1500\,\mu m.s^{-1}$ ($u^* = 21$). The same trend were observed in Section 2.4.2.1 for the conjugation kinetics, correspondingly for the velocities of 75 and 15 $\mu m.s^{-1}$. Increase of flow velocity beyond a certain value ($u^* \sim 0.2$) loses its role in enhancing the immunoreaction rate, because the kinetics approaches a highly reaction-limited state. In the latter state, the reaction rate gains such a low proportion compared to the mass transport strength that increasing the supply rate of reactants does not result in a faster process. In such reaction-limited states, the reaction rate is the limiting progress rate factor, not the replenishment rate. Effects of the flow velocity on the other reactions considered in this research, i.e., self-assembly and conjugation, are compared to the immunoreaction kinetics in Section 2.5.1.3.

Figure 2.16 also shows that a maximum of around 54% of the total available Abs on the interface (θ_0) would potentially bind the Ags, for an Ag concentration of $65.7\,nM$. This observation is attributed to the kinetic properties of HSP70 and the relatively low concentration of the protein in the bulk. The simulation outcomes in this regard can be analytically verified. Through substitution of the kinetic parameters into Eq. (2.15), one can find the maximum dimensionless surface concentration of bound HSP70s ($c_{s,max}^* = c_{s,max}.\theta_0^{-1}$), as a function of protein' concentration. The $c_{s,max}^*$ values found from the simulations and also from the analytical approach are presented in Figure 2.17 below, for a number of concentrations.

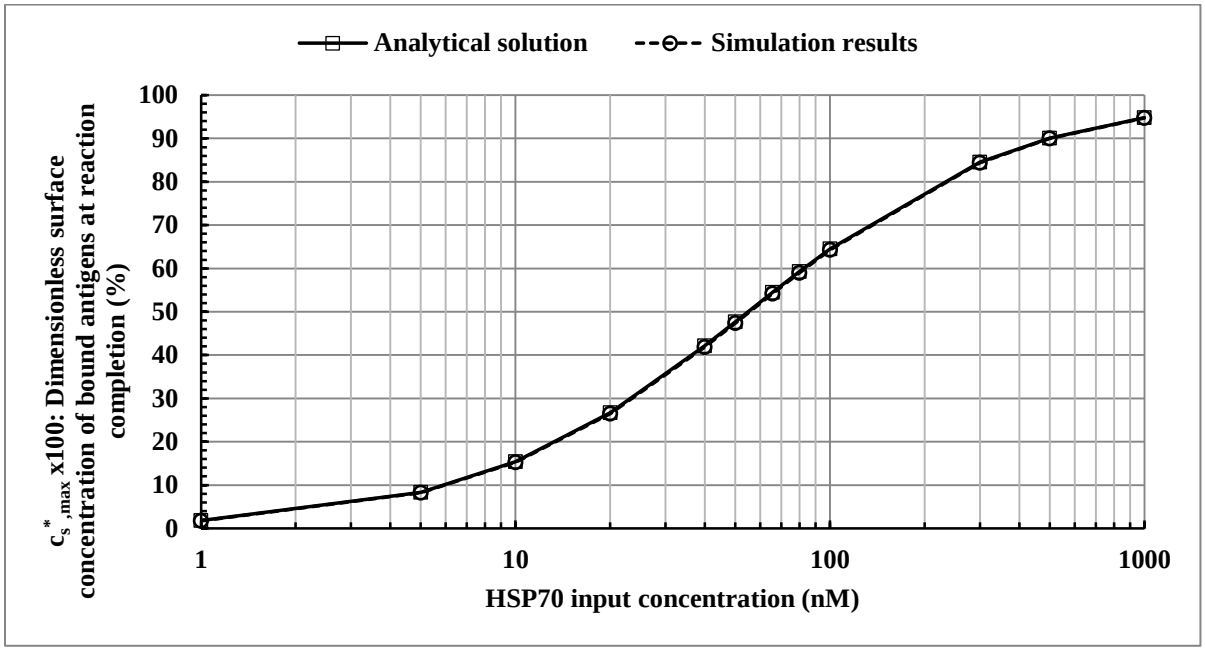

Figure 2.17: Analytically calculated dimensionless surface concentration of bound HSP70s ($c^*_{s,max}$) along with the numerical counterparts, plotted for a range of input concentrations, in logarithmic scale. At lower input concentrations, the surface density of bound antigens is considerably lower than the maximum possible. Data points are connected by straight-line segments to aid visualization.

Figure 2.17 is a plot of the dimensionless surface concentration of bound HSP70s recorded at the immunoreaction completion ($c^*_{s,max}$), versus the input bulk fluid concentration of HSP70 in nM, from both the numerical and the analytical solutions. For lower than $10\,nM$ concentrations of the Ag, below 10% of the total binding sites can be occupied by the Ags, and as can be verified from Eq. (2.15), this amount is not dependent on the time (t), or the initial Ab-loading density (θ_0). This observation is particularly important in the design of detection systems for quantification of extremely low analyte concentrations, such as $1\,nM$. Figure 2.17 also shows that the simulation results are in close agreement with the analytical solutions, as the difference is less than 1% across all the concentrations.

2.4.3.2 The Effect of the Microchannel Height on HSP70' Immunoreaction Kinetics

One of the first and maybe the easiest to alter geometrical parameters for enhancing the immunoreaction kinetics is the microchannel height. Figure 2.18 below shows the simulated transient

process of the immunoreaction, represented as the growth of the dimensionless surface concentration of bound analytes ($c_s^* = c_s.\theta_0^{-1}$) over time, plotted for a number of microchannel heights.

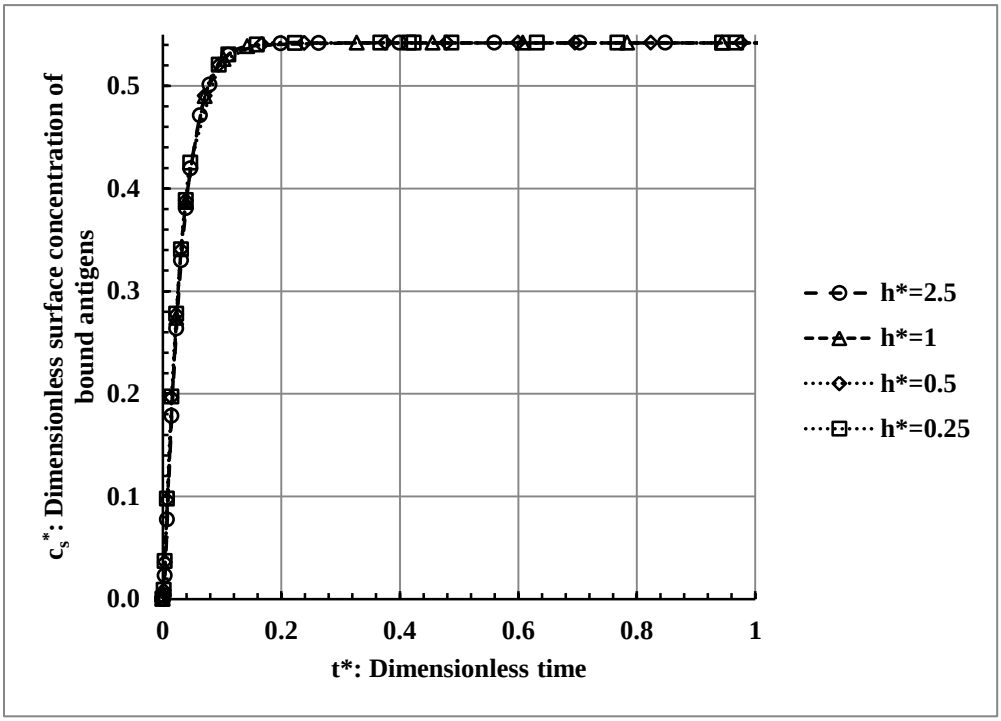

Figure 2.18: Transient evolution of dimensionless surface concentration of bound HSP70s, predicted for the immunoreaction in microchannels of varied heights. The input concentration of HSP70 is $65.7\ nM$, and flow velocity is $150\ \mu m.s^{-1}$. The height is non-dimensionalized by a reference height of $40\ \mu m$: $h^* = h/(40\ \mu m)$, and time is non-dimensionalized by the corresponding process time ($T_{comp} = 29'\!:28"$): $t^* = t.T_{comp}^{-1}$. Immunoreaction kinetics does not exhibit a strong dependency on microchannel height, as the resulting kinetic curves differ by less than 1% at each moment.

As can be seen in Figure 2.18, variation in the microchannel height has minimal effects on the immunoreaction kinetic of HSP70. The difference in the resulting kinetic curves is less than 1% at each moment. The same observation was made for the case of self-assembly and the conjugation kinetics. The explanations detailed in Sections 2.4.1.2 and 2.4.2.2, respectively for the SAM formation and Ab-conjugation kinetics, apply here for the corresponding observation in the immunoreaction. In summary, mainly because of the conserved reaction-limited nature of the kinetics

during the microchannel height change (Da$\sim 10^{-5}$), the immunoreaction progress rate remains almost the same.

From the hydrodynamic point of view, and as with the self-assembly kinetics (Sections 2.4.1.2), the thickness of the depletion zone (δ_c) is much less than the height of the microchannel. Therefore, the channel height variations considered here does not noticeably affect the kinetics.

Physically, as discussed for the self-assembly kinetics (Sections 2.4.1.2), for microchannel heights exceeding a few micrometers, there is an abundance of reagents present in the reaction environment. Due to the reaction limitation (Da $\ll 1$), the thickness of the depletion zone is much less than the height ($\delta_c \ll h$). Therefore, change of microchannel height does not affect the reaction progress rate. h_{min} is a measure of the level of abundance of reagents in the reaction environment (Section 2.4.1.2). h_{min} is calculated according to Eq. (2.25) in the following, for a number of Ags concentrations, and $\theta_0 = 4.38 \times 10^{-11}\ mol.m^{-2}$:

$$\begin{cases} h_{min} = 0.44\ \mu m, \text{if: } c_0 = 100\ nM \\ h_{min} = 0.88\ \mu m, \text{if: } c_0 = 50\ nM \\ h_{min} = 43.8\ \mu m, \text{if: } c_0 = 1\ nM \end{cases}$$

The above calculation shows that for protein concentrations higher than $50\ nM$ and for the microchannel heights exceeding few microns, there is an abundance of proteins present in the reaction environment ($h_{min} \ll h$). Therefore, height variations do not noticeably impact the immunoreaction progress rate. For $c_0 \sim 1\ nM$, h_{min} approaches the height of the microchannel ($h_{min} \sim h$). However, Simulation results show that for $c_0 = 1\ nM$ the decrease of microchannel height even to $10\ \mu m$ increases the process time by less than 1%. However, there exists a point from which lowering the h increases the reaction completion time, due to the shortage of proteins in the reaction environments. The potential shortage of proteins for the completion of reaction can be examined by simulations, as exemplified for the immunoreaction kinetics in the following section.

2.4.3.3 The Effect of Anti-HSP70 Surface Concentration on the Immunoreaction Kinetics

Surface concentration of available sites for the analyte binding (θ_0) was shown in Sections 2.4.1.3 and 2.4.2.3 to have negligible effect on the overall kinetics of both the self-assembly and Ab conjugation reactions. In this section, the effect of θ_0 variation on the HSP70' immunoreaction

kinetics is studied by numerical simulation and shown to be significant. As pointed out in Section 2.4.2.3, θ_0 is a function of the functionalization method used [1, 11, 19, 54].

Figure 2.19 illustrates the transient process of the HSP70' immunoreaction, simulated for a number of Ab-loading densities in the range of $4.38 \times 10^{-7} \leq \theta_0 \leq 4.38 \times 10^{-13}\ mol.m^{-2}$, corresponding to $10^{-2} \leq \theta_0^* \leq 10^4$. θ_0 is non-dimensionalized by a reference value of $4.38 \times 10^{-11}\ \mathrm{mol.m^{-2}}$: ${\theta_0}^* = \theta_0/(4.38 \times 10^{-11}\ mol.m^{-2})$. The antigen input concentration is 65.7 nM, flow velocity is $150\ \mu m.s^{-1}$, and time is non-dimensionalized by the corresponding process time ($\mathrm{T}_{comp} = 29'\!:28''$): $t^* = t.\mathrm{T}_{comp}^{-1}$. Contrary to the observed insignificant role of θ_0 in the thiol self-assembly and the Ab conjugation, an increase in the number of potential sites for the Ag binding results in slower immunoreaction kinetics. For example, the transient process curve corresponding to the ${\theta_0}^* = 10^4$ ($\theta_0 = 4.38 \times 10^{-7}$), which is the highest surface concentration of the Ab, is always behind the corresponding curves of lower Ab surface densities, shown in the figure. As pointed out in Section 2.4.1.3, escalation of θ_0 increases the number of reaction sites that should be occupied by antigens. As a result, slower kinetics are normally expected. The latter expectation can be alternatively justified by consideration of the change of reaction rate potential relative to the mass transport strength, or the change of Damköhler number (Da). The latter group increases linearly with θ_0. In the new situation, the mass-transport rate (denominator of Da) should be enhanced to compensate for the θ_0 increase. Otherwise, the reaction progress rate becomes lower than the original situation. For example, according to Eq. (2.21):

$$10^2 \overset{\theta_0^*}{\rightarrow} 10^4 \overset{Immunoreaction}{\Longrightarrow} 5.22 \times 10^{-3} \overset{\mathrm{Da}}{\rightarrow} 0.52$$

The resulting considerably higher Damköhler number, which indicates a nearly transport-limited reaction, entails a noticeably decelerated kinetics, compared to the previous case. A more detailed explanation is given in Section 2.5.2.

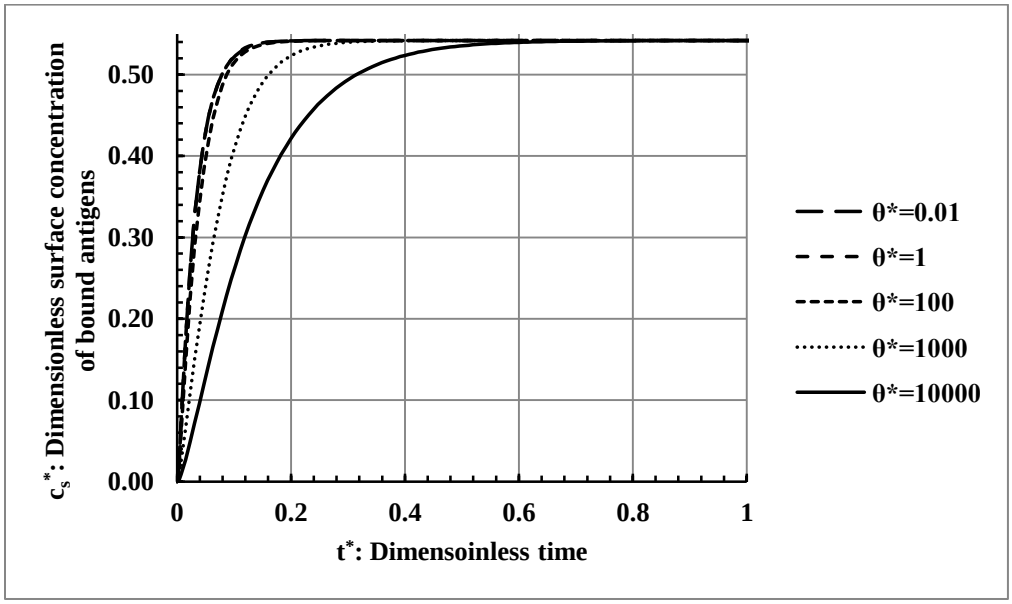

Figure 2.19: Simulated transient process of HSP70 immunoreaction, illustrated as the dimensionless surface concentration of bound HSP70 (c_s^*) over time (dimensionless), plotted for a number of initial anti-HSP70 surface concentrations (θ_0^*-dimensionless). θ_0 is non-dimensionalized by a reference value of $4.38 \times 10^{-11}\ mol.m^{-2}$: ${\theta_0}^* = \theta_0/(4.38 \times 10^{-11}\ mol.m^{-2})$, the antigen input concentration is $65.7\ nM$, flow velocity is $150\ \mu m.s^{-1}$, and time is non-dimensionalized by the corresponding process time ($T_{comp} = 29'{:}\,28''$): $t^* = t.T_{comp}^{-1}$. θ_0^* increase results in slower immunoreaction kinetics.

The other important observation from Figure 2.19 is that decreasing the Ab surface density below $\theta_0^* = 100$ ($\theta_0 = 4.38 \times 10^{-9}\ mol.m^{-2}$) does not result in a significantly enhanced transient kinetics. For example, the difference between the corresponding curves of $\theta_0^* = 100$ ($\theta_0 = 4.38 \times 10^{-9}\ mol.m^{-2}$) and $\theta_0^* = 1$ ($\theta_0 = 4.38 \times 10^{-11}\ mol.m^{-2}$) is less than 1% at each moment. This observation is contrary to the expected faster reaction associated with lower θ_0 amounts, discussed earlier in this section. The decrease of θ_0 from $\theta_0^* = 100$ to $\theta_0^* = 1$ leads to the following changes in the Da and ϵ, due to Eq. (2.21)-(2.22):

$$5.22 \times 10^{-3} \overset{\text{Da}}{\rightarrow} 5.22 \times 10^{-5}$$

$$0.59 \overset{\epsilon}{\rightarrow} 59.3$$

The reason behind the observed weak sensitivity of the kinetics to decrease of the θ_0 below $\theta_0^* = 100$ is that the binding capacity (ϵ) of the reaction has become extremely low there ($\epsilon = 0.59$). By definition, binding capacity (ϵ) is a measure of the amount of analytes available for each reaction spot [138]. In the case of $\epsilon = 0.59$, which corresponds to $\theta_0^* = 100$ ($\theta_0 = 4.38 \times 10^{-9}\, mol.m^{-2}$), θ_0 or the number of reaction sites per unit surface area (the denominator of ϵ) is noticeably larger than the number of analytes present in the bulk fluid (the numerator of ϵ). In other words, not enough analytes are available for each reaction spot. In such situations, even a favorable change in the θ_0 cannot effectively enhance the kinetics. Moreover, further decrease of θ_0 below the amount of $4.38 \times 10^{-11}\, mol.m^{-2}$ does not noticeably enhance the kinetics either, although ϵ increases considerably due to the mentioned variation. The kinetics undergo minor changes because in that amount of θ_0, the fully reaction-limited region is reached: $\mathrm{Da} = 5.22 \times 10^{-5}$. Therefore, a subsequent decrease in the Da, e.g., by reducing the θ_0 or increasing the flow velocity, does not necessarily enhance the kinetics.

Physically, θ_0 directly determines the abundance or shortage of reagents in the reaction environment, mentioned in Section 2.4.1.3. h_{min} is a measure of the level of abundance of reagents in the reaction environment (Section 2.4.1.2). The latter parameter is calculated below for the immunoreaction kinetics, according to Eq. (2.25), and for $\theta_0 = 4.38 \times 10^{-11}\, mol.m^{-2}$:

$$\begin{cases} h_{min} = 0.44\ \mu m, \text{if: } c_0 = 100\ nM \\ h_{min} = 43.8\ \mu m, \text{if: } c_0 = 1\ nM \end{cases}$$

The above calculations show that for $c_0 = 1\ nM, h_{min}$ approaches the height of the microchannel ($h_{min} \sim h = 40\ \mu m$). In other words, the amount of analytes available in the bulk is close to the minimum amount required. Presence of convective transport of analytes ($u_{avg} = 150\ \mu m.s^{-1}$) might compensate for the shortage of analytes in the bulk. However, for $\theta_0^* \geq 100$, corresponding to $h_{min} \geq 438\ \mu m$, the shortage of analytes in the bulk fluid becomes considerable and the decrease of reaction progress rate turns to be noticeable (Figure 2.19).

The observed dependency of the immunoreaction kinetics on the θ_0 in its higher amounts ($\theta_0^* \geq 100$), rather than lower values, suggests the presence of a probably variable flow rate dependency corresponding to different amounts of θ_0 (Ab-loading densities). To examine this speculation, the calculated immunoreaction completion times for a number of Ab surface densities (θ_0) were

simulated in a range of flow velocities between $15 \leq u_{avg} \leq 1500\ \mu m.s^{-1}$, depicted in Figure 2.20 below.

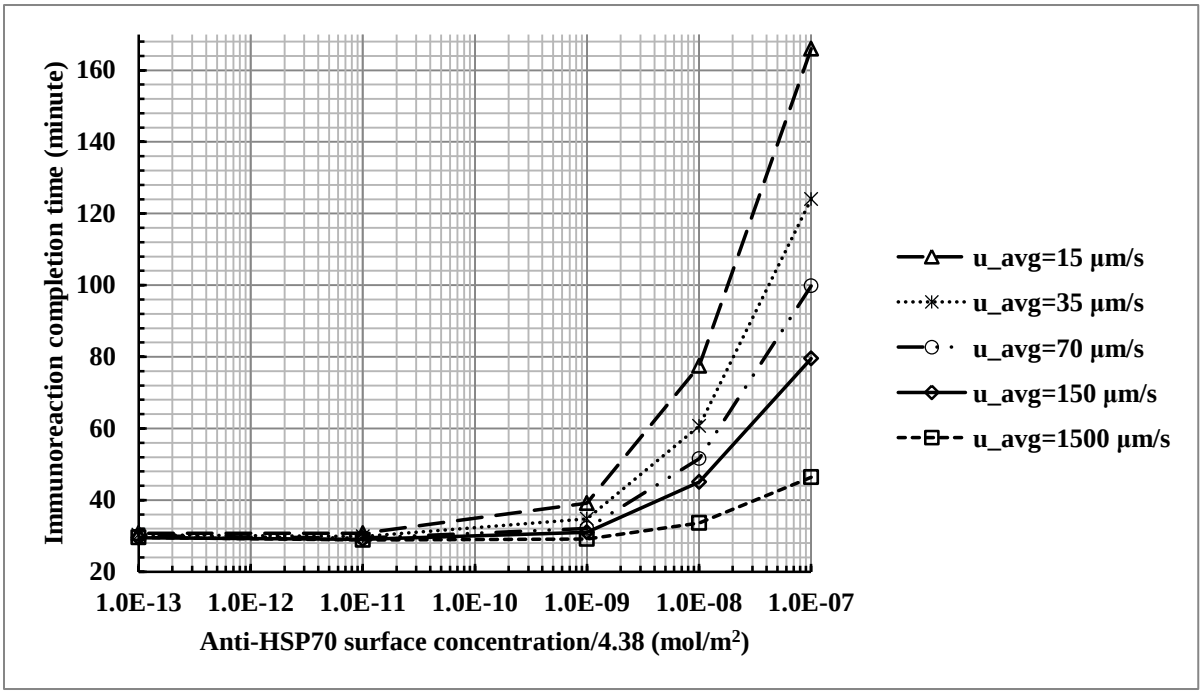

Figure 2.20: Calculated HSP70' immunoreaction completion times versus surface concentration of immobilized anti-HSP70 (θ_0), simulated for a number of input flow velocities. Higher θ_0 amounts result in slower kinetics and magnified flow rate dependencies. Data points are connected by straight-line segments to aid visualization.

Figure 2.20 shows that higher anti-HSP70 surface concentrations ($4.38 \times 10^{-9} < \theta_0^{high} \leq 4.38 \times 10^{-7} mol.m^{-2}$) exhibit relatively higher flow rate dependencies compared to lower Ab loading densities ($4.38 \times 10^{-11} \leq \theta_0^{low} \leq 4.38 \times 10^{-9} mol.m^{-2}$). Regarding the immunoreaction kinetics, this trend is not favorable since at the θ_0^{high}, considerably higher flow velocities should be used to achieve a reasonable process time. For instance, for $\theta_0 = 4.38 \times 10^{-7}$, to decrease the immunoreaction completion time from 166 minutes to 46 minutes, the flow velocity should be increased for two orders of magnitude, from 15 to $1500\ \mu m.s^{-1}$. The total consumption of the analytes is proportional to the product of the flow velocity and the reaction completion time [127]. Therefore, this flow-velocity increase results in outstanding cost elevations, as the HSP70

consumption is considerably increased by around 30 times. On the other hand, use of a higher velocity might cause problems because sometimes enough sample analytes are not available. However, upon implementation of lower surface concentrations of Ab (θ_0^{low}), the reaction progress rate remains relatively independent of flow rate changes. For instance, in the case of $\theta_0 = 4.38 \times 10^{-9}\, mol.m^{-2}$, increasing the flow velocity for two orders of magnitude, from 15 to 1500 $\mu m.s^{-1}$ decreases the reaction completion time by around 10 minutes (from $39':10"$ to $29':8"$), respectively, i.e., less than 26%. In such Ab-loading density, use of a low flow velocity of about 15 $\mu m.s^{-1}$ results in a reasonable process time of around 40 minutes.

The other important observation is that a moderate flow velocity of around 70 $\mu m.s^{-1}$ exhibits a favorable, relatively "stable" kinetics against the Ab surface-loading density (θ_0) change. In other words, using this flow velocity, the reaction completion time does not undergo a dramatic change upon possible variations of θ_0. Moreover, the reaction completion time is reasonable ($29 < \mathrm{T}_{comp} < 100$ minutes) through all Ab loading densities, without the drawback of intensely increased Ag consumptions associated with higher flow velocities, such as 1500 $\mu m.s^{-1}$. The maximum amount of immunoreaction completion time elevation, with respect to the original case, is around 230% with a velocity of 70 $\mu m.s^{-1}$, as a result of maximum increase in the θ_0 from the nominal value of $4.38 \times 10^{-13}\, mol.m^{-2}$ for 6 orders of magnitude to $4.38 \times 10^{-7}\, mol.m^{-2}$. However, the latter ratio is 450% for the 15 $\mu m.s^{-1}$, with a maximum of around 3 hours needed for the immunoreaction completion. For the flow velocity of 1500 $\mu m.s^{-1}$, the maximum process time change is around 50%, however, with around two orders of magnitude more Ag consumption, compared to the case of $u_{avg} = 70\ \mu m.s^{-1}$. Upon increasing the flow velocity from $70\mu m.s^{-1}$ to $150\mu m.s^{-1}$, i.e., more than two times, the maximum elevation in immunoreaction completion time changes from 230% to 170%, which might not be deemed advantageous since the Ag consumption is approximately doubled as well. Moreover, in the range of $4.38 \times 10^{-11} \leq \theta_0 \leq 4.38 \times 10^{-9}\, mol.m^{-2}$, which falls in the HIAs' practical Ab-loading densities [19, 85], the flow velocity of 70 $\mu m.s^{-1}$ does not undergo a immunoreaction completion time variation of more than 5%, around 29 minutes. Accordingly, simulation results here suggest using the flow velocity of 70 $\mu m.s^{-1}$, as this amount has both favorable properties of relatively fast kinetics and low Ag consumption.

The last important observation from Figure 2.20 is that the lower end of the Ab-loading density spectrum ($\theta_0 < 4.38 \times 10^{-11}\, mol.m^{-2}$) exhibits a nearly velocity-independent behavior, with an interestingly so called "fast" kinetics, discussed earlier in this section. Use of these densities brings

about the lowest possible immunoreaction time. However, implementation of such low Ab-loading densities, e.g., $\theta_0 = 4.38 \times 10^{-12}\, mol.m^{-2}$, results in weak detection signals and lower sensitivity levels. Therefore, employment of a capture system with an extremely low loading density of Abs is not recommended in HIAs [7, 8, 14].

From the above discussion, the best recommended anti-HSP70 loading density to implement is between $\theta_0 = 4.38 \times 10^{-11}$ and $\theta_0 = 4.38 \times 10^{-9}\, mol.m^{-2}$. In this range, a flow velocity of around $70\ \mu m.s^{-1}$ is sufficient for maintaining a relatively rapid immunoreaction, with a completion time of around 29 minutes. Moreover, in this θ_0 range, the Ag consumption is kept reasonably low, without the drawback of prolonged process times. This range of Ab-loading density also matches the practical loading density resulting from the thiolic functionalization protocol ($\theta_0 = 4.38 \times 10^{-11}\, mol.m^{-2}$) characterized in this research, with experimentally proven rich detection signals [11, 12]. In such a θ_0 range, the kinetics is nearly independent of the flow velocity changes around the nominal value chosen before ($u_{avg} = 70\ \mu m.s^{-1}$), and there is no necessity for employment of higher flow velocities, which are associated with increased protein consumption and additional costs.

Effects of the surface loading density of reaction sites (θ_0) on the reactions considered in this research, i.e., thiol self-assembly, conjugation and immunoreaction, are compared to one another in Section 2.5.2.

2.5 Comparison of the Kinetics of Reactions in the Functionalization Process

In the following section, major differences observed among the three kinetics considered before, i.e., the SAM formation, the Ab/SAM conjugation, and the Ag/Ab immunoreaction, are comparatively studied. To perform quantitative comparisons, dimensionless kinetic representative numbers are calculated, including: the Damköhler number (Da), the Peclet number (Pe), and the binding capacity (ϵ). The effects of following important variables on each of the above-mentioned reactions are examined: the flow velocity (u_{avg}), the concentration (c_0), and the available surface concentration of binding sites (θ_0). The effect of microchannel height variation is not considered here, as it was observed to have an insignificant role in the three kinetics covered.

2.5.1 Flow Velocity and Concentration Effects

The following section compares the flow velocity and concentration dependency of the above three kinetics. The reaction cited in the topic is the focus of study, and other reactions are compared to it, in terms of kinetic properties.

A unified trend was not observed in the flow rate dependency of the above reaction kinetics considered in this research. However, all the reactions showed considerable reagent concentration dependencies, resulting in approximately exponential kinetic enhancements with increasing reagent concentration. This behavior is expected, since according to Eq. (2.15), the concentration (c) appears in the time constant of the exponential function, which describes the progress of the reactions.

In the following, the flow rate dependencies of the reactions are comparatively examined.

2.5.1.1 Flow Rate dependency in Thiols Self-assembly Kinetics

The SAM formation was demonstrated to have a weak flow rate dependency, as shown in Figure 2.4, whereas, Ab/SAM conjugation completion time had a strong reliance on the flow rate (Figure 2.9), similar to that of the immunoreaction kinetics (Figure 2.14). Upon increasing the flow velocity from zero to $150\ \mu m.s^{-1}$, the self-assembly periods were reduced by less than 7% on average, across all the concentrations considered in this thesis. However, the conjugation and immunoreaction completion times were decreased by around one order of magnitude at each concentration. These observations can be explained by consideration of the relative importance of various physical phenomena present, through calculation of the dimensionless kinetics representative

numbers, including the Damköhler number (Da), the Peclet number (Pe), and the reaction capacity (ϵ). As discussed in Section 2.3, the Damköhler number compares the relative strengths of reaction and mass transport. In the self-assembly kinetics, the Damköhler number is calculated to be around $\sim 10^{-8}$ to $\sim 10^{-7}$ - independent of the concentration (Section 2.4.1.1). For this clearly low Damköhler number, the mass transport strength is much higher than the reaction rate, and the kinetics is evidently reaction-limited. This fact also implies that further increase in flow rate does not contribute to a significantly better kinetics.

The bulk concentration of thiols weakly affects the flow rate dependency of the self-assembly kinetics. This trend is manifested in a very weak flow rate dependency in the lower concentrations, $10 < c_0^{low} < 100 \mu M$, where due to increase of flow velocity from zero to $150\ \mu m.s^{-1}$, the process time decreases by less than 3%. On the other hand, a weak flow rate dependency is observed in the higher concentrations, $c_0^{high} \geq 100 \mu M$, where the average decrease in the process time is below 8%. For c_0^{low}, a moderate amount of thiols is available in the bulk fluid for chemisorption on each reaction spot, defined by the binding capacity, via Eq. (2.22): $\epsilon < 5.5 \times 10^3$. In general, this situation indicates a moderate binding capacity and allows for an effective alteration of the kinetic properties, which might occur due to a considerable change in the relative strength of reaction compared to the mass transport capacity (Damköhler number), as discussed in Sections 2.4.1.1 and 2.4.3.3. One can increase the Peclet number by enhancing the flow velocity, which enhances the role of convection with respect to diffusion. However, increasing the Peclet number, even for two orders of magnitude, i.e., by increasing the flow velocity from around zero to $1500\ \mu m.s^{-1}$, does not contribute to relatively better kinetics for the self-assembly reaction (less than 3% of reduction in T_{comp}). This observation is expected because a better mass transport rate happens in a highly reaction-limited region ($\mathrm{Da} = 5.54 \times 10^{-9}$: if $u_{avg} = 1500\ \mu m.s^{-1}$). Therefore, the kinetics cannot effectively benefit from the increased transport rate. For c_0^{high}, such as $10\ mM$, the binding capacity (ϵ) is considerably higher: $\epsilon = 5.48 \times 10^5$. The magnification of the velocity from zero to $150\ \mu m.s^{-1}$ increases the Peclet number from zero to around 10, according to Eq. (2.20). Therefore, the role of mass transport becomes a bit more important. Thus, increasing the flow velocity results in better kinetics, although not significantly better (average decrease in the T_{comp} is below 8%), as illustrated in Figure 2.4. The latter effect occurs because the Peclet number increases in a highly reaction-limited kinetics: $\sim 10^{-8} < \mathrm{Da} < \sim 10^{-7}$ (Eq. 2.20).

2.5.1.2 Anti-HSP70 Conjugation Kinetics

As mentioned in the beginning of Section 2.5.1.1, the Ab/SAM conjugation has more flow-rate dependency than the SAM-formation kinetics (compare Fig. 3.4 and Fig. 3.9), although both have a reaction-limited nature. As mentioned in Section 2.4.2.1, reaction-limitation refers to situations in which increase of flow velocity is not expected to cause a considerable kinetics enhancement. However, the latter condition does not correspond to a complete independency of the reaction-progress rate from the flow rate. In other words, there is always a possibility to increase the rate of reaction by augmentation of the mass transport rate (though not necessarily significant). For the current kinetic specifications, $0 < u_{ave} < 150\ \mu m.s^{-1}$, and due to Eq. (2.21), the range of the Damköhler number can be calculated as follows:

$$5.11 \times 10^{-8} < \mathrm{Da}_{\,self-assembly} < 5.89 \times 10^{-7}$$

$$1.34 \times 10^{-9} < \mathrm{Da}_{\,conjugation} < 8.06 \times 10^{-7} (\sim 10^{-6})$$

At the beginning of the flow velocity change, the Da has almost the same magnitude for both the self-assembly and conjugation kinetics, and therefore, the two reactions have the same kinetic natures. However, for the conjugation kinetics case, the change in the Damköhler number upon implementation of the flow-through mode is more substantial, compared to the SAM-formation kinetics. For the conjugation reaction, the Da changes by about three orders of magnitude, while the ratio for the self-assembly is only around ten times. In other words, the relative strengths of reaction and mass transport undergos a higher level of decrease in the conjugation kinetics. On the other hand, the binding capacities (ϵ) of the two kinetics are different, and the Ab/SAM conjugation has a substantially higher binding capacity (ϵ) for the practical concentrations of reagents considered in this research. According to Eq. (2.21):

$$5.48 \times 10^{1} < \epsilon_{self-assembly} < 5.48 \times 10^{5}\text{: if } 1\ \mu M < c_0 < 10\ mM$$

$$9.1 \times 10^{4} (\sim 10^{5}) < \epsilon_{conjugation} < 9.1 \times 10^{7} (\sim 10^{8})\text{: if } 0.1\ mM < c_0 < 100\ mM$$

Reactions with higher binding capacities normally have higher levels of sensitivity to the increase of analyte replenishment rate on the reaction surface. This phenomenon was exemplified in section 2.4.2.1 for the case of conjugation kinetics in which samples with elevated concentrations of EDC had elevated binding capacities, and as a result, the flow-through mode implementation was

better able to enhance the kinetics, compared to lower concentration samples (Figure 2.9). In conclusion, the conjugation kinetics has the following differences with the self-assembly kinetics:

- The conjugation kinetics experiences a higher level of change in the relative strength of reaction compared to the mass transport capacity (Da change), upon implementation of the flow-through mode.
- The conjugation kinetics has a higher binding capacity (higher ϵ).

These two differences show that the two reactions have considerably different kinetic properties and can justify the observed greater flow rate dependency in the conjugation kinetics than the self-assembly kinetics.

2.5.1.3 HSP70 Immunoreaction Kinetics

HSP70 Immunoreaction kinetics showed a great potential for enhancement using the flow-through mode, studied in Section 2.4.3.1. The same observation was made for the Ab-conjugation kinetics in Section 2.4.2.1. Upon increasing the flow velocity from zero to $150\ \mu m.s^{-1}$, the conjugation and immunoreaction completion times were decreased by around one order of magnitude at each concentration. Calculation of the Damköhler number can help in explaining the trend seen. For the immunoreaction kinetics, and due to Eq. (2.21), the Damköhler number falls in the following range:

$$5.22 \times 10^{-5} < \mathrm{Da} < 7.88 \times 10^{-3}$$

corresponding to two hypothetical velocity extremes, respectively: the flow-assisted mode with $u_{avg} = 150\ \mu m.s^{-1}$, and the zero-flow, diffusion-only transport mode ($u_{avg} = 0$). Calculation of the Da for the zero-flow mode is repeated below:

$$\mathrm{Da} = \frac{k_a \theta_0}{\frac{D}{h} + u} = \frac{1.8 \times 10^2 m^3.(mol.s)^{-1}\ .\ 4.38 \times 10^{-11} mol.m^{-2}}{\frac{4 \times 10^{-11}\ m^2.s^{-1}}{40 \times 10^{-6}\ m} + 0\ m.s^{-1}} = \frac{7.88 \times 10^{-13}}{1 \times 10^{-6} + 0} = 7.88 \times 10^{-3}$$

This value is at least four orders of magnitude more than the Damköhler number corresponding to the self-assembly kinetics and Ab-conjugation kinetics, discussed in Sections 2.2.3.1 and 2.4.2. In other words, the immunoreaction kinetics is four orders of magnitude more transport-limited than the self-assembly or conjugation kinetics. Accordingly, the comparatively high flow rate dependency of the

immunoreaction can be fairly justified by considering its kinetics state, which is very close to the transport-limited region.

Beyond a flow velocity of about $70\,\mu m.s^{-1}$ negligible enhancements were observed in the immunoreaction kinetics. As shown in Figure 2.16, the difference between the kinetic curves corresponding to higher than $70\,\mu m.s^{-1}$ of flow velocity is less than 1%. This observation was attributed to the reaction-limited state of the kinetics at this velocity (Da$\sim 10^{-4}$), and also total employment of convective transport for improving the kinetics (Section 2.4.3.1). The Peclet number can be calculated to estimate the contribution of convection to the mass transport: $\mathrm{Pe} = 70$, calculated from (2.20). This Peclet number confirms seventy times more contribution from the convention in analytes transport relative to diffusion. As a result, the immunoreaction kinetics has already benefited from a truly dominant convective transport. Consequently, the kinetics does not show a noticeable enhancement due to increased flow velocity beyond $70\,\mu m.s^{-1}$. In summary, the relatively close to transport-limited nature of the immunoreaction kinetics (Da~ 0.01) justifies the reason behind the substantial enhancement of the kinetics upon employment of flow-through mode.

2.5.2 Effect of the Surface Concentration of Available Binding Sites

The effect of changing the surface concentration of available binding (reaction) sites (θ_0) on the overall kinetics can be predicted by calculation of the Damköhler number (Da), as the main kinetics descriptive tool, the binding capacity (ϵ), and the Peclet number (Pe) [28, 135, 138, 139]. Due to the magnification of the θ_0, the Damköhler number is augmented at the same rate as the θ_0 increase, presented by Eq. (2.21). As a result, the reaction progress rate is normally expected to be reduced, compared to the original situation, assuming a constant analyte transport rate. The kinetic deceleration is expected to occur due to the presence of more reaction sites in case of a magnified θ_0, without any enhancement in the mass transport strength. At the same time, the binding capacity, defined by $\epsilon = c_0 h.\theta_0^{-1}$, is decreased from the original value, at exactly the same rate. As pointed out in Section 2.3, the binding capacity (ϵ) is a measure of the number of analytes present in the bulk fluid, relative to the number of binding sites available on the reactive surface. A decrease in the binding capacity means more binding sites are available for occupation by the analytes, with the same number of analytes present in the bulk fluid, relative to the original case. This situation is intuitively expected to cause a slower kinetics, since more time is needed to reach the same surface-loading density of captured analytes, than in the previous case. The last parameter that might affect the overall kinetics

during a change in the θ_0 is the Peclet number that determines the dominancy level of the mass transport by convection or diffusion. The Peclet number is especially important where the change in the θ_0 is initiated in a transport-limited reaction (Da$\sim$1) with dominancy of diffusion. In the latter case, the diffusion rate of analytes toward the reaction surface determines the reaction rate, and convection is not present or is negligible compared to diffusion (Pe $\ll$ 1). Therefore, an active convective replenishment of analytes on the reaction surface is not present or strong enough to compensate for the deceleration of kinetics by an increase of θ_0. Thus, any change in kinetic parameters that can move the reaction toward transport-limitation, e.g., increase of θ_0, has its highest impact in deceleration of the kinetics when diffusion dominates the mass transport. Based on above discussion, the increase of θ_0 is normally expected to decelerate the kinetics. However, it is proposed here that depending on the relative intensity of these three dimensionless numbers, the Da, the ϵ, and the Pe, before the θ_0 increase, the overall kinetics might become:

1- Much slower, for a transport-limited kinetics (Da$\sim$1); specially, when diffusion dominates the mass transport (Pe $\ll$ 1).

2- Moderately slower, for a reaction-limited kinetics that is close to becoming transport-limited during the change ($0 < \mathrm{Da} < 1$); specially, when the binding capacities is relatively low ($\epsilon < 100$), such as the HSP70's immunoreaction kinetics.

3- Nearly unchanged for fully reaction-limited kinetics (Da$\sim$0), such as the self-assembly kinetics or Ab conjugation.

For the first case in which the reaction becomes much slower as a result of the θ_0 growth, the kinetics is originally transport-limited (Da$\sim$1). In such situation, any increase in the Da noticeably slows the kinetics down. In particular, the kinetics deceleration rate is significant upon an increase in the Da (due to the θ_0 increase here), if the dominant transport mode is diffusion. This condition is present in the immunoreaction kinetics for high amounts of θ_0 ($4.38 \times 10^{-9} < \theta_0^{high} \leq 4.38 \times 10^{-7} mol.m^{-2}$), even for higher Peclet numbers, such as $\mathrm{Pe} = 15$. With such a Peclet number, convention has a more profound role in the mass transport than the diffusion does. For example, for $\theta_0 = 4.38 \times 10^{-8}\ mol.m^{-2}$, and due to Eq. (2.20) and Eq. (2.21):

$$\mathrm{Da} = 0.5 \text{ and } \mathrm{Pe} = 15, \text{ if } u_{avg} = 15\ \mu m.s^{-1}$$

Such kinetics is close to the transport-limited region (Da~1). As shown in Figure 2.20, the reaction completion times are decreased noticeably due to the increase of θ_0. Moreover, the intensity of kinetic changes is lowered by increasing the flow velocity (augmentation of the Pe) or, in other words, further domination of convention, compared to diffusion (Section 2.4.3.3).

In the second case, where $0 < \mathrm{Da} < 1$, the kinetics become moderately slower upon an increase in the θ_0; specially, when ϵ is relatively small ($\epsilon < 100$). For example in the immunoreaction kinetics, the Damköhler number varies from $5.25 \times 10^{-5} \overset{\mathrm{Da}}{\rightarrow} 5.25 \times 10^{-3}$, corresponding to a θ_0 increase of $4.38 \times 10^{-11} \overset{\theta_0}{\rightarrow} 4.38 \times 10^{-9}\ mol.m^{-2}$. The magnitude of the Da at the beginning of the θ_0 range is indicative of a reaction-limited kinetics (Da~10^{-5}), although the reaction is around three orders of magnitude more transport-limited than the self-assembly and conjugation kinetics. Such a kinetics becomes progressively more sensitive to the θ_0 change, since during the θ_0 magnification the kinetics is being transformed toward a transport-limited situation. However, at the beginning of the θ_0 change, the reaction-limited kinetics is not very sensitive to the θ_0 alteration. This speculation was demonstrated numerically in Figure 2.20, corresponding to $\theta_0 = 4.38 \times 10^{-11}\ mol.m^{-2}$, where reaction completion times were not altered considerably due to the change of θ_0 (Section 2.4.3.3). Upon any intensification from this θ_0, the Damköhler number increases noticeably closer to the transport-limited region, and as a result, a slower kinetics is anticipated (note: mass transport strength is conserved). On the other hand, lowering the binding capacity (ϵ) also results in a slower kinetics. This effect may magnify the impact of moving the kinetics into a more transport-limited condition (increase of Da). However, the contribution of the binding-capacity decrease is not outstanding, since ϵ is considerably low at the beginning of the θ_0 evolution range, and becomes much lower if θ_0 is increased:

$$4.38 \times 10^{-11} \overset{\theta_0}{\rightarrow} 4.38 \times 10^{-9} \overset{Immunoreaction}{\Longrightarrow} 59.4 < \epsilon < 5.94 \times 10^{-1}$$

By definition, a low binding capacity (ϵ) brings about a weak adsorption or binding strength for the reaction [135, 138]. This inference comes from the formulation of the number ($\epsilon = c_0 h.\theta_0^{-1}$), where a small ϵ might be due to a relatively high θ_0 (plenty of reaction spots), compared to a low number of analytes present in the bulk fluid. In such situations, not enough analytes are available for each reaction spot, and consequently, the kinetics changes are not marked. Considering the overall effects, a lowered ϵ and also an increased Da both indicate a moderately slower kinetics if θ_0 increases, although the change is not initially huge. This trend is also partially because of being close to

reaction-limitation at the beginning of the change, at which point the rather low binding capacity ($\epsilon < 100$) has magnified the kinetics insensitivity toward θ_0 change.

In the third category, θ_0 increase does not play an important role because the kinetic is fully reaction-limited. In this category, although both Da increase and ϵ decrease are indicative of a decelerated kinetics, the net change in the overall kinetics is not considerable. This speculation is valid because the kinetics is highly reaction-limited ($\mathrm{Da} \ll 1$), and remains reaction-limited throughout the course of θ_0 change. Highly reaction-limited processes are nearly insensitive to changes in the mass transport strength (the denominator of the Da), and or reaction strength (the numerator of the Da). For example, in the conjugation reaction, the kinetics is highly reaction-limited ($\mathrm{Da} \sim 10^{-8}$), and upon increasing the θ_0 even for two orders of magnitude ($4.68 \times 10^{-11} \overset{\theta_0}{\rightarrow} 4.68 \times 10^{-9}$), the Damköhler number remains close to zero ($\sim 10^{-8} \overset{\mathrm{Da}}{\rightarrow} \sim 10^{-6}$). Therefore, the reaction is still highly reaction-limited. The binding capacity (ϵ) does not diminish to a low value, despite experiencing a dramatic decrease upon the same change in θ_0 ($\sim 10^{7} \overset{\epsilon}{\rightarrow} \sim 10^{5}$). In summary, since the change in ϵ is happening in a reaction limited-condition ($\mathrm{Da} \ll 1$), θ_0 cannot noticeably alter the kinetics.

Physically, the different trends seen here between the first two reactions considered (self-assembly and conjugation) and the immunoreaction can be attributed to the abundance of reagents in the bulk for the first two, and a near-shortage of analytes for the immunoreaction. Detailed discussion is given in Sections 2.4.1.3, 2.4.2.3, and 2.4.3.3.

2.6 Summary

This chapter presents the construction of a finite element model to study the kinetics of reactions involved in the in-situ functionalization of HIAs, based on the self-assembled monolayers of thiols. The examined reactions include the thiolic self-assembly, the Ab/SAM conjugation reaction, and the HSP70 immunoreaction. The effect of a number of parameters on the overall reaction kinetics is numerically studied, including the analytes concentration in the bulk, the surface loading density of binding sites, and the microfluidic parameters such as the flow rate and the microchannel height.

The numerical simulations revealed that in the thiols self-assembly, the conventional 24-hour process time can possibly be reduced to 15 minutes by adopting a bulk fluid concentration of $10\ mM$, called here the fast-SAM protocol. In the Ab-conjugation kinetics, a $5\ mM$ concentration of EDC is enough to complete the conjugation reaction in one hour, while the corresponding concentrations used in conventional protocols are considerably higher. Based on the model predictions and experimental studies available, it is proposed that a $5\ mM$ concentration of EDC results in the optimum conjugation yield, and using higher concentrations in the one-hour protocol may lead to decreased conjugation yields. Through examination of the HSP70' immunoreaction kinetics, the requisite reaction conditions to achieve its optimum kinetics are determined. The optimum kinetics results in a minimal immunoreaction completion time (T_{comp}~29 minutes) and analyte consumption.

The SAM-formation kinetics has an insignificant dependency on the flow rate, and the average amount of reduction in the reaction completion time, due to the increase of flow velocity, is below 7%. The microchannel height (h) and the surface packing density of thiols (θ_0) do not play a significant role in the self-assembly kinetics, if the height is in the order of few microns (or higher) and $7.3 \times 10^{-10} \leq \theta_0 < 7.3 \times 10^{-7}\ mol.m^{-2}$, which is encountered in this thesis. The latter conclusions can be reached by consideration of the fundamental properties of self-assembly reaction, without simulations, reported in the thesis.

The Ab/SAM conjugation kinetics shows a significant dependency on the flow rate. Simulation results demonstrate that using the flow-through mode, even for $15\ \mu m.s^{-1}$ of flow velocity, effectively enhances the transient process of the conjugation kinetics by around one order of magnitude. The microchannel height and the surface packing density have the same effect on the conjugation kinetics as on the self-assembly kinetics.

The immunoreaction kinetics demonstrates a strong flow velocity dependency. As with the Ab-conjugation kinetics, the immunoreaction is effectively enhanced by more than one order of magnitude by implementation of the flow-through mode, with a typical flow velocity of $15\ \mu m.s^{-1}$. The microchannel height has same effects on the immunoreaction kinetics as does on the self-assembly and conjugation kinetics. In addition, the kinetics slows down upon increasing the Ab surface-loading density from the nominal value of $\theta_0 = 4.38 \times 10^{-9}\ mol.m^{-2}$. For the microchannel heights considered in this thesis (few microns) the latter observation can be reached by consideration of the fundamental properties of the immunoreaction. Numerical simulations reveal that using higher amounts of θ_0 ($4.38 \times 10^{-9} < \theta_0^{high} \leq 4.38 \times 10^{-7} mol.m^{-2}$), e.g., $\theta_0 = 4.38 \times 10^{-8}\ mol.m^{-2}$, necessitates employment of higher flow velocities (u_{avg}~$1500\ \mu m.s^{-1}$) to maintain the reaction progress rate at almost the same level (T_{comp}~30 minutes). This elevated flow velocity utilization, implies an increased rate of protein consumption compared to the lower flow velocity case (u_{avg}~$15\ \mu m.s^{-1}$). The best flow velocity is determined to be around $70\ \mu m.s^{-1}$ in terms of a reasonably fast immunoreaction kinetics (T_{comp}~29 minutes), and minimal HSP70 consumption throughout the experiments. Moreover, the best range of Ab-loading density in terms of immunoreaction completion time, and also a rich detection signal strength is determined to be ($4.38 \times 10^{-11} \leq \theta_0 \leq 4.38 \times 10^{-9}\ mol.m^{-2}$) which includes the Ab-loading density used in this research ($\theta_0 = 4.38 \times 10^{-11}\ mol.m^{-2}$).

In brief, the following are the major findings from the numerical simulations of the in-situ functionalization kinetics, to be experimentally verified in the next chapter:

1- A complete thiolic self-assembled monolayer can be formed from a 15-minute incubation of the immunoassays' reaction surface in a $10\ mM$ solution of 11-MUA and 1-OT (the thiols employed in this research) in ethanol.

2- The conventionally reported 1-3 hour Ab/SAM conjugation processes with $100\ mM$ EDC concentration can be modified to a $5\ mM$ EDC protocol, requiring one hour for conjugation completion. Numerical simulation predicts that the conventional $100\ mM$ concentration of EDC, requires less than 10 minutes to complete. Considering possible chemical reaction paths suggests that a reduced conjugation yield is expected for the $100\ mM$ reaction compared to the $5\ mM$ EDC case, when both undergo the same one hour process times.

3- Based on the immunoreaction kinetic properties of HSP70 and the functionalization protocols suggested here, a 29-minute immunoreaction time is expected for a $65.7\,nM$ bulk fluid concentration of HSP70 in a flow-through mode with $70\ \mu m.s^{-1}$ of flow velocity. This process time implies a considerable time saving compared to the long incubation times (several hours) used in conventional immunoassays.

Chapter 3
Improvement of the Kinetics of Functionalization Reactions: Experimental Verification

3.1 Introduction

In the last chapter, reactions involved in the SAM-based in-situ functionalization of an HIA were numerically simulated. The reactions involved were the SAM formation, the Ab/SAM conjugation, and the immunoreaction of HSP70. It was shown that the conventional 24-hour self-assembly process time can be reduced to 15 minutes, by adaptation of thiol concentration. Moreover, numerical simulations and the analysis of available experimental data revealed that the conventional one-hour/100 mM EDC conjugation protocol may not lead to the maximum possible conjugation reaction yield. Thereafter, performing the Ab conjugation using a 5 mM EDC sample, with a one-hour process time was suggested. An Ab conjugation yield superior to that achieved with conventional processes is expected from this protocol. Finally, the immunoreaction kinetics of HSP70' was studied. The best flow velocity was determined to be 70 $\mu m.s^{-1}$, which allows achieving a reasonably fast (~29 minutes) immunoreaction completion time without increased protein consumption levels.

In this chapter, the target is experimental verification of the above numerical findings. First, the 15-minute SAM formation protocol, called here the "fast-SAM" protocol, is examined by binding proteins to the reaction surfaces that are coated with SAM. The SAM formation protocol' performance is assessed by attaching a standard biotin/streptavidin pair to the SAM and characterizing the resulting loading densities by LSPR spectroscopy. Additionally, fluorescently labeled Abs are attached to the fast SAM, and their resulting loading density is characterized by the fluorescent microscopy and AFM. The second and third sets of experiments involve examination of the anti-HSP70 conjugation protocol and studying the resulting immunoreaction kinetics of the HSP70, respectively. The role of EDC concentration in the Ab conjugation is monitored in real time using the QCM technique, and the resulting Ab-loading density is calculated. This step is followed by HSP70 capturing from the bulk fluid by the functionalized surface of the QCM crystal, while the immunoreaction is also monitored in real time. The results agree closely with the numerical model predictions and are indicative of the following achievements: a successful 15-minute self-assembly,

the highest possible loading density of the Ab from a $5\ mM$/one-hour EDC conjugation process, and an enhanced 29-minute HSP70 immunoreaction, using a $70\ \mu m.s^{-1}$ flow velocity.

3.2 Fast-SAM Protocol Verification by Protein Binding

In this section the fast-SAM protocol is examined by binding proteins to the SAM and assessing the protein loading density. The resulting loading density from binding of proteins to the fast SAM is compared to that of conventional SAMs. LSPR spectroscopy of nanoparticles, fluorescent microscopy, and AFM are used to measure the protein loading density.

3.2.1 Confirmation by LSPR Spectroscopy of Nanoparticles

This section details the first step in assessing the capability of a fast-SAM protocol to form a high-quality bio-interface. A SAM of 11-MUA and 1-OT were formed by incubation of gold nanoparticle chips in an ethanolic $10\ mM$ solution for 20 minutes, which is slightly above the 15 minutes prediction of the model (Section 2.4.1.1). This 5-minute safety margin was taken to compensate for possible uncertainties present in the modeling. The 15-minute fast SAM is later tried as well, as detailed in Sections 3.2.2 and 3.3. The performance of this novel, rapid SAM formation protocol was compared with a conventional 24-hour incubation protocol [11, 12]. Protein-binding capacity of the thiolic SAM was investigated using biotin-streptavidin. For this purpose, the SAM loaded gold nanoparticle chips were modified with EDC to allow attachment of EZ-Link amine PEG3 biotin to the 11-MUA molecules. Binding reactions were monitored in real time using LSPR spectroscopy [33, 64]. The resulting LSPR absorbance peak shift was comparable to the experimental results for biotin-streptavidin reported in the literature [12]. Results of this study suggest that formation of a high quality thiolic SAM within 20 minutes on gold nanoparticles surfaces is possible and could greatly reduce the time and cost compared to conventional 24-hour incubation protocols [11, 12].

3.2.1.1 Materials and Devices

Thiols employed in this research are 11-MUA with carboxylic end groups, and 1-OT that serves as a spacer and support for 11-MUA, both purchased from Sigma Aldrich (Oakville, Canada). The SAM solvent used was pure ethanol, purchased from Commercial Alcohols (Boucherville, Canada). EZ-Link amine PEG3 biotin from Sigma Aldrich was bound to the SAM and then used to capture streptavidin purchased from Invitrogen (Burlington, Canada). In order to bind the biotin to the SAM,

EDC and NHS from Fisher Scientific (Ottawa, Canada) were used, according to the chemistry outlined in Section 2.2.3.2. Electron beam lithography (EBL) [157] was used to generate patterns which were later used to fabricate square gold nanoparticles using a lift-off process [158]. The gold nanoparticles were designed in an array with a periodicity of $300\,nm$, an edge to edge spacing of $200\,nm$, and dimensions of $100 \times 100 \times 50\,nm$. A 1-2 nm layer of chrome was used as an adhesion layer, beneath $50\,nm$ of gold. The $1 \times 1\,mm$ nanoparticle array area was centered on a $10 \times 10\,mm$ glass chip with a thickness of $500\,\mu m$ diced from Pyrex wafers, shown in Figure 3.1 [158].

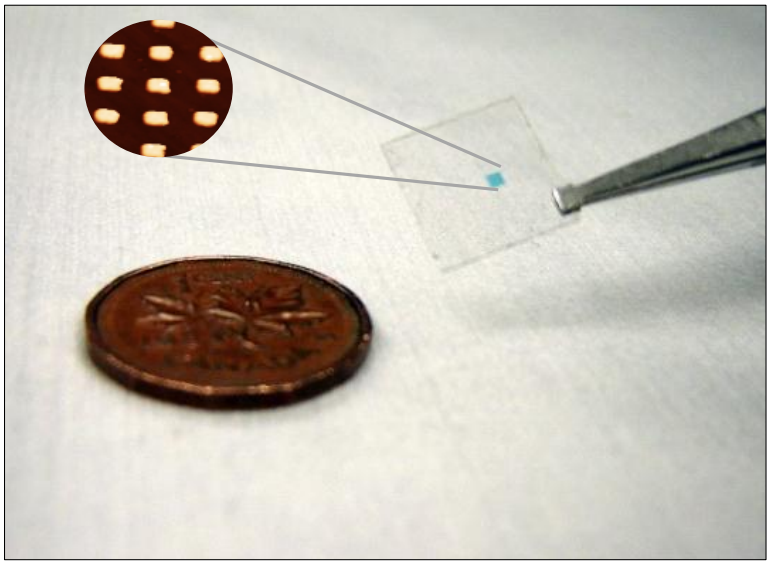

Figure 3.1: Photograph of the gold nanoparticle chip containing a $1 \times 1\,mm$ array of nanoparticles on glass. Inset demonstrates an AFM image of the array. The nanoparticles are around $200\,nm$ apart. Reprinted with permission from [158].

3.2.1.2 Experimental Setup and Methodology[2]

The binding of biomolecules to gold nanoparticles results in a change in optical properties of the surrounding medium, which causes their LSPR peak to shift. This measurable optical response can be directly correlated to the degree of surface adsorption [33]. In this study, the LSPR peak was monitored in real time in transmission mode with an Ocean Optics USB4000 spectrometer, equipped with a white light source and fiber optic cables (Dunedin, USA). The fluids were pumped through a

2- The functionalization protocols modified by the author of this thesis, including the fast-SAM protocol and the antibody conjugation protocol were implemented in the LSPR experiments by Mr. Ryan Denomme and Mrs. Chelsea Marr.

fluid injection setup using a Harvard Apparatus Pico Plus syringe pump (Holliston, USA). Sample injection was done with a 6-port injection valve (Valco, Houston, USA). The nanoparticle chip was housed in a flow cell made of PDMS, fabricated using a molding process. The integrated pumping and sample injection system enables implementation of small sample sizes. Unless stated otherwise, all the experiments were performed at an ambient temperature of 22 ℃. The optical spectroscopic and fluidic setup used for this study is shown in Figure 3.2 below.

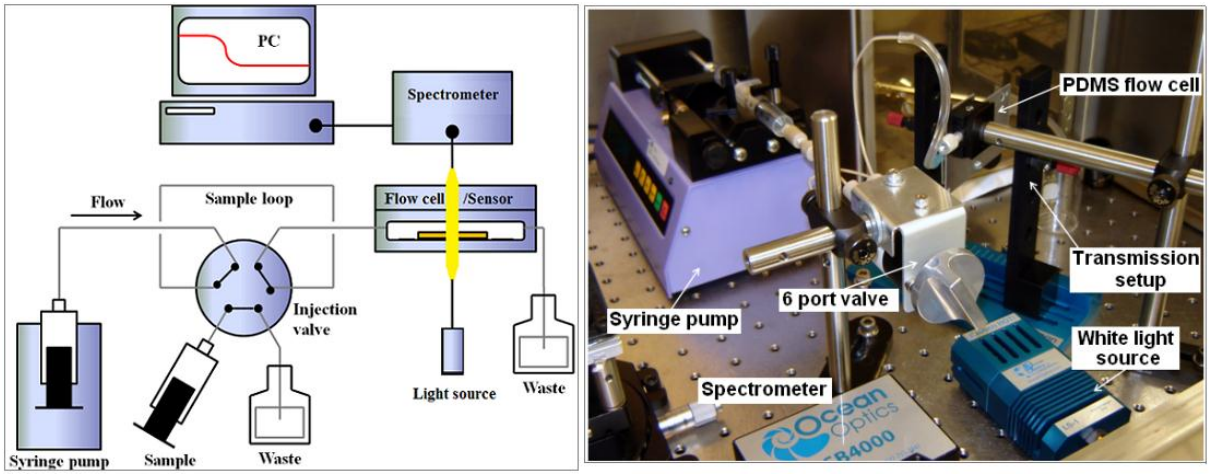

Figure 3.2: Schematic (left) and photograph (right) of the LSPR micro-injection analysis setup for real-time monitoring of protein binding, reprinted with permission from [158] and [159], respectively. Fluids are delivered by a syringe pump through a direction selection valve into a micro-flow cell, which contains the gold-nanoparticle coated chip. Reactions are monitored by recording the changes in the absorbance peak position of the nanoparticles using a PC.

The nanoparticles' chips were cleaned using a UV/ozone cleaner, followed by thorough rinsing with DI water, IPA and ethanol, and dried with a stream of nitrogen [158]. After cleaning, the chips were incubated in the self-assembly solution for 20 minutes with no pumping. The ratio of thiols in the solution was 1:3 (11-MUA:1-OT) to prevent steric hindrance [11]. The chips were then rinsed with pure ethanol to remove any unbound SAM molecules. Immediately after this SAM formation protocol, the chips were incubated in a $5\,mM$ solution of EDC/NHS for one hour, followed by a thorough rinsing in DI water. The functionalized chip was then mounted in the micro-injection setup shown in Figure 3.2. After rinsing with PBS, a $1\,mM$ biotin solution was injected into the flow injection setup, and the binding reaction was monitored in real time using LSPR. Following biotin

binding, the system was rinsed with PBS to remove any excess. Finally, the biotin/streptavidin interaction was monitored while a 166 nM solution of streptavidin in PBS was injected.

3.2.1.3 Mathematical Model, Results and Discussion

As discussed in Section 2.4.1.1, implementation of a high concentration of thiol such as 10 mM results in a fast 15-minute self-assembly process, compared to conventional 24-hour processes [11, 12]. Moreover, the self-assembly kinetics has a weak dependency on the flow rate, and increasing the flow rate from zero to even 1000 $\mu m.s^{-1}$ cannot reduce the process time by more than 16%. Therefore, to enhance the kinetics, adopting the higher thiol concentration of 10 mM is enough, with no need to employ the flow-through mode. In addition, increasing the height of the microchannel from 40 μm to 80 μm, or even higher to 5 mm, results in less than 1% of reduction in the self-assembly completion time (Section 2.4.1.2). For these reasons, the simulation results, outlined in Section 2.4.1, can be implemented here for formation of SAM, by incubation of the chip substrate in self-assembly solutions, without employing microfluidics. The nanoparticle chip was incubated in the self-assembly solution for 20 minutes without any pumping or stirring. The 20-minute incubation time is close to the model' predicted 15-minute self-assembly completion time. As predicted in Section 2.4.1.1, 15 minutes is enough for the self-assembly completion; however, a 5-minute safety margin was taken, as the model might have not taken into account the uncertainties present in experimental conditions, such as temperature fluctuations. A 20-minute self-assembly time is still promising, since conventional self-assembly protocols often take 24 hours to complete the process [11, 12]. The typical configuration of the nanoparticle chip flow cell is shown in Figure 3.3.

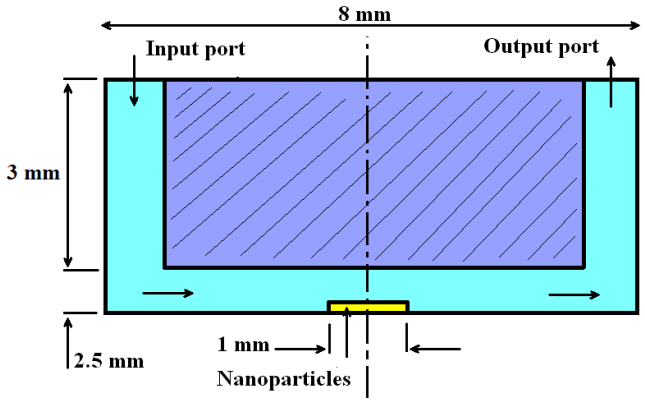

Figure 3.3: Typical configuration of the nanoparticles in the flow cell, reprinted with permission from [159].

The quality of the SAM formed by the 20 minutes of incubation was assessed experimentally by binding a standard biotin-streptavidin pair to the nanoparticles. The binding of biotin to the SAM and subsequent capturing of streptavidin on the immobilized biotin was monitored in real-time using the flow injection LSPR setup shown in Figure 3.2. Figure 3.4 below shows the real time LSPR peak position during the test.

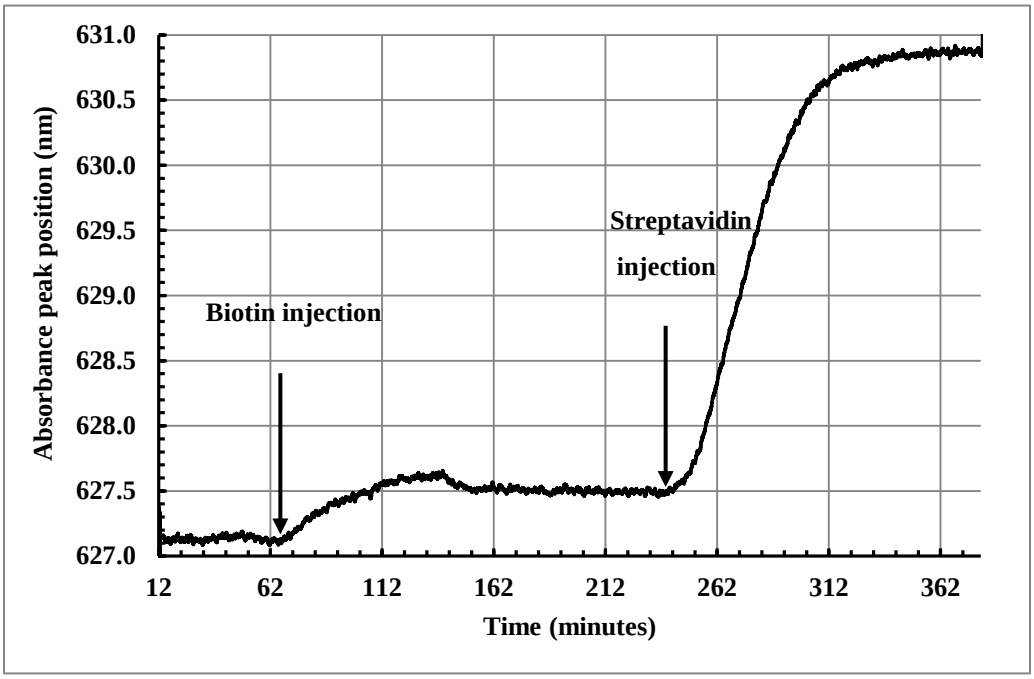

Figure 3.4: Successful faster than conventional SAM-formation demonstrated by immobilization of biotin-streptavidin pairs, through implementation of localized surface plasmon resonance (LSPR) of metal nanoparticles. Injection of biotin, and subsequently streptavidin, results in their binding to the SAM coated chip and biotin, respectively. Binding reactions are monitored by measuring and leads to the increase of LSPR absorbance peak position of the nanoparticles. Reprinted with permission from [159].

Upon injection of the biotin, a peak position shift of 0.47 nm was observed using the chip loaded with the SAM. This pick shift is three times less than the 1.6 nm peak shift reported in the literature when using a 24-hour incubation (value adjusted from the literature to match the experimental conditions here) [12]. This difference may be due to a higher EDC modification efficiency resulting from the use of higher EDC concentrations, compared to the experimental condition here [12]. However, it could also be due to a more packed SAM using a 24-hour incubation. Upon completion

of the biotin injection, streptavidin was injected and captured by the immobilized biotin groups. A considerably high streptavidin concentration of $166\,nM$ was used to make sure that most of the available biotin sites were filled. In this case, a saturation peak shift of $3.37\,nm$ was observed, which is very close to the value of $3.8\,nm$ reported in the literature for a 24-hour incubation [12]. This very small difference indicates similar binding density for the two processes. Interestingly, the smaller biotin shift using the SAM formed in 20 minutes did not seem to reduce the binding density of the streptavidin, perhaps because streptavidin is much larger than biotin. Therefore, the probable increased number of biotin sites resulting from the conventional method does not allow more streptavidin to bind due to steric hindrance between the streptavidin molecules. However, the rather high LSPR peak shift observed in our experiments could also be a good indication of a high-quality biotin layer formed over the SAM and thus a successful SAM formation protocol. The results of the protein-binding experiments performed using both 20-minutes and conventional 24-hour SAM formation protocols are summarized in Table 3.1.

Table 3.1: LSPR peak shift due to SAM/biotin and biotin/streptavidin binding for conventional and a fast 20-minute SAM formed on gold nanoparticles. Adapted with permission from [159]. Standard deviation above and below the average for three trials is reported for each entry.

Process	SAM/biotin binding	Biotin/streptavidin binding
Conventional SAM (24 hours) [12]	$1.6\,nm$	$3.8\,nm$
SAM formed in 20 minutes	$0.47 \pm 0.06\,nm$	$3.37 \pm 0.15\,nm$

3.2.2 Confirmation by Fluorescent and Atomic Force Microscopy

In this section, the fast-SAM protocol performance is assessed by examining the loading density of Abs immobilized on the SAM. Planar gold chips were incubated in thiolic $10\ mM$ solutions for 15 minutes to form the SAM. Another set of samples was also prepared using the conventional 24-hour protocol [11, 12]. The binding capacity of a fluorescent-labeled Ab to the SAM surface was compared using samples prepared with both protocols. For this purpose, the SAM-loaded chips were modified with EDC to provide a high binding surface for Ab immobilization, according to the protocol outlined in Section 1.3.2.2. Tetramethyl-rhodamine conjugated polyclonal goat gamma globulin was bound to the gold chips, and the Ab coverage was imaged using epi-fluorescence microscopy. The AFM was used to characterize the loading density of the Ab. For both protocols, the resulting loading density of the Ab was comparable to the predicted values in the literature [19]. High resolution AFM images confirmed an Ab binding density close to the literature predictions. Formation of a defect-free SAM within 15 minutes on planar gold surfaces would greatly cut down the time and cost compared to the conventional 24-hour incubations.

3.2.2.1 Experimental Methods

The thiols used were 11-MUA with carboxylic end groups, and 1-OT that serves as a spacer and support for 11-MUA, both purchased from Sigma Aldrich (Oakville, Canada). The SAM solvent used was pure ethanol, purchased from Commercial Alcohols (Boucherville, Canada). Hexane was purchased from same supplier. Acetone and isopropyl alcohol (IPA) were purchased from Caledon (Georgetown, Canada). The Ab that was bound to the SAM was Tetramethyl-rhodamine conjugated goat immuno gamma globulin, called here RFP, standing for rhodamine dye fluorescent protein, acquired from Invitrogen (Burlington, Canada). Phosphate buffered Saline (PBS) was prepared in the Environmental Genomics and Biomarker Development facility, University of Waterloo. The carbodiimide used is EDC, acquired from Sigma Aldrich.

Gold coated glass substrates were purchased from Platypus Technologies, LLC (Madison, USA) and then diced into $1.27 \times 1.27\ cm$ (0.5" × 0.5") chips. Fluorescent images were captured by a Zeiss Axiovert inverted epi-fluorescence microscope set at $550\ nm$ (Toronto, Canada). The AFM images were captured in air with a Digital Instruments NanoScope III (Santa Barbara, USA) in tapping mode. Images were obtained at a scan rate of $2\ Hz$ with a silicon cantilever. The cantilever length was

$125\ \mu m$ and the resonance frequency was set at $307 - 375\ kHz$. A drive voltage between 150 and $200\ mV$ was used. Unless stated otherwise, all the experiments were performed at an ambient temperature of 22 ℃.

The first step in the functionalization process was cleaning the gold substrate. The detailed cleaning protocol can be found in Appendix A. In brief, the gold chips were rinsed for 2 minutes with hexane to remove the hydrophobic contaminants. Then the chips were quickly transferred to ethanol for another 2-minute wash to remove the hydrophilic contaminants, followed by 10-minute acetone, 2-minute IPA and 2-minute DI water washes. Finally, the chips were thoroughly rinsed with the SAM solvent (ethanol), completely dried with a stream of Nitrogen and incubated under the self-assembly solution for the intended period. The conventional self-assembly protocol can be found in Appendix B. The ratio of thiols in the solution was always kept at $1:3$ (11-MUA:1-OT) to avoid the steric hindrance [11]. Then the chips were rinsed thoroughly with pure ethanol to remove any unbound SAM molecules from the gold surface. Immediately after the SAM formation, the chips were loaded with fluorescent Abs. A $10\ mM$ PBS buffer of pH 7.4 was used, containing a maximum $0.05\ mg/ml$ of Abs and $100\ mM$ of EDC as the Ab/SAM crosslinker [19]. The rate of evaporation from the chip surface was controlled by placing the chips in a humidified chamber during the crosslinking process. A microscope glass slide cover slip was laid on the chip surface to further reduce the surface evaporation. The chips were kept at -4℃ overnight and rinsed the following day with large volumes of $10\ mM$ PBS. The detailed conjugation protocol can be found in Appendix C. The moisture was removed from the surface, and the chip was scanned using the AFM/fluorescent microscopy.

3.2.2.2 Mathematical Model, Results and Discussion

The height of the self-assembly chamber was shown in Section 2.4.1.2 to have a negligible effect on the self-assembly completion time. Therefore, the simulation results for the zero-flow mode in Section 2.4.1 can be used for prediction of the self-assembly completion time when the experiment is done in a self-assembly chamber with a typical configuration as shown in Figure 3.5.

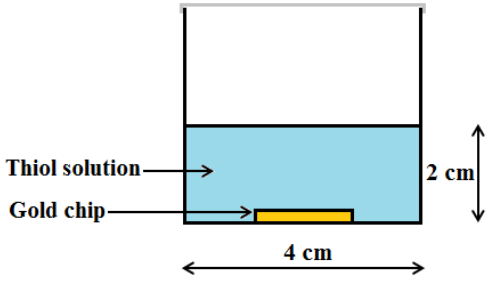

Figure 3.5: Typical configuration of the self-assembly chamber (not to scale). Thiolic self-assembly is initiated on the gold surface by immersion of the chip in the thiol solution.

To compare the quality of the SAMs resulting from the fast protocol, to the SAMs formed according to the conventional 24-hour process, a fluorescent Ab was bound to the chips prepared by both these methods [19]. Figure 3.6 was generated using epi-fluorescence imaging and displays a comparison of these two chips showing similar and uniform binding patterns. A uniform surface distribution of bound Abs usually suggests a successful immobilization protocol, which here implies a uniform spread of the thiol molecules over the chip surface area [151]. In addition, the number of Abs immobilized per unit area is in accordance with the protocol predictions, shown by AFM in the following.

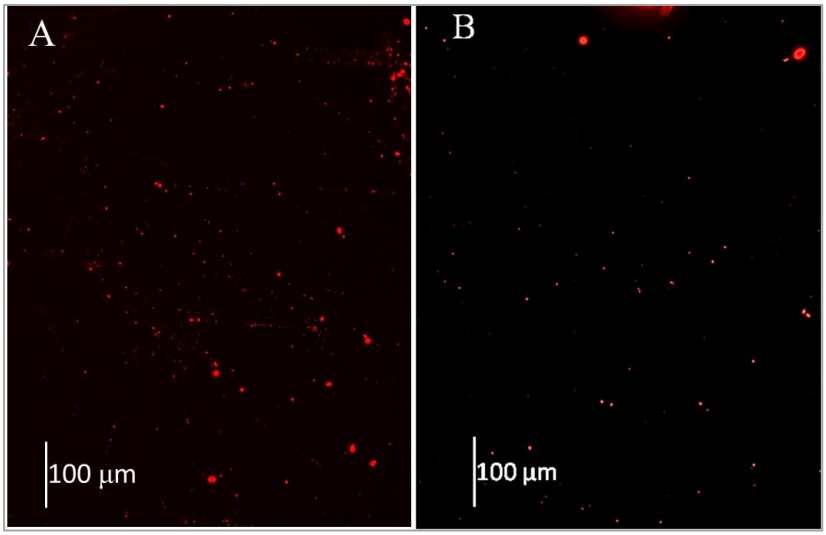

Figure 3.6: Images captured from the fluorescent antibodies, immobilized on the gold surface, by the epi-fluorescence microscope. Fluorescent antibodies are uniformly bound to SAM and distributed on the chip for both SAM formation protocols; A: Fast SAM, B: Conventional 24-hour protocol.

In order to quantify the binding density of the Abs, the AFM was used. AFM imaging was repeated for only a maximum of 6 times for each chip due to the Ab instability at room temperature [160]. The images generated by the AFM for the fast and conventional 24-hour SAM protocols are shown in Figure 3.7. The right hand AFM images in Figure 3.7 belong to the conventional protocol results. The fast-SAM protocol demonstrates loading densities almost equal to those of the conventional 24-hour SAM protocol, presented in Figure 3.7. Figure 3.7-A and A` show a 10 $\mu m^2$ of the chip chosen randomly for Ab-loading density measurement. Figure 3.7-B and B` present the zoomed-in images of this region showing two and three objects, respectively. Figure 3.7-C and C` show the side view of these two objects. The AFM used in this research have a maximum resolution of 2 $nm$ for solid objects with a sampling number of 512 per each 1 $\mu m$ ($1\mu m/512 \sim 2\ nm$). It can be observed in Figure 3.7-C and C` that the objects have a smooth height transition at their edges. Moreover, their relative height is around 7 nm, which is in accordance with the values reported for the Abs' height in the literature [161]. Therefore, the objects seen in the AFM image are considered to be Ab clusters bound to the surface (Figure 3.7-B, B`, C and C`). Hence, assuming that each Ab is around 14 nm in width [162, 163], the object in Figure 3.7-B on the left is considered a cluster of around 6 Abs and the one in the right is a cluster of 10 Abs. Similar speculations can be made about the objects observed in the corresponding fast SAM process. The protocol followed to crosslink the Ab to the SAM allows clustering. The latter event occurs because Abs have carboxylic groups as well as amine groups [1], and therefore, the crosslinker can potentially attach Abs to each other, forming Ab clusters. Repeated AFM imaging was performed for each chip able to resolve between zero to two clusters per square micrometer in the conventional protocol, and a corresponding maximum of 3 clusters in the fast-SAM protocol. Using this data, a distribution of 0-2 clusters/μm^2 and 0-3 clusters/μm^2 was calculated for the conventional and fast-SAM protocols, respectively, which are comparable to the expected value of 0.44-2.2 Abs/μm^2, reported in the literature [38]. The lower than expected binding density observed might be due to denaturation of the Abs over time [160], during the AFM experiments. In each protocol, fluorescent microscopy was performed for more than three times, and AFM experiments was repeated for two sets of chips. The fluorescent imaging confirmed the uniformity of Ab binding, while the AFM experiments verified repeatability of the above distribution range of Ab loading density. AFM can only provide local data about the Ab loading density and cannot be used to image large surface areas, without sacrificing the resolution [164]. Accordingly, the surface area which was imaged at each time was not increased above one square micrometer to keep the resolution around 2 nm (discussed earlier in this section). On the other hand, AFM imaging can be conducted

for a maximum of 6 experiments for each chip with considerably large overall dimensions of $1.27 \times 1.27\ cm$, due to the instability of the Abs in the room temperature [160]. These two facts, i.e., the small surface area imaged by the AFM and small number of experiments that can be conducted on each chip, prevent providing a meaningful statistical data on the mode of Ab surface density distribution. At any case, the fluorescent imaging performed confirms a uniform spread of Abs for the chips loaded with fast SAMs, showing the same pattern as the chips loaded with conventional protocols. Moreover, the protein characterization results from the AFM experiments, summarized in Table 3.2, match the literature data for both protocols. Therefore, the fast SAM protocol entails the same protein binding capability as the conventional protocol.

The results of the Ab binding experiments performed in the chips prepared using both fast and conventional 24-hour SAM formation protocols are summarized in Table 3.2.

Table 3.2: SAM/antibody binding characterization of samples prepared using the fast SAM and 24-hour conventional protocols, demonstrating a satisfactory Ab binding capability for the fast-SAM protocol.

SAM formation protocol	Average height of the antibody/type	Antibody loading density
Fast SAM (15 minutes)	7 nm / rhodamine goat IgG	0-3/μm^2
Conventional 24 hour		0-2/μm^2
The literature data	7 nm / bovine IgG [161]	0.44-2.2 /μm^2 [12, 19]

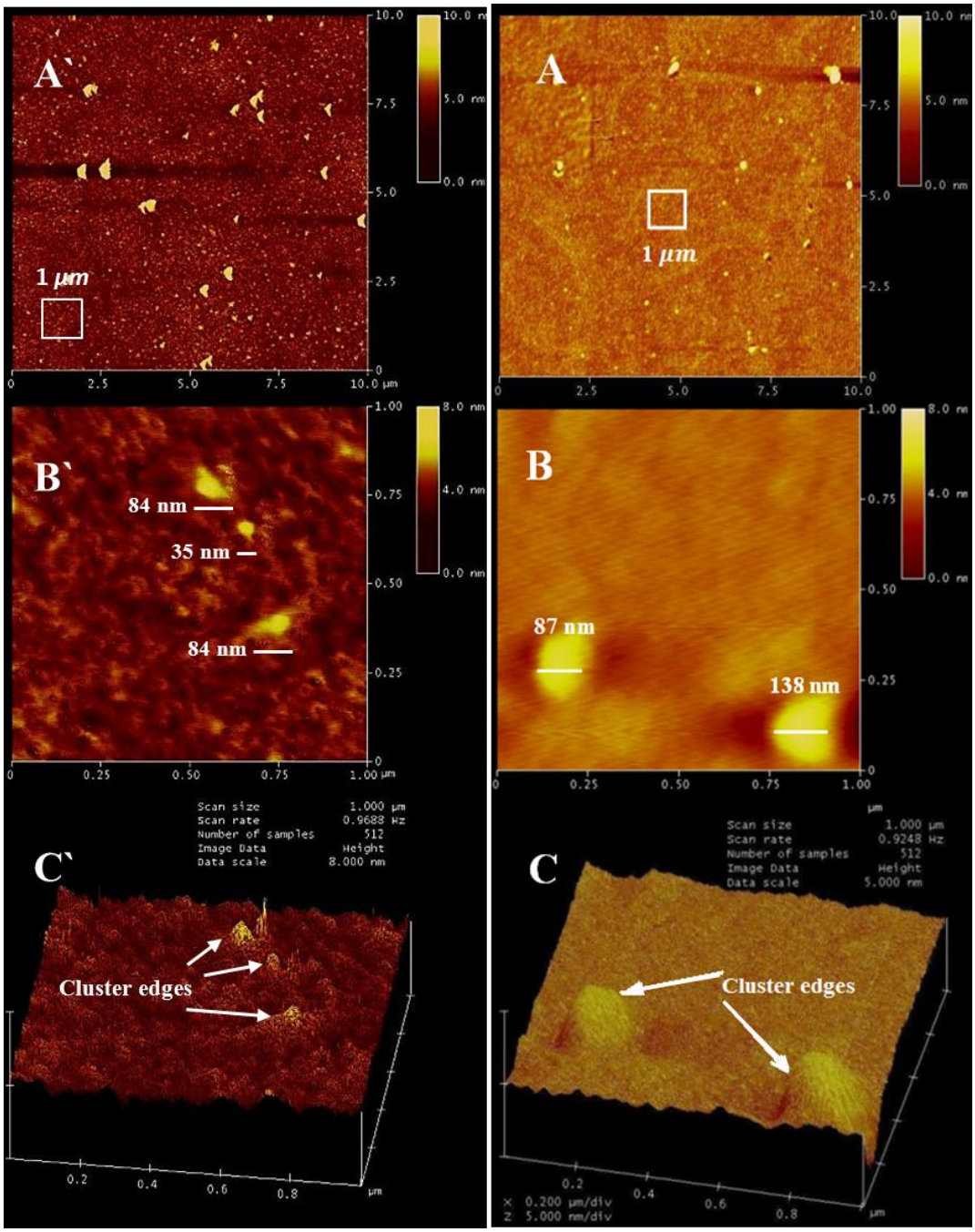

Figure 3.7: AFM image of the fluorescent antibodies bound to samples prepared using the fast SAM (on the left) and conventional self-assembly protocol (on the right). A and A`: a 1 $\mu m^2$ region of the chip is selected randomly; B and B`: clusters of antibodies; and C, C`: antibody clusters' side view with smooth height transitions.

3.3 Antibody Conjugation and HSP70 Immunoreaction Experiments

In this section, QCM is used to verify the numerical model predictions, summarized in Section 2.6, mainly for the Ab conjugation and immunoreaction of HSP70. In brief, numerical simulations revealed that the conventional one-hour/$100\,mM$ EDC conjugation protocol may not lead to the maximum possible reaction yield. Thereafter, performing the Ab conjugation using a $5\,mM$ EDC sample, with a one-hour process time was suggested. Moreover, the immunoreaction is expected to complete in around 29-minute ($T_{comp} = 29': 22"$), for a $65.7\,nM$ bulk fluid concentration of HSP70 in a flow-through mode with $70\,\mu m.s^{-1}$ of flow velocity. The purpose of the QCM experiments is to examine the efficiency of the suggested conjugation protocol. Moreover, QCM is used to monitor the immunoreaction of HSP70 in real time and validate the predicted reaction completion time.

To confirm the main predictions of the model, the SAM of 11-MUA and 1-OT was coated on the QCM crystal in 15 minutes from a $10\,mM$ thiol solution. The carboxylic head groups of the SAM molecules were activated by a number of EDC and NHS concentrations in PBS for one hour to bind the Ab, with the goal of finding the maximum conjugation yield. HSP70 (Ag) was then introduced to the system in all cases, resulting in its immobilization to the Ab. The Ab and Ag binding reaction was performed in a closed flow cell, with micrometer overall dimensions where the sample flow rate of analytes over the planar gold surface was held at a constant rate of $70\,\mu m.s^{-1}$. The reactions were continuously monitored by QCM. The device precisely measures small amounts of mass deposited on the surface of the quartz crystal through monitoring changes in its resonance frequency [165-167]. Here, QCM is used in a real time configuration with a flow injection analysis system and flow cell.

3.3.1 Materials and Methods[3]

Gold-coated quartz crystals with a resonance frequency of $5\ MHz$ were acquired from Stanford Research Systems (Sunnyvale, USA). Crystals were cleaned before and regenerated after each experiment using a piranha solution. Prior to cleaning, glassware and tweezers used in the process were rinsed with DI water and dried under a nitrogen stream. The piranha solution consisted of a 3: 1 100% sulphuric acid to 30% hydrogen peroxide mixture (WARNING: Piranha is a dangerous and highly reactive solution. It may explode upon contact with organic solvents. During use, extreme

3- The functionalization protocol modified by the author of this thesis, including the fast SAM protocol and the antibody conjugation protocol was implemented in the QCM experiments by Mr. Brendan Smith and the author.

caution is needed at all times). The crystals were soaked in this solution for 12 minutes, then thoroughly rinsed with DI water, dried, and then stored in containers inside of plastic bags filled with nitrogen, and placed inside of a nitrogen desiccator. They were used no more than one week after cleaning.

The experimental setup, schematically shown in Figure 3.8, consisted of a Pump 11 Pico Plus Syringe Pump from Harvard Apparatus (Holliston, USA), which pumped the carrier fluid (PBS) at a constant rate from a $5\,mL$ BD syringe into a Valco six port, two-position selector valve (C22Z, Houston, USA) via PEEK tubing bought from McMaster-Carr (Los Angeles, USA). The fluid was pumped through the valve, and into a flow cell mounted on a QCM200 crystal holder (Stanford Research Systems), where it made contact with the chrome/gold coated crystal. The fluid was then pumped from the flow cell into a waste beaker. The sample was injected into a sample loop (Tygon R-3603) through a fill port on the six port valve. The crystal holder was interfaced with a QCM200 instrument (Stanford Research Systems) through the crystal oscillator electronics module, and experimental data was displayed on a PC using QCM200 software (Stanford Research Systems).

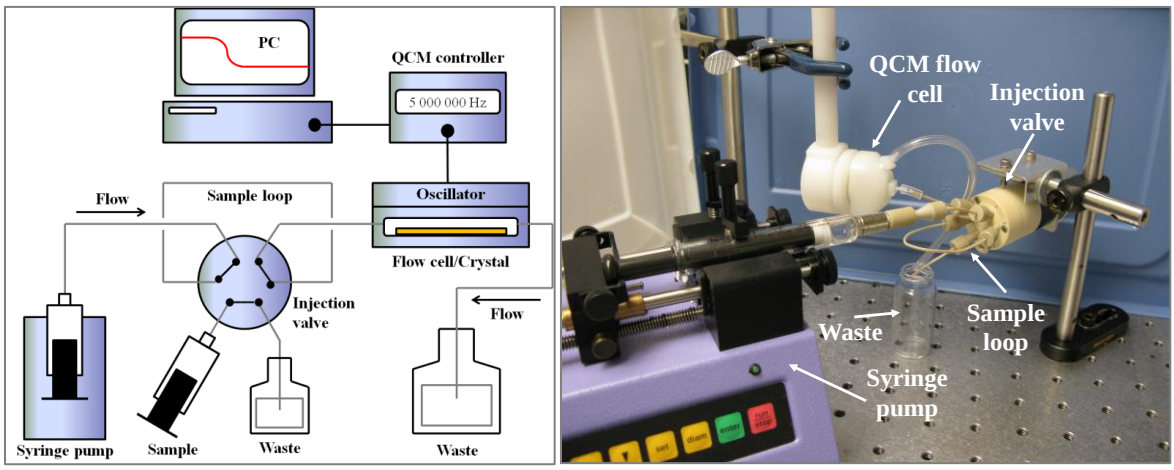

Figure 3.8: Schematic (left) and photograph (right) of the QCM micro-injection analysis setup for real-time monitoring of HSP70 immunoreaction. Fluids are delivered by a syringe pump through a direction selection valve into a micro-flow cell, which contains the gold-coated quartz crystal. Reactions are monitored by recording the changes in the resonance frequency of the quartz crustal using a PC.

As in Section 3.2, 11-MUA and 1-OT were purchased from Sigma Aldrich (Oakville, Canada), and EDC and NHS were both purchased from Fischer Scientific (Ottawa, Canada). Salmonid HSP70

(ADI-SPP-763-D) and its Ab, rabbit anti-HSP70 (SPC-313D), were purchased from StressMarq Biosciences (Victoria, Canada).

3.3.2 Immunoreaction Kinetics Prediction in a Micro-flow Cell

The QCM is used in a micro-fluid injection setup where the internal geometry of the QCM crystal holder (flow cell) is in microns, and the microliter sample sizes resemble a miniaturized micro-reaction environment. The geometry of the micro-flow cell, Figure 3.9, is different from the hypothetical microchannel simulated in Chapter 2 and shown in Figure 2.1. For example, the side input of the hypothetical microchannel is moved to the top of the micro-flow cell.

The computational model used in Chapter 2 to study the immunoreaction kinetics was modified to accommodate the geometry of the QCM micro-flow cell. Upon applying a flow rate of 7 $\mu l/min$ at the inlet, the average cross-sectional flow velocity decreases linearly from 131.5 $\mu m.s^{-1}$ at the cylindrical cross-section A (immediate to inlet) to 11.14 $\mu m.s^{-1}$ at the cross-section B, Figure 3.9. The mathematical formulations, boundary conditions and the numerical solver presented in Sections 2.2 were used to model the immunoreaction kinetics in the QCM micro-reaction chamber, in 3D (see Appendix E for illustrations).

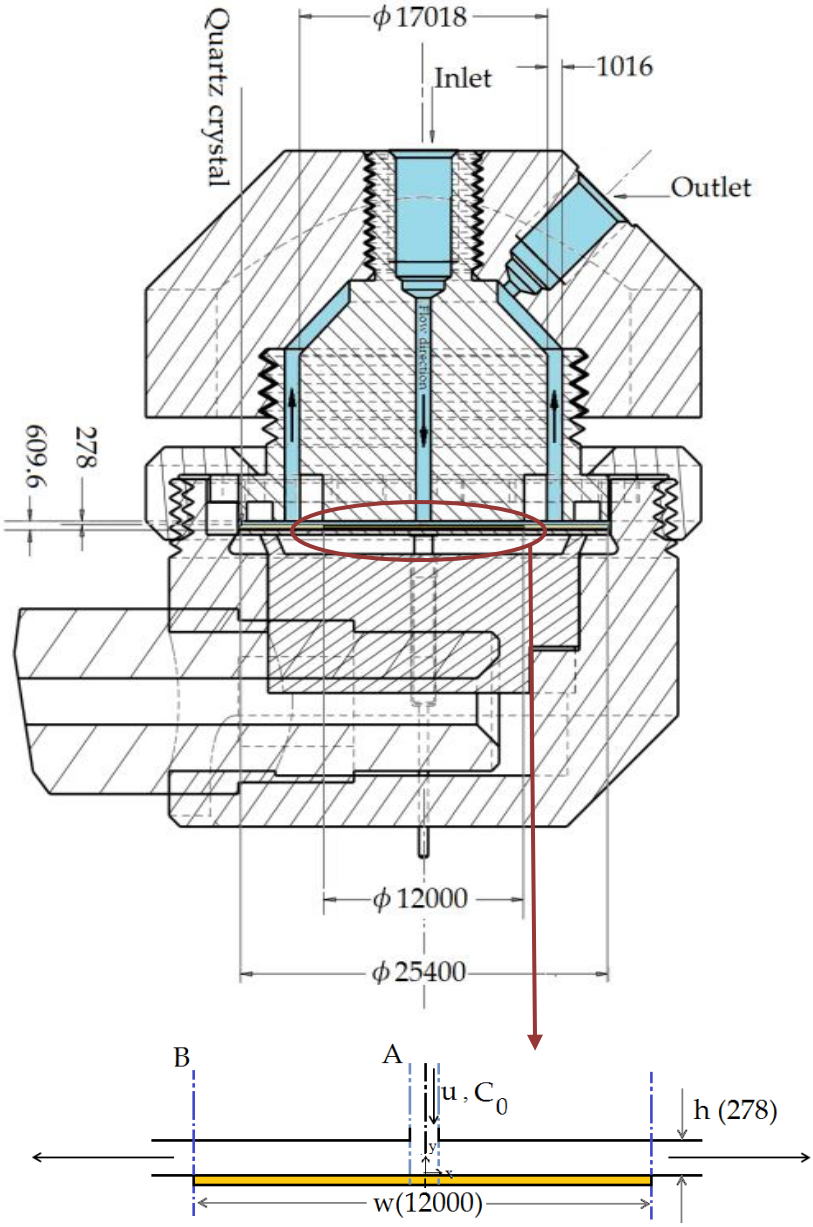

Figure 3.9: Exploded drawing of the QCM200 crystal holder with its schematic representation of the gold-coated crystal in the QCM micro-flow cell (not in scale). Analytes enter the channel from the top inlet and exit from sides. Reactions take place within a diameter w, and h is the microchannel height. Dimensions are in micrometers.

The transient process of HSP70 immunoreaction in the micro-flow cell is simulated and plotted in Figure 3.10 below, along the predicted kinetics of the microchannel, corresponding to Figure 2.1

(Section 2.4.3) simulated for a flow velocity of 70 $\mu m.s^{-1}$. The latter velocity is quite close to the average of the flow-velocity in the micro-flow cell ($11.14 \leq u_{avg} \leq 131.5$), i.e., 71.3 $\mu m.s^{-1}$. In the figure, the simulated dimensionless surface concentration of bound HSP70 molecules ($c_s^* = c_s.\theta_0^{-1}$) is plotted for the first 30 minutes of the reaction for both geometries, i.e., the QCM micro-flow cell and the microchannel studied in Section 2.4.3. The kinetics corresponding to the micro-flow cell has a transiently slower kinetics at the first few minutes. However, the immunoreaction completion time is almost the same for both cases. The process time of the QCM micro-flow cell is $30': 16"$. The latter process time is only 6% more than that of microchannel simulated in Chapter 2. Therefore, upon applying an inlet flow rate of 7 $\mu l.s^{-1}$, corresponding to an average flow velocity of around 71.3 $\mu m.s^{-1}$, an immunoreaction completion time of $30': 16"$ is expected in the QCM micro-flow cell.

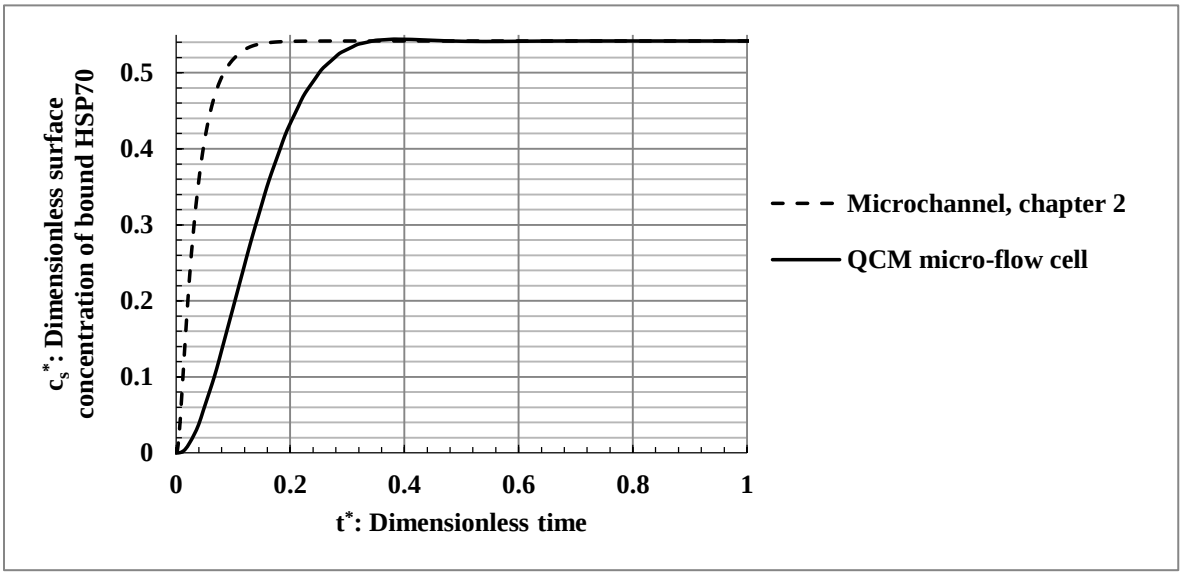

Figure 3.10: HSP70 immunoreaction transient process, simulated for the reaction in the QCM micro-flow cell, and the microchannel, outlined in Chapter 2, Section 2.4.3. Dimensionless surface concentration of bound antigens (c_s^*) calculated for a constant inlet antigen concentration of $65.7\ nM$ are plotted over time. Time is non-dimensionalized by the process time of the microchannel (T_{comp} = 29 minutes and 22 seconds: $t^* = t.T_{comp}^{-1}$). The micro-flow cell has a slower transient kinetics; however, the reaction is completed for both geometries at almost the same time. The process time in the micro-flow cell is only 6% lengthier (T_{comp} = 30 minutes and 16 seconds).

The minimal kinetic differences observed in the simulations between the two geometries (the microchannel simulated in Chapter 2 and the QCM micro-flow cell) could be predicted by consideration of the effects of geometrical changes on the kinetics in two regions of the micro-reaction chamber:

- The entrance section immediate to the inlet in which the flow changes its direction by 90°, including the entrance length after cross-section A in Figure 3.9.

- The region between cross-section A and B, excluding the entrance length immediate to section A.

In the first region, the replenishment rate of analytes is presumably the maximum possible in the whole micro-reaction chamber. The latter expectation is reasonable due to change of flow direction by 90°, and therefore, the level of analytes mixing in the micro-reaction chamber is at the highest. As shown by Feidman et. al. [137], higher levels of mixing results in increased rates of immunoreaction. Therefore, the immunoreaction is completed in this region sooner or almost at the same time as the rest of the reaction surface. On the other hand, this region constitutes less than 3% of the total surface area of the QCM crystal ($\phi = 12000\,\mu m$, see Figure 3.9). Accordingly, this region should not impose a significant impact on the overall reaction completion time. It is worth noting that due to the low flow velocities encountered ($u_{avg} < 150\,\mu m.s^{-1}$), the entrance length, where the transient effects occur, is quite small (few microns) and can be reasonably neglected (see Section 2.2).

In the second region, the flow velocity decreases linearly in the radial direction of the flow. Upon applying a flow rate of $7\,\mu l/min$ at the inlet, the average cross-sectional flow velocity decreases linearly from around $131.5\,\mu m.s^{-1}$ at the cylindrical cross-section A (immediate to inlet) to $11.14\,\mu m.s^{-1}$ at the cross-section B (Figure 3.9). The above flow rate ($7\,\mu l/min$) results in an average flow velocity of $71.3\,\mu m.s^{-1}$ over the reaction surface of the QCM crystal, i.e., the closet possible[4] to the optimum flow velocity of $70\,\mu m.s^{-1}$ (see Section 2.4.3.3). It was shown in Section 2.4.3.1 that increase of flow velocity beyond $10\,\mu m.s^{-1}$ results in minimal changes in the process time (Figure 2.15). Assuming a constant flow velocity of $70\,\mu m.s^{-1}$ instead of the velocity

[4]- The flow rate resolution of the micropump used is $1\,\mu l/min$ and does not allow implementation of an exact flow velocity of $70\,\mu m.s^{-1}$.

range encountered in the micro flow cell ($11.14 \leq u_{avg} \leq 131.5$) results in less than 7% of variation in the process time (Figure 2.1). If the flow velocity was kept constant at $131.5\ \mu m.s^{-1}$, the process time would have been $29':8"$ or around 1% less than that of $70\ \mu m.s^{-1}$ (Section 2.4.3.1). On the other hand, if the flow velocity were a constant value of $11.14\ \mu m.s^{-1}$, then reaction would have been completed in $31':15"$ or 7% more than that of $70\ \mu m.s^{-1}$, with a process time of $29':22"$. Therefore, radial change of flow velocity imposes minimal impacts (less than 7%) on the kinetics, when the flow velocity is considered to be $70\ \mu m.s^{-1}$.

The other important geometrical differences between the two geometries which might impact the kinetics include the extension of the reaction surface by 8 times from $1500\ \mu m$ to $12000\ \mu m$, and the increase of channel height by about 7 times. The entrance region, immediate to the inlet is reasonably neglected here, as it is only 3% of the total surface area of the reaction surface (discussed before). It is worth noting that only half of the reaction surface length should be included in the calculations, because the micro-flow cell is axisymmetric. Despite these geometric differences in effect, calculation of the kinetic descriptive dimensionless numbers, such as Da and Pe, reveals that the simulation results presented in Chapter 2 can be reasonably used to predict the process time of the QCM micro-flow cell. The dimensionless kinetic representative numbers of the two geometries are summarized in Table 3.3 below.

Table 3.3: Dimensionless kinetic representative numbers for the HSP70 immunoreaction kinetics in two geometries: the microchannel considered in Chapter 2 (Figure 2.1) and the QCM micro-flow cell (Figure 3.9), $\boldsymbol{\theta_0 = 4.36 \times 10^{-11}, c_0 = 65.7\ nM}$.

	Flow velocity ($\mu m.s^{-1}$)	Damköhler number, $\mathrm{Da} = \frac{k_a \theta_0}{\frac{D}{h} + u_{avg}}$	Peclet number, $\mathrm{Pe} = \frac{u_{avg} h}{D}$	Binding capacity, $\epsilon = \frac{c_0 h}{\theta_o}$	Reaction/convention capacity, $\beta = \frac{k_a \theta_0}{u_{avg}(\frac{h}{l})}$
Fig. 2.1' kinetics	$u_{avg} = 70$	1.11×10^{-4}	70	59.4	6.34×10^3
Fig. 3.9' kinetics	$u_{avg} = 71.3$	1.10×10^{-4}	495.5	412.6	3.54×10^3

The main parameters that change among the two geometries are the microchannel height (h) and the reaction surface length (l), excluding flow velocity variations. The latter assumption is reasonable as the radial velocity change is expected to impose less than 7% of change on the reaction completion time, mentioned earlier in this section. Alteration of these parameters is expected to cause the following changes in the kinetics dimensionless numbers, according to Table 3.3 and the definitions given in Section 2.3:

1- The Damköhler number (Da), as the main kinetics predictive tool, does not change significantly here (Da~10^{-4}). Specially, since the average of flow velocity inside the micro-flow cell is around 70 $\mu m.s^{-1}$, the Damköhler number difference between the two geometries is less than 1% for the average velocity ($\mathrm{Da} = 1.1 \times 10^{-4}$). Therefore, the reaction-limited nature of the reactions does not vary and a noticeable kinetic property alteration is not expected.

2- The Peclet number linearly increases for around 7 times in average, from Figure 2.1 to Figure 3.9, due to increase of the microchannel height from 40 to 278 μm. In other words, in

the QCM micro-flow cell, convection has become about 7 times stronger (in average) than the previous geometry. In general, elevation of the Peclet number might result in a faster reaction. However, a considerable change in the reaction kinetics is not expected here. This expectation is reasonable because of the reaction-limitation encountered. In other words, the kinetics corresponding to Figure 2.1 had already employed the potential of convection for enhancing the kinetics ($\mathrm{Pe} = 70$), in a reaction-limited state dominated by convection (see Table 3.3). Thus, further increase in the convection weight (in micro-flow cell), compared to diffusion, cannot significantly alter the reaction progress rate. For the immunoreaction of HSP70, changing the microchannel height does not play an important role in the kinetics, as shown in Section 2.4.3.2.

3- The binding capacity (ϵ) is augmented by around 7 times by increasing the microchannel height. This variation is normally expected to results in a faster reaction; however, the binding capacity is still low ($\epsilon < 5 \times 10^2$). In Section 2.4.3.3, the analogous variations enough to alter the kinetics were at least four orders of magnitude, corresponding to an increase in θ_0 from 4.38×10^{-11} to $4.38 \times 10^{-7} mol.m^{-2}$. Accordingly, the change of binding capacity (ϵ), as a result of geometry changes here, is not expected to significantly change the immunoreaction kinetics of HSP70.

4- The reaction/convection capacity (β) in the QCM micro-flow cell is approximately half of that of the microchannel studied in Chapter 2. The lower β corresponds to an overall higher rate of convective transport strength in the QCM micro-flow cell with respect to reaction strength, compared to the other geometry. A higher convective mass transport strength is normally expected to result in better replenishment of the analytes on the reaction surface and accordingly a decreased process time. However, the kinetics is reaction-limited, which means the reaction progress rate is limited by the rate of reaction not the mass transport strength. Thus, the higher overall convective mass transport in the QCM micro-flow cell is not expected to result in a noticeably lower process time.

In conclusion, the overall kinetics is expected to experience minimal variations as a result of the geometry and flow velocity changes mentioned in this section. The latter expectation was confirmed by simulations, demonstrating around 6% of increase in the process time of the QCM micro-flow cell, compared to that of the hypothetical microchannel examined in Chapter 2.

Calculation and use of dimensionless numbers in prediction of the kinetic properties, exemplified above, can be safely implemented for kinetic design of any microfluidic HIA that is used to assay HSP70 with new reaction conditions other than those examined in Chapter 2. For kinetic predictions, there is no need to model the new reaction. Moreover, the numerical model constructed in Chapter 2 can be easily modified for other flow velocity ranges, concentrations, and kinetic properties of other proteins of interest. The generalization claimed here can be realized through calculation of the kinetic dimensionless numbers corresponding to the new reaction conditions, and by comparing them with their counterparts reported in the previous chapter. The results are quite outstanding here, as the level of change in geometry was extremely high: the microchannel height was increased by around seven times and the reactive length was stretched around one order of magnitude. As confirmed above, there is no need for the full-size computational modeling of the new reaction conditions. The modeling in full scale might be cumbersome, mainly due to the considerably increased computational effort needed. The generalization of simulation findings from Chapter 2 is experimentally strengthened and detailed in the following section.

3.3.3 Functionalization Protocol

The functionalization chemistry which was detailed in Sections 1.3.2.2 and 2.2.3.2 is schematically drawn here step by step in Figure 3.11. Clean QCM crystal was coated with thiol molecules to form the SAM. The fast-SAM technique was used, which involves the incubation of the QCM crystal in a $10\ mM$ 1-OT:11-MUA (3: 1) ethanol solution for a 15-minute period. Following the incubation, the crystal was rinsed gently with ethanol and DI water, and inserted into an aqueous solution of EDC and NHS for a one-hour incubation to allow for chemical modification of the 11-MUA head groups. Then, the crystal was rinsed in DI, dried with N_2, and inserted into the QCM flow cell. A $13\ mM$ PBS solution (pH=7.4) was used as the carrier fluid. PBS was pumped over the crystal at a rate of $7\ \mu L/min$, corresponding to an average flow velocity around $70\ \mu m.s^{-1}$, until a stable frequency baseline was obtained. The anti-HSP70 ($320\ \mu L$) was then injected into the sample loop through the injection port of the valve, and allowed to flow over the crystal for one hour at the same flow rate. Following the frequency response to the Ab conjugation with the SAM-coated crystal and the re-stabilization of the signal, HSP70 ($46.6\ \mu g/ml \equiv 65.7\ nM, 320\ \mu L$) was injected into the system at the same flow rate for one hour and the frequency response due to its immobilization was monitored.

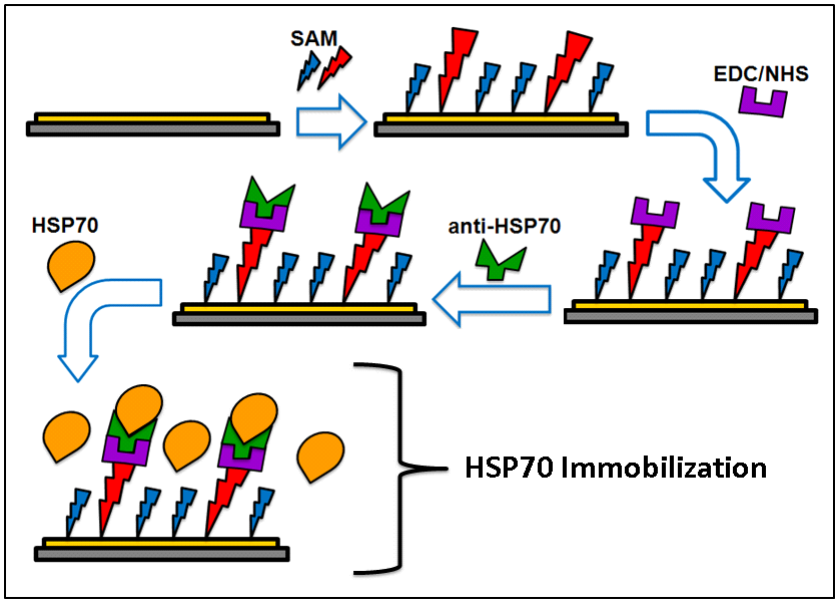

Figure 3.11: Step-by-step process of the functionalization for immobilization of HSP70 on the gold crystal surface, including: (i) thiol self-assembly, (ii) EDC/NHS activation of SAM, and (iii) anti-HSP70 conjugation, followed by HSP70 immunoreaction and immobilization on the crystal surface.

3.3.4 Frequency Data Analysis

Upon surface adsorption of the biomolecules to the crystal surface, the natural resonance frequency (f) of the crystal is changed, which can be correlated to the amount of mass deposited. The frequency response change recorded by the QCM (Δf) was used to calculate the mass change in unit area (Δm), due to the adsorption of molecules, via the Sauerbrey equation [168]:

$$\Delta f = -\Delta m / C \tag{3.1}$$

where C is the mass sensitivity constant ($C = 17.7\ ng \cdot cm^{-2} Hz^{-1}$ for a 5 MHz crystal) [169]. This relation holds only for systems in which the crystal mass is much greater than that of the adsorbed layers, the layers do not slip over the crystal surface, and are rigid and or thin enough so they do not trap fluid [170]. Protein layers lack rigidity [171-173], but they are semi-covalently bonded to the substrate, [10] and, as a result, have negligible slippage. Liquid is also trapped by adsorbed proteins [174, 175]; however, this error can be reduced by capacitance adjustments in the QCM. Moreover, relative frequency changes are concerned here rather than global values. On the other hand, the goal

of this study is not to determine exact amounts of molecules adsorbed, but to study the kinetic model predictions on the functionalization protocols, summarized in Section 2.6. Therefore, the above relationship can still be used.

3.3.5 Results and discussion

In this section, first the performance of the model predicted one-hour/5 mM anti-HSP70 conjugation process is experimentally accessed by measuring the loading density of anti-HSP70 on the QCM crystal. Moreover, the resulting HSP70 binding efficiency is calculated and the immunoreaction completion time is measured. The QCM experiments confirm an acceptable correlation between the model predictions and the experimental results for the HSP70 functionalization and immunoreaction kinetics.

3.3.5.1 Verification of the Model Predictions on the Optimal EDC Concentration

In Section 2.4.2, the kinetic properties of the conjugation reaction were numerically explored. According to the simulations results, typical EDC concentrations of 50-100 mM, used in conventional protocols, require less than 20 minutes for conjugation completion. However, conventional protocols often recommend a corresponding 1-3 hour process time for above concentrations (Figure 2.9) [12, 19]. This improper timing is expected to reduce the conjugation yield (Section 2.4.2). On the other hand, the predicted concentration for a one-hour process is 5 mM, expected to result in a higher than conventional conjugation efficiency.

This section examines the accuracy of the model predictions for conjugation conduction from an optimal EDC concentration of 5 mM. This concentration was shown by Fourier Transform Infrared (FT-IR) spectroscopy to result in a superior reaction yield, thus, higher Ab loading densities are expected compared to lower and higher concentrations of EDC. The process time in the above-mentioned study was kept constant at 90 minutes for all concentrations from 2 mM to 100 mM EDC solutions [151]. The 90-minute crosslinking process time is close to the model predicted 100-minute process for a 2 mM EDC concentration. On the other hand, a 90-minute process time is much more than needed for the higher concentrations (50 or 100 mM), according to our model predictions. This overexposure to cross-linking reagents may cause undesirable reaction paths with unwanted by-products and result in in lower crosslinking efficiencies and Ab loading densities. This section also examines the latter claim using QCM.

To assess the performance of the one-hour/5 mM EDC/NHS conjugation process, the resulting loading density of Ab was examined for a number of EDC concentrations, lower, higher and equal to the 5 mM concentration. An anti-HSP70 (Ab) concentration of 1 $\mu g/ml$ (dilution factor of 1: 1000) was used for conjugation with the SAM. The protocol described in Section 2.2.3.2 was used in activating the QCM quartz crystal for Ab conjugation using EDC concentrations of $0, 2, 5, 50$, and $100\ mM$. Other parameters are as follows: a 15-minute fast-SAM protocol was implemented for thiol self-assembly, NHS was used at the same concentration as EDC, and the incubation times were kept constant at one hour.

Figure 3.12 below presents the real-time frequency response plot of the anti-HSP70/SAM conjugation reaction, initiated for a number of EDC concentrations, and anti-HSP70 concentration of 1 $\mu g/ml$. Moreover, the immunoreaction of HSP70 with its immobilized Ab is plotted for a constant HSP70 bulk concentration of 4.6 $\mu g/ml$. Figure 3.13 represents the calculated mass loading density of anti-HSP70 and the HSP70 immobilized on the QCM crystal surface corresponding to each EDC concentration used. The results are also summarized quantitatively in Table 3.4, which includes the calculated mass loading densities for both anti-HSP70 and HSP70 at each concentration of EDC/NHS.

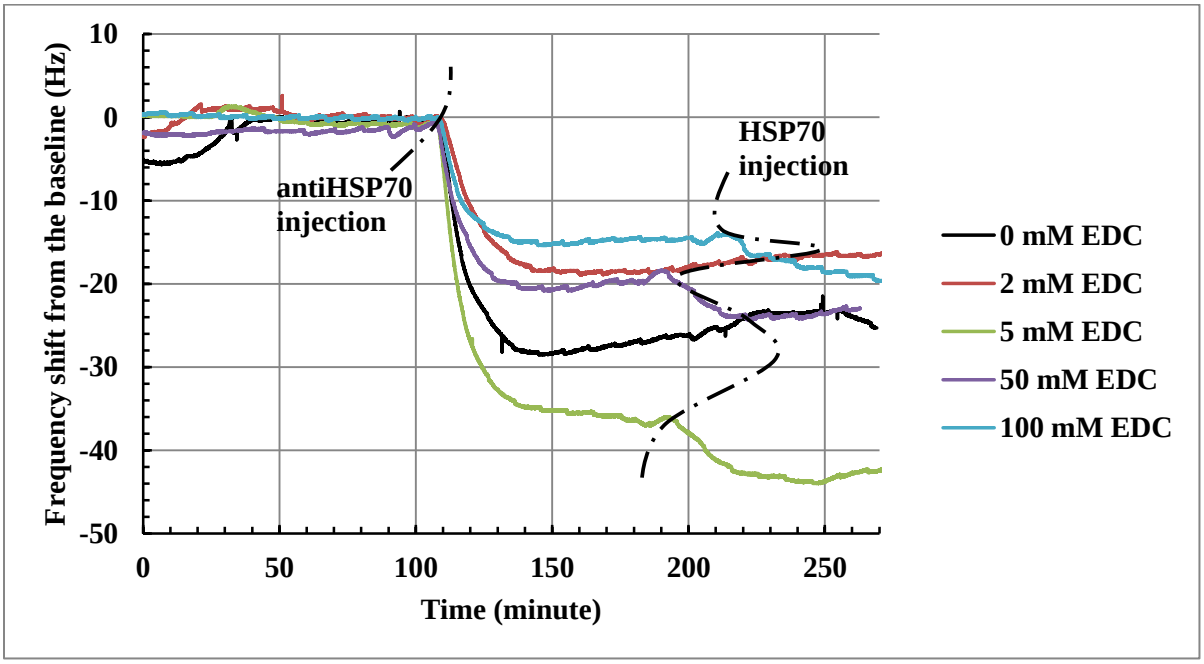

Figure 3.12: QCM frequency response plots of anti-HSP70 conjugation and HSP70 binding for different EDC concentrations. The first drop in frequency corresponds to the anti-HSP70/SAM conjugation reaction, and the second drop is due to the immunoreaction of HSP70 with anti-HSP70. The maximum drop in resonance frequency or maximum binding of proteins occurs for an EDC concentration of 5 mM. The baseline resonance frequency obtained before antibody injection was 5×10^6 Hz.

As shown in Figure 3.12 and Figure 3.13, conjugation from a 5 mM EDC solution results in optimal Ab and protein mass densities on the QCM crystal, i.e., $617 \pm 9\, ng/cm^2$ and $100 \pm 20\, ng/cm^2$, respectively. At an anti-HSP70 mass loading density of $617\, ng/cm^2$, a complete Ab monolayer emerges on the SAM. The latter event occurs because a monolayer mass density of $200 - 550\, ng/cm^2$ is reported for similar immunoglobulin G (IgG) proteins [176]. The mass density depends on the orientation of the Ab, with two possible options: flat-on and end-on. The flat-on orientation results in lower densities compared to the end-on situation [176]. This loading density shows that the anti-HSP70 layer is densely packed with an end-on orientation, remains highly active, and allows for the large HSP70 binding density. Moreover, the rather high mass density of the Ab on the quartz crystal surface implies that the fast-SAM protocol was quite successful in forming a high quality self-assembled monolayer over the gold surface of the QCM crystal. The most important conclusion from the highest level of Ab-loading density achieved here, is that 60 minutes is enough

for the completion of the conjugation process from an EDC/NHS concentration of $5\,mM$, in agreement with the numerical prediction.

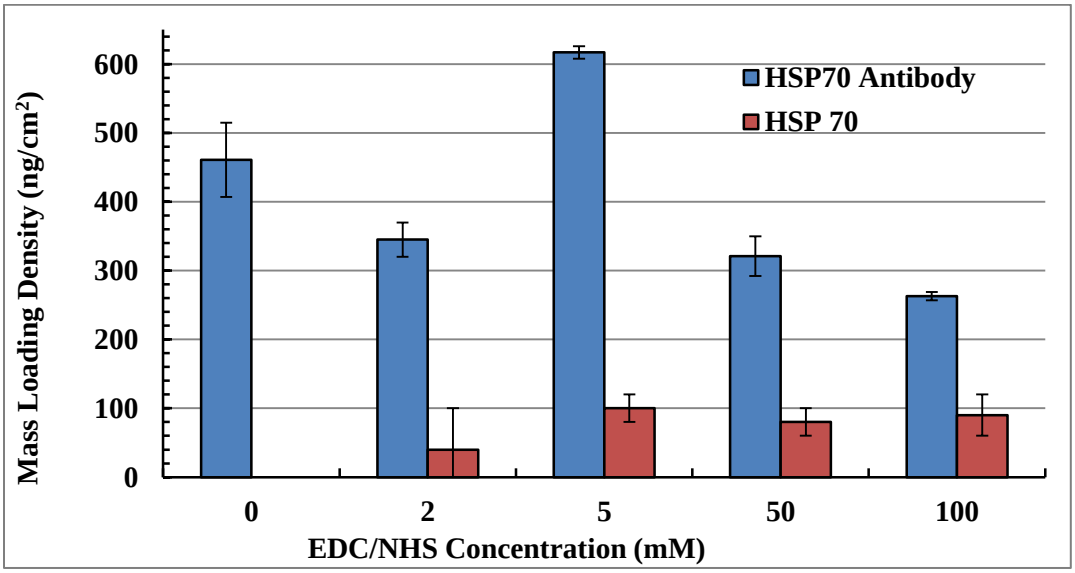

Figure 3.13: Average mass loading density of antibodies immobilized on the QCM crystal, corresponding to each EDC concentration. The highest mass density for both anti-HSP70 and HSP70 binding is demonstrated to be for the 5 mM EDC concentration, determined to result in optimal reaction condition. Standard deviation above and below the average for three trials is shown by error bars.

Figure 3.13 shows that HSP70 binding efficiency strongly depends on the EDC concentration. Ab binding performed with no chemical modification by EDC ($0\,mM$) resulted in a surprisingly high anti-HSP70 mass density of $461 \pm 54\,ng/cm^2$. However, the immobilized Abs were not able to later bind HSP70 from the bulk fluid. This observation can be attributed to the existence of the SAM/anti-HSP70 binding through a combination of other non-covalent effects, such as hydrophobic, electrostatic or hydrogen bonding forces [177]. The same observation has been reported for human IgG adsorption to CH_3-terminated SAMs, in which a high binding density of $239\,ng/cm^2$ was demonstrated [177]. Despite the Ab binding observed for the $0\,mM$ EDC concentration, the lack of HSP70 binding in the subsequent step is indicative of an inactive Ab, immobilized perhaps due to denaturation or poor orientation that leads to steric hindrance. As noted above, the trend seen in the $0\,mM$ case for the Ab and protein binding can also be explained by considering the possible electrostatic binding between Ab and the SAM-modified crystal surface. LSPR spectroscopy studies

have shown that the carboxylic acid group of 11-MUA can be deprotonated when the SAM is subjected to an alkaline pH and moderately low concentration of ions; such conditions are present in this experiment using the PBS buffer. The presence of a shorter methyl-terminated thiol, such as 1-OT here, facilitates the deprotonation, since the steric hindrance and hydrogen bonding between the neighboring end carboxylates is eliminated by the dilution of 11-MUA in the monolayer. In such situations, the carboxylic groups of 11-MUA and the amino acid groups of Ab gain oppositely charged states and form ion pairs, which leads to their electrostatic bonding [11]. Although the Ab/SAM binding is present in the $0\,mM$ case, Figure 3.12 and Figure 3.13 show that there is negligible or no subsequent Ag (HSP70) binding present. This finding further strengthens the notion of electrostatic bonds between Abs and SAM over the sensor surface, without the semi-covalent bonding mediated by EDC. Compared to semi-covalent bonds resulted from the EDC mediation, electrostatic bonds are often relatively weak and may not withstand the rinsing process before or after the Ab/Ag binding [1, 19]. The EDC/NHS zero crosslinking protocol outlined in Section 2.2.3.2 results in semi-covalent link formation between the SAM and Ab [19]. Accordingly, the presence of EDC/NHS is vital to produce a semi-covalent bond between the Ab and the SAM, and therefore, to maintain a so called active Ab on the bio-interface for subsequent protein-binding steps.

The other EDC/NHS concentrations ($2\,mM$, $50\,mM$, and $100\,mM$) resulted in protein binding that occurred in the subsequent step but did not demonstrated favorable Ab mass densities. The $2\,mM$ EDC sample showed an improved Ab binding ($345 \pm 25\,ng/cm^2$) compared to 50 and $100\,mM$ samples, but inferior protein binding ($40 \pm 60\,ng/cm^2$) with much larger variability. Significant HSP70 mass densities of $80 \pm 20\,ng/cm^2$ and $90 \pm 30\,ng/cm^2$ were observed from the conjugation with EDC concentrations of $50\,mM$ (Ab density: $321 \pm 29\,ng/cm^2$) and $100\,mM$ (Ab-loading density: $263 \pm 6\,ng/cm^2$), respectively. In order to further understand the trends observed here for the different EDC/NHS concentrations, the reaction between the EDC/NHS and the carboxyl groups of 11-MUA, and the possible by-products, must be considered. For the $2\,mM$ EDC/NHS sample, Ab binding is considerable ($345 \pm 25\,ng/cm^2$), however, the protein binding is inferior to that of higher EDC/NHS concentrations. As detailed in Section 2.4.2.1 and noted earlier in this section, FT-IR studies has revealed that at EDC/NHS concentration of $2\,mM$, unreacted acid groups and anhydride by-products were present on the surface, after a 90-minute process [151]. Presence of these chemicals suggests an incomplete reaction, as more than 90 minutes have been needed for the conjugation completion, i.e., 100 minutes was predicted. In the QCM experiments

conducted here, the process time is 40 minutes less than the required 100-minute period. Therefore, electrostatic binding of the Ab to the SAM might have happened. In other words, there was not enough time to form a complete semi-covalently bound Ab layer on top of the SAM to reliably immobilize HSP70. In any case, the $2\,mM$ sample was able to bind HSP70, because at least a considerable proportion of the Abs were semi-covalently bound to the SAM and remained active. At 50-100 mM, urea by-products were present [151], implying possible overexposure to crosslinking reagents due to a prolonged process. The QCM results here indicate that the uric chemical by-products formed might have imposed a negative effect on the Ab conjugation efficiency. However, the effect was not observed to be detrimental to the process success, and moderate protein binding was detected. In the $2\,mM$ EDC/NHS experiment, almost the same level of Ab binding was seen as in the 50 and $100\,mM$ tests. However, a large variability in HSP70 binding was present, which might possibly be due to the unwanted, non-covalent interaction of the Abs with the unreacted acid groups and anhydride by-products present on the surface, at this specific concentration [151]. As mentioned before, non-covalent bonds are often relatively weak and unreliable, and as a result, they may not withstand the rinsing process before or after the Ab/Ag binding [1, 19]. No chemical by-products were detected at the $5\,mM$ concentration of EDC/NHS [151]. Among all the concentrations the $5\,mM$ sample displayed the most effective Ab and HSP70 binding. This observation strengthens the presence of a complete conjugation for the $5\,mM$ case, as this concentration lead to the highest Ab and protein mass density.

Table 3.4: QCM frequency response to the binding of anti-HSP70 to the SAM, followed by HSP70 binding to a functionalized gold-coated crystal at different concentrations of EDC/NHS. The anti-HSP70 concentration was held constant at a $1\,\mu g/ml$, and the HSP70 concentration was constant at $4.6\,\mu g/ml$. Standard deviation above and below the average for three trials is reported for each entry.

EDC/NHS concentration (mM)	Anti-HSP70 binding (Hz)	Anti-HSP70 loading density (ng/cm^2)	HSP70 binding (Hz)	HSP70 loading density (ng/cm^2)
0	26.1 ± 3.04	461 ± 54	0.00 ± 0.00	0 ± 0
2	19.5 ± 1.41	345 ± 25	2.3 ± 3.3	40 ± 60
5	34.9 ± 0.49	617 ± 9	5.8 ± 0.83	100 ± 20
50	18.2 ± 1.63	321 ± 29	4.4 ± 0.99	80 ± 20
100	14.9 ± 0.35	263 ± 6	4.9 ± 1.8	90 ± 30

3.3.5.2 Verification of the Model Prediction on the Immunoreaction Completion Time

In Section 2.4.3, the effects of main kinetic parameters on the immunoreaction progress rate were explored, including protein concentration and flow rate. The immunoreaction completion time was simulated for a practical input concentration range of Ags between 1-100 nM. Significant flow-rate dependences were observed for all concentrations. Using a flow velocity of 150 $\mu m.s^{-1}$, the process times were decreased by at least one order of magnitude, at each concentration, illustrated in Figure 2.14. Associated kinetic properties of a representative Ag concentration of 65.7 nM were examined in more detail, studying the flow rate effects on the transient process, and the steady state kinetics. It was shown that increasing the flow velocity beyond approximately 70 $\mu m.s^{-1}$ might not necessarily lead to significant steady state or transient kinetic improvements. Beyond this velocity the dimensionless surface concentration of bound Ags (c_s^*) differ by less than 1% on average between the curves at each moment (Figure 2.16). An optimum immunoreaction completion time of around 29 minutes ($T_{comp} = 29':22"$) was predicted for a flow velocity of 70 $\mu m.s^{-1}$, and an input HSP70 concentration of 65.7 nM (4.6 $\mu g/ml$). This process time provides a considerable time saving compared to the conventional 4-12 hour processes [20, 28], to be experimentally verified in this section.

In the previous section, the suggested conjugation protocol and main model findings were examined using the QCM method, which at the same time involved real time monitoring of the HSP70 binding to its Ab. Clearly, the results of the conjugation verification experiments for the 5 mM EDC/NHS protocol can also be used to verify the model predictions on the proposed 29-minute HSP70 kinetics.

In Figure 3.14 below, the QCM frequency response to the sequential binding of anti-HSP70 and HSP70 is plotted again. An EDC/NHS concentration of 5mM was used along with the Ab and HSP70 concentrations of 1 $\mu g/ml$, and 4.6 $\mu g/ml$, respectively.

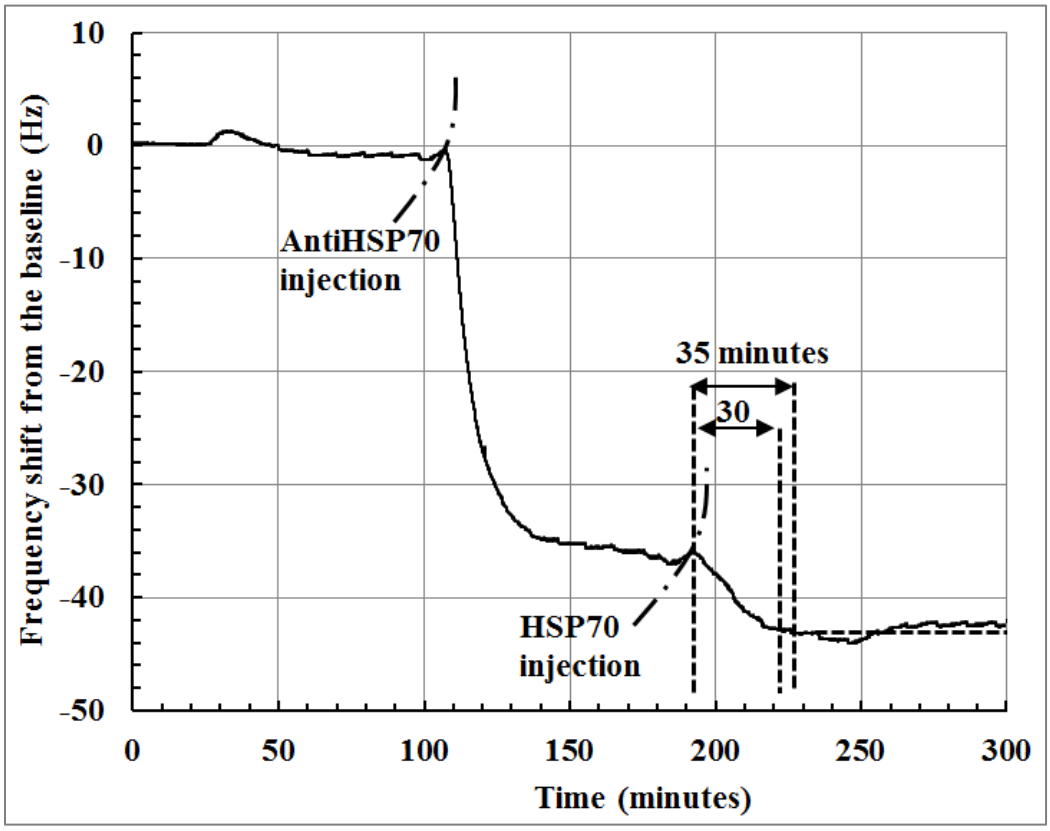

Figure 3.14: The QCM frequency response plot of the anti-HSP70/HSP70 binding for a $65.7\ nM$ protein concentration and a flow velocity of 70 $\mu m.s^{-1}$. The first drop in frequency corresponds to the anti-HSP70/SAM conjugation reaction, and the second drop is due to the immunoreaction of HSP70 with anti-HSP70. The immunoreaction is observed to finish by around 30-35 minutes. The baseline resonance frequency obtained before antibody injection was 5×10^6 Hz .

Figure 3.14 shows that the QCM resonance frequency drops immediately after the HSP70 injection, and after 30-35 minutes reaches a stable value. This amount corresponds to the resonance frequency of the HSP70-loaded crystal, previously functionalized with the Ab-conjugated SAM. The reason behind the fluctuations observed might be the minute temperature fluctuations in the lab during the experiment, although the variation is around $2\ Hz$. The resonance frequency does not change much after 30-35 minutes, even after running the buffer fluid in the system for one hour. This observation suggests that the immunoreaction was completed by the end of 30-35 minutes, which is very close to the model' predicted value of 29 minutes.

The agreement between the model predictions on the kinetics and experiments was expected and confirms the flexibility of the model in prediction of the HSP70' kinetic properties. There are a number of reasons that can justify the above claim. First of all, the kinetic rate constants used in the model were adopted from reasonably accurate SPR kinetic experiments for the HSP70, available in the literature [31, 155] (Section 2.4.3). Secondly, the probe (Ab) loading density is kinetically optimal ($\theta_0 \sim 10^{-11}\, mol.m^{-2}$) and results in a reasonably fast immunoreaction (~ 30 minutes- Section 2.4.3.3). On the other hand, the functionalization of a bio-interface with such Ab-loading density leads to a relatively stable kinetics with respect to possible flow velocity fluctuations (Section 2.4.3.3) that happen during the experiment. In addition, through calculation of kinetic dimensionless numbers it was shown that the HSP70 kinetic is nearly independent from the geometric property changes (Section 3.3.2), which might be present in the micro-flow cell. These facts all add to the flexibility of the model constructed in Chapter 2 for predicting the kinetics of HSP70 in real experimental conditions, such as the QCM micro-injection setup implemented in this chapter. It is also worth noting that the focus of this thesis was not studying the reaction rate constants, but rather enhancing the kinetics of conventional functionalization protocols for assaying proteins (exemplified by HSP70 here). The aim was enhancing the kinetics of the reaction at each stage of the functionalization process, while keeping the reagent consumption reasonable.

3.4 Summary

This chapter examines the modified functionalization protocols, which was suggested in Chapter 2. The modified protocols allow for optimal functionalization of a microfluidic HIA, with enhanced reaction kinetics and minimal protein consumption levels. Experiments were conducted to assess and compare the performance of the modified protocols with respect to conventionally employed counterparts. In this regard, the following processes were examined: the self-assembly of thiols on gold, the anti-HSP70/SAM conjugation, and the HSP70 immunoreaction.

The proposed 15-minute/10 mM thiol fast-SAM protocol demonstrated the same or close Ab-binding capability as the conventional 24-hour self-assembly process. The fast-SAM protocol was examined through assessment of the resulting loading density of the following analytes:

- Biotin/streptavidin: binding characterization performed by LSPR spectroscopy of nanoparticles,
- Tetramethyl-rhodamine conjugated polyclonal goat gamma globulin: binding assessment was conducted via epi-fluorescence microscopy and AFM,
- Anti-HSP70/HSP70: binding efficiency was examined by QCM technique.

For HSP70 experiments, the Ab mass density was superior to the loading density of the same Ab using conventional SAM techniques, suggesting that the fast-SAM protocol have resulted in the same or better quality relative to the conventional protocol.

The proposed one-hour/5 mM EDC conjugation protocol was proven successful in the immobilization of anti-HSP70 on the surface of QCM gold-coated quartz crystals. The resulting Ab mass density was very close or superior to the Ab mass densities that resulted from the conventional one-hour/100 mM EDC protocol. Moreover, the resulting HSP70 binding was comparable or superior to the corresponding results of the conventional protocols.

This chapter also investigates the generality of the modeling techniques and predictions of Chapter 2 for being extended and used in microfluidic HIAs. Kinetic descriptive dimensionless numbers such as the Damköhler number and the Peclet number were calculated and used to forecast general kinetic behavior of HSP70 immunoreaction in a micro-flow cell. For this purpose, the kinetic dimensionless numbers of the new case were compared to those of a hypothetical microchannel, modeled in Chapter

2. Analysis of the kinetic dimensionless numbers was proven effective in prediction of the kinetic properties, and then the model main forecast, i.e., the immunoreaction completion time, was experimentally verified using a micro-fluid injection QCM setup. Optimal conditions for the immunoreaction, proposed in Chapter 2, were applied in the QCM experiments, including employment of the fast-SAM protocol, a one-hour/5mM EDC anti-HSP70 conjugation protocol, and 70 $\mu m.s^{-1}$flow velocity. The QCM frequency response was shown to reach its plateau in around 30-35 minutes which was very close to the model predicted process time of $29': 22"$.

Chapter 4
Conclusions and Future Work

4.1 Conclusions and Contributions of This Thesis

This thesis has been devoted to the improvement of the kinetics of in-situ functionalization protocols for immobilization of proteins in heterogeneous immunoassays (HIAs), for biosensing applications. The thesis is composed of two main parts: in the first part (Chapters 2), a numerical model is constructed to study the kinetics of main reactions involved in the functionalization and analyte-binding stage of a microfluidic-based HIA. The following reactions are examined: the SAM formation, the Ab/SAM conjugation, and the HSP70' immunoreaction. Development of numerical models for studying the kinetics of the first two reactions is among major contributions of this thesis. The numerical studies target both minimal process times and reagent-consumption levels. The second part (Chapter 3) is devoted to a step-by-step verification and application assessment of the main model predictions, including a considerably faster than conventional SAM formation protocol, an Ab/SAM conjugation protocol with superior reaction yield, and an optimal HSP70 immunoreaction process. Specifically, the major conclusions and contributions of this thesis are as follows:

1- The numerical study of the thiols' microfluidic self-assembly process is the first kinetic study on the field (Chapter 2). The simulation findings can be used to modify the microfluidic and conventional methods of thiol self-assembly. Self-assembly kinetics of thiols in a microchannel was modeled for different input thiol concentrations, flow velocities, microchannel heights and thiol final loading density on gold. In the following, the most important findings are presented:

   a) The most effective tool for enhancing the SAM-formation kinetics is increasing the input thiols' concentration, which, if properly adapted ($10\ mM$), can reduce the self-assembly completion time from the conventional 24-hour incubations to 15 minutes (fast-SAM protocol).

   b) The flow-velocity increase does not lead to a considerably faster overall reaction. Upon increasing the flow rate from zero to even $1000\ \mu m.s^{-1}$, the reaction completion time is at best improved by 16%, and by less than 7% on average, across all the thiol concentrations considered in this thesis.

c) The microchannel height does not play a significant role in the kinetics. For microchannel heights exceeding a few micrometers, increase of height cannot decrease the reaction completion time by more than 1% at each moment.

d) The thiol packing density or the surface concentration of available self-assembly sites on the reaction surface (θ_0), does not noticeably affect the self-assembly kinetics. Packing density decrease, even for two orders of magnitude from $\theta_0 = 7.3 \times 10^{-9} mol.m^{-2}$, enhances the kinetics by less than 1% at each moment.

2- The feasibility of the fast-SAM protocol was successfully studied by protein conjugation on the SAMs formed according to the protocol. The resulting SAM was able to bind proteins with the same quality as the SAM formed according to conventional protocols. The fast-SAM protocol was examined by binding a fluorescent protein to the SAM-coated gold surfaces, using fluorescent microscopy and AFM (Chapter 3). Moreover, the protein binding was monitored in real time using QCM technique. This fast 15-minute protocol is promising in clinical and analytical applications to reduce the lengthy process times associated with conventional 24-hour thiolic SAM formation protocols.

3- To best of our knowledge, the zero-length crosslinking reaction for the Ab/SAM conjugation in microfluidic systems is modeled in this thesis for the first time. This part of the thesis deals with the EDC mediated binding of amine-containing molecules, such as antibodies, to carboxylic acids, such as the 11-MUA thiol molecules used in this research. The Ab conjugation reaction was studied against the fluidic and geometrical parameters mentioned above for SAM kinetics, and the most important findings are summarized as follows:

a) The model-predicted, zero-flow conjugation completion time for the 5 mM EDC samples agrees with the conventional process times that suggest a conjugation time of around 60 minutes. However, for higher EDC concentrations, such as $100\,mM$, the numerical findings deviate from the conventionally recommended process times. The deviation implies that in conventional processes, the reaction surfaces were probably over-exposed to the reagents, leading to lower conjugation yields (Chapter 2).

b) The flow velocity increase can substantially enhance the kinetics. Use of the flow-through mode, even for a velocity of $15\ \mu m.s^{-1}$, decreases the process time by about one order of magnitude.

c) The microchannel height does not play an important role in the kinetics. For microchannel heights exceeding a few micrometers, increase of height cannot decrease the reaction completion time by more than 1% at each moment (as is the case with SAM's kinetics).

d) The SAM's practical packing densities and the resulting Ab surface loading densities do not play an important role in the conjugation kinetics, similar to that of the self-assembly kinetics (mentioned above). Decrease (or increase) of the final Ab packing density (θ_0), even for two orders of magnitude from $\theta_0 = 4.38 \times 10^{-11} mol.m^{-2}$, enhances (or decelerates) the kinetics by less than 1% at each moment.

4- The proposed possibility of overexposure to the crosslinking reagents and the resulting conjugation yield decrease was experimentally proved. For this purpose, anti-HSP70 was conjugated to a SAM-coated QCM crystal, with varied EDC concentrations and a constant conjugation termination time (60 minutes) predicted by the model. The conjugation success level was examined by calculating the resulting Ab mass density on the QCM crystal. The results were indicative of an optimal conjugation protocol from a $5\,mM$ EDC sample, with superior Ab immobilization capabilities and highest amount of HSP70/Ab binding (Chapter 3).

5- To find the optimal kinetic performance of a microfluidic-based HSP70 HIA, the immunoreaction of HSP70 in a hypothetical microchannel has been numerically investigated. The simulations examined the main fluidic and geometric parameters listed for the SAM and Ab-conjugation kinetics. The HSP70' immunoreaction kinetics includes the following important characteristics:

a) Contrary to the SAM and conjugation kinetics, for practical Ag concentrations between 1-100 nM, the Ag (HSP70) never binds all the binding sites (anti-HSP70s) immobilized on the surface, irrespective of the reaction time. In other words, there are always a number of free binding sites (Abs) available on the surface, depending on the initial concentration of Ag (HSP70) in the bulk.

b) The flow velocity increase substantially enhances the immunoreaction kinetics. Use of the flow-through mode, even for a low flow velocity of 2.5 $\mu m.s^{-1}$($2.5 \leq u_{avg}^{low} \leq$

$150\ \mu m.s^{-1}$), has substantially decreased the process time, by around one order of magnitude, compared to the zero-flow mode.

c) As with the SAM and conjugation kinetics, the microchannel height does not much affect the kinetics. Increasing the height above $10\ \mu m$, cannot enhance the kinetics by more than 1% at each moment. This finding provides an embodied flexibility for the design of microfluidic systems.

d) Contrary to the SAM and conjugation kinetics, higher Ab loading densities ($4.38 \times 10^{-9} < \theta_0^{high} \leq 4.38 \times 10^{-7} mol.m^{-2}$) bring about considerably slower kinetics ($30 < T_{comp} < 166$ minutes), necessitating higher flow velocities ($u_{avg}^{high} \geq 1500\ \mu m.s^{-1}$) to maintain reasonably fast kinetics (T_{comp}~30 minutes). Increased flow velocities are associated with correspondingly higher protein consumption and elevated costs of experiments.

6- Based on the numerical simulations, the optimal range of Ab-loading density is proposed: $4.38 \times 10^{-11} \leq \theta_0 \leq 4.38 \times 10^{-9}\ mol.m^{-2}$. In this range, the kinetics can be enhanced by the flow-through mode using the lowest possible increase in HSP70 consumption, while keeping the detection signal reasonably rich. Interestingly, this range includes the Ab-loading density ($\theta_0 = 4.38 \times 10^{-9}\ mol.m^{-2}$) that resulted from the functionalization method employed in this research through thiolic SAM functionalization and zero-length carbodiimide Ab conjugation.

7- In the optimal anti-HSP70 loading density described above, the optimal flow velocity was numerically shown to be around $70\ \mu m.s^{-1}$, exhibiting the best transient process and also minimal long term immunoreaction completion time. Increasing the flow velocity beyond this amount does not result in a noticeable decrease in the process time.

8- Kinetic descriptive dimensionless numbers, including Damköhler, Peclet, and binding capacity, have been employed to generalize the above simulation findings. This generalization can be used for overall kinetic predictions in practical experiments involved in microfluidic-based HIAs.

9- The applicability of the above kinetic simulation findings and the kinetic dimensionless numbers have been successfully proved by examining the HSP70 immunoreaction in a QCM

micro-flow cell. The reaction was conducted according to the model predictions, including the 15-minute /10 mM SAM protocol, Ab conjugation performed from a one-hour/5 mM EDC protocol, and flow velocity kept at 70 $\mu m.s^{-1}$. The resulting immunoreaction completion time was around 30-35 minutes, very close to the model-predicted completion time of around 29 minutes.

4.2 Proposed Extensions of the Thesis Work

Suggestions for extending the current work are briefly addressed below in two general categories:

1- **Continuing research on enhancing the kinetics of conventional and fast SAM protocols**: In this research, the success of the fast-SAM protocol was indirectly examined by immobilization of proteins on the SAM, and measurement of the resulting protein loading densities. However, the indirect approach does not provide a clear understanding on the reaction mechanism and possible chemical paths of the reaction. In this regard, the experimental results conducted here were indicative of unknown trends in the thiol self-assembly reaction. Slightly more than conventional Ab loading densities was observed during the characterization the fast-SAM protocol. Possibly, carboxyl-ended thiols (11-MUA) lose their activity in the prolonged conventional SAM formation processes due to the oxidation, or desorb from the surface to be replaced by other spacer thiols (1-OT). To examine this speculation, it is required to assess the chemical decomposition of SAM-coated surfaces over time, using techniques such as, x-ray photoelectron spectroscopy (XPS) [175, 178]. On the other hand, one can conduct and characterize the fast-SAM protocol directly with techniques such as, surface plasmon resonance (SPR), and possibly investigate the model findings for the flow-through mode as well. SPR allows for real time monitoring of binding or surface reaction events such as chemisorption of thiols on gold surfaces [144, 147].

2- **Enhancing the kinetics of antibody/SAM conjugation using microfluidics**: Using the flow-through mode, i.e., convection assisted analyte transport in addition to diffusion, was numerically shown to have a great potential for enhancing the Ab-conjugation kinetics (Chapter 2). In other words, achieving a considerably faster reaction is feasible by employment of microfluidics. In Chapter 3, an optimum one-hour/5 mM EDC mediated conjugation process was successfully tried. As predicted by the FEM model, the mentioned process time can be potentially reduced for more than one order of magnitude to 4 minutes, using the flow through mode with a typical flow velocity of around $15\ \mu m.s^{-1}$. Therefore, research on enhancing the conjugation kinetics moves forward greatly, if the potential of microfluidics can be employed. In parallel to the enhancement of the kinetics, it is also vital to determine the resulting reaction paths and chemical by-products to assess the performance of kinetically enhanced processes, using techniques such as FT-IR spectroscopy [151].

Appendix A
Substrate Cleaning Protocol and Analysis

Generally, three major cleaning procedures are implemented for cleaning gold substrates in biosensors: alcohol-based cleaning, piranha-based cleaning, and incubation of the substrate in a heated piranha solution [179]. The alcohol-based protocol is selected here due to its satisfactory performance, as well as technical and safety issues. It is shown that the alcohol-based cleaning protocol results in the same or a higher level of protein immobilization on gold than the piranha-based cleaning protocol's [179]. Alcohol-based cleaning is time consuming; however, the alcohol based protocol does not entail the hazards associated with piranha [180, 181]. In the alcohol-based method, the gold substrate is washed with a sequence of alcohols to remove its hydrophilic and hydrophobic contaminants [36]. Here, the procedure developed by Park et al. [179] is employed for planar gold with the addition of hexane to ascertain the removal of hydrophobic contaminants [36].

Substrate Cleaning Procedure

The cleaning procedure consists of 2-minute rinsing with pure ethanol, followed by 2-minute hexane wash, then, a brief rinse with ethanol followed by a 10-minute acetone wash, and then 2-minute ethanol, and finally, IPA wash for 2 minutes. Finally, all the surfaces are thoroughly rinsed with de-ionized (DI) water and dried with a stream of nitrogen gas.

Surface Cleaning Characterization

Using AFM imaging, the gold substrate surfaces were examined before and after the cleaning procedure. Figure A.1 shows that alcohol-based cleaning altered the topography of the gold surface. Due to the cleaning, the root-mean-square (r_q-rms) roughness [161] of the gold was reduced from $1.72 \pm 0.01\ nm$ in the untreated gold surface to $1.12 \pm 0.01\ \ nm$. Moreover, the mean roughness (r_a) changed from $1.34 \pm 0.01\ nm$ in untreated gold to $0.78 \pm 0.01\ nm$ after the cleaning. The difference is attributed to the accumulation of contaminants that were adsorbed to the gold surface and washed during the cleaning procedure.

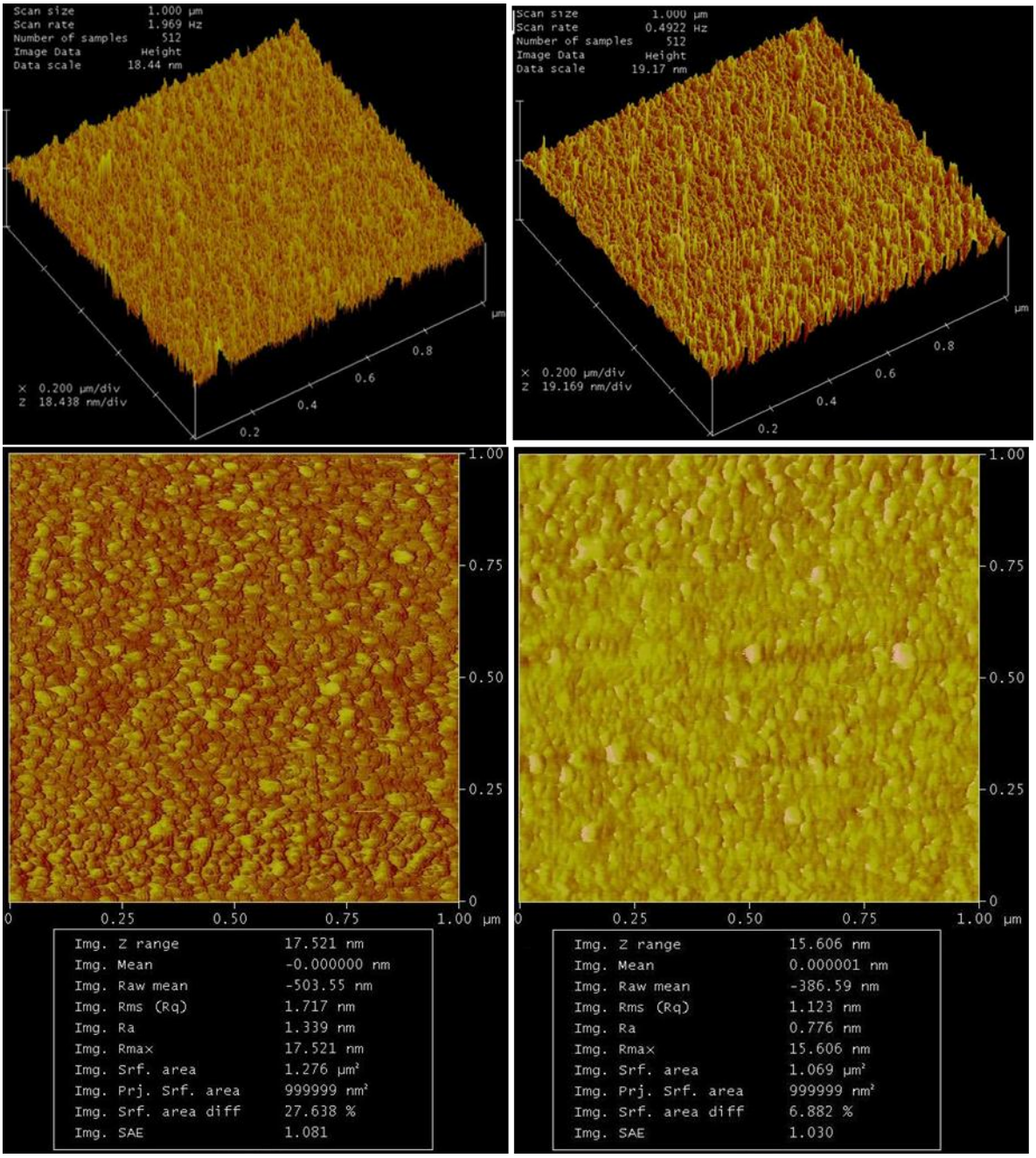

A.1: AFM images of the untreated gold before (left) and after alcohol-based cleaning procedure (right): the surface roughness is decreased due to the cleaning.

Appendix B
Thiols Conventional Self-assembly Protocol and Analysis

Self-assembly Procedure

Immediately after the cleaning step, the gold substrate should be treated with the self-assembly solution in order to prevent spontaneous adsorption of contaminants, especially adventitious hydrocarbons [36, 182]. Straight chain thiols, among them those chosen for this research, could "scrub" these hydrocarbon impurities from the surface due to the high affinity of their sulphur groups to gold [182]. Despite this ability, initializing the self-assembly on a fresh, clean surface is still recommended for formation of a defect free SAM [36, 182, 183].

The planar gold substrates were incubated in the $15\ ml$ of $1\ mM$ $(1:3)$ solution of 11-MUA and 1-OT in ethanol. The $(1:3)$ ratio was chosen to avoid steric hindrance and also to provide proper support for the thiol with the carboxylic functional group, i.e., 11-MUA [11, 38]. The volume of thiol solution is much higher than the volume of the reaction boundary layer at the gold surface, supposedly with a thiol concentration gradient. Therefore, it is reasonable to assume a constant thiol concentration above the substrate [36]. To prevent oxidation of SAM, and because of safety issues, the immersed gold substrates were left in a tightly capped vial, under the fume hood. The self-assembly was terminated after 24 hours by rinsing the gold substrate with copious amounts of ethanol and drying with nitrogen gas. Since SAMs are highly prone to oxidation when subjected to air, the SAM was used immediately after formation for Ab conjugation or kept in backfilled nitrogen vials for no more than 72 hours.

SAM Characterization

SAM-coated chips were examined by AFM following the self-assembly process. The results were compared with the AFM images captured in the cleaning step. Figure B.1 shows that the cleaned gold substrate ($r_q = 1.12 \pm 0.01$) were less rough than the SAM-covered gold ($r_q = 1.21 \pm 0.01$). The topographical properties of the gold substrate were changed after the self-assembly process (Figure B.1). Thus, an additional second layer is formed on the surface of the cleaned gold substrate, which is attributed to the chemisorption of the thiols (compare Figure A.1 and Figure B.1). The topographic changes observed here follow the same trend as those reported in the literature [161]. It is worth

noting that the trends observed are mainly concerned here rather than the global values. The difference in the values reported here and those stated elsewhere is due to the difference in the initial roughness of the gold substrate used [161, 184].

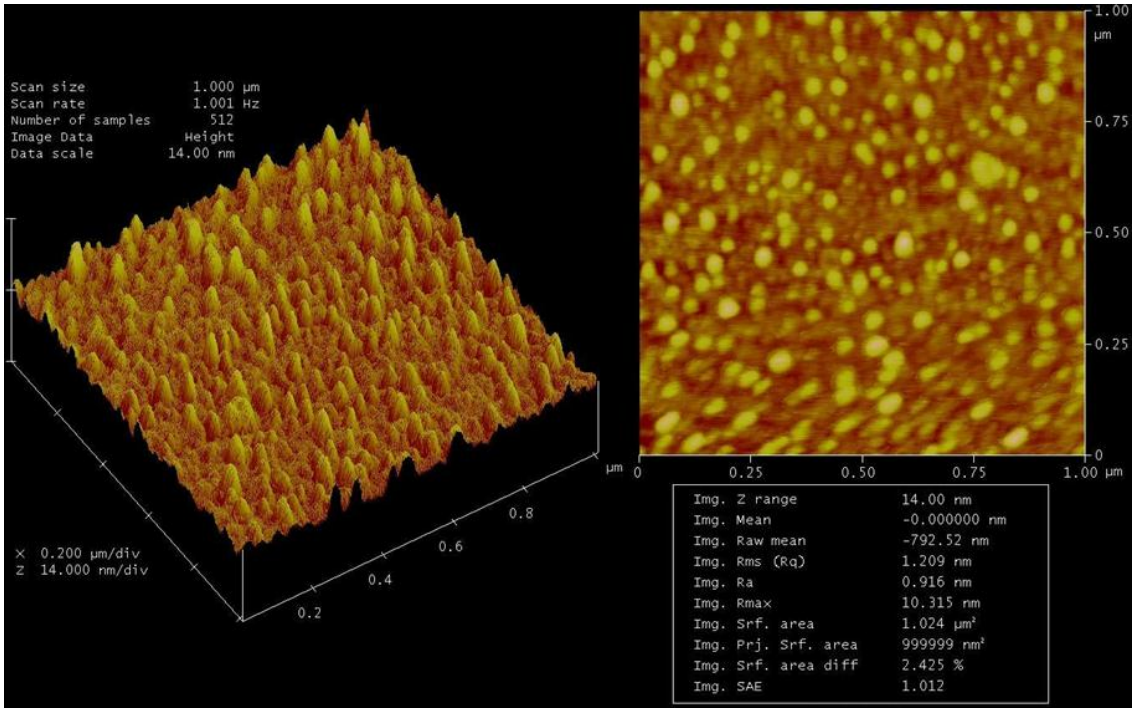

Figure B.1: AFM image of the SAM on gold, the cleaned gold substrate ($r_q = 1.12 \pm 0.01$) is less rough than the SAM-covered gold ($r_q = 1.21 \pm 0.01$).

Table B.1 below summarizes the functionalization characterization results outlined in Appendix A and B.

Table B.1: Surface topographic properties before and after SAM formation, addition of layers increased the roughness (measurments in nm).

Surface	r_a (mean roughness)	r_q (RMS roughness)
Untreated gold	1.34 ($\pm$0.01)	1.72 ($\pm$0.01)
Cleaned gold	0.78 ($\pm$0.01)	1.12 ($\pm$0.01)
Cleaned gold [161]	0.79	0.98
SAM (Thiols)	0.92 ($\pm$0.01)	1.21 ($\pm$0.01)

Appendix C

Antibody/SAM Conventional Conjugation Protocol and Analysis

Antibody/SAM Conjugation

Just after the completion of SAM formation, the chip was immersed in an activating buffer. The activating buffer consisted of a PBS solution with a pH of 7.4 and concentration of $50\ mM$. $100\ mM$ of EDC was also dissolved in the buffer. In order to verify the Ab/SAM conjugation protocol, a fluorescently labeled protein, tetramethyl-rhodamine conjugated goat immuno gamma globulin (RFP), was dissolved in the activating buffer. Using the fluorescent protein enables visualization of the conjugation results under a fluorescent microscope. The maximum concentration of the protein was $0.05\ mg/ml$.

The chip immersed in the activating buffer was kept at $-4℃$ overnight. The following day, the chip was rinsed with copious amounts of $10\ mM$ PBS and dried; after which, the chip was ready for characterization.

Antibody/SAM Conjugation Characterization

Fluorescent microscopy and AFM are used to characterize the conjugation protocol implemented, and the experimental work is detailed in the following sections.

Fluorescent Microscopy

The number of fluorescent spots observable and their distribution over the surface reflect the success of the conjugation protocol used. The fluorescent microscopy revealed two issues in the functionalization protocol: precipitation and a lower-than-expected number of fluorescent spots detectable.

The first obstacle to overcome is the precipitation of the fluorescent Abs and crystallization of the buffer salts on the chip surface, illustrated in Figure C.1 below. The maximum amount of precipitation was observed at the boundary of the solution-chip interface where the conjugation reagents were dropped on the chip surface. To limit this edge-precipitation, the rate of evaporation from the chip surface was controlled by containing the chip-conjugation reagents in a wet capped vial

during the crosslinking process. A microscope glass slide cover slip was laid on the chip surface to further reduce the surface evaporation and minimize the Ab consumption.

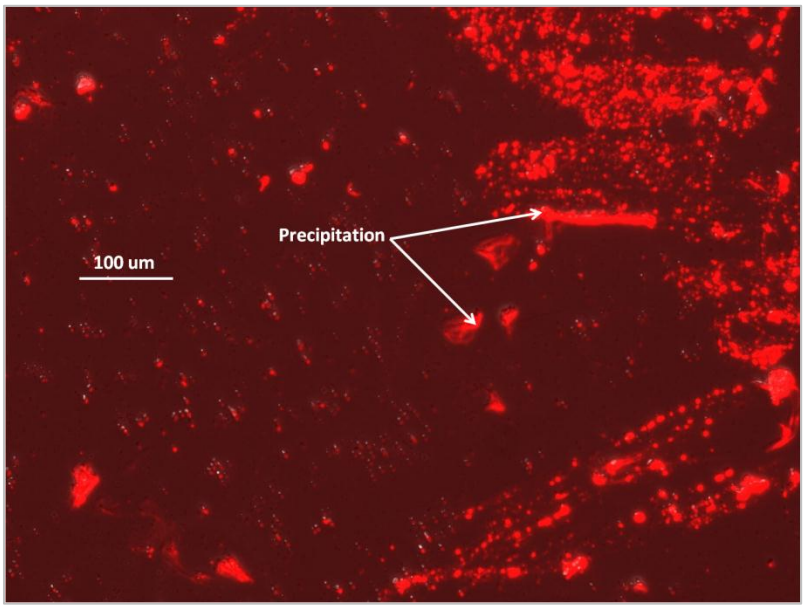

Figure C.1: Precipitation on the chip surface, fluorescent image captured from immobilized RFPs on the SAM coated gold chip.

Although the control of surface evaporation improved the quality of the Ab immobilization (compare Figure C.1 and Figure C.2), the precipitation problem was not completely eliminated. Experimental studies on amide bond formation confirm an inevitable intrinsic level of precipitation associated with EDC chemistries due to the presence of both carboxylic and amine groups in Abs [19], mentioned in Section 1.3.2.2. To keep the precipitation level minimal, lowering the concentration of EDC from the initial value ($100\,mM$) is suggested, until precipitation is nearly eliminated [19]. However, since the control of surface evaporation resulted in satisfactory precipitation control here, the concentration of EDC was not changed from the original value of $100\,mM$.

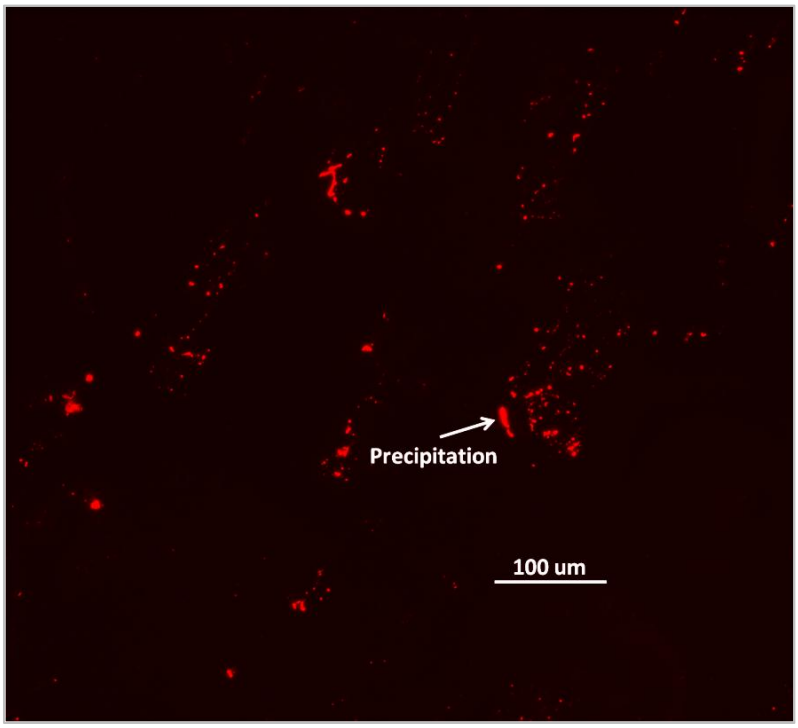

Figure C.2: Less precipitation due to a lowered evaporation rate

The second aim of conjugation characterization is to determine the strength of the immobilization protocol used by counting the number of Abs bound to the chip surface. Two regions of the chip were chosen as representative areas, and the number of fluorescent spots was counted there (Figure C.3). The regions chosen were the areas with the minimum or maximum density of Abs detectable, along with the least amount of precipitation present. By visual inspection, the lower middle left corner of Figure C.3 has the smallest number of fluorescent spots and was chosen as the representative area of minimum immobilization strength. The upper middle right corner is the representative area for the maximum binding density. The number of shiny spots with maximum detection resolution of 1.1 μm [185] was counted in a $50\,\mu m \times 50\,\mu m$ square, and approximately 20-45 fluorescent spots were detectable.

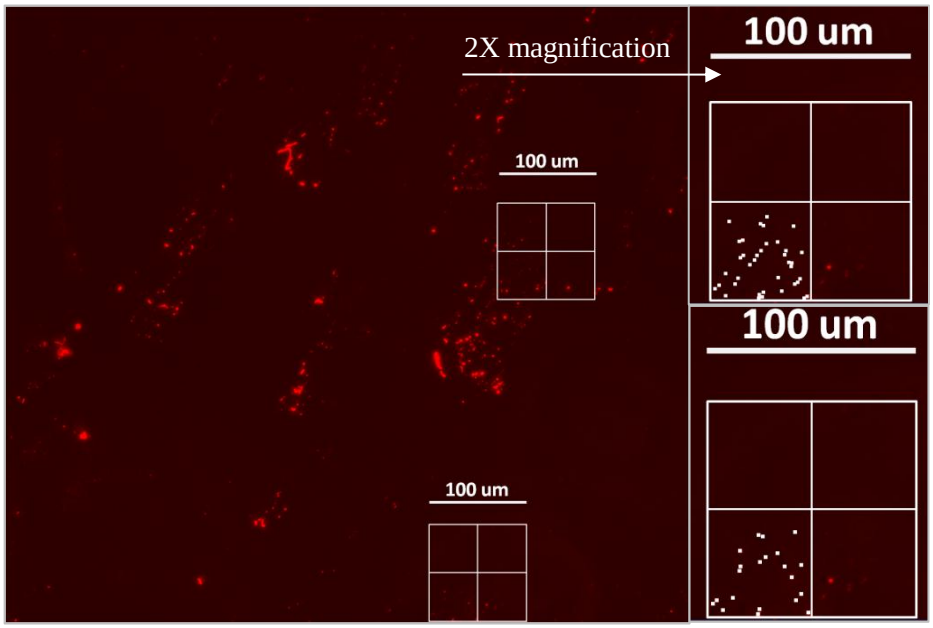

Figure C.3: Immobilization strength; the antibodies are colored with white dots and counted in two representative precipitation free areas. 20-45 shiny spots were resolved in each $50\mu m \times 50\mu m$ area.

While the existence of fluorescent spots corresponds directly to the immobilization of Abs on the surface, they are not each related to a singular Ab. The latter speculation is valid because the upper resolution limit of the microscope used is $1.1\,\mu m$ [185], and it cannot resolve a single Ab that requires a mean precision of about $14\ nm$ [186]. The fluorescent spots are thus attributed to a dense accumulation of Abs (cluster) attached to the surface. The clustering occurs because the conjugation chemistry used can attach Abs together [19], as explained in Section 1.3.2.2.

The resulting surface loading density of Abs is comparable to the corresponding protein loading density reported in the literature. The EDC conjugation chemistry is reported to have a yield of 1-5% in the present reaction environment [19]. Therefore, the total surface concentration of the available sites for Ab immobilization is between $7.3 \times 10^{-13}\ to\ 3.65 \times 10^{-12}\ mol.m^{-2}$, corresponding to 250-1250 binding events in an $50\mu m \times 50\mu m$ area. Here, 20-45 shiny spots were resolved in each $50\mu m \times 50\mu m$ area. It is proposed that the fluorescent spots detected here (Figure C.3) are Ab clusters that have been crosslinked to each other and also to the surface. The detected clusters are at least $1.1\ \mu m$ in width Figure C.3). Since each RFP is around $14\ nm$ width [162, 163], it is estimated that each cluster contains at least around 80 immobilized Abs. Therefore, a rough estimate of the

number of crosslinked Abs within each cluster is approximately 1600 - 3600 Abs in each $50\mu m \times 50\mu m$ area. This value is above the corresponding literature predictions (250-1250) [19]; however, because of possible clustering events, the number of Abs bound to the surface might be lower than 1600-3600. Since the RFPs are roughly 14 nm width [162], they are, in principle, only detectable by AFM or spatially modulated illumination (SMI) microscopes [187, 188]. Figure C.4 shows the distribution of single florescent proteins over the surface, captured by an ultra-sensitive SMI microscope with a resolution limit of 10 nm [186].

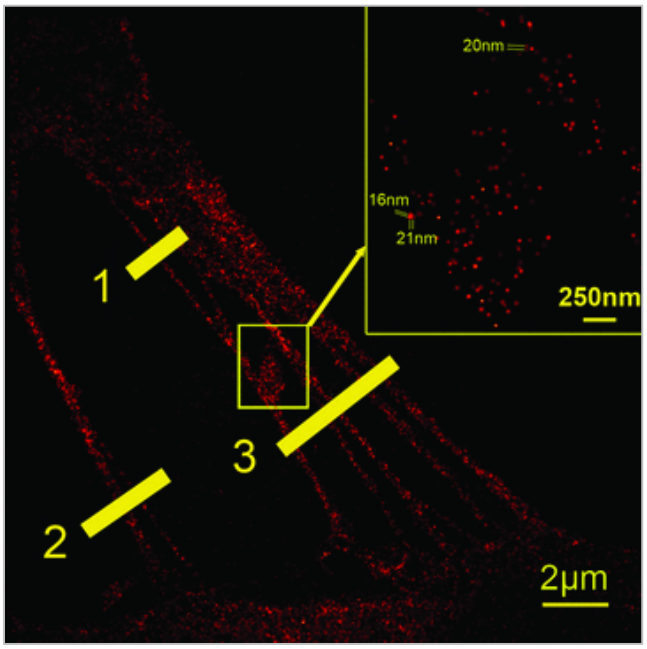

Figure C.4: Single fluorescent protein imaging, RFPs are roughly 14 nm width. Reprinted with permission from [186].

In those regions of the chip where no shiny spot is detectable, no conclusions can be made regarding the strength of the immobilization protocol. Nevertheless, as shown in Figure C.3, the protocol effectively produced a strong bond between the carboxylic group of SAM and the amine group of Ab. On the other hand, visual counting of the binding events cannot provide a qualitative scientific conclusion about the immobilization protocol. High resolution imaging has not been conducted here; however, the existence of Abs was examined through AFM imaging. This characterization method strengthens the results of fluorescent microscopy. In Chapter 3, a more rigorous method for characterization of Abs' loading density is presented through employment of QCM technique.

Appendix D

Exploded Drawing of the Micro-flow Cell

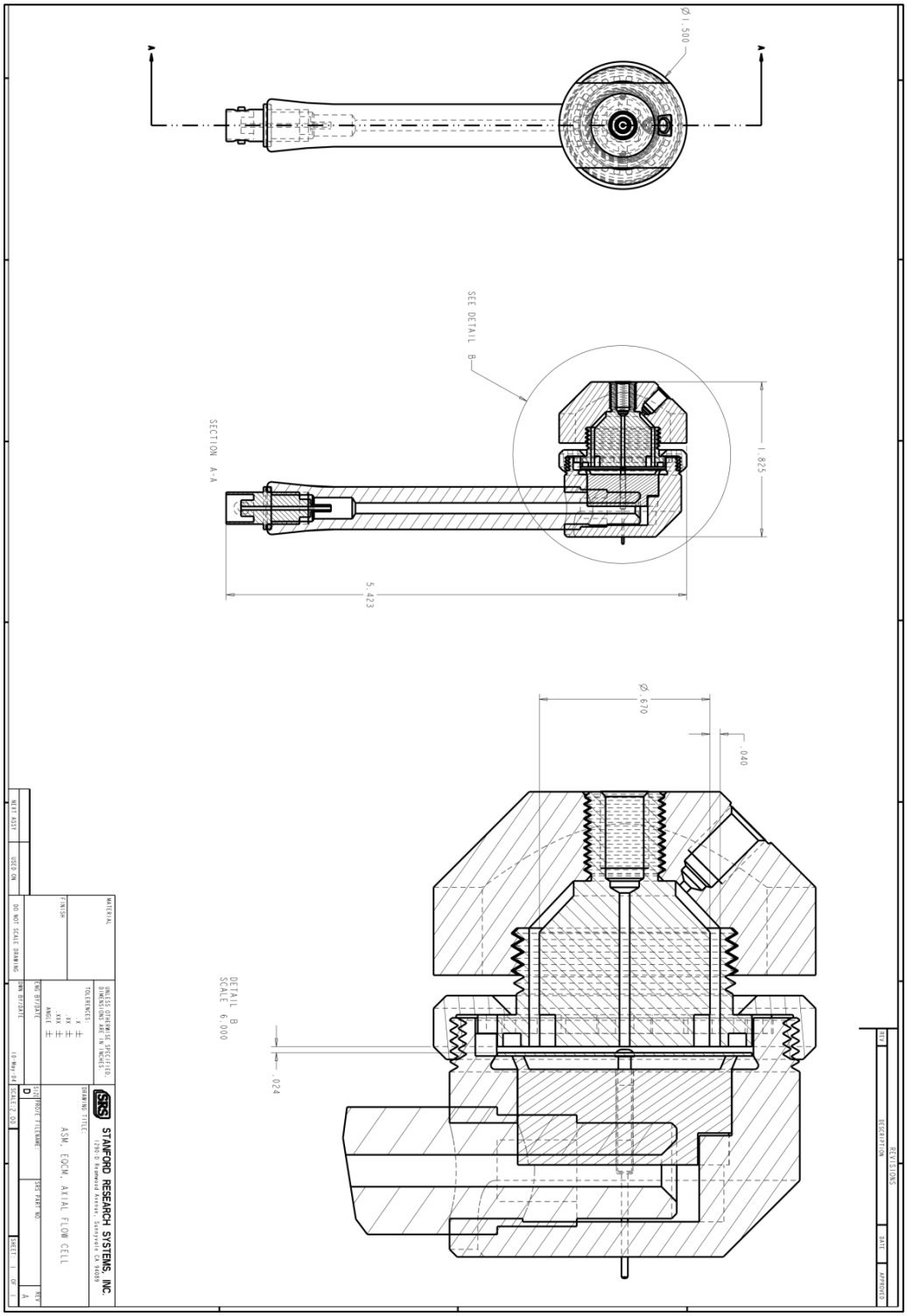

Appendix E

COMSOL 3D Simulations of Immunoreaction Kinetics

The following figures show the distribution of flow velocity (u) and dimensionless surface concentration of antigens (c_s^*), generated on the surface of the QCM crystal presented in Figure 3.9.

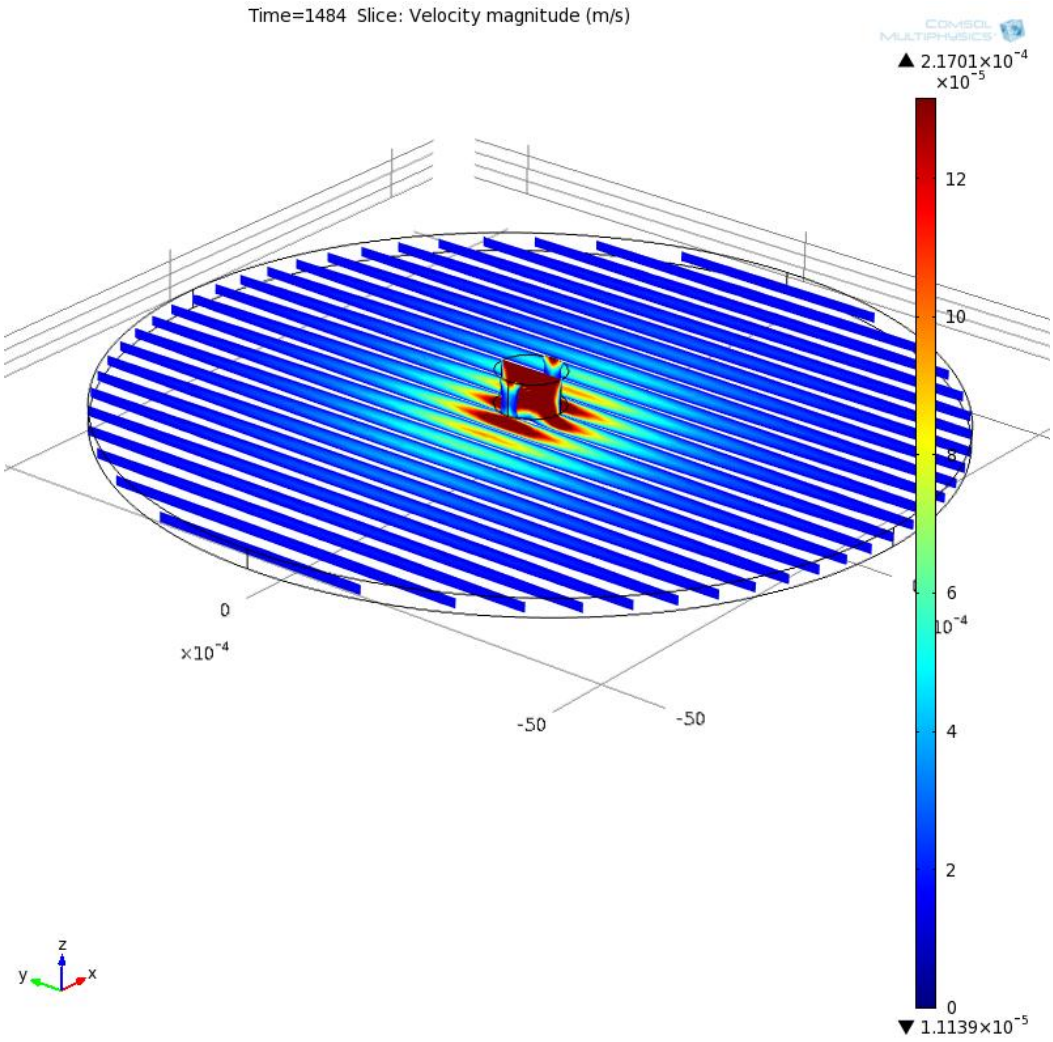

Figure E.1: Simulated velocity distribution in the QCM micro-reaction chamber, illustrated in hypothetical planes parallel to the YZ plane. At each plane, velocity profile reaches its maximum at the mid-plane of the QCM micro-reaction chamber. Velocity decreases in the radial direction. An inlet flow rate of 7 $\mu l.min^{-1}$ results in a maximum mid-plane velocity of around $16.7\ \mu m.s^{-1}$ at the outlet. The average cross-sectional velocity is $11.14\ \mu m.s^{-1}$ at the outlet.

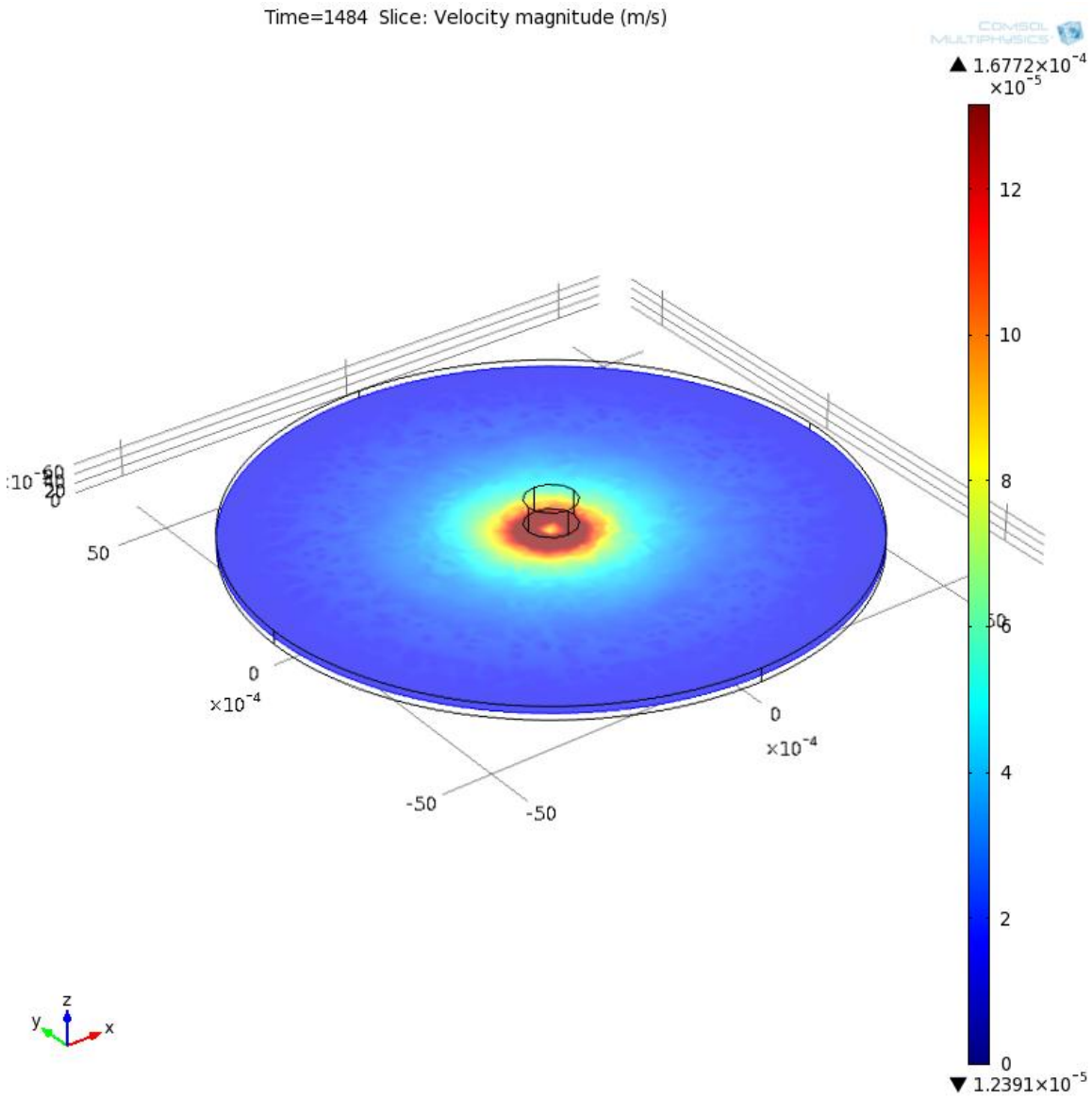

Figure E.2: Simulated velocity distribution in the mid-plane of the QCM micro-reaction chamber. Velocity decreases in the radial direction. An inlet flow rate of 7 $\mu l.min^{-1}$ results in a maximum mid-plane velocity of around 16.7 $\mu m.s^{-1}$ at the outlet.

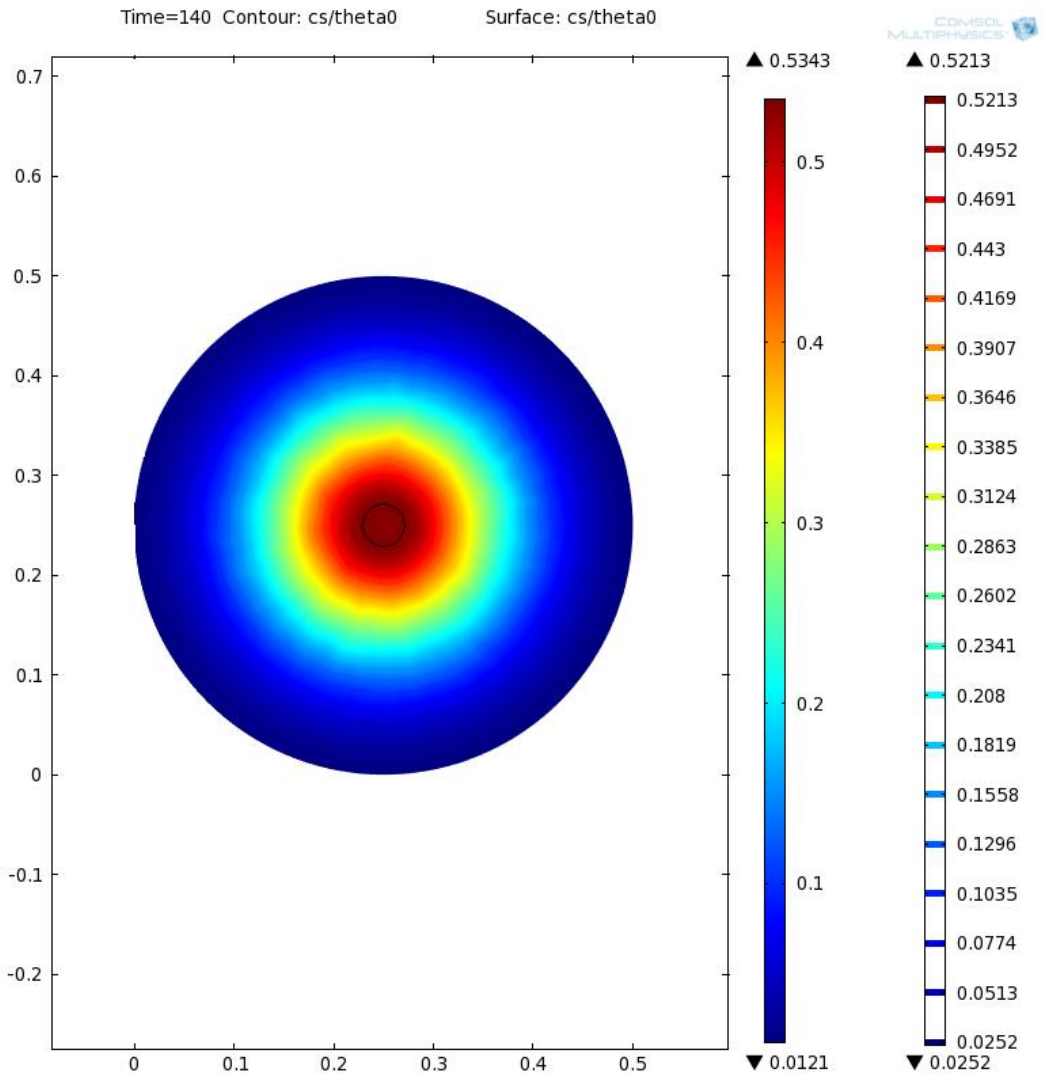

Figure E.3: Simulated radial distribution of the dimensionless surface concentration of antigens ($c_s^* = c_s . \theta_0^{-1}$) over the QCM crystal at $t = 140$ seconds. The reaction progress rate decreases in the radial direction, which is the direction of the flow. The inlet concentration of antigens is $65.7\ nM$, and the expected surface concentration of bound antigens at the completion of the reaction is $c_s^* = 0.54$.

Appendix F
List of Publications

Journal Papers ready for submission (under supervisor's review):

- Sasan Asiaei, Patricia Nieva, "Modeling of self-assembled monolayers fast formation kinetics in microchannels," to be submitted to the *microfluidics and nanofluidics, Springer* (Section 2.4.1).
- Sasan Asiaei, Patricia Nieva, Mathilakath M. Vijayan, "Self-assembled monolayers' fast kinetics of adsorption on gold, modeling and confirmation by protein binding," to be submitted to the *ACS Journal of Physical Chemistry B* (Section 3.2.2).
- Brendan Smith, Ryan Denomme, Sasan Asiaei, Mathilakath M. Vijayan, Patricia Nieva "Development and optimization of a label-free heat shock protein 70 immobilization protocol using a quartz crystal microbalance," to be submitted to the *Biosensors and Bioelectronics* (Section 3.3).

Journal papers under preparation:

- Sasan Asiaei, Patricia Nieva, "Increasing the binding rate of 70kDa heat shock proteins to its immobilized antibody in microfluidics systems through enhancing the conjugation rate of antibodies, numerical modeling of conjugation kinetics and characterization by quartz crystal microbalance," (Sections 2.4.2 and 3.3).
- Sasan Asiaei, Patricia Nieva, "Modeling and optimization of 70kDa heat shock proteins immunoreaction kinetics in microfluidic immunoassays, finite element modeling and characterization by quartz crystal microbalance," (Sections 2.4.3 and 3.3).

Conference Proceedings

- Sasan Asiaei, Ryan. C. Denomme, Chelsea Marr, Patricia. M. Nieva and Mathilakath. M. Vijayan Patricia Nieva, Mathilakath M. Vijayan, "Fast self-assembly kinetics of alkanethiols on gold nano-particles via microfluidic localized surface plasmon resonance spectroscopy," in SPIE: Microfluidics, BioMEMS, and Medical Microsystems, San Francisco, California, USA, 2012, pp. 825107. (Section 3.2.1).

Permissions

The permission/licence acquired for reprinting Figure 1.2, adapted from [9]:

Title: Self-Assembled Monolayers of Thiolates on Metals as a Form of Nanotechnology
Author: J. Christopher Love et al.
Publication: Chemical Reviews
Publisher: American Chemical Society
Date: Apr 1, 2005
Copyright © 2005, American Chemical Society
Logged in as: Sasan Asiaei, Account# 3000556552

Permission/license is granted for your order at no charge

This type of permission/license, instead of the standard Terms & Conditions, is sent to you because no fee is being charged for your order. Please note the following:

- Permission is granted for your request in both print and electronic formats, and translations.
- If figures and/or tables were requested, they may be adapted or used in part.
- Please print this page for your records and send a copy of it to your publisher/graduate school.
- Appropriate credit for the requested material should be given as follows: "Reprinted (adapted) with permission from (COMPLETE REFERENCE CITATION). Copyright (YEAR) American Chemical Society." Insert appropriate information in place of the capitalized words.

One-time permission is granted only for the use specified in your request. No additional uses are granted (such as derivative works or other editions). For any other uses, please submit a new request.

The licence acquired for reprinting Figure 1.3, adapted from [19]:

ELSEVIER LICENSE

This is a License Agreement between Sasan Asiaei ("You") and Elsevier ("Elsevier") provided by Copyright Clearance Center ("CCC"). The license consists of your order details, the terms and conditions provided by Elsevier, and the payment terms and conditions.

- All payments must be made in full to CCC. For payment instructions, please see information listed at the bottom of this form**.**

Supplier	Elsevier Limited The Boulevard,Langford Lane Kidlington,Oxford,OX5 1GB,UK
Registered Company Number	1982084
Customer name	Sasan Asiaei
Customer address	200 University Avenue west Waterloo, ON, N2L 3G1
Licence number	2982460849542
License date	Sep 05, 2012
Licensed content publisher	Elsevier
Licensed content publication	Elsevier Books
Licensed content title	Bioconjugate Techniques
Licensed content author	Greg T. Hermanson
Licensed content date	2008
Number of pages	2
Start page	213
End page	214
Type of use	reuse in a thesis/dissertation
Portion	figures/tables/illustrations
Number of figures/tables/illustrations	1
Format	Both print and electronic
Are you the author of this Elsevier chapter?	No
Will you be translating?	No
Title of your thesis/dissertation	Microfluidic-based In-Situ Functionalization for Detection of Proteins in Heterogeneous Immunoassays
Expected completion date	Sep 2012
Estimated size	127
Permission price	00.00

The permission acquired for reprinting Figures 3.1 and 3.2, adapted from [158]:

From: Ryan Denomme <rdenomme@uwaterloo.ca>, Date: January 13, 2013

Subject: Re: A question for referencing your thesis

Sent to: Sasan Asiaei <sasiaei@engmail.uwaterloo.ca>

Hi Sasan,

Yes, I give you permission to use those 2 figures in your thesis given you reference my thesis as the source.

Thanks,

Ryan

From: sasiaei@engmail.uwaterloo.ca, Date: January 13, 2013

Subject: A question for referencing your thesis

Sent to: Ryan Denomme <rdenomme@uwaterloo.ca>

Dear Ryan,

Hope everything is going well on your side.

I am currently modifying my thesis for final submission to UW-Space. As I have talked and showed you my thesis, I have referred to your thesis (in my thesis) in the following pictures:

1- Figure 3.1 (in my thesis): Photograph of the gold nanoparticle chip ... ., Reprinted with permission from [158].

2- Figure 3.2 (in my thesis): Schematic of the LSPR micro-injection analysis setup.... ., Reprinted with permission from [158].

- [158] refers to your thesis.

I am wondering to know if that is fine with you that I include the above mentioned pictures from your thesis with above mentioned referrals (in my thesis).

Thank you,

Sasan

The permission acquired for reprinting Figures 3.2, 3.3, 3.4 and Table 3.1, adapted from [159]:

From: Scott McNeill <scottm@spie.org>, Date: August 1, 2012

Subject: Re: Reprint permission request

Sent to: Sasan Asiaei <sasiaei@engmail.uwaterloo.ca>

Dear Sasan Asiaei,

Thank you for seeking permission from SPIE to reprint material from our publications. As an author of the cited work, you retain co-owner rights to the original content therein. Publisher's permission is hereby granted under the following conditions: (1) the material to be used has appeared in our publication without credit or acknowledgment to another source; and (2) you credit the original SPIE publication. Include the authors' names, title of paper, volume title, SPIE volume number, and year of publication in your credit statement.

Sincerely,

Scott McNeill for

Eric Pepper, Director of Publications

SPIE

P.O. Box 10, Bellingham WA 98227-0010 USA

360/676-3290 (Pacific Time) eric@spie.org

From: sasiaei@engmail.uwaterloo.ca, Date: July 29, 2012

Subject: Reprint permission request

Sent to: reprint_permission@spie.org

Dear Sir./Madam.,

I am wondering if you would please process my permission request to reprint from the following paper in the SPIE proceedings, in which I was the first author:

- Title: "Fast self-assembly kinetics of alkanethiols on gold nanoparticles: simulation and characterization by localized surface plasmon resonance spectroscopy (Proceedings Paper)"
- Volume, issue, and page numbers: 8251-pages: 825107

- What you would like to reproduce: Figures: 1, 2, 4, and table 1
- Where you will republish the requested material: In my PhD thesis

Thank you,
Sasan Asiaei

The licence acquired for reprinting Figure C.4, adapted from [186]:

JOHN WILEY AND SONS LICENSE

This is a License Agreement between Sasan Asiaei ("You") and John Wiley and Sons ("John Wiley and Sons") provided by Copyright Clearance Center ("CCC"). The license consists of your order details, the terms and conditions provided by John Wiley and Sons, and the payment terms and conditions.

- All payments must be made in full to CCC. For payment instructions, please see information listed at the bottom of this form.

Licence number	2958280777039
License date	Jul 29, 2012
Licensed content publisher	John Wiley and Sons
Licensed content publication	Journal of Microscopy
Licensed content author	P. Lemmer, M. Gunkel, Y. W Eiland, P. Müller,D. Baddeley, R. Kaufmann, A. Urich, H. Eipel, R. Amberger, M. Hausmann, C. Cremer
Licensed content date	Jul 24, 2009
Start page	163
End page	171
Type of use	Dissertation/Thesis
Requestor type	University/Academic
Format	Both print and electronic
Portion	figure/table
Number of figures/tables/illustrations	1
Original Wiley figure/table number(s)	Figure 3
Will you be translating?	No
Will you be translating?	No
Order reference number	N/A
Total	0.00 USD

References

[1] E. Gizeli and C. R. Lowe, *Biomolecular Sensors.* London, New York: Taylor & Francis, 2002.

[2] J. March, *Advanced Organic Chemistry: Reactions, Mechanisms, and Structure.* New York; Toronto: Wiley, 2007.

[3] J. Liu, C. Hansen and S. R. Quake, "Solving the "World-to-Chip" interface problem with a microfluidic matrix," *Anal. Chem.,* vol. 75, pp. 4718-4723, 09/01, 2003.

[4] G. S. Fiorini and D. T. Chiu, "Disposable microfluidic devices: fabrication, function, and application," *BioTechniques,* vol. 38, pp. 429-446, 2005.

[5] K. G. Olsen, D. J. Ross and M. J. Tarlov, "Immobilization of DNA hydrogel plugs in microfluidic channels," *Anal. Chem.,* vol. 74, pp. 1436-1441, 03/01, 2002.

[6] R. A. Zangmeister and M. J. Tarlov, "DNA displacement assay integrated into microfluidic channels," *Anal. Chem.,* vol. 76, pp. 3655-3659, 07/01, 2004.

[7] F. S. Ligler, "Perspective on optical biosensors and integrated sensor systems," *Anal. Chem.,* vol. 81, pp. 519-526, 01/15, 2009.

[8] F. B. Myers and L. P. Lee, "Innovations in optical microfluidic technologies for point-of-care diagnostics," *Lab on a Chip,* vol. 8, pp. 2015-2031, 12, 2008.

[9] J. C. Love, L. A. Estroff, J. K. Kriebel, R. G. Nuzzo and G. M. Whitesides, "Self-assembled monolayers of thiolates on metals as a form of nanotechnology," *Chem. Rev.,* vol. 105, pp. April, 2005.

[10] S. Ferretti, S. Paynter, D. A. Russell, K. E. Sapsford and D. J. Richardson, "Self-assembled monolayers: a versatile tool for the formulation of bio-surfaces," *TrAC Trends in Analytical Chemistry,* vol. 19, pp. 530-540, 2000.

[11] M. D. Malinsky, K. L. Kelly and G. C. Schatz, "Chain length dependence and sensing capabilities of the localized surface plasmon resonance of silver nanoparticles chemically modified with alkanethiol self-assembled monolayers," *J. Am. Chem. Soc.,* vol. 123, pp. 1471-1482, February 21, 2001.

[12] A. J. Haes and R. P. Van Duyne, "A nanoscale optical biosensor: sensitivity and selectivity of an approach based on the localized surface plasmon resonance spectroscopy of triangular silver nanoparticles," *J. Am. Chem. Soc.,* vol. 124, pp. 10596-10604, 09/01; 2011/12, 2002.

[13] D. K. Schwartz, "Mechanisms and kinetics of self-assembled monolayer formation," *Annu. Rev. Phys. Chem.,* vol. 52, pp. 107-137, 2001.

[14] X. Fan, I. M. White, S. I. Shopova, H. Zhu, J. D. Suter and Y. Sun, "Sensitive optical biosensors for unlabeled targets: A review," *Anal. Chim. Acta,* vol. 620, pp. 8-26, 7/14, 2008.

[15] R. Bashir, "BioMEMS: State-of-the-art in detection, opportunities and prospects," *Adv. Drug Deliv. Rev.,* vol. 56, pp. 1565-1586, 20040922, 2004.

[16] T. James, M. S. Mannoor and D. V. Ivanov, "BioMEMS - Advancing the frontiers of medicine," *Sensors,* vol. 8, pp. 6077-6107, 2008.

[17] Y. Wang, H. Xu, J. Zhang and G. Li, "Electrochemical sensors for clinic analysis," 2008.

[18] G. T. Roman and R. T. Kennedy, "Fully integrated microfluidic separations systems for biochemical analysis," *Journal of Chromatography A,* vol. 1168, pp. 170-188, 10/19, 2007.

[19] Greg T. Hermanson, *Bioconjugate Techniques.* USA: Academic Press, 2008.

[20] D. Wild, *The Immunoassay Handbook.* New York, NY:. Nature Publishing Group: 2005.

[21] E. P. Diamandis and T. K. Christopoulos, *Immunoassay.* San Diego: Academic Press, 1996.

[22] A. H. Ng, U. Uddayasankar and A. R. Wheeler. Immunoassays in microfluidic systems. *Anal Bioanal Chem 397(3),* pp. 991-1007. 2010.

[23] P. Parham, *The Immune System.* New York : London: Garland Pub. ; Current Trends, 2000.

[24] G. B. Pier, *Immunology, Infection, and Immunity.* Washington, D.C.: ASM Press, 2004.

[25] R. P. Ekins, "The estimation of thyroxine in human plasma by an electrophoretic technique," *Clinica Chimica Acta,* vol. 5, pp. 453-459, .

[26] R. S. Yalow and S. A. Berson, "Assay of plasma insulin in human subjects by immunological methods," *Nature,* vol. 184 (Suppl 21), pp. 1648, 1959.

[27] F. Y. H. Lin, Y. Gao, D. Li and P. M. Sherman, "Development of microfluidic-based heterogeneous immunoassays," *Frontiers of Bioscience (Scholar Edition),* vol. 2, pp. 73-78, 2010.

[28] Y. Gao, "Development of a high-throughput electrokinetically-controlled heterogeneous immunoassay microfluidic chip," *Doctoral Dissertation Retrieved from ProQuest Dissertations and Theses,* pp. 1-235, 2008.

[29] J. Homola, *Surface Plasmon Resonance Based Sensors.* Leipzig: Springer, 2006.

[30] J. Homola, "Present and future of surface plasmon resonance biosensors," *Anal Bioanal Chem,* vol. 377, pp. 528-539, 2003.

[31] Y. Sun, X. Liu, D. Song, Y. Tian, S. Bi and H. Zhang, "Sensitivity enhancement of wavelength modulation surface plasmon resonance biosensor by improving the baseline solution," *Anal. Chim. Acta*, vol. 569, pp. 21-26, 5/31, 2006.

[32] Y. Sun, Y. Bai, D. Song, X. Li, L. Wang and H. Zhang, "Design and performances of immunoassay based on SPR biosensor with magnetic microbeads," *Biosensors and Bioelectronics*, vol. 23, pp. 473-478, 11/30, 2007.

[33] K. A. Willets and R. P. Van Duyne, "Localized surface plasmon resonance spectroscopy and sensing," *Annu. Rev. Phys. Chem.*, vol. 58, pp. 267-297, 2007.

[34] W. C. Bigelow, D. L. Pickett and W. A. Zisman, "Oleophobic monolayers : I. Films adsorbed from solution in non-polar liquids," *J. Colloid Sci.*, vol. 1, pp. 513-538, 12, 1946.

[35] R. G. Nuzzo and D. L. Allara, "Adsorption of bifunctional organic disulfides on gold surfaces," *J. Am. Chem. Soc.*, vol. 105, pp. 4481-4483, 06/01, 1983.

[36] Asemblon Co, "Gold Preparation Procedure," 2008.

[37] D. J. Revell, J. R. Knight, D. J. Blyth, A. H. Haines and D. A. Russell, "Self-assembled carbohydrate monolayers: formation and surface selective molecular recognition," *Langmuir*, vol. 14, pp. 4517-4524, 1998.

[38] C. D. Bain and G. M. Whitesides, "Formation of two-component surfaces by the spontaneous assembly of monolayers on gold from solutions containing mixtures of organic thiols," *J. Am. Chem. Soc.*, vol. 110, pp. 6560–6561, 1988.

[39] K. A. Peterlinz and R. Georgiadis, "In situ kinetics of self-assembly by surface plasmon resonance spectroscopy," *Langmuir*, vol. 12, pp. 4731-4740, 1996.

[40] S. C. Terry, J. H. Jerman and J. B. Angell, "A gas chromatographic air analyzer fabricated on a silicon wafer," *Electron Devices, IEEE Transactions on*, vol. 26, pp. 1880-1886, 1979.

[41] A. Manz, N. Graber and H. M. Widmer, "Miniaturized total chemical analysis systems: A novel concept for chemical sensing," *Sensors Actuators B: Chem.*, vol. 1, pp. 244-248, 1, 1990.

[42] G. M. Whitesides, "The origins and the future of microfluidics," *Nature*, vol. 442, pp. 368, 2006.

[43] H. A. Stone and S. Kim, "Microfluidics: Basic issues, applications, and challenges," *AICHE J.*, vol. 47, pp. 1250-1254, 2001.

[44] P. Auroux, D. Iossifidis, D. R. Reyes and A. Manz, "Micro total analysis systems. 2. Analytical standard operations and applications," *Anal. Chem.*, vol. 74, pp. 2637, 2002.

[45] E. Verpoorte, "Beads and chips: new recipes for analysis," *LAB ON A CHIP*, vol. 3, pp. 60N-68N, 2002.

[46] D. Erickson and L., "Electrokinetically controlled DNA hybridization microfluidic chip enabling rapid target analysis," *Anal. Chem.*, vol. 76, pp. 7269-7277, 2004.

[47] S. K. Sia, V. Linder, B. A. Parviz, A. Siegel and G. M. Whitesides, "An integrated approach to a portable and low-cost immunoassay for resource-poor settings," *Angewandte Chemie-International Edition*, vol. 43, pp. 498-502, 2004.

[48] T. Vilkner, D. Janasek and A. Manz, "Micro total analysis systems. Recent developments," *Anal. Chem.*, vol. 76, pp. 3373, 2004.

[49] A. Bange, H. B. Halsall and W. R. Heineman, "Microfluidic immunosensor systems," *Biosens. Bioelectron.*, vol. 20, pp. 2488-2503, 2005.

[50] P. Dittrich and T., "Micro total analysis systems. Latest advancements and trends," *Anal. Chem.*, vol. 78, pp. 3887-3907, 2006.

[51] C. Rivet, H. Lee, A. Hirsch, S. Hamilton and H. Lu, "Microfluidics for medical diagnostics and biosensors," *Chemical Engineering Science*, vol. 66, pp. 1490-1507, 2011.

[52] A. Bernard, B. Michel and E. Delamarche, "Micromosaic Immunoassays," *Anal. Chem.*, vol. 73, pp. 8-12, 01/01, 2001.

[53] C. J. Huang, K. Bonroy, G. Reekmans, W. Laureyn, K. Verhaegen, I. De Vlaminck, L. Lagae and G. Borghs, "Localized surface plasmon resonance biosensor integrated with microfluidic chip," *Biomed Microdevices*, vol. 11, pp. 893-901, 2009.

[54] Z. L. Zhang, C. Crozatier, M. Le Berre and Y. Chen, "In situ bio-functionalization and cell adhesion in microfluidic devices," *Microelectronic Engineering*, vol. 78-79, pp. 556-562, 3, 2005.

[55] S. Choi and J. Chae, "Methods of reducing non-specific adsorption in microfluidic biosensors," *J Micromech Microengineering*, vol. 20, pp. 075015, 2010.

[56] H. Zhu and M. Snyder, "Protein chip technology," *Curr. Opin. Chem. Biol.*, vol. 7, pp. 55-63, 2, 2003.

[57] D. Qin, Y. Xia and G. M. Whitesides, "Rapid prototyping of complex structures with feature sizes larger than 20 mu m," *Adv Mater*, vol. 8, pp. 917-&, 1996.

[58] J. E. Butler, "Comparative studies on the interaction of proteins with a polydimethylsiloxane elastomer. I. Monolayer protein capture capacity (PCC) as a function of protein pl, buffer pH and buffer ionic strength," *Journal of Molecular Recognition*, vol. 10, pp. 36-51, 1997.

[59] D. C. Duffy, J. C. McDonald and J. A. Olivier, "Rapid prototyping of microfluidic systems in poly (dimethylsiloxane)," *Anal. Chem.*, vol. 70, pp. 4974-4984, 1998.

[60] Y. Xia and G. M. Whitesides, "Soft Lithography," *Angewandte Chemie International Edition,* vol. 37, pp. 550-575, 1998.

[61] D. S. Peterson, "Solid supports for micro analytical systems," *Lab on a Chip,* vol. 5, pp. 132-139, 2005.

[62] C. T. Lim and Y. Zhang, "Bead-based microfluidic immunoassays: The next generation," *Biosensors and Bioelectronics,* vol. 22, pp. 1197-1204, 2007.

[63] D. N. Kim, Y. Lee and Won-Gun K., "Fabrication of microfluidic devices incorporating bead-based reaction and microarray- based detection system for enzymatic assay," *Sensors & Actuators: B.Chemical,* vol. 137, pp. 305-312, 2009.

[64] J. N. Anker, W. Paige Hall, O. Lyandres, N. C. Shah, Jing Zhao and R. P. Van Duyne, "Biosensing with plasmonic nanosensors," *Nature Materials,* vol. 7, pp. 442-453, 06, 2008.

[65] W. Tsai and P. Pai, "Surface plasmon resonance-based immunosensor with oriented immobilized antibody fragments on a mixed self-assembled monolayer for the determination of staphylococcal enterotoxin B," *Microchimica Acta,* vol. 166, pp. 115-122, 2009.

[66] A. Kausaite, M. Van Dijk, J. Castrop, A. Ramanaviciene, J. P. Baltrus, J. Acaite and A. Ramanavicius, "Surface plasmon resonance label-free monitoring of antibody antigen interactions in real time," *Biochemistry and Molecular Biology Education,* vol. 35, pp. 57-63, 2007.

[67] S. Balasubramanian, A. Revzin and A. Simonian, "Electrochemical desorption of proteins from gold electrode surface," *Electroanalysis,* vol. 18, pp. 1885-1892, 2006.

[68] J. Soo Ko, H. C. Yoon, H. Yang, H. Pyo, K. Hyo Chung, S. Jin Kim and Tae Kim, "A polymer-based microfluidic device for immunosensing biochips," *Lab on a Chip,* vol. 3, pp. 106-113, .

[69] B. V. Chikkaveeraiah, V. Mani, V. Patel, J. S. Gutkind and J. F. Rusling, "Microfluidic electrochemical immunoarray for ultrasensitive detection of two cancer biomarker proteins in serum," *Biosens. Bioelectron.,* vol. 26, pp. 4477, 2011.

[70] R. Kurita and Y., "On- chip enzyme immunoassay of a cardiac marker using a microfluidic device combined with a portable surface plasmon resonance system," *Anal. Chem.,* vol. 78, pp. 5525-5531, 2006.

[71] R. Kuritaa, Y. Hirataa, S. Yabukia, Y. Yokotaa, D. Katoa, Y. Satoa, F. Mizutanib and O. Niwaa, "Surface modification of thin polyion complex film for surface plasmon resonance immunosensor," *Sensors & Actuators: B.Chemical,* vol. 130, pp. 320-325, 2008.

[72] V. N. Morozov and T. Y. Morozova, "Electrospray deposition as a method to fabricate functionally active protein films," *Anal. Chem.,* vol. 71, pp. 1415, 1999.

[73] G. J. M. Bruin, "Recent developments in electrokinetically driven analysis on microfabricated devices," *Electrophoresis,* vol. 21, pp. 3931-3951, 2000.

[74] D. Li, *Electrokinetics in Microfluidics.* Amsterdam ; Boston : Elsevier Academic, 2004.

[75] J. Eijkel, "The use of capillarity for passive flow handling in lab on a chip devices," *Lab on a Chip, Miniaturization for Chemistry and Biology,* vol. 6, pp. 1405-1408, 2006.

[76] S. Haeberle and R. Zengerle, "Microfluidic platforms for lab-on-a- chip applications," *LAB ON A CHIP,* vol. 7, pp. 1094-1110, 2007.

[77] H. A. Stone, A. D. Stroock and A. Ajdari, "Engineering flows in small devices," *Annual Review of Fluid Mechanics,* vol. 36, pp. 381-411, 2004.

[78] D. Li, "Electro- viscous effects on pressure- driven liquid flow in microchannels," *Colloids Surf. Physicochem. Eng. Aspects,* vol. 195, pp. 35-57, 2001.

[79] M. Madou, J. Zoval, G. Jia, H. Kido, J. Kim and N. Kim, "Lab on a CD," *Annu. Rev. Biomed. Eng.,* vol. 8, pp. 601, 2006.

[80] S. Lai, S. Wang, J. Luo, L. J. Lee, S. Yang and M. J. Madou, "Design of a compact disk-like microfluidic dlatform for enzyme-linked immunosorbent assay," *Anal. Chem.,* vol. 76, pp. 1832-1837, 04/01, 2004.

[81] K. Sato, M. Yamanaka, T. Hagino, M. Tokeshi, H. Kimura and T. Kitamori, "Microchip-based enzyme-linked immunosorbent assay microELISA system with thermal lens detection," *Lab on a Chip, Miniaturization for Chemistry and Biology,* vol. 4, pp. 570-575, 2004.

[82] M. Smoluchowski, "Zur kinetischen theorie der brownschen molekular bewegung undder suspensionen," *Ann. d. Phys,* vol. 21, pp. 756, 1906.

[83] A. Enistein, "On the movement of small particles suspended in a stationary liquid demanded by the molecular-kinetic theory of heat," *Ann. d. Phys,* vol. 17, pp. 549, 1905.

[84] A. Enistein, "On the theory of brownian movement," *Ann. d. Phys.,* vol. 19, pp. 371, 1906.

[85] J. S. Rossier, G. Gokulrangan, H. H. Girault, S. Svojanovsky and G. S. Wilson, "Characterization of protein adsorption and immunosorption kinetics in photoablated polymer microchannels," *Langmuir,* vol. 16, pp. 8489-8494, 2000.

[86] D. Juncker. Simultaneous detection of C-reactive protein and other cardiac markers in human plasma using micromosaic immunoassays and self-regulating microfluidic networks. *Biosens. Bioelectron. 19(10),* pp. 1193-1202. 2004.

[87] S. Rodriguez-Mozaz. Analysis of bisphenol A in natural waters by means of an optical immunosensor. *Water Res. 39(20),* pp. 5071-5079. 2005.

[88] S. Rodriguez-Mozaz. Simultaneous multi-analyte determination of estrone, isoproturon and atrazine in natural waters by the RIver ANAlyser (RIANA), an optical immunosensor. *Biosens. Bioelectron. 19(7),* pp. 633-640. 2004.

[89] D. Hoegger, P. Morier, C. Vollet, D. Heini, F. Reymond, J. Rossier and S. Rossier, "Disposable microfluidic ELISA for the rapid determination of folic acid content in food products," *Anal Bioanal Chem,* vol. 387, pp. 267-275, 2007.

[90] K. S. Phillips and Q. Cheng, "Microfluidic immunoassay for bacterial toxins with supported phospholipid bilayer membranes on poly(dimethylsiloxane)," *Anal. Chem.,* vol. 77, pp. 327-334, 2005.

[91] M. Tavaria, T. Gabriele, I. Kola and R. Anderson, "A hitchhiker's guide to the human Hsp70 family," *Cell Stress Chaperones,* vol. 1, pp. 23-28, 1996.

[92] M. M. Vijayan, C. Pereira, G. Kruzynski and G. K. Iwama, "Sublethal concentrations of contaminant induce the expression of hepatic heat shock protein 70 in two salmonids," *Aquatic Toxicology,* vol. 40, pp. 101-108, 1, 1998.

[93] G. K. Iwama, P. T. Thomas, R. H. B. Forsyth and M. M. Vijayan, "Heat shock protein expression in fish," *Biomedical and Life Sciences,* vol. 8, pp. 35-56, 1998.

[94] B. Vinocur and A. Altman, "Recent advances in engineering plant tolerance to abiotic stress: achievements and limitations," *Curr. Opin. Biotechnol.,* vol. 16, pp. 123-132, 4, 2005.

[95] I. J. Benjamin and D. R. McMillan, "Stress (heat shock) proteins - Molecular chaperones in cardiovascular biology and disease," *Circulation Research,* vol. 83, pp. 117-132, 1998.

[96] M. Nishikawa, S. Takemoto and Y. Takakura, "Heat shock protein derivatives for delivery of antigens to antigen presenting cells," *International Journal of Pharmaceutics,* vol. 354, pp. 23-27, 2008.

[97] H. Bendz, S. C. Ruhland, M. J. Pandya, O. Hainzl, S. Riegelsberger, C. Brauechle, M. P. Mayer, J. Buchner, R. D. Issels and E. Noessner, "Human Heat Shock Protein 70 Enhances Tumor Antigen Presentation through Complex Formation and Intracellular Antigen Delivery without Innate Immune Signaling," *J. Biol. Chem.,* vol. 282, pp. 31688-31702, Oct, 2007.

[98] A. J. McClellan and J. Frydman, "Molecular chaperones and the art of recognizing a lost cause," *Nature Cell Biology,* vol. 3, pp. 51-53, 2001.

[99] U. Feige, R. I. Morimoto, I. Yahara and B. S. Polla, *Stress-Inducible Cellular Responses.* Germany: Birkhausel Verlag, 1996.

[100] H. Sakahira, P. Breuer, M. K. Hayer-Hartl and F. U. Hartl, "Molecular chaperones as modulators of polyglutamine protein aggregation and toxicity," *Proceedings of the National Academy of Sciences of the United States of America,* vol. 99, pp. 16412-16418, 2002.

[101] C. Georgopoulos and W. J. Welch, "Role of the major heat shock proteins as molecular chaperones," *Annual Review of Cell Biology*, pp. 601-634, 1993.

[102] D. A. Parsell, A. S. Kowal, M. A. Singer and S. Lindquist, "Protein disaggregation mediated by heat-shock protein Hsp104," *Nature*, vol. 372, pp. 475-478, 1994.

[103] A. Banh, M. M. Vijayan and J. G. Sivak, "Hsp70 in bovine lenses during temperature stress," *Molecular Vision*, vol. 9, pp. 323-328, 2003.

[104] F. Schramm, J. Larkindale, E. Kiehlmann, A. Ganguli, G. Englich, E. Vierling and P. Von Koskull-Doring, "A cascade of transcription factor DREB2A and heat stress transcription factor HsfA3 regulates the heat stress response of Arabidopsis," *Plant Journal*, vol. 53, pp. 264-274, 2008.

[105] J. B. Cara, N. Aluru, F. J. Moyano and M. M. Vijayan, "Food-Deprivation induces HSP70 and HSP90 protein expression in larval gilthead sea bream and rainbow trout," *Comparative Biochemistry and Physiology, Part B*, vol. 142, pp. 426-431, 2005.

[106] E. S. Chang, "Stressed-out lobsters: Crustacean hyperglycemic hormone and stress proteins," *Integrative and Comparative Biology*, vol. 45, pp. 43-50, 2005.

[107] C. Methling, N. Aluru, M. M. Vijayan and J. F. Steffensen, "Effect of moderate hypoxia at three acclimation temperatures on stress responses in Atlantic cod with different haemoglobin types," *Comparative Biochemistry and Physiology, Part A*, vol. 156, pp. 485-490, 2010.

[108] C. Corporeau and M. Auffret, "In situ hybridisation for flow cytometry: A molecular method for monitoring stress-gene expression in hemolymph cells of oysters," *Aquatic Toxicology*, vol. 64, pp. 427-435, 2003.

[109] S. Wiseman, E. H. Jorgensen, A. G. Maule and M. M. Vijayan, "Contaminant loading in remote Arctice lakes affects cellular stress-related proteins expression in feral charr," *Polar Biology*, vol. 34, pp. 933-937, 2011.

[110] J. Roigas, E. S. Wallen, S. A. Loening and P. L. Moseley, "Heat shock protein (HSP72) surface expression enhances the lysis of a human renal cell carcinoma by IL-2 stimulated NK cells," *Adv. Exp. Biol.*, vol. 451, pp. 225-229, 1998.

[111] G. Multhoff, C. Botzler, L. Jennen, J. Schmidt, J. Ellwart and R. Issels, "Heat shock protein 72 on tumor cells: a recognition structure for natural killer cells," *The Journal of Immunology*, vol. 158, pp. 4341-4350, 1997.

[112] C. Botzler, H. J. Kolb, R. D. Issels and G. Multhoff, "Noncytotoxic alkyl-lysophospholipid treatment increases sensitivity of leukemic K562 cells to lysis by natural killer (NK) cells," *Int. J. Cancer*, vol. 65, pp. 633-638, 1996.

[113] G. Multhoff, C. Botzler, M. Wiesnet, G. Eibner and R. Issels, "CD3-large granular lymphocytes recognize a heat-inducible immunogenic determinant associated with the 72-kD heat shock protein on human sarcoma cells," *Blood,* vol. 86, pp. 1374-1382, 1995.

[114] R. Suto and P. K. Srivastava, "A mechanism for the specific immunogenicity of heat shock protein-chaperoned peptides," *Science,* vol. 269, pp. 1585-1588, 1995.

[115] H. Udono and P. K. Srivastava, "Heat Shock Protein 70-associated Peptides Elicit Specific Cancer Immunity," *J. Exp. Med.,* vol. 178, pp. 1391-1396, 1993.

[116] P. Matzinger, "The danger model: a renewed sense of self," *Science,* vol. 296, pp. 301-305, 2002.

[117] P. Matzinger, "Tolerance, danger, and the extended family," *Annu. Rev. Immunol.,* vol. 12, pp. 991-1045, 1994.

[118] M. Santarosa, D. Favaro, M. Quaia and E. Galligioni, "Expression of Heat Shock Protein 72 in Renal Cell Carcinoma: Possible Role and Prognostic Implications in Cancer Patients," *European Journal of Cancer,* vol. 33, pp. 873-877, 1997.

[119] K. Nanbu, I. Konishi, M. Mandai, H. Kuroda, A. A. Hamid, T. Komatsu and T. Mori, "Prognostic significance of heat shock proteins HSP70 and HSP90 in endometrial carcinomas," *Cancer Detection and Prevention,* vol. 22, pp. 549-55, 1998.

[120] S. Ray, Y. Lu, S. H. Kaufmann, C. W. Gustafson, J. E. Karp, I. Boldogh, A. P. Fields and A. R. Brasier, "Genomic mechanisms of p210BCR-ABL signaling: induction of heat shock protein 70 through the gata response element confers resistance to paclitaxel-induced apoptosis," *The Journal of Biological Chemistry,* vol. 279, pp. 35604-35615, 2004.

[121] M. Abe, J. B. Manola, W. K. Oh, D. L. Parslow, D. J. George, C. L. Austin and P. W. Kantoff, "Plasma levels of heat shock protein 70 in patients with prostate cancer: a potential biomarker for prostate cancer," *Clinical Prostate Cancer,* vol. 3, pp. 49-53, 2004.

[122] G. Valen, G. K. Hansson, A. Dumitrescu and J. Vaage, "Unstable angina activates myocardial heat shock protein 72, endothelial nitric oxide synthase, and transcription factors NFkB and AP-1," *Cardiovascular Research,* vol. 47, pp. 49-56, 2000.

[123] S. G. Thompson, J. Kienast, S. D. M. Pyke, F. Haverkate and Van De Loo, Jurgen C.W., "Hemostatic factors and the risk of myocardial infarction or sudden death in patients with angina pectoris," *The New England Journal of Medicine,* vol. 332, pp. 635-641, 1995.

[124] A. A. Knowlton, S. Kapadia, G. Torre-Amione, J. Durand, R. Blies, J. Young and D. L. Mann, "Differential expression of heat shock proteins in normal and failing human hearts," *Journal of Molecular and Cellular Cardiology,* vol. 30, pp. 811-818, 1998.

[125] S. G. Han, V. Castranova and V. Vallyathan, "Heat shock protein 70 as an indicator of early lung injury caused by exposure to arsenic," *Molecular and Cellular Biochemistry,* vol. 277, pp. 153-164, 2005.

[126] N. M. Green, "Avidin," *Advances in Protein Chemistry,* vol. 29, pp. 85-133, 1957.

[127] G. Hu, Y. Gao and D. Li, "Modeling micropatterned antigen-antibody binding kinetics in a microfluidic chip," *Biosensors Bioelectron.,* vol. 22, pp. 1403-1409, 15 Feb, 2007.

[128] A. Hatch, A. E. Kamholz, K. R. Hawkins, M. S. Munson, E. A. Schilling, B. H. Weigl and P. Yager, "A rapid diffusion immunoassay in a T-sensor," *Nat Biotech,* vol. 19, pp. 461-465, print, 2001.

[129] G. Hu, Y. Gao, P. M. Sherman and D. Li, "A microfluidic chip for heterogeneous immunoassay using electrokinetical control," *Microfluid Nanofluid,* vol. 1, pp. 346-355, 2005.

[130] D. G. Myszka, T. A. Morton, M. L. Doyle and I. M. Chaiken, "Kinetic analysis of a protein antigen-antibody interaction limited by mass transport on an optical biosensor," *Biophys. Chem.,* vol. 64, pp. 127-137, 2/28, 1997.

[131] D. G. Myszka, X. He, M. Dembo, T. A. Morton and B. Goldstein, "Extending the range of rate constants available from BIACORE: interpreting mass transport-influenced binding data," *Biophys. J.,* vol. 75, pp. 583-594, 8, 1998.

[132] P. Schuck, "Kinetics of ligand binding to receptor immobilized in a polymer matrix, as detected with an evanescent wave biosensor. I. A computer simulation of the influence of mass transport," *Biophys. J.,* vol. 70, pp. 1230-1249, 3, 1996.

[133] R. A. Vijayendran, F. S. Ligler and D. E. Leckband, "A computational reaction-diffusion model for the analysis of transport-limited kinetics," *Anal. Chem.,* vol. 71, pp. 5405-5412, 12/01, 1999.

[134] M. Zimmermann, E. Delamarche, M. Wolf and P. Hunziker, "Modeling and optimization of high-sensitivity, low-volume microfluidic-based surface immunoassays," *Biomed. Microdevices,* vol. 7, pp. 99-110, 06, 2005.

[135] S. Jomeh and M. Hoorfar, "Numerical modeling of mass transport in microfluidic biomolecule-capturing devices equipped with reactive surfaces," *Chem. Eng. J.,* vol. 165, pp. 668-677, 12/1, 2010.

[136] M. Sigurdson, Dazhi Wang and C. D. Meinhart, "Electrothermal stirring for heterogeneous immunoassays," *Lab on a Chip,* vol. 5, pp. 1366-1373, 12, 2005.

[137] H. C. Feidman, M. Sigurdson and C. D. Meinhart, "AC electrothermal enhancement of heterogeneous assays in microfluidics," *Lab on a Chip,* vol. 7, pp. 1553-1559, 11, 2007.

[138] T. Gervais and K. F. Jensen, "Mass transport and surface reactions in microfluidic systems," *Chemical Engineering Science,* vol. 61, pp. 1102-1121, 2, 2006.

[139] T. Squires and S. Quake, "Microfluidics: Fluid physics at the nanoliter scale," *Review of Modern Physics*, vol. 77, pp. 977-1016, 2005.

[140] F. M. White, *Fluid Mechanics.* Dubuque, IA: McGraw-Hill, 2008.

[141] S. Childress, *An Introduction to Theoretical Fluid Mechanics.* New York, NY: American Mathematical Society, 2009.

[142] L. S. Jung and C. T. Campbell, "Sticking probabilities in adsorption of alkanethiols from liquid ethanol solution onto gold," *The Journal of Physical Chemistry B,* vol. 104, pp. 11168-11178, November 30, 2000.

[143] M. Himmelhaus, F. Eisert and M. Buck, "Self-assembly of n-alkanethiol monolayers. A study by IR-visible sum frequency spectroscopy (SFG)," *The Journal of Physical Chemistry B,* vol. 104, pp. 576-584, January 27, 2000.

[144] L. Jung and C. Campbell, "Sticking probabilities in adsorption from liquid solutions: Alkylthiols on gold," *Physical Review Letters,* vol. 84, pp. 5164-5167, 2000.

[145] H. M. Schessler, D. S. Karpovich and G. J. Blanchard, "Quantitating the balance between enthalpic and entropic forces in alkanethiol/gold monolayer self-assembly," *J. Am. Chem. Soc.,* vol. 118, pp. October, 1996.

[146] S. Xu, S. Cruchon-Dupeyrat, J. Garno, G. Liu, G. Jennings, T. Yong and P. Laibinis, "In situ studies of thiol self-assembly on gold from solution using atomic force microscopy," *Journal of Chemical Physics,* vol. 108, pp. 5002-5012, 1998.

[147] F. S. Damos, R. C. S. Luz and L. T. Kubota, "Determination of thickness, dielectric constant of thiol films, and kinetics of adsorption using surface plasmon resonance," *Langmuir : The ACS Journal of Surfaces and Colloids,* vol. 21, pp. 602-609, Jan 18, 2005.

[148] R. Shelkov, M. Nahmany and A. Melman, "Selective esterifications of alcohols and phenols through carbodiimide couplings," *Organic and Biomolecular Chemistry,* vol. 2, pp. 397-401, 20040207, 2004.

[149] L. C. Chan and B. G. Cox, "Kinetics of amide formation through carbodiimide/n-hydroxybenzotriazole (HOBt) couplings," *J. Org. Chem.,* vol. 72, pp. 8863-8869, 11/01, 2007.

[150] A. Williams and I. T. Ibrahim, "A new mechanism involving cyclic tautomers for the reaction with nucleophiles of the water-soluble peptide coupling reagent 1-ethyl-3-(3'-(dimethylamino)propyl)carbodiimide (EDC)," *J. Am. Chem. Soc.,* vol. 103, pp. 7090-7095, 12/01, 1981.

[151] S. Sam, L. Touahir, J. Salvador Andresa, P. Allongue, J. -. Chazalviel, L. A. Gouget, d. V. Henry, A. Moraillon, F. Ozanam, N. Gabouze and S. Djebbar, "Semiquantitative study of the

EDC/NHS activation of acid terminal groups at modified porous silicon surfaces," *Langmuir,* vol. 26, pp. 809-814, 01/19, 2010.

[152] COMSOL AB (1998), *COMSOL Multiphysics Reference Guide: Time-Dependent Solver*. Stockholm, Sweden: 2011.

[153] G. R. G. Liu, *The Finite Element Method : A Practical Course*. Oxford ; Boston: Butterworth-Heinemann, 2003.

[154] K. Nam, T. Kimura and A. Kishida, "Controlling coupling reaction of EDC and NHS for preparation of collagen gels using ethanol/water co- solvents," *Macromolecular Bioscience,* vol. 8, pp. 32, 2008.

[155] Y. Sun, N. Bi, D. Song, Y. Bai, L. Wang and H. Zhang, "Preparation of titania sol–gel matrix for the immunoassay by SPR biosensor with magnetic beads," *Sensors Actuators B: Chem.,* vol. 134, pp. 566-572, 9/25, 2008.

[156] C. Lin, H. Chen, C. Yu, P. Lu, C. Hsieh, B. Hsieh, Y. Chang and C. Chou, "Quantitative measurement of binding kinetics in sandwich assay using a fluorescence detection fiber-optic biosensor," *Anal. Biochem.,* vol. 385, pp. 224-228, 2/15, 2009.

[157] C. Vieu, F. Carcenac, A. Pépin, Y. Chen, M. Mejias, A. Lebib, L. Manin-Ferlazzo, L. Couraud and H. Launois, "Electron beam lithography: resolution limits and applications," *Appl. Surf. Sci.,* vol. 164, pp. 111-117, 2000.

[158] R. C. Denomme, "A label-free biosensor for heat shock protein 70 using localized surface plasmon resonance," *Master's Thesis Retrieved from UWSpace*, pp. 1-89, 2012.

[159] S. Asiaei, R. C. Denomme, C. Marr, P. M. Nieva and M. M. Vijayan, "Fast self-assembly kinetics of alkanethiols on gold nanoparticles: Simulation and characterization by localized surface plasmon resonance spectroscopy," in *SPIE: Microfluidics, BioMEMS, and Medical Microsystems*, San Francisco, California, USA, 2012, pp. 825107.

[160] L. Zhengjian, W. Jianhua and C. Guoping, "The wettability and topography of self-assembled protein monolayer linked by alkanethiols," in *3rd International Conference on Bioinformatics and Biomedical Engineering, iCBBE 2009, 2009, Startdate 20090611-Enddate 20090613*, Beijing, 2009, pp. 1-4.

[161] M. Veiseh, M. H. Zareie and M. Zhang, "Highly selective protein patterning on gold-silicon substrates for biosensor applications," *Langmuir,* vol. 18, pp. 6671-6678, 08/01, 2002.

[162] U. Nobbmann, M. Connah, B. Fish, P. Varley, C. Gee, S. Mulot, J. Chen, L. Zhou, Y. Lu, F. Sheng, J. Yi and S. E. Harding, "Dynamic light scattering as a relative tool for assessing the molecular integrity and stability of monoclonal antibodies," *Biotechnology and Genetic Engineering Reviews,* vol. 24, pp. 117-128, 2007.

[163] M. Gunkel, F. Erdel, K. Rippe, P. Lemmer, R. Kaufmann, C. Hörmann, R. Amberger and C. Cremer, "Dual color localization microscopy of cellular nanostructures," *Biotechnology Journal,* vol. 4, pp. 927-938, 2009.

[164] P. J. Eaton, *Atomic Force Microscopy.* Oxford: Oxford : Oxford University Press, 2010.

[165] T. Vo-Dinh, "Biosensors and biochips: advances in biological and medical diagnostics," *Fresenius J. Anal. Chem.,* vol. 366, pp. 540-551, 2000.

[166] E. Briand, C. Gu, S. Boujday, M. Salmain, J. M. Herry and C. M. Pradier, "Functionalisation of gold surfaces with thiolate SAMs: Topography/bioactivity relationship - A combined FT-RAIRS, AFM and QCM investigation," *Surf Sci,* vol. 601, pp. 3850-3855, 15 Sept., 2007.

[167] L. Wang, C. Wu, Z. Hu, Y. Zhang, R. Li and P. Wang, "Sensing Escherichia coli O157:H7 via frequency shift through a self-assembled monolayer based QCM immunosensor," *Journal of Zhejiang University: Science B,* vol. 9, pp. 121-131, Feb., 2008.

[168] G. Sauerbrey, "The use of quartz oscillators for weighing thin layers and for microweighing," *Zeitschrift Für Physik (1959),* vol. 155, pp. 206-222, 1959.

[169] Stanford research systems (1980), *QCM 200, Operation and Service Manual.* Sunnyvale, CA: 2010.

[170] F. Hook, M. Rodahl, P. Brzezinski and B. Kasemo, "Energy dissipation kinetics for protein and antibody-antigen adsorption under shear oscillation on a quartz crystal microbalance," *Langmuir,* vol. 14, pp. 729-734, 02/01; 2012/04, 1998.

[171] M. Thompson, C. L. Arthur and G. K. Dhaliwal, "Liquid-phase piezoelectric and acoustic transmission studies of interfacial immunochemistry," *Anal. Chem.,* vol. 58, pp. 1206-1209, 05/01; 2012/04, 1986.

[172] M. D. Ward and D. A. Buttry, "In situ interfacial mass detection with piezoelectric transducers," *Science,* vol. 249, pp. 1000-1007, August 31, 1990.

[173] H. Su, S. Chong and M. Thompson, "Interfacial hybridization of RNA homopolymers studied by liquid phase acoustic network analysis," - *Langmuir,* vol. 12, pp. 2247-2255, 1996.

[174] M. Muratsugu, F. Ohta, Y. Miya, T. Hosokawa, S. Kurosawa, N. Kamo and H. Ikeda, "Quartz crystal microbalance for the detection of microgram quantities of human serum albumin: relationship between the frequency change and the mass of protein adsorbed," - *Anal. Chem.,* vol. 65, pp. 2933, 1993.

[175] F. Caruso, D. N. Furlong and P. Kingshott, "Characterization of ferritin adsorption onto gold," *J. Colloid Interface Sci.,* vol. 186, pp. 129-140, 2/1, 1997.

[176] C. Zhou, J. Friedt, A. Angelova, K. Choi, W. Laureyn, F. Frederix, L. A. Francis, A. Campitelli, Y. Engelborghs and G. Borghs, "Human immunoglobulin adsorption investigated by means of quartz crystal microbalance dissipation, atomic force microscopy, surface acoustic wave, and surface plasmon resonance techniques," *Langmuir*, vol. 20, pp. 5870-5878, 07/01; 2012/04, 2004.

[177] V. Silin, H. Weetall and D. J. Vanderah, "SPR studies of the nonspecific adsorption kinetics of human IgG and BSA on gold surfaces modified by self-assembled monolayers (SAMs)," *J. Colloid Interface Sci.*, vol. 185, pp. 94-103, 1/1, 1997.

[178] K. E. Nelson, L. Gamble, L. S. Jung, M. S. Boeckl, E. Naeemi, S. L. Golledge, T. Sasaki, D. G. Castner, C. T. Campbell and P. S. Stayton, "Surface characterization of mixed self-assembled monolayers designed for streptavidin immobilization," *Langmuir*, vol. 17, pp. 2807-2816, 05/01, 2001.

[179] T. Park, J. Choo, M. Lee, Y. S. Kim, E. K. Lee and H. S. Lee, "Enhancement of the protein loading density by a pre-cleaning process of a gold substrate: Confocal laser scanning microscopic study," *Analytical Sciences*, vol. 20, pp. 1255-1258, 2004.

[180] Safety office, University of Waterloo (1957). Hazardous waste segregation. *(2012, 10/24)*, 2006.

[181] University of Waterloo (1957), *University of Waterloo Safety Manual*. Waterloo, ON: 2010.

[182] S. A. Christine Wittmann, *Immobilisation of DNA on Chips I*. Germany: Springer, 2005.

[183] H. G. Hansma, L. I. Pietrasanta, I. D. Auerbach, C. Sorenson, R. Golan and P. A. Holden, "Probing biopolymers with the atomic force microscope: A review," *Journal of Biomaterials Science, Polymer Edition*, vol. 11, pp. 675-683, 2000.

[184] A. Vertova, A. Forlini and S. Rondinini, "Probing the electron transfer process of cytochrome c embedded in mixed thiol SAM on electrodeposited gold," *J. Electrochem. Soc.*, vol. 159, pp. 81, 2012.

[185] Carl Zeiss MicroImaging GmbH, Germany, "Axio observer inverted microscope manual," 2008.

[186] P. Lemmer and G., "Using conventional fluorescent markers for far-field fluorescence localization nanoscopy allows resolution in the 10-nm range," *J. Microsc.*, vol. 235, pp. 163-171, 2009.

[187] D. Baddeley, C. Batram, Y. Weiland, C. Cremer and U. J. Birk, "Nanostructure analysis using spatially modulated illumination microscopy," *Nature Protocols*, vol. 2, pp. 2640-2646, 2007.

[188] J. Reymann, D. Baddeley, M. Gunkel, P. Lemmer, W. Stadter, T. Jegou, K. Rippe, C. Cremer and U. Birk, "High-precision structural analysis of subnuclear complexes in fixed and live cells via

spatially modulated illumination (SMI) microscopy," *Chromosome Res.*, vol. 16, pp. 367-382, May, 2008.